Dynamics in the Hopf bundle, the geometric phase and implications for dynamical systems

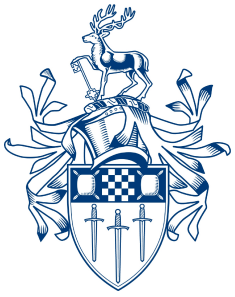

Rupert Way

Department of Mathematics
University of Surrey, U.K.

A thesis submitted for the degree of
Doctor of Philosophy

December 2008

Abstract

A Hopf bundle framework is constructed within $\mathbb{C}^n$, in terms of which general paths on $\mathbb{C}^n \setminus \{0\}$ are viewed and analyzed. The resulting hierarchy of spaces is addressed both theoretically and numerically, and the consequences for numerics and applications are investigated through a wide range of numerical experiments.

The geometric reframing of $\mathbb{C}^n$ in this way - in terms of an intrinsic fibre bundle - allows for the introduction of bundle-theoretic quantities in a general dynamical setting. The roles of the various structural elements of the bundle are explored, including horizontal and vertical subspaces, parallel translation and connections. These concepts lead naturally to the association of a unique geometric phase with each path on $\mathbb{C}^n \setminus \{0\}$. This phase quantity is interpreted as a measure of the spinning in the S^1 fibre of the Hopf bundle induced by paths on $\mathbb{C}^n \setminus \{0\}$, relative to a given connection, and is shown to be an important quantity.

The implications of adopting this bundle viewpoint are investigated in two specific contexts. The first is the case of the lowest-dimensional Hopf bundle, $S^1 \to S^3 \to S^2$. Here the quaternionic matrices are used to develop a simplified, geometrically intuitive formulation of the bundle structure, and a reduced expression for the phase is used to compute numerical phase results in three example systems. The second is the case where paths in $\mathbb{C}^n \setminus \{0\}$ are generated by solutions to a particular class of parameter-dependent first-order ODEs. This establishes a direct link between the dynamical characteristics of such systems and the underlying bundle geometry. A variety of systems are examined and numerical phase results compiled. The numerics reveal an important correlation between the spectral properties of the path-generating ODEs and the resultant geometric phase change values. The details of this observed link are recorded in a conjecture.

Acknowledgements

I would like to thank my supervisor, Professor Tom Bridges.

Contents

Chapter 1

Introduction

This thesis explores the concept of geometrically reframing a class of dynamical problems in order to expose and utilize elements of underlying structure. The focus of the investigation is the Hopf bundle. This is an S^1 fibre bundle, which may be regarded as sitting within each copy of $\mathbb{C}^n \setminus \{0\}$. Paths of vectors in $\mathbb{C}^n \setminus \{0\}$ are described and analyzed in terms of this framework, giving rise to geometrical elements rarely considered in the context of such paths, let alone in the context of the dynamical systems which often generate them. The *geometrical phase* associated with any such path is a measure of the motion induced within the S^1 fibres of the bundle by the path on $\mathbb{C}^n \setminus \{0\}$; it is seen to be an important quantity. This work addresses these concepts not only from a theoretical perspective, but also from a numerical perspective, with emphasis placed on the practical computation of the phase and other related numerical results.

1.1 Overview

The Hopf bundle $S^1 \to S^{2n-1} \to \mathbb{C}P^{n-1}$ is a principal fibre bundle with fibre S^1 and total space S^{2n-1}. Standard spherical projection maps paths in $\mathbb{C}^n \setminus \{0\}$ to paths on S^{2n-1}, which may then be viewed in terms of this bundle structure. This procedure provides a way of dividing up the motion of paths induced on S^{2n-1} in to motion on the base manifold $\mathbb{C}P^{n-1}$ plus motion in the fibres S^1. We are thus able to associate *bundle-theoretic* quantities and characteristics with *general paths on* $\mathbb{C}^n \setminus \{0\}$.

In order to fully describe motion induced within fibres, a connection is required. This is a mathematical rule defining how to pass horizontally from fibre to fibre within the bundle; it is essentially a way of calibrating motion in the fibres of the bundle. This work develops all of these concepts in detail, showing precisely how

they fit together to culminate in the observation that each path in $\mathbb{C}^n \setminus \{0\}$ has associated with it a unique phase quantity which describes the spinning in the fibres induced by the motion on $\mathbb{C}^n \setminus \{0\}$, relative to some given calibration. Often called the geometric phase, this quantity can be thought of as an underlying geometric "ticking-clock" mechanism associated with any such path. Of particular interest is the phase change associated with *closed* paths in $\mathbb{C}^n \setminus \{0\}$. The choice of connection is seen to be central to the calculation of the phase.

The lowest-dimensional ($n = 2$) case provides an opportunity to gain an intuitive understanding of the geometrical structures in use here. In this case the bundle is called the classical Hopf bundle, $S^1 \to S^3 \to S^2$, and the spaces are of low enough dimension for aspects of the geometry to be concretely visualizable. The horizontal and vertical spaces of this bundle are described in terms of the well-known quaternionic matrices, and this leads to simplified, explicit expressions for all the geometric features considered.

The thesis then proceeds to consider the subject from a numerical perspective, describing the development of several Matlab programs which compute the geometrical phase for certain classes of paths in $\mathbb{C}^n \setminus \{0\}$. Both the $\mathbb{C}^2$ case (using the reduced quaternionic matrix formulation) and the general $\mathbb{C}^n$ case are addressed. For most of the numerical phase calculations, the starting point is a system of the form

$$\begin{aligned} &u_x = A(x,\lambda)u \\ &x \in I \subset \mathbb{R}, \quad \lambda \in \Lambda \subset \mathbb{C}, \quad u \in \mathbb{C}^n \setminus \{0\}, \quad A \in M_n(\mathbb{C}) \end{aligned} \tag{1.1}$$

with given boundary conditions, where $A(x,\lambda)$ is an $n \times n$ matrix depending analytically on λ and differentiably on x, and I and Λ are given subsets. The typical case considered is when λ is an eigenvalue parameter, the x-domain is doubly-infinite ($I = \mathbb{R}$), and the matrix $A(x,\lambda)$ is asymptotically constant w.r.t. x in both directions:

$$A_\infty(\lambda) := \lim_{x \to \pm\infty} A(x,\lambda) \qquad \forall \lambda \in \Lambda \tag{1.2}$$

A number of paths in $\mathbb{C}^n \setminus \{0\}$ are defined with reference to this system, some explicitly in terms of its solutions. Computation of the phase associated with such paths creates a direct bridge between dynamical properties of the system and the underlying bundle structure defined here. Initial numerical results lead to the central conjecture of the thesis, which implies that computing the phase change associated with a very specific form of closed path in $\mathbb{C}^n \setminus \{0\}$ allows us to calculate the locations of discrete eigenvalues λ of the system (1.1) used to generate that path.

The remainder of the thesis investigates numerical phase results in a range of systems associated with different physical problems, of varying dimension and asymptotic structure. Current research problems are addressed and the results, often supportive of the central conjecture, are fascinating. These numerics constitute an investigation of the Hopf fibre bundle and the induced phase in a numerical context.

1.2 Background and motivation

Eigenvalue/eigenfunction systems of the form (1.1), (1.2) arise frequently in a wide range of applications, including hydrodynamics, quantum physics and physiology. Linear systems such as these commonly result from the linearization of a nonlinear system, for example during the linearization of a PDE about a solitary wave solution. Such spectral problems have recently been addressed using exterior algebra and the Evans function, to determine discrete eigenvalues which correspond to bounded eigenfunctions, as described in [1]. The analyses involve (i) determining the eigenvectors and eigenvalues of $A_\infty(\lambda)$, (ii) selecting the most attractive and most repellent eigenvectors (i.e. those corresponding to eigenvalues of most positive and most negative real parts), (iii) integrating the system $u_x = Au$ separately from each of these initial condition vectors along 1-dimensional spaces, and finally (iv) applying a matching (Evans) function to the resulting solutions to determine the admissibility of the solution as a whole. The details of this, the Evans function method, are not relevant to this work, however the technique does illustrate the importance of preferred subspaces in asymptotic problems like this. Indeed this observation originally motivated many of the ideas of this thesis - specifically the notion of using structures inherent to a problem to break up the system space in to smaller spaces, such as 1-dimensional spaces, e.g. S^1 fibres.

The Evans function method is applied in [2] and [3] to the stability analyses of solutions in hydrodynamics, in [4] to the stability analysis of travelling wave solutions of a KdV-Burgers equation, in [5] to the stability analysis of a Hocking-Stewartson pulse solution to the complex Ginzburg-Landau equation, and in [6] to the stability analysis of solutions of the fifth-order KdV equation.

A topic closely related to this work is the Berry phase in quantum mechanics, although expositions of this concept deal exclusively in quantum systems, as seen in [7], [8], [9] and [14].

1.3 The test-case

Throughout the work we refer to the following system on $\mathbb{C}^2$, which we call the "test-case":

$$u_x = A(x,\lambda)u, \qquad x \in \mathbb{R},\ \lambda \in \Lambda = \mathbb{C} \setminus \{(-\infty,-1]\},\ u = \begin{pmatrix} u_1 \\ u_2 \end{pmatrix} \in \mathbb{C}^2 \tag{1.3}$$

where

$$A(x,\lambda) = \begin{pmatrix} 0 & 1 \\ \lambda + 1 - 2f(x) & 0 \end{pmatrix} \tag{1.4}$$

$$f(x) = \frac{3}{2}\mathrm{sech}^2\frac{1}{2}x \tag{1.5}$$

This system is derived from a PDE problem in quantum mechanics; it is of the form (1.1), (1.2) and is amenable to analysis in the $n = 2$ classical Hopf bundle framework as described above. It is analytically solvable and has isolated eigenvalues $\lambda = -3/4, 0, 5/4$ and a continuous spectrum on the real axis along $(-\infty, -1]$ (which explains the choice of Λ). The system-at-infinity is

$$A_\infty(\lambda) = \lim_{x\to\pm\infty} A(x,\lambda) = \begin{pmatrix} 0 & 1 \\ \lambda + 1 & 0 \end{pmatrix} \tag{1.6}$$

which has eigenvalues $\mu_\pm(\lambda) = \mp\sqrt{\lambda+1}$ with associated eigenvectors $\xi_\pm(\lambda) = \begin{pmatrix} 1 \\ \mp\sqrt{\lambda+1} \end{pmatrix}$. For the eigenvector of $A_\infty(\lambda)$ corresponding to the eigenvalue of most negative real part write

$$u_\infty(\lambda) = \xi_+(\lambda) = \begin{pmatrix} 1 \\ -\sqrt{\lambda+1} \end{pmatrix} \tag{1.7}$$

Remark 1.3.1. *As notation, for $u \in \mathbb{C}^n$ the complex conjugate transpose is written $u^H := \bar{u}^T$, and the norm is $|u| = (u^H u)^{1/2}$.*

1.4 Thesis outline

Broadly speaking, the first half of the thesis concerns theoretical developments, while the second half concerns numerical investigations.

Chapter 2 is a review of fibre bundle theory. It is intuitive and geometric in nature, with great emphasis placed on visualizing the various structures involved. This approach is particularly appropriate given the numerical context of many of the later results, and the consequent need for a solid geometrical interpretation.

Chapter 3 develops the Hopf bundle framework in detail, including local coordinates, parallel translation and the natural connection. It sets out the logical sequence of concepts leading to the precise description of the phase associated with a path in $\mathbb{C}^n \setminus \{0\}$, for both general paths and paths generated by solving linear systems.

Chapter 4 considers the $n = 2$ classical Hopf bundle in closer detail. Simplified expressions for bundle elements are derived in terms of the quaternionic matrices. Connections are considered, and the natural connection is shown to be the only connection in this bundle. A simplified expression for the phase is derived, again in terms of the quaternionic matrices, and numerical phase results for three systems are presented, the last of which is the test-case.

Chapter 5 focuses on numerically investigating phase results in the test-case system, using the general n-complex-dimensional formulation (as opposed to the quaternionic matrix description of the previous chapter). Three types of path in the system space $\mathbb{C}^2$ are defined, referred to as γ_1, γ_2 and γ_3 paths. Phases associated with these types of paths are computed and the results discussed. This leads to the central conjecture of the thesis. The chapter ends with some related numerical results.

Chapter 6 extends the numerical investigations to cover three more systems: the Hocking-Stewartson pulse system, the Rayleigh equation system and a Schrödinger equation system. Numerical results for a large number of cases are presented and discussed, with continual reference to the central conjecture.

Chapter 7 concludes the thesis by summarizing its results and achievements, and discussing future work directions.

Chapter 2

Fibre bundle preliminaries - with illustrations

We recall the basic facts of bundle theory on which this thesis is based and introduce nomenclature. Several pictures are presented, which should be thought of as analogies for the actual mathematical structures involved in the theory. Many of the structures involved in bundles can be described in different but equivalent ways mathematically (dual representations) and this duality is often easiest to understand in the context of pictures of well-known geometrical structures.

2.1 Principal bundles

Let (P, M, G, π) be a principal fibre bundle with total space P over base manifold M, with Lie group G acting on the right on P, and projection $\pi : P \to M$. Let $q \in P$, $x = \pi(q) \in M$, $p \in \pi^{-1}(x)$. Let the group right-action on P be denoted by Φ:

$$\Phi : G \times P \to P \tag{2.1}$$

$$\Phi(g, p) = \Phi_g(p) = p \cdot g \tag{2.2}$$

We can think of the group as being an action which pushes points in the bundle around the bundle *along* the fibres. Locally we can picture the situation as in Figure 2.1. Note that we only consider *principal* bundles in this work.

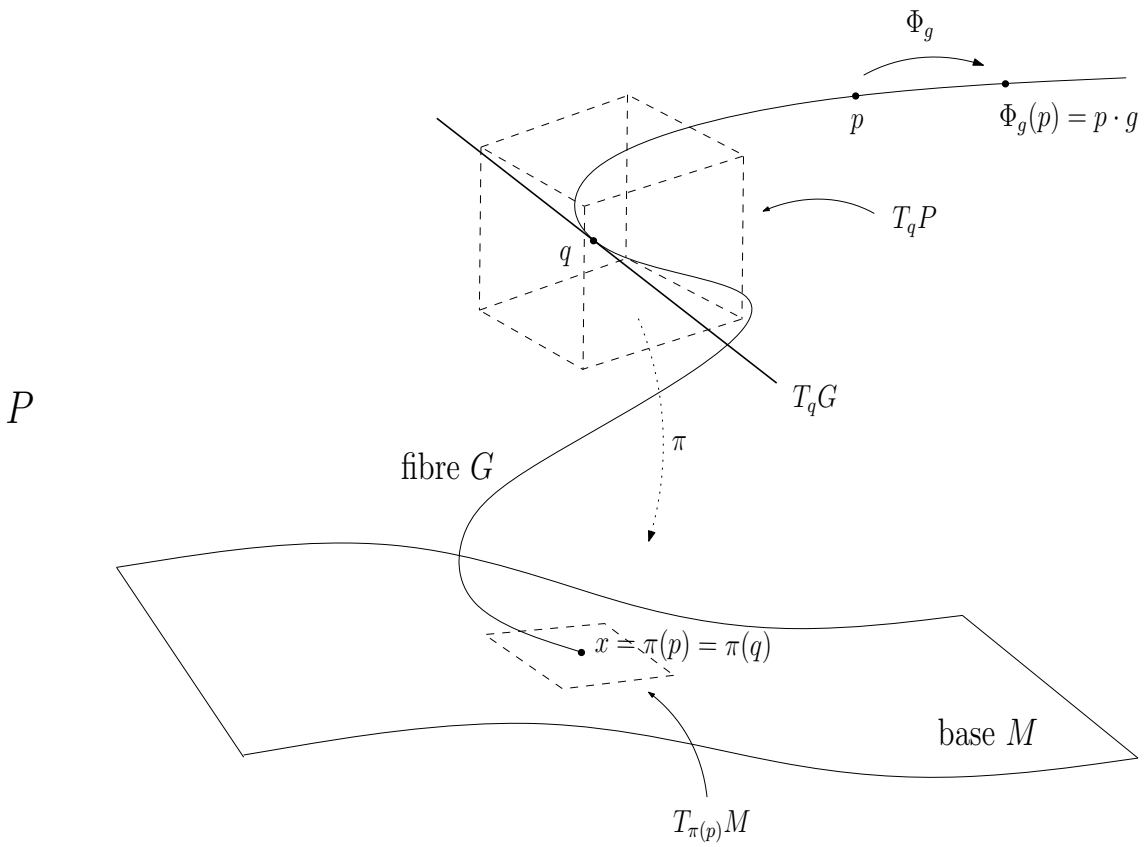

Figure 2.1: Visualizing a local representation of a principal bundle.

2.2 Horizontal spaces, vertical spaces and connections: the two viewpoints

2.2.1 The vector space viewpoint

At any point q, the tangent space T_qP to the bundle can be decomposed naturally in to two spaces, one tangent to the fibre, called the vertical subspace V_qP, and one transverse to the fibre, which, providing it satisfies certain conditions detailed below, we call the horizontal space H_qP. So we have the decomposition $T_qP = V_qP \oplus H_qP$. The vertical space is defined uniquely by

$$V_qP = \ker(\pi_*) \tag{2.3}$$

where $\pi_* : T_qP \to T_{\pi(q)}M$ is the push-forward of π, and it is clear how vertical spaces at different points in the bundle are related - they just transform smoothly with the fibre, since any parametrization of the fibre yields a parametrization of V_qP. However, there is in general no such unique way of describing the remaining space in T_qP once V_qP is taken out. But this is something we need to do in order to relate tangent spaces at different points in the bundle, and hence to define differentiation processes on the bundle; this leads to the definition of horizontal spaces in the bundle. The concept of the horizontal space H_qP is a way of describing these left-over spaces, of dimension $[\dim(T_qP) - \dim(T_qG)]$, in T_qP once the vertical space is taken out, which *varies smoothly* in the bundle, i.e. it gives us a consistent way of moving from fibre to fibre through the bundle. For principal bundles, in addition to being smoothly-varying, we require that H_qP is invariant under the group action. The assignment of such horizontal spaces is called a *connection* in a bundle:

Definition 2.2.1. *A connection in a principal bundle is a smoothly-varying assignment to each point $q \in P$ of a subspace H_qP of T_qP such that*

$$(i) \quad T_qP = V_qP \oplus H_qP \qquad \forall q \in P \tag{2.4}$$

$$(ii) \quad (\Phi_g)_*(H_qP) = H_{\Phi_g(q)}P \qquad \forall g \in G, q \in P \tag{2.5}$$

Figure 2.2 illustrates the situation. The first condition says that H_qP must be transverse to the fibre (which is necessary in order for it to span the rest of T_qP). The second condition says that if we use $(\Phi_g)_*$ to "push" $H_qP \subset T_qP$ *along* the fibre, then the result is the same as if we first push q along the fibre using Φ_g to the point $\Phi_g(q)$ and then form the subspace $H_{\Phi_g(q)}P$ at that point. (Note

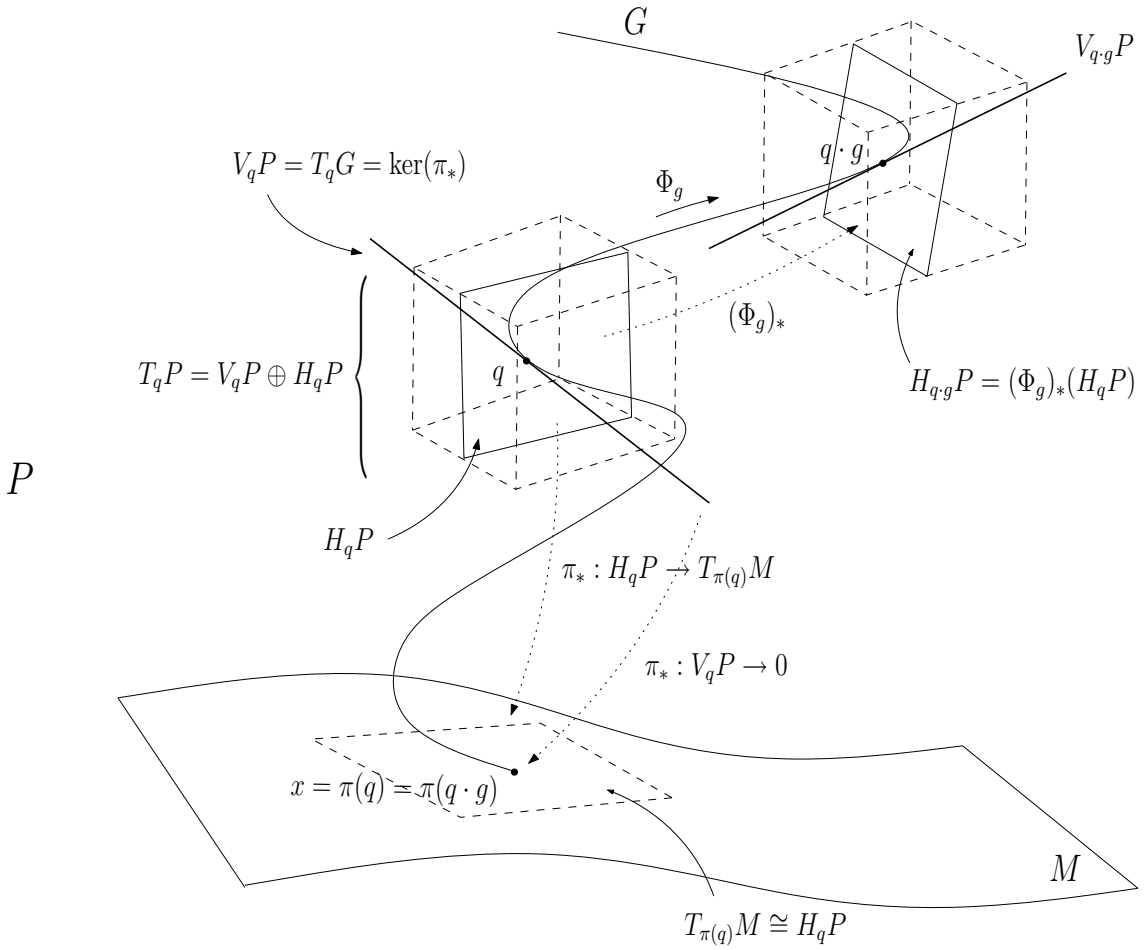

Figure 2.2: Horizontal spaces.

$(\Phi_g)_* : T_qP \to T_{\Phi_g(q)}P$ is the push-forward of Φ_g.) So a connection in a principal bundle is just a right-invariant distribution on the bundle which is transverse to the fibre at each point.

Remark 2.2.1. *An equivalent condition to condition (i) above is*

$$(i)\ \pi_*(H_qP) = T_{\pi(q)}M \qquad \forall q \in P \tag{2.6}$$

This just says that the dimension of H_qP has to be great enough to fill up the rest of T_qP completely once T_qG is taken out: since π_* maps T_qG to zero, and locally the bundle is a product space, the image of H_qP under π_* must have the same dimension as $T_{\pi(q)}M$ (i.e. they are isomorphic).

2.2.2 The differential form viewpoint

Now, since the bundle group is a Lie group, there is a canonical identification of the tangent space to the fibre at each point q with the Lie algebra $\mathfrak{g}$ of G, so we can write $T_qG \cong \mathfrak{g}$, which leads to the following differential-form-based description of a connection.

From Figure 2.2 it is clear that a choice of H_qP in fact defines a projection of T_qP on to T_qG, and hence on to $\mathfrak{g}$. Figure 2.3 shows this explicitly: $\mathcal{V}$ is a vector in T_qP which is projected via H_qP to a vector in V_qP. This is also intuitively clear for higher dimension situations, not only that pictured, since we are just dealing with intersections of linear spaces. We thus have a linear map $T_qP \to \mathfrak{g}$, i.e. a $\mathfrak{g}$-valued differential 1-form on P, with kernel H_qP. This representation of a connection as a differential form is called a *connection 1-form*, but we need a few more definitions before we can describe it fully: let $\mathfrak{g} \cong T_eG$ be the Lie algebra of G, where e is the identity in G, let $\mathfrak{X}_L(G)$ be the set of all left-invariant vector fields on G. Take $\xi \in \mathfrak{g}$. Let $X_\xi \in \mathfrak{X}_L(G)$ be the unique left-invariant vector field on G corresponding to ξ, i.e. such that $X_\xi(e) = \xi$. Each $\xi \in \mathfrak{g}$ induces a flow on P. Let $g_\xi(t)$ be the unique integral curve of X_ξ passing at $t = 0$ through $e \in G$, then $g_\xi(t)$ is a one-parameter subgroup of G.

Definition 2.2.2. *The exponential map* $\exp : \mathfrak{g} \to G$ *is defined by*

$$\exp(\xi) = g_\xi(1) \tag{2.7}$$

and it can be shown that

$$\exp(t\xi) = g_\xi(t) \in G \tag{2.8}$$

Figure 2.4 gives an idea of how these objects can be represented geometrically.

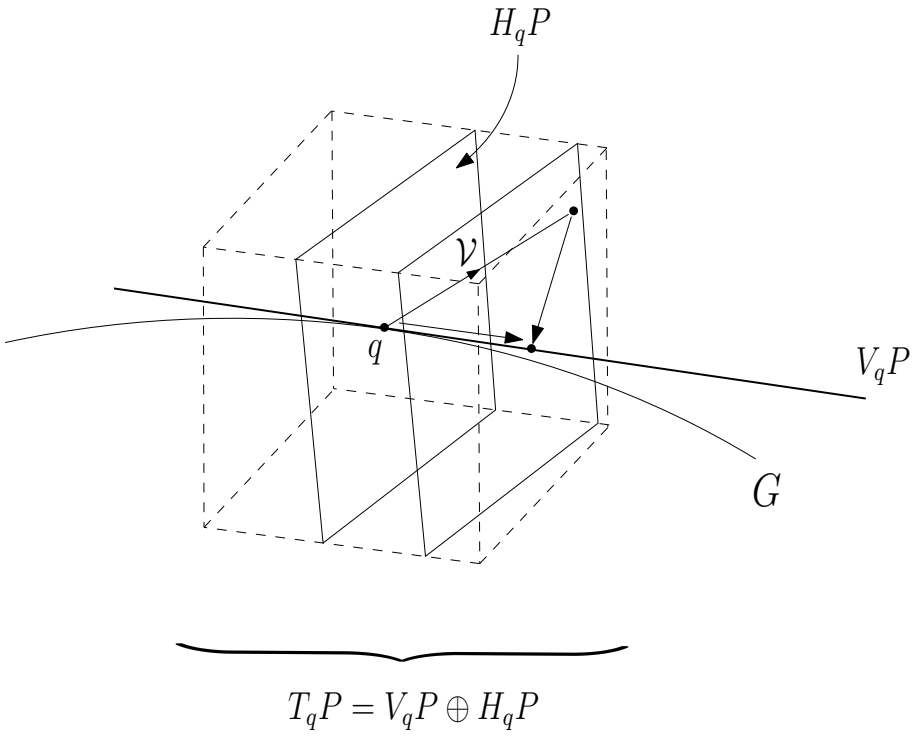

Figure 2.3: Using H_qP to project $\mathcal{V} \in T_qP$ on to V_qP.

Definition 2.2.3. *The infinitesimal generator of the action Φ, corresponding to ξ, is a vector field ξ_P on P defined by*

$$\xi_P(q) = \frac{d}{dt}\Phi(g_\xi(t), q)\Big|_{t=0} \tag{2.9}$$

and so for $\Phi(g, q) = q \cdot g$ we get

$$\begin{aligned} \xi_P(q) &= \frac{d}{dt}\Phi(g_\xi(t), q)\Big|_{t=0} && (2.10)\\ &= \frac{d}{dt}\big(q \cdot g_\xi(t)\big)\Big|_{t=0} && (2.11)\\ &= \frac{d}{dt}\big(q \cdot \exp(t\xi)\big)\Big|_{t=0} && (2.12)\\ &= q\ \xi && (2.13) \end{aligned}$$

and we can now proceed to the formal definition of a connection 1-form on a principal bundle:

Definition 2.2.4. *A connection 1-form on P is a $\mathfrak{g}$-valued 1-form $\omega_q : T_qP \to \mathfrak{g}$, satisfying, for each $q \in P$,*

$$(i) \quad \omega_q(\xi_P(q)) = \xi \qquad \forall \xi \in \mathfrak{g} \tag{2.14}$$

$$(ii) \quad \omega_{\Phi_g(q)}([(\Phi_g)_*\big|_q]\mathcal{V}) = \mathrm{Ad}_g(\omega_q(\mathcal{V})) \qquad \forall \mathcal{V} \in T_qP,\ \forall g \in G \tag{2.15}$$

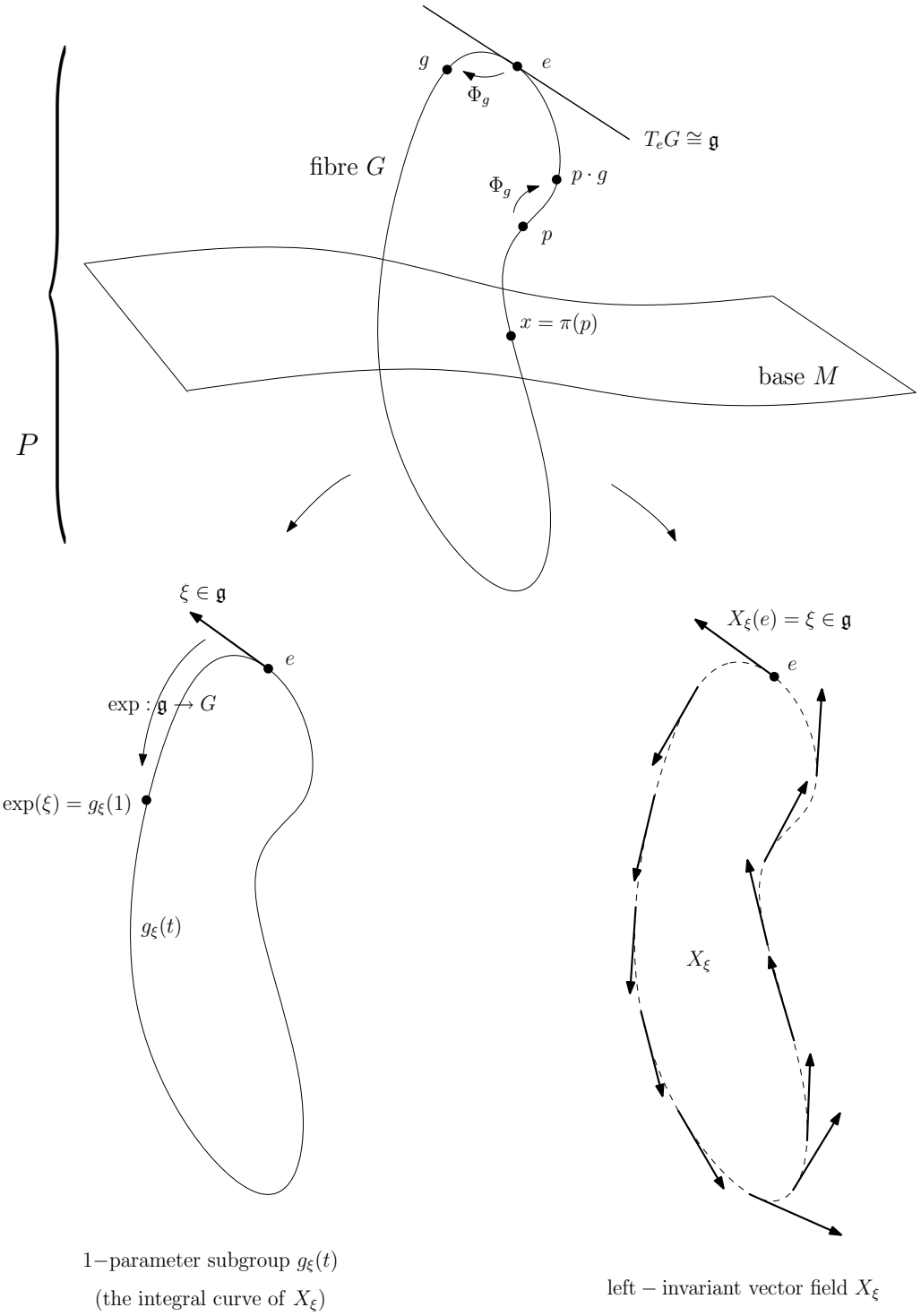

Figure 2.4: A right-action on a principal fibre bundle.

$\mathrm{Ad}_g : \mathfrak{g} \to \mathfrak{g}$ is the adjoint action at $g \in G$ (i.e. the derivative of conjugation, evaluated at e), which in our case will only ever be given by

$$\mathrm{Ad}_g(\sigma) = g^{-1}\sigma g \qquad g \in G,\ \sigma \in \mathfrak{g}, \tag{2.16}$$

which holds for matrix groups. So condition (ii) becomes:

$$\omega_{\Phi_g(q)}([(\Phi_g)_*\big|_q]\mathcal{V}) = \Phi_g^{-1}(\omega_q(\mathcal{V}))\Phi_g \qquad \forall \mathcal{V} \in T_qP,\ \forall g \in G \tag{2.17}$$

We can visualize this as in Figure 2.5, which we can very loosely think of as: if you apply ω_{qg} to the tangent vector $((\Phi_g)_*\mathcal{V})$ at $q \cdot g \in P$, then this is the same as if you start at $q \cdot g \in P$, then transform *back* along the fibre under g^{-1} *then* apply ω_q to the tangent vector $\mathcal{V}$ at the original point q, then transform *forwards* along the fibre under g returning to $q \cdot g$. This characterization of the connection,

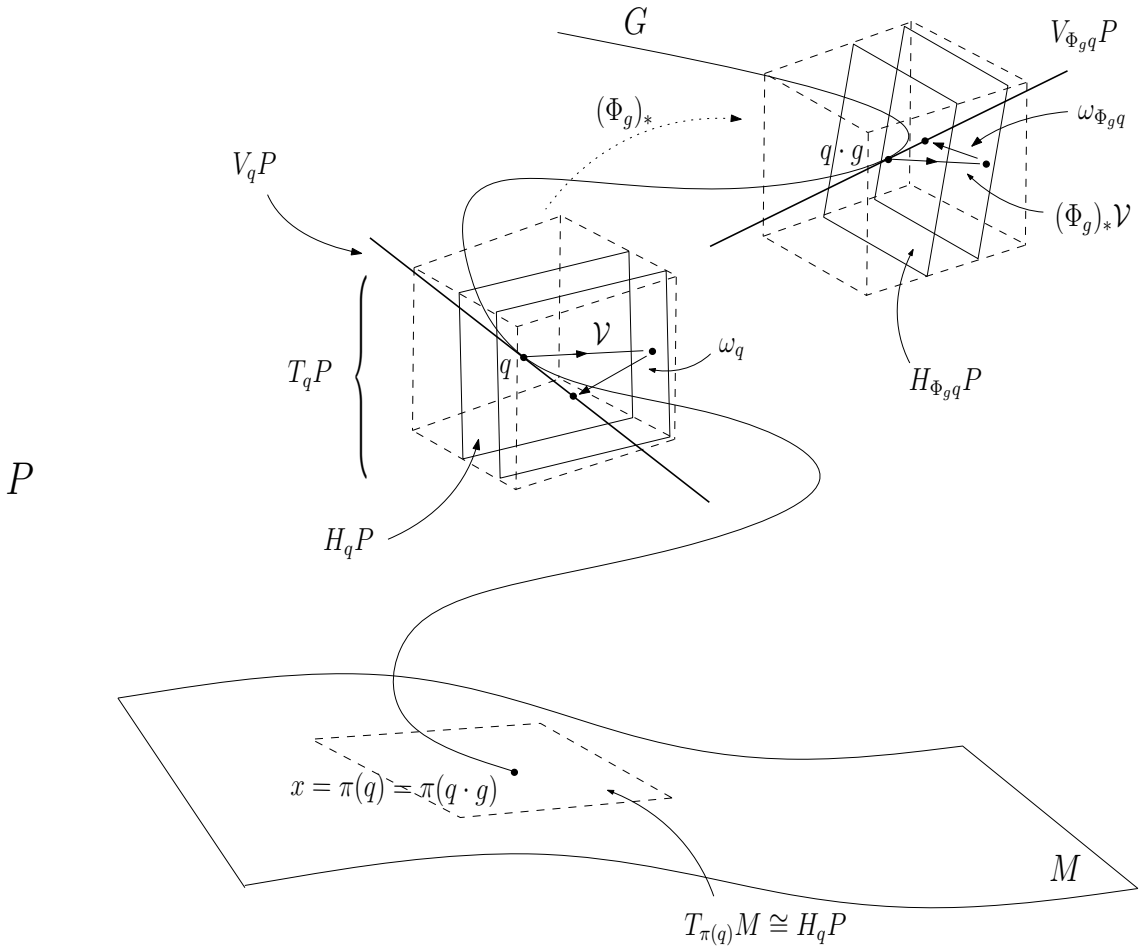

Figure 2.5: G-invariance of the connection form.

which is essentially based on tangent covectors, is just the representation dual to

the previous one (Definition 2.2.1), which is essentially based on tangent vectors. Notice in particular the duality between equations (2.5) and (2.17).

Remark 2.2.2. *If we do not need to specify the point at which a connection form is evaluated, we may denote it by just ω instead of ω_q.*

References [10]- [15] provide good material on manifolds and bundles.

2.3 Parallel translation

In the context of all these diagrams depicting horizontal subspaces, the notions of horizontality and parallel translation become very easy to understand. Suppose we now have a path in the bundle given by $t \mapsto q(t) \in P$ with $t \in [c, d] \subset \mathbb{R}$.

Definition 2.3.1. *Path $q(t) \in P$ is horizontal w.r.t. a given connection if the tangent vector $\dot{q}(t)$ lies in the horizontal subspace determined by the connection, $H_{q(t)}P$, for each t.*

Remark 2.3.1. *Recall, horizontal subspaces are by definition in the kernel of the associated connection 1-form ω, so path $q(t)$ is horizontal w.r.t. ω iff $\omega(\dot{q}(t)) = 0\ \forall t$. i.e. the projection of the tangent vector $\dot{q}(t)$ on to the vertical space at $q(t)$ is zero, at every point of the path.*

Figure 2.6 illustrates a horizontal path: $q(t)$ is a path through bundle P, and at each of the three points $q(t_1), q(t_2), q(t_3)$ the tangent space to the bundle is depicted (as a dashed-line box), along with the horizontal and vertical subspaces $H_{q(t_i)}$ and $V_{q(t_i)}$. Also shown are the tangent vectors to the path at the three points - these tangent vectors lie in the horizontal subspaces, representing the horizontal nature of the path. Now, since there is in general some flexibility in the choice of horizontal spaces in a bundle (subject to the conditions of the definition), a path can be horizontal w.r.t. one connection while simultaneously being not horizontal w.r.t. another. In Figure 2.6, we would represent a connection w.r.t. which $q(t)$ is not horizontal by tilting the horizontal space inside one or more of the "tangent space boxes" by some angle (or angles), since then the tangent vectors would not lie inside the horizontal spaces for every t.

Now, if path $q(t)$ is not horizontal w.r.t. a given connection ω, then we can derive an expression which describes how far it deviates from being horizontal. We do this by considering the separation, in the fibre, between $q(t)$ and a second path, $\hat{q}(t)$, which starts at the same point $q(c) = \hat{q}(c)$ in the bundle, and *is* horizontal. Any

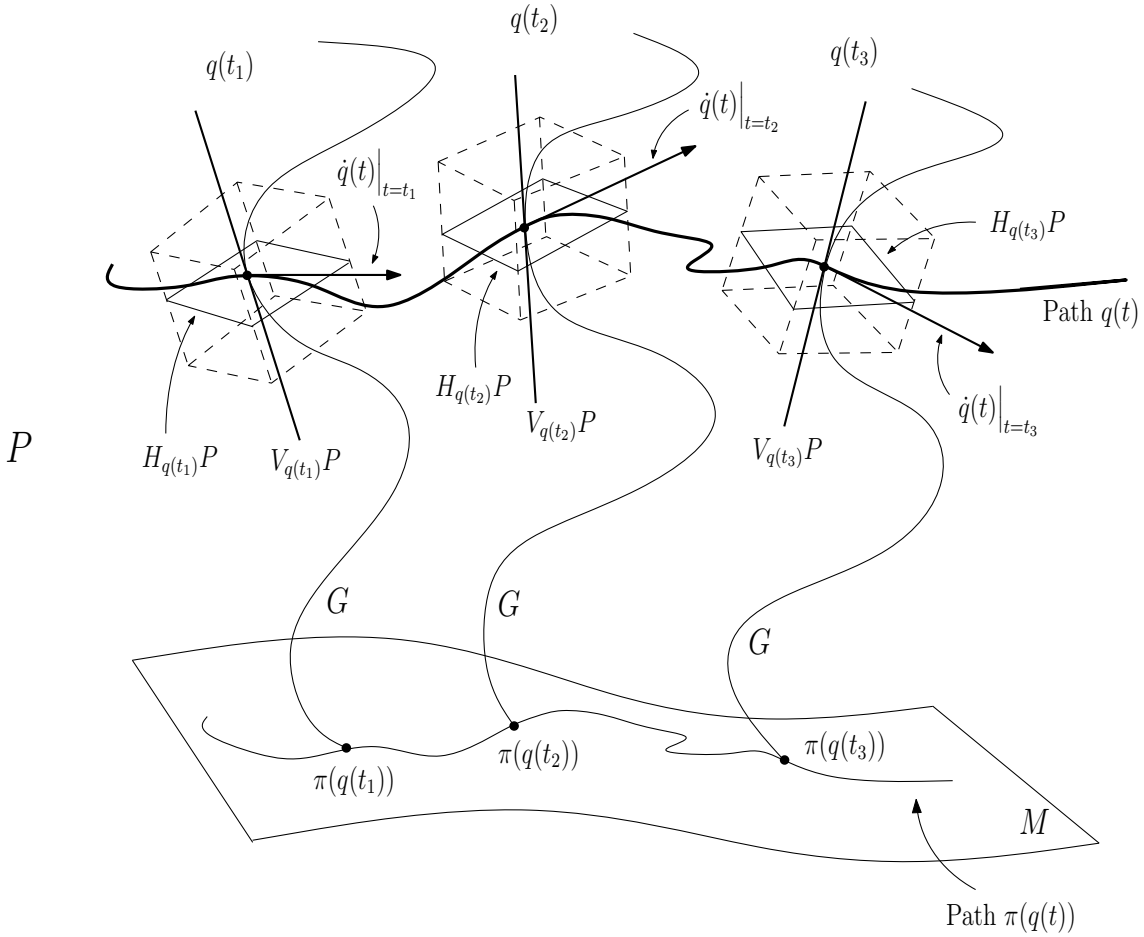

Figure 2.6: A horizontal path $q(t)$ through principal bundle (P, M, π, G).

path in bundle P which maps, under π, to the same path on base M as does $q(t)$ is called a *lift* of $q(t)$. If a lift of $q(t)$ is horizontal w.r.t. ω then it is called a *horizontal lift* of $q(t)$, and translating (i.e. evaluating) some quantity along a horizontal path (as opposed to a non-horizontal path) is called *parallel translation*. So $\hat{q}(t)$ is a horizontal lift of $q(t)$ and we analyze it as follows. Using local coordinates for the local product structure in the bundle, every point on path $\hat{q}(t)$ can be written as the product of the point $q(t)$ and some element of the fibre, say $a \in G$. But since this is the case for *every* point along the path, we get a whole curve $a(t) \in G$ which measures the difference between the two curves in the bundle:

$$\hat{q}(t) = q(t)a(t) \tag{2.18}$$

We can think of $a(t)$ as a sort of "fine-tuning" variable, which, when varied by the right amount as $q(t)$ proceeds along its course, enables us to shift $\hat{q}(t)$ around the fibre exactly the right amount necessary for it to remain horizontal. $a(t)$ will then be an expression describing how much $q(t)$ deviates from being horizontal. To obtain the equation which governs this required motion in the fibre, we differentiate (2.18) w.r.t. t, apply the connection form ω, then use the horizontal and right-equivariance conditions, '$\omega(\dot{\hat{q}}(t)) = 0$' and (2.17) respectively. This yields the first-order differential equation for $a(t)$:

$$\dot{a}(t)a^{-1}(t) = -\omega(\dot{q}(t)) \tag{2.19}$$

with $a(c) = e$ required to satisfy $q(c) = \hat{q}(c)$. Detailed derivations of this equation are given in [12] (p.69), [13] (p.265) and [17] (p.364). This equation shows us precisely how $a(t)$ must vary as we move along $q(t)$ in order for $\hat{q}(t)$ to be the unique horizontal lift starting at $q(c)$. We summarize the concepts of horizontal lifts and parallel translation in Figure 2.7.

Remark 2.3.2. *This method for generating horizontal paths also applies for paths $\hat{q}(t)$ which start at points in the fibre attached to $q(c)$, other than $q(c)$ itself. This just involves taking the initial condition $a(c)$, for (2.19), to be some value other than the identity in G, and would be represented on Figure 2.7 by sliding the path $\hat{q}(t)$ up the fibre G so that $q(c)$ and $\hat{q}(c)$ are separated by a value $a(c)$ in the fibre.*

Remark 2.3.3. *It is important to remember that the diagrams in this chapter are merely pictorial analogies for the mathematical objects involved. In particular, fibres are always pictured here as being 1-dimensional, when in reality they can be of any dimension. For example, in Figure 2.7, the shift in the fibre is portrayed as being a*

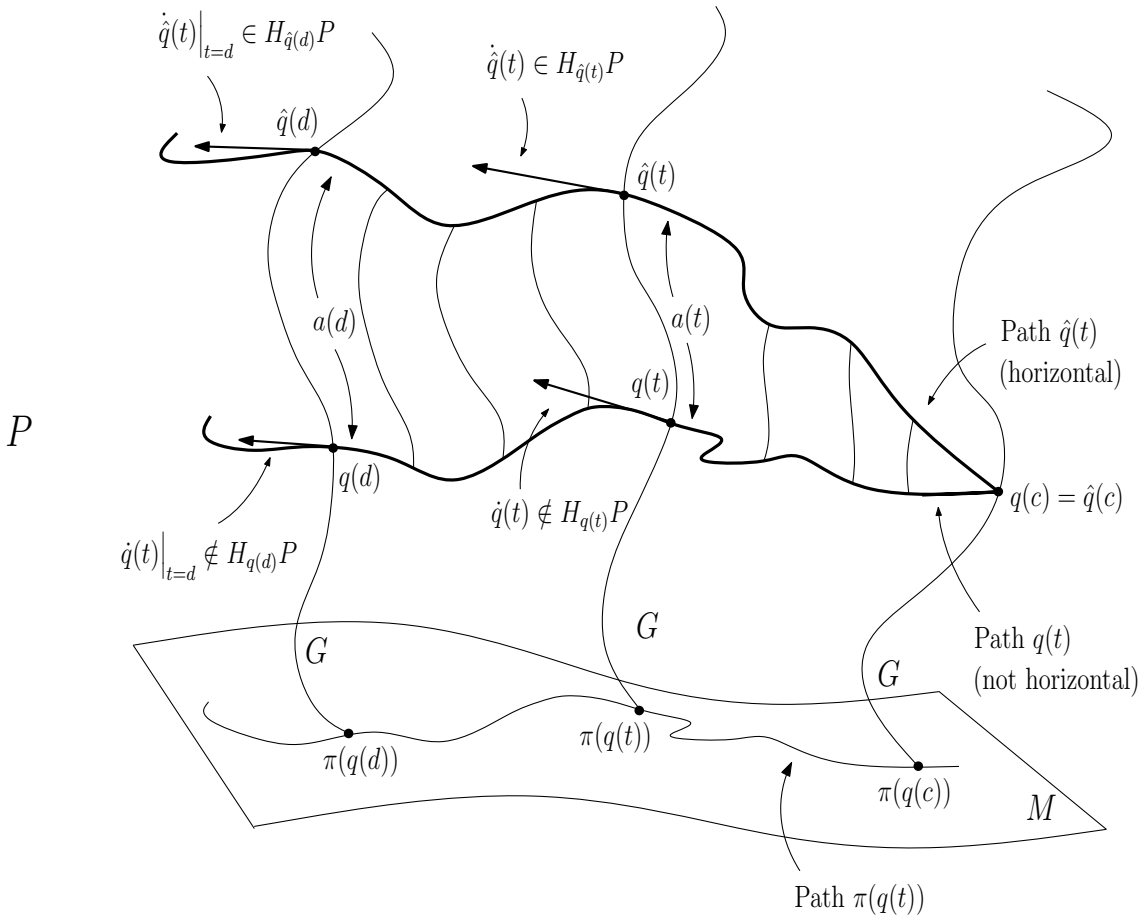

Figure 2.7: Generating a horizontal path $\hat{q}(t)$ from a non-horizontal path $q(t)$ by applying a shift $a(t)$ in the fibre.

simple shift up or down the fibre, but really the shift $a(t)$ is a path in the group G, whatever that may be.

This concludes our review of fibre bundles, and our collection of very clear diagrams showing previously uncollated ways of thinking about the basic geometry of fibre bundles.

Chapter 3

The Hopf bundle: parallel translation, the natural connection and the phase

In this chapter we introduce and analyze the concept which essentially underpins this thesis: namely that whenever we have a path in $\mathbb{C}^n \setminus \{0\}$, such as a solution to a system of ODEs, if we regard $\mathbb{C}^n$ as the highest-dimensional space in a natural hierarchy of spaces, then this path induces motion on smaller structures inside $\mathbb{C}^n$. Deconstruction of paths in this way is possible by viewing trajectories in $\mathbb{C}^n$ in terms of a fibre bundle, and applying various concepts from bundle theory to analyze motion on the induced structures.

This perspective of looking inside spaces to see how trajectories induce motion on smaller spaces under various fibrations or projections has not received a great deal of attention in the literature, as it is often assumed that the whole story of an ODE system is contained in the manifold on which solutions lie. However, this is not always the case, as we demonstrate in this work. The one main exception to the lack of attention the subject has received is in the context of Berry phases in quantum mechanics, due to the centrality of projection operators in the theory. Such work tends to operate exclusively in the language of quantum mechanics, which gives the treatment a very different feel to that presented here, and yields what is arguably a less accessible approach to the concept. This presentation is intended to be a relatively straight-forward approach, of relevance in a general ODE/dynamical-systems context.

3.1 Motivation

The idea of looking at projections of paths is largely motivated by the eigensystem (1.1) introduced in Chapter 1. The key observation is that

> *in this eigensystem context, each solution eigenvector u in fact represents a whole equivalence class $[u]$ of valid solutions, related by complex scalar multiplication, each with the same eigenvalue.*

So if u is a solution, then so is cu for any complex $c = re^{i\theta}$. Hence each solution u contains information superfluous to its role as an eigenvector, but which is nevertheless present in standard analyses: a magnitude factor r and a phase factor θ. Therefore a natural space on which to consider solutions to this system is in fact complex projective space $\mathbb{C}P^{n-1}$, and of special interest is how the "extra" information behaves if we move along *paths* of eigenvectors in $\mathbb{C}^n$. To investigate this we combine standard spherical projection with projection by the Hopf map.

3.2 The Hopf map

The Hopf map is defined as the projection $\pi : S^{2n-1} \to \mathbb{C}P^{n-1}$ which sends each $z \in S^{2n-1}$, written as a complex n-tuple, to the point in $\mathbb{C}P^{n-1}$ with corresponding homogeneous coordinates:

$$\begin{array}{ccc} z = (z_1, z_2, \ldots, z_n) & \mapsto & [z_1, z_2, \ldots, z_n] \\ \in S^{2n-1} \subset \mathbb{C}^n & & \in \mathbb{C}P^{n-1} \end{array} \tag{3.1}$$

It can be proved, by exhibiting an atlas of bundle charts which satisfy the conditions required in the definition of a fibre bundle, as in [16], that this map is the projection map of a principal $U(1)$-bundle with base $\mathbb{C}P^{n-1}$ and total space S^{2n-1}:

$$\begin{array}{ccc} U(1) & \to & S^{2n-1} \\ & & \downarrow \pi \\ & & \mathbb{C}P^{n-1} \end{array}$$

where $U(1)$ is the first unitary group: complex numbers of absolute value 1, under multiplication. This is the Hopf bundle. For $n = 2$ this gives the well-known classical Hopf bundle $S^1 \to S^3 \to S^2$ (since $\mathbb{C}P^1 \simeq S^2$), but the term "Hopf bundle" is also used to refer to higher-dimensional cases. In terms of the notation of Chapter 2, we now have $P = S^{2n-1}$, $M = \mathbb{C}P^{n-1}$, $G = U(1)$ and $\mathfrak{g} = i\mathbb{R}$.

Remark 3.2.1. *For $n = 2$ we can write the Hopf projection explicitly as*

$$\begin{array}{rcccl} \pi: & \mathbb{C}^2 \supset S^3 & \rightarrow & S^2 & \\ & (z_1, z_2) & \mapsto & \pi(z_1, z_2) & = \left(\overline{z}_1 z_2 + z_1 \overline{z}_2 \ , \ i(\overline{z}_1 z_2 - z_1 \overline{z}_2) \ , \ |z_1|^2 - |z_2|^2\right) \end{array}$$

Then by direct calculation we have

$$|\pi(z_1, z_2)|^2 = \left(|z_1|^2 + |z_2|^2\right)^2 \tag{3.2}$$

so that

$$(z_1, z_2) \in S^3 \Rightarrow \pi(z_1, z_2) \in S^2 \tag{3.3}$$

and each point on $S^3 \subset \mathbb{C}^2$ is indeed mapped by π to a point on $S^2 \subset \mathbb{R}^3$. Furthermore, for $e^{i\theta} \in U(1)$,

$$\pi\big(e^{i\theta}(z_1, z_2)\big) = \pi\big((e^{i\theta} z_1, e^{i\theta} z_2)\big) = \pi\big((z_1, z_2)\big),$$

so π is easily seen to be $U(1)$-invariant as required.

Further information on the Hopf map may be found in many standard texts, such as [19]- [22]. We have introduced the Hopf bundle here using the traditional complex number z notation, as is common, because it is a very natural way to describe the progression from complex numbers to complex projective space. However, since we now proceed to consider dynamics in the bundle, we switch to a more dynamical-system oriented notation, using letters v and w for points in S^{2n-1}, again written as complex n-tuples.

Take $v \in S^{2n-1} \subset \mathbb{C}^n$. In terms of a Hopf bundle structure, v can be represented locally as a point in the product space $S^1 \times \mathbb{C}P^{n-1}$: if $v = e^{i\theta} w$, where $w \in S^{2n-1}$ and $\theta \in \mathbb{R}$, then v is represented by the pair $(e^{i\theta}, [w])$, with $[w] \in \mathbb{C}P^{n-1}$. So both w and $e^{i\theta} w$ are points on S^{2n-1}, and in these coordinates, the projection map is just

$$\begin{array}{rcl} \pi : S^{2n-1} & \rightarrow & \mathbb{C}P^{n-1} \\ e^{i\theta} w & \mapsto & [w] \end{array} \tag{3.4}$$

In other words, for each element $[w] \in \mathbb{C}P^{n-1}$ we have a complete S^1-fibre of points in S^{2n-1} which all map to the same point in the base. The quantity θ parametrizing the fibres is called the *phase*, and it is a way of measuring the separation between points in S^{2n-1} which correspond to the same point in $\mathbb{C}P^{n-1}$. Note that since the vertical vectors of a bundle are defined to be vectors tangent to the fibres, parametrizing the fibres by θ in this way means that the vertical vectors may be referred to as just span$\{\frac{\partial}{\partial \theta}\}$. We now show how the Hopf map can be used to analyze paths in $\mathbb{C}^n$.

3.3 A hierarchy of spaces

The basic idea is to take a path of points in $\mathbb{C}^n \setminus \{0\}$ and project these points firstly on to the unit sphere S^{2n-1} inside $\mathbb{C}^n$, then on to projective space $\mathbb{C}P^{n-1}$ inside S^{2n-1} using the Hopf map. In doing so we are choosing to reframe the system in terms of a fibre bundle, essentially dividing up motion along a path on S^{2n-1} in to a $\mathbb{C}P^{n-1}$ component and an S^1 component. Although we consider only the Hopf S^1-bundle structure throughout this work, other fibres could potentially be used to extend the concept in other ways.

Thus we have a natural hierarchy of spaces on which paths of vectors are considered (with our choice of variables listed on the left for easy reference):

$$\begin{array}{rl} (u \in) & \mathbb{C}^n \quad \cong \quad \mathbb{R}^{2n} \\ & \downarrow \\ (u \in) & \mathbb{C}^n \setminus \{0\} \\ & \downarrow \\ (v, w \in) & S^{2n-1} \\ & \downarrow \\ ([v], [w] \in) & \mathbb{C}P^{n-1} \end{array} \tag{3.5}$$

Any path on $\mathbb{C}^n \setminus \{0\}$ may be projected on to the spaces beneath it, and the behaviour of the induced paths investigated. Figure 3.1 illustrates the situation for $n = 2$, with $\mathbb{C}^2$ viewed as $\mathbb{R}^4$, spherical projection denoted by P and one dimension suppressed. The rest of this chapter details how to use the Hopf bundle structure to "extract" an S^1 phase factor from paths in $\mathbb{C}^n \setminus \{0\}$; and also how, if we have a system of equations which generates paths on $\mathbb{C}^n \setminus \{0\}$, then using these projections we can derive systems induced on the lower spaces and characterize the role of the phase factor in the resulting dynamics.

3.4 Parallel translation in the Hopf bundle

As shown in Section 2.3, given a parametrization of the local product structure of a bundle, we can write down the condition for parallel translation in the bundle w.r.t. a given connection, in terms of that connection 1-form (equation (2.19)). We do this now for the Hopf bundle, with the natural parametrization $v = e^{i\theta}w$.

Let $x \in \mathbb{R}$ be a path-parametrization variable, say $x \in [x_0, x_1] \subset \mathbb{R}$, then let v depend on x so that $v(x)$ is a path on S^{2n-1}. In order to show how different paths on S^{2n-1} are related by the phase during motion, let the local coordinate representation on $S^1 \times \mathbb{C}P^{n-1}$ depend on the path-parameter also: let $\theta \in \mathbb{R}$ depend on x and write

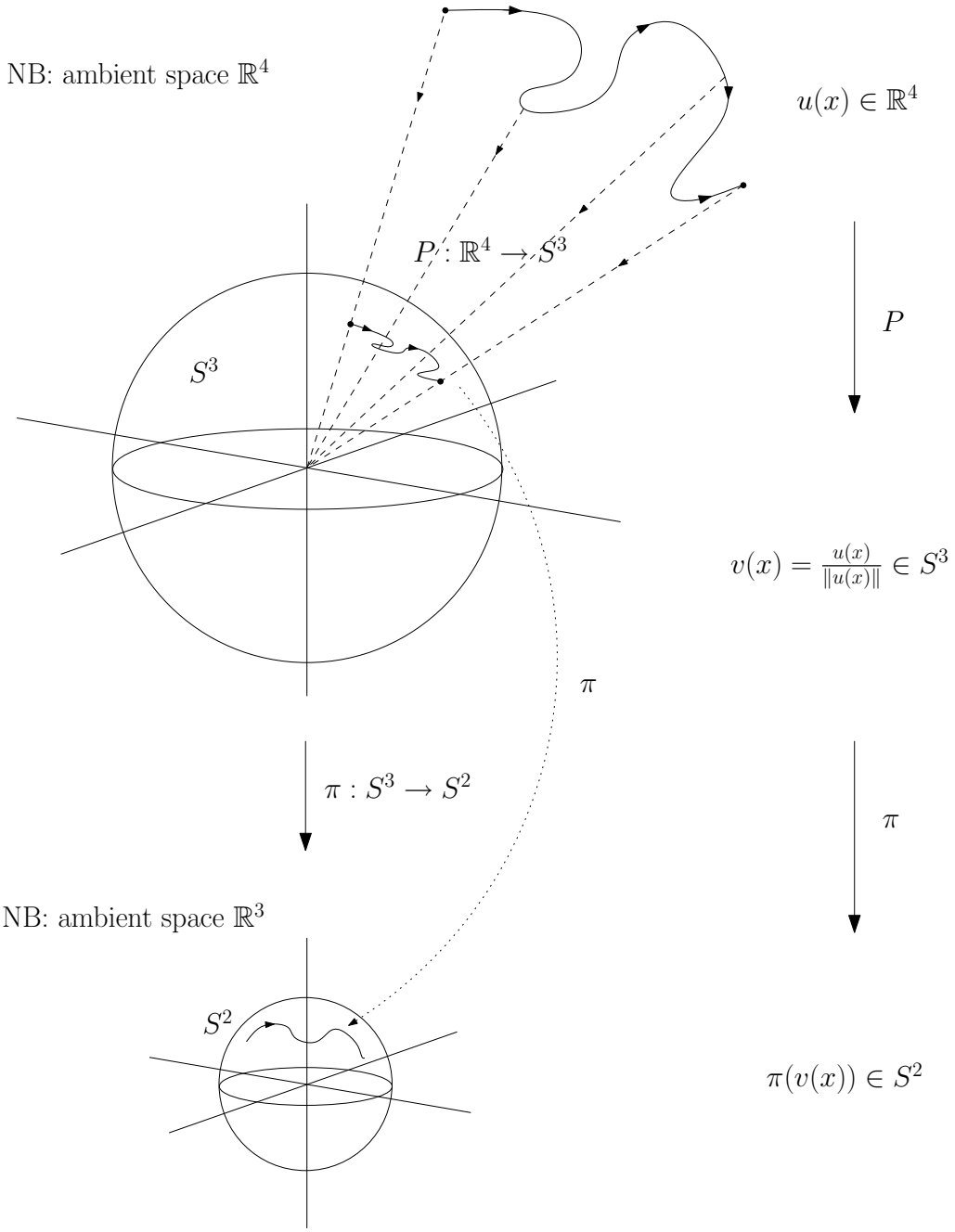

Figure 3.1: illustration of the projection sequence $\pi \circ P : \mathbb{R}^4 \to S^3 \to S^2$

$v(x) = e^{i\theta(x)}w(x)$, where $w(x)$ is also a path on S^{2n-1}. Since v and w are both paths of points on the sphere, which correspond to the same points in $\mathbb{C}P^{n-1}$, and the local coordinates for the fibre and the base are now x-dependent, this equation effectively separates motion in the fibre from motion on the base manifold.

Equation (2.19) and the related discussion then imply that $w(x)$ is horizontal w.r.t. a connection ω iff

$$\left[\frac{d}{dx}(e^{-i\theta(x)})\right]e^{i\theta(x)} = -\omega(v_x) \tag{3.6}$$

$$\Leftrightarrow \theta_x(x) = -i\omega(v_x) \tag{3.7}$$

This then is the general equation which tells us how, as x goes from x_0 to x_1, $\theta(x)$ must vary as $v(x)$ moves around the sphere in order for $w(x)$ to remain horizontal w.r.t. ω.

Remark 3.4.1. *Taking a step back for a moment, a 1-form is loosely-speaking just an object whose "purpose" is to be integrated along some 1-dimensional space. Therefore, the obvious question to ask of any connection 1-form ω on a bundle is - what does integration of the 1-form along various paths in the bundle yield? Well, equation (3.7) provides the answer to this question for the Hopf bundle:*

> *integration of a connection 1-form along a path on S^{2n-1} gives precisely i times the phase curve required to maintain horizontality of the path on S^{2n-1} obtained via the local product structure given above.*

The interesting aspect of this interpretation of the path-integral of a connection form is that it is entirely dependent on the specific local product structure considered here. Other local coordinates for the group action will in general lead to more complicated expressions on the LHS of equation (3.7) because terms will not cancel so neatly, and in general a clear interpretation such as this will not be possible.

Now, in considering what this equation reveals in any practical situation, there are clearly two issues to face: firstly, what is the connection form ω to be used in the equation? And secondly, what is the path $v(x)$ whose tangent vector $v_x(x)$ is to be used in the equation? We consider the issue of the path $v(x)$ shortly in Section 3.6, but first we describe the natural connection form on the Hopf bundle, which is the connection form of primary interest in this thesis.

3.5 The natural connection on the Hopf bundle

Using the notation of Chapter 2, so as to maintain the distinction between a point on a manifold and a tangent vector to the manifold at that point, we have

Definition 3.5.1. *For $q \in S^{2n-1}$ and $\mathcal{V} \in T_qS^{2n-1}$ vectors in $\mathbb{C}^n$, the natural connection on the Hopf bundle is given by $\omega_q(\mathcal{V}) = q^H\mathcal{V}$.*

3.5.1 Verifying the natural connection

To verify that the natural connection form is in fact a valid connection form, we check that it is a Lie-algebra-valued 1-form on S^{2n-1} which satisfies properties (i) and (ii) of Definition 2.2.4. Take $q \in S^{2n-1}$, $\mathcal{V} \in T_qS^{2n-1}$, and let $\omega_q(\mathcal{V}) = q^H\mathcal{V}$. Now since $\mathcal{V}$ is a tangent vector to the sphere $S^{2n-1} \subset \mathbb{C}^n$ it can be expressed in the form

$$\mathcal{V} = (I - qq^H)w + i\alpha q \qquad \text{for some } \alpha \in \mathbb{R}, w \in \mathbb{C}^n \tag{3.8}$$

This equation concerns the projection of a vectorfield on to the tangent space T_qS^{2n-1}; this is a special case of projection on to the tangent space of a Stiefel manifold, as seen in [23] and [24] in the context of continuous orthogonalization of linear systems of ODEs. Applying the connection form to the tangent vector $\mathcal{V}$ written in this form then gives

$$\begin{aligned}
\omega_q(\mathcal{V}) = q^H\mathcal{V} &= q^H[(I - qq^H)w + i\alpha q] && (3.9)\\
&= (q^H - q^Hqq^H)w + i\alpha q^Hq && (3.10)\\
&= (q^H - q^H)w + i\alpha \qquad \text{since } q^Hq = 1 && (3.11)\\
&= i\alpha && (3.12)
\end{aligned}$$

and so ω_q does map tangent vectors to the Lie algebra $i\mathbb{R}$ as required, $\omega_q : T_qS^{2n-1} \to \mathfrak{g}$. Now to verify properties (i) and (ii) of Definition 2.2.4:

- (i): As shown in (2.13), for right action Φ, and for any given $\xi \in \mathfrak{g}$ and $q \in S^{2n-1}$, the infinitesimal generator is given by $\xi_P(q) = q\xi$, and so

$$\omega_q(\xi_P(q)) = \omega_q(q\ \xi) = q^Hq\ \xi = \xi \tag{3.13}$$

  as required.

- (ii): Now let $\gamma(s)$ be a path in S^{2n-1} s.t. $\gamma(0) = q$, with tangent vector $\mathcal{V}$ at q, i.e.

$$\mathcal{V} = \frac{d}{ds}\gamma(s)\Big|_{s=0} \tag{3.14}$$

Then the action of $U(1)$ on $\gamma(s)$ is

$$\Phi_g(\gamma(s)) = \gamma(s) \cdot g \tag{3.15}$$

so that

$$\begin{aligned}
[(\Phi_g)_*\big|_q]\ \mathcal{V} &= [(\Phi_g)_*\big|_q]\ \Big(\frac{d}{ds}\gamma(s)\Big|_{s=0}\Big) && (3.16)\\
&= \frac{d}{ds}\Phi_g(\gamma(s))\Big|_{s=0} && (3.17)\\
&= \frac{d}{ds}(\gamma(s)\cdot g)\Big|_{s=0} && (3.18)\\
&= \Big(\frac{d}{ds}\gamma(s)\Big|_{s=0}\Big)g && (3.19)\\
&= \mathcal{V}g \qquad \forall g \in U(1) && (3.20)
\end{aligned}$$

and hence

$$\begin{aligned}
\omega_{\Phi_g q}([(\Phi_g)_*\big|_q]\mathcal{V}) &= \omega_{q\cdot g}(\mathcal{V}g) && (3.21)\\
&= (qg)^H(\mathcal{V}g) && (3.22)\\
&= g^H q^H \mathcal{V} g && (3.23)\\
&= g^{-1}(q^H\mathcal{V})g \qquad \text{since } g \in U(1) \text{ here} && (3.24)\\
&= \mathrm{Ad}_g(\omega_q(\mathcal{V})) && (3.25)
\end{aligned}$$

as required.

Therefore the natural connection form is indeed a valid connection form.

3.5.2 The natural connection along a path

Now returning to the case of a path of vectors $v(x) = \begin{pmatrix} v_1(x) \\ \vdots \\ v_n(x) \end{pmatrix} \in S^{2n-1} \subset \mathbb{C}^n$, the natural connection form at points along the path may be written as

$$\begin{aligned}
\omega &= v^H dv && (3.26)\\
&= \mathrm{Re}(v^H dv) + i\,\mathrm{Im}(v^H dv) && (3.27)
\end{aligned}$$

But, as can be verified directly by writing $v_1 = (x_1 + iy_1), \ldots, v_n = (x_n + iy_n)$, the condition $\|v\| = 1$ implies that

$$\mathrm{Re}(v^H dv) = 0 \tag{3.28}$$

so that

$$\omega = i\,\mathrm{Im}(v^H dv) \tag{3.29}$$

Then since $v = u/\|u\|$, we can write ω in terms of vectors in the space at the top of the hierarchy, $\mathbb{C}^n$, so that paths of vectors in $\mathbb{C}^n$ immediately generate the associated natural connection 1-forms on S^{2n-1}:

$$\omega = i\,\mathrm{Im}(v^H dv) = i\,\frac{\mathrm{Im}(u^H du)}{(u^H u)} \tag{3.30}$$

Note that $v^H dv$ and $u^H du$ are entirely different objects: the former has zero real part while the latter generally does not; writing ω as in (3.30) simply provides a straightforward way of expressing the connection in terms of u.

3.5.3 Parallel translation w.r.t. the natural connection

Updating equation (3.7) so as to refer specifically to the natural connection we have that $w(x)$ is horizontal w.r.t. ω iff

$$\theta_x(x) = -iv^H v_x = \mathrm{Im}(v^H v_x) \tag{3.31}$$

3.6 Evaluating the phase along paths in the Hopf bundle

Now, taking account of

- the hierarchy of spaces and projections defined here,
- the parallel translation condition (3.7) and
- the natural connection form (3.30),

we see that associated with each path of vectors $u(x)$ in $\mathbb{C}^n \setminus \{0\}$ is a unique phase curve $\theta(x)$, which describes *the deviation from horizontality w.r.t. the natural connection, in the Hopf bundle, of the projection of the path u(x) on to the real sphere* S^{2n-1} *inside* $\mathbb{C}^n$. The calculation and observation of this phase curve $\theta(x)$ occupies

a central role in the numerical investigations in the latter part of this thesis; we therefore now show explicitly how to obtain the phase curve for a general path in $\mathbb{C}^n \setminus \{0\}$, then describe the particular case when the path is governed by a linear system of ODEs on $\mathbb{C}^n \setminus \{0\}$.

3.6.1 The phase calculation for a general path in $\mathbb{C}^n \setminus \{0\}$

Denote by $\hat{\gamma}$ a general path $\mathbb{R} \supset [x_0, x_1] \to \mathbb{C}^n \setminus \{0\}$. Take $x \in [x_0, x_1]$, and let the path be given by $u(x) = (u_1(x), \ldots, u_n(x))$ in standard coordinates. Let γ denote the path $[x_0, x_1] \to S^{2n-1}$ obtained by spherical projection. Write the connection form on S^{2n-1} as $\omega = f(u)du$ in standard coordinates, as in (3.30). Then the integral of the connection form along the induced path γ on S^{2n-1} is calculated by pulling back the connection form to the real line and evaluating the ordinary integral there:

$$\begin{aligned} \int_\gamma \omega &= \int_{[x_0,x_1]} (\gamma)^* \omega && (3.32) \\ &= \int_{x_0}^{x_1} \Big(f(u(x)) \frac{du}{dx} \Big) dx && (3.33) \\ &= \int_{x_0}^{x_1} \Big(i \, \frac{\mathrm{Im}(u^H u_x)}{(u^H u)} \Big) dx && (3.34) \end{aligned}$$

and hence, by (3.7),

the phase curve $\theta(x)$ associated with path $\hat{\gamma}$ is given by

$$\theta(x) = \int_{x_0}^{x} \Big(\frac{\mathrm{Im}(u(s)^H u_s(s))}{(u(s)^H u(s))} \Big) ds \qquad (3.35)$$

This equation, around which much of this thesis centres, is important because it reveals how, with each path $\hat{\gamma}$ in $\mathbb{C}^n \setminus \{0\}$, is associated an implicit dynamical S^1 phase factor, with a fundamental geometrical significance. An exposition of the same mathematical object, in the context of the quantum geometric phase, may be found in [14], p.204. The accuracy of any numerical solution to equation (3.35) will depend directly on the accuracy of the expressions used for u and u_x. We now consider the special case where u_x is known precisely, through its relationship with u, by choosing u to be the solution to a system of ODEs on $\mathbb{C}^n \setminus \{0\}$ as follows.

3.6.2 The phase calculation for paths induced by $u_x = Au$

Suppose we have the linear system of ODEs

$$u_x = Au, \qquad u(x) \in \mathbb{C}^n \setminus \{0\}, \; x \in \mathbb{R}, \; A \in M_n(\mathbb{C}), \; u(0) = u_0 \qquad (3.36)$$

where $M_n(\mathbb{C})$ denotes the set of all $n \times n$ complex matrices. This induces a system on the sphere inside $\mathbb{C}^n \setminus \{0\}$; we derive this system, then use local product coordinates in the Hopf bundle to show how the phase motion on S^1 is manifested in this case.

3.6.2.1 Projecting on to the sphere

Let $u(x)$ be the solution to (3.36). Projection of this path on to S^{2n-1} is of course given by:

$$v(x) = \frac{u(x)}{\|u(x)\|} \in S^{2n-1} \subset \mathbb{C}^n \tag{3.37}$$

Remark 3.6.1. *Visualizing this projection is possible by imagining $u(x)$ as a path in real $2n$-dimensional space, which is then projected on to the sphere S^{2n-1} embedded in $\mathbb{R}^{2n}$, in analogy with either of the $\mathbb{R}^3 \to S^2$ or $\mathbb{R}^2 \to S^1$ cases, which are intuitively clear.*

The evolution of $v(x)$ is then calculated as follows

$$\begin{aligned}
v_x &= \Big(\frac{u}{\|u\|}\Big)_x && (3.38)\\
&= \frac{u_x}{\|u\|} + u\big[(u^H u)^{-1/2}\big]_x && (3.39)\\
&= \frac{u_x}{\|u\|} + u\Big(\frac{-1}{2}\Big)(u^H u)^{-3/2}(u_x^H u + u^H u_x) && (3.40)\\
&= \frac{Au}{\|u\|} - \frac{1}{2}\,\frac{u}{\|u\|}\,\frac{1}{\|u\|^2}\,\Big[(Au)^H u + u^H(Au)\Big] \qquad \text{by (3.36)} && (3.41)\\
&= \frac{Au}{\|u\|} - \frac{1}{2}\,\frac{u}{\|u\|}\left[\frac{u^H}{\|u\|}A^H\frac{u}{\|u\|} + \frac{u^H}{\|u\|}A\frac{u}{\|u\|}\right] && (3.42)\\
&= Av - \frac{1}{2}\,v[v^H A^H v + v^H A v] \qquad \text{by (3.37)} && (3.43)\\
&= Av - v\ \mathrm{Re}(v^H A v) \qquad \text{since } \frac{1}{2}(\overline{z} + z) = \mathrm{Re}(z) && (3.44)
\end{aligned}$$

so the trajectory $v(x)$ induced on S^{2n-1} by (3.36) satisfies

$$v_x = Av - v\ \mathrm{Re}(v^H A v) \tag{3.45}$$

or, writing $v^H A v = \mathrm{Re}(v^H A v) + i\,\mathrm{Im}(v^H A v)$,

$$v_x = (I - vv^H)Av + iv\,\mathrm{Im}(v^H A v), \tag{3.46}$$

which will be of use shortly because of the way the RHS splits in to real and complex parts.

3.6.2.2 Projecting on to $\mathbb{C}P^{n-1}$ and the dynamics of the phase

Next write points of the trajectory $v(x) \in S^{2n-1}$ in terms of their local coordinate representation on $S^1 \times \mathbb{C}P^{n-1}$ again: $v(x) = e^{i\theta(x)}w(x)$, then differentiate this expression w.r.t. x and substitute the sphere dynamics equation (3.46):

$$
\begin{aligned}
v(x) &= e^{i\theta(x)}w(x) && (3.47)\\
\Rightarrow w_x &= (e^{-i\theta(x)}v(x))_x && (3.48)\\
&= e^{-i\theta}v_x - ie^{-i\theta}\theta_x v && (3.49)\\
&= e^{-i\theta}[(I - vv^H)Av + iv\,\mathrm{Im}(v^H Av)] - ie^{-i\theta}\theta_x v \qquad \text{by (3.46)} && (3.50)\\
&= (I - ww^H)Aw + iw\,\mathrm{Im}(w^H Aw) - iw\theta_x \qquad \text{since } v^H Av = w^H Aw\\
&= (I - ww^H)Aw + iw(\mathrm{Im}(w^H Aw) - \theta_x) && (3.51)
\end{aligned}
$$

This equation then describes how the dynamics induced by (3.36) on $\mathbb{C}P^{n-1}$ are coupled to the dynamics induced within fibres: it shows explicitly how, given the trajectory $v(x)$, the dynamics of $\theta(x)$ affects paths of points $w(x)$ in the same equivalence classes, $[v(x)]$. Figure 3.2 illustrates the situation, and the following points are emphasized:

- For $x \in [x_0, x_1] \subset \mathbb{R}$, both $v(x)$ and $w(x)$ are paths in S^{2n-1}.
- The path $v(x)$ has initial condition $v(x_0)$ and is determined by equation (3.46).
- At each point of the path $v(x)$, there is a whole S^1-fibre of points $w(x) = e^{-i\theta(x)}v(x)$ which map to the same point on the base $\mathbb{C}P^{n-1}$.
- The path $w(x)$ has initial data $\{v(x_0), \theta(x_0)\}$ and is determined by equation (3.51) *including* the expression $\theta_x(x)$.
- $\theta_x(x)$ is of course arbitrary: we can choose any function we like. It defines how, as v and w move through S^{2n-1} simultaneously, w moves around in the fibre attached to v. This function represents a choice of how to move from fibre to fibre through the bundle.
- If we pick $\theta_x(x) = 0$ then equation (3.51) for $w(x)$ is the same as equation (3.46) for $v(x)$, so that v and w follow paths on S^{2n-1} governed by the same equation, and just stay separated by a constant phase $\theta(x_0)$. i.e. if v and w are separated by a constant phase $\theta(x_0)$ at $x = x_0$ then they will remain separated by phase $\theta(x_0)$ for all x.

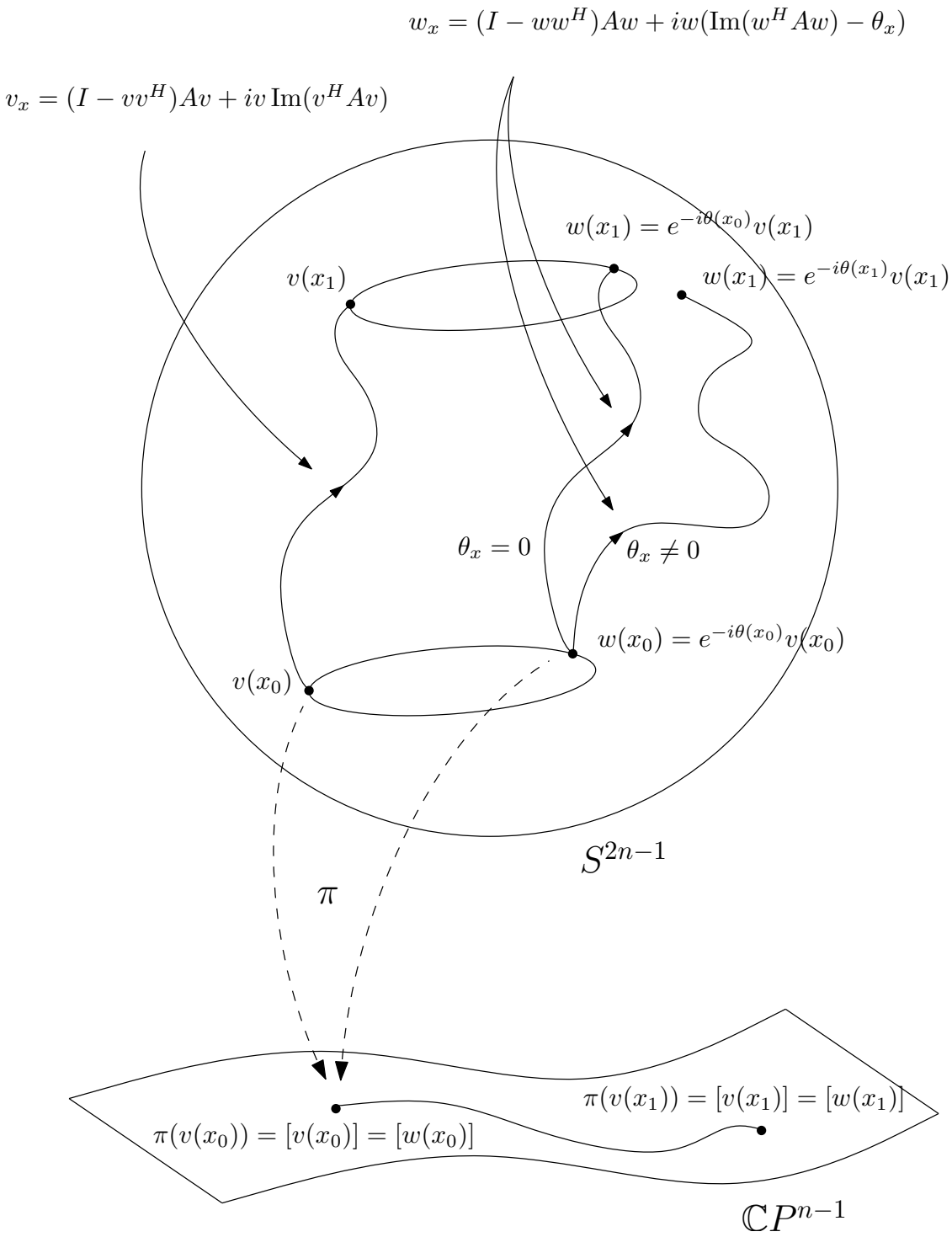

Figure 3.2: Illustration of how paths induced on S^{2n-1} by $u_x = Au$ are related by phase $\theta(x)$

The most interesting feature of equation (3.51) is how the RHS splits in to two parts, the second of which involves the connection on the bundle. The connection here is given by $i\,\mathrm{Im}(w^H Aw)$ (e.g. see (3.8), (3.12) and (3.46)) so that the vanishing of the second term corresponds to parallel translation in the bundle:

> *the path $w(x)$ induced by $u_x = Au$ is horizontal w.r.t. the natural connection iff*
>
> $$\theta_x(x) = \mathrm{Im}(w^H Aw) \tag{3.52}$$

So in this case the equation for w reduces to

$$w_x = (I - ww^H)Aw \tag{3.53}$$

and we see that even though $\theta(x)$ is in general an arbitrary function, the expressions used throughout the analysis, although completely natural and uncontrived, result in a neat splitting of w_x in to two distinct parts, out of which the notion of parallel transport w.r.t. the natural connection automatically emerges. One interesting point to note about the horizontal case is that then the equation of motion (3.53) is of the same form as the equation of motion of the equivalent *real* system, i.e. of a real variable $w \in S^{n-1} \subset \mathbb{R}^n$ under the motion induced by a real system $u_x = Au$, $u \in \mathbb{R}^n, A \in M_n(\mathbb{R})$. The fact that these real and complex systems of equal dimension share the same equation of motion precisely when the motion in the complex system is horizontal w.r.t. the natural connection is an interesting observation, however it is not clear whether it has any deeper significance or applications.

Remark 3.6.2. *It should also be noted that equation (3.53) coincides precisely with a special case of the equation used in the continuous orthogonalization method of Drury [26]. Thus the equation itself is familiar, however, its interpretation as an expression of horizontality of dynamics w.r.t the natural connection is new. The methods of geometric integration and continuous orthogonalization for preserving constraint manifolds in numerical integration have been studied extensively [27], [28], [29], and applied specifically to the problem of calculating the Evans function in [24]. Thus the overlap between the material presented in this thesis and previous studies on continuous orthogonalization may be quite large; establishing and interpreting the connections would form an interesting extension beyond this work.*

Thus, we find that for paths induced by $u_x = Au$, equation (3.35) for the phase curve $\theta(x)$ reduces to

$$\theta(x) = \int_{x_0}^{x} \Big(\frac{\mathrm{Im}(u(s)^H Au(s))}{(u(s)^H u(s))} \Big) ds \tag{3.54}$$

Having set up the general theory of the phase in the Hopf bundle and shown how this gives rise to each path of vectors in $\mathbb{C}^n \setminus \{0\}$ having an associated phase curve, we now focus attention on the lowest dimensional case, the $S^1 \to S^3 \to S^2$ bundle, to show how the concepts apply there. We will then proceed to solve phase equations numerically in a wider variety of situations.

Chapter 4

Investigating the Hopf bundle using the quaternionic matrices

In this chapter we show how the quaternionic matrices can be used to describe the classical Hopf bundle. By providing a concrete coordinate system within which to work, this new application of the matrices reveals many interesting geometrical aspects of the bundle. We show explicitly how parallel transport fits in to the picture, how we can extract the phase for certain dynamics within the bundle, and finally we observe the motion of the phase in a few numerical examples.

4.1 The quaternionic matrices

The basis quaternions are given by $1, i, j, k$, satisfying $i^2 = j^2 = k^2 = ijk = -1$. The quaternions in general are defined as $\mathbb{H} = \{a + bi + cj + dk : a, b, c, d \in \mathbb{R}\}$. The quaternionic matrices $J_1, J_2, J_3, K_1, K_2, K_3$ are defined as

$$J_1 = \begin{pmatrix} 0 & -1 & 0 & 0 \\ 1 & 0 & 0 & 0 \\ 0 & 0 & 0 & -1 \\ 0 & 0 & 1 & 0 \end{pmatrix}, J_2 = \begin{pmatrix} 0 & 0 & -1 & 0 \\ 0 & 0 & 0 & 1 \\ 1 & 0 & 0 & 0 \\ 0 & -1 & 0 & 0 \end{pmatrix},$$
$$J_3 = \begin{pmatrix} 0 & 0 & 0 & -1 \\ 0 & 0 & -1 & 0 \\ 0 & 1 & 0 & 0 \\ 1 & 0 & 0 & 0 \end{pmatrix} \tag{4.1}$$

$$K_1 = \begin{pmatrix} 0 & 0 & 0 & 1 \\ 0 & 0 & -1 & 0 \\ 0 & 1 & 0 & 0 \\ -1 & 0 & 0 & 0 \end{pmatrix}, K_2 = \begin{pmatrix} 0 & 1 & 0 & 0 \\ -1 & 0 & 0 & 0 \\ 0 & 0 & 0 & -1 \\ 0 & 0 & 1 & 0 \end{pmatrix},$$
$$K_3 = \begin{pmatrix} 0 & 0 & 1 & 0 \\ 0 & 0 & 0 & 1 \\ -1 & 0 & 0 & 0 \\ 0 & -1 & 0 & 0 \end{pmatrix} \tag{4.2}$$

Together they form a basis for $\mathfrak{so}(4)$, the Lie algebra of the Lie group of rotations about a fixed point in $\mathbb{R}^4$, $S0(4)$; they are featured in many standard texts, such as [25]. They are called quaternionic matrices because of their intimate link with the quaternions; for example, if we represent $x = a + bi + cj + dk \in \mathbb{H}$ by the matrix

$$\begin{pmatrix} a & b & c & d \\ -b & a & -d & c \\ -c & d & a & -b \\ -d & -c & b & a \end{pmatrix} = aI_4 + bK_2 + cK_3 + dK_1 \tag{4.3}$$
$$= a \begin{pmatrix} 1 & 0 & 0 & 0 \\ 0 & 1 & 0 & 0 \\ 0 & 0 & 1 & 0 \\ 0 & 0 & 0 & 1 \end{pmatrix} + b \begin{pmatrix} 0 & 1 & 0 & 0 \\ -1 & 0 & 0 & 0 \\ 0 & 0 & 0 & -1 \\ 0 & 0 & 1 & 0 \end{pmatrix}$$
$$+c \begin{pmatrix} 0 & 0 & 1 & 0 \\ 0 & 0 & 0 & 1 \\ -1 & 0 & 0 & 0 \\ 0 & -1 & 0 & 0 \end{pmatrix} + d \begin{pmatrix} 0 & 0 & 0 & 1 \\ 0 & 0 & -1 & 0 \\ 0 & 1 & 0 & 0 \\ -1 & 0 & 0 & 0 \end{pmatrix}, \tag{4.4}$$

then in this format, quaternionic addition and multiplication are represented by standard matrix addition and multiplication. (I_n is the n-dimensional identity matrix.) The J_is and K_is are skew-symmetric and satisfy

$$J_i^2 = -I_4 \qquad K_i^2 = -I_4 \qquad i = 1, 2, 3$$

$$J_i J_j = \epsilon_{ijk} J_k \quad K_i K_j = \epsilon_{ijk} K_k \qquad i, j, k = 1, 2, 3, \text{ all different}$$

(where ϵ_{ijk} is 1 for even permutations, -1 for odd permutations and 0 otherwise.) The J_is and K_is are related by the quaternionic matrix conjugation operator R:

$$R = \begin{pmatrix} 1 & 0 & 0 & 0 \\ 0 & -1 & 0 & 0 \\ 0 & 0 & -1 & 0 \\ 0 & 0 & 0 & -1 \end{pmatrix} \tag{4.5}$$

and we have

$$\begin{aligned} K_1 &= R^T J_3 R \\ K_2 &= R^T J_1 R \\ K_3 &= R^T J_2 R \end{aligned} \tag{4.6}$$

so that any results in terms of the J_is could equally well be written in terms of the K_is and vice versa.

Proposition 4.1.1. *For each $\xi \in \mathbb{R}^4$, $\xi \neq 0$, $\{\xi, K_1\xi, K_2\xi, K_3\xi\}$ is an orthogonal basis for $\mathbb{R}^4$.*

Proof. First, for each $i = 1, 2, 3$, $\langle \xi, K_i\xi \rangle = 0$, by skew-symmetry.
Second, for each $i \neq j$,

$$\langle K_i\xi, K_j\xi \rangle = \langle \xi, K_i^T K_j\xi \rangle = \langle \xi, -K_iK_j\xi \rangle = \langle \xi, -\epsilon_{ijk}K_k\xi \rangle = 0, \tag{4.7}$$

again by skew-symmetry. □

Thus if we take a 4-vector $v \in S^3 \subset \mathbb{R}^4$, then since v is itself a vector normal to S^3, we have $T_vS^3 = \text{span}\{K_1v, K_2v, K_3v\}$. In this way the quaternionic matrices provide a straightforward method for describing tangent spaces to the 3-sphere explicitly in terms of four real coordinates. Moreover, this description is closely linked with the geometry of the Hopf bundle, as we show below.

4.2 The Hopf bundle again

4.2.1 The different coordinate representations of the Hopf bundle

We consider here the Hopf bundle $S^1 \to S^3 \to S^2$, as described in Section 3.2. This case is very useful and features a lot in the literature because it is of low enough dimension to allow us to visualize elements of the geometry using various coordinate systems. However, what most texts omit to mention is that there are many different but geometrically equivalent Hopf-S^1 actions on S^3 - in the sense that the defining characteristics of the resulting bundles are the same - and that in any specific situation it is the choice of group action which dictates the particular

coordinate representation given. If we have complex coordinates $(z_1, z_2) \in S^3 \subset \mathbb{C}^2$ then the standard S^1 group action is written

$$\begin{aligned} \Phi : S^1 \times S^3 &\rightarrow S^3 \\ (e^{i\theta}, (z_1, z_2)) &\mapsto (e^{im\theta} z_1, e^{in\theta} z_2), \qquad \text{with } m, n \in \mathbb{Z} \setminus \{0\} \end{aligned} \tag{4.8}$$

But for a principal bundle the group action is required to be free, which is the case in this standard form if and only if $m, n = \pm 1$. (However, this is not the most general form of free S^1 action on $\mathbb{C}^2$, as we shall see in Section 4.2.5 below.) Different combinations of $m, n = \pm 1$ correspond to different ways of rotating points in S^3. Confusingly, this leads to a variety of slightly different coordinate representations of the Hopf bundle in the literature. For example, Cushman even uses two different representations within one book, [22] (p.367, p.374), and Chruściński and Jamiołkowski [14] use yet another. These simply correspond to different choices of coordinates at some stage in the analyses, often just a different ordering of the three coordinates for S^2. Moreover, in the following investigation of the Hopf bundle, which uses the quaternionic matrices to describe the tangent space to the bundle, evenly permuting these matrices in the analysis corresponds to selecting a different S^1 action, as will hopefully become clear as the discussion progresses.

Remark 4.2.1. *As stated by Hou and Hou in [30], the symmetry properties encountered in the Hopf bundle are a consequence of S^3 being a parallelizable manifold (a parallelizable n-manifold is a manifold with exactly n smoothly varying linearly-independent tangent vector fields at each point). The only n-spheres which are parallelizable manifolds are S^1, S^3 and S^7, which are the manifolds of unit complex numbers, quaternions and octonions $\mathbb{O}$ respectively. Now, a division algebra A is an algebra with unit element which, for each non-zero element $a \in A$, also contains its inverse $a^{-1} \in A$, and it can be shown that the only division algebras with a norm - with which to potentially form a unit manifold - are in fact $\mathbb{R}$, $\mathbb{C}$, $\mathbb{H}$ and $\mathbb{O}$. Thus "division algebras lie at the very core of the classification of possible symmetries in nature". These fundamental issues lie outside the scope of this thesis, we simply include a few lines on the matter to give an idea of the underlying issues which generate the remarkable symmetries encountered here.*

4.2.2 An explicit coordinate representation of the Hopf bundle

Take $z \in S^3 \subset \mathbb{C}^2$. We consider only the $m = n = 1$ S^1 action above, so we have

$$\Phi : S^1 \times S^3 \rightarrow S^3 \tag{4.9}$$
$$(e^{i\theta}, z) \mapsto e^{i\theta} z \tag{4.10}$$

The form of the coordinates we choose for the Hopf map throughout the following is

$$\pi : \mathbb{C}^2 \rightarrow \mathbb{R}^3 \tag{4.11}$$
$$\begin{pmatrix} z_1 \\ z_2 \end{pmatrix} \mapsto \begin{pmatrix} 2\mathrm{Re}(z_1\bar{z_2}) \\ 2\mathrm{Im}(z_1\bar{z_2}) \\ |z_1|^2 - |z_2|^2 \end{pmatrix} \tag{4.12}$$
$$= \begin{pmatrix} \bar{z_1}z_2 + z_1\bar{z_2} \\ i(\bar{z_1}z_2 - z_1\bar{z_2}) \\ |z_1|^2 - |z_2|^2 \end{pmatrix} \tag{4.13}$$

Then write z as

$$z = \begin{pmatrix} z_1 \\ z_2 \end{pmatrix} = \begin{pmatrix} x_1 + iy_1 \\ x_2 + iy_2 \end{pmatrix} = \begin{pmatrix} x_1 \\ x_2 \end{pmatrix} + i \begin{pmatrix} y_1 \\ y_2 \end{pmatrix} \tag{4.14}$$

and define a correspondence between the real and complex coordinates by setting

$$v = \begin{pmatrix} x_1 \\ x_2 \\ y_1 \\ y_2 \end{pmatrix} = \begin{pmatrix} \mathrm{Re}(z_1) \\ \mathrm{Re}(z_2) \\ \mathrm{Im}(z_1) \\ \mathrm{Im}(z_2) \end{pmatrix} \in S^3 \subset \mathbb{R}^4 \tag{4.15}$$

In these coordinates π becomes

$$\pi : \begin{pmatrix} x_1 \\ x_2 \\ y_1 \\ y_2 \end{pmatrix} \mapsto \begin{pmatrix} 2(x_1x_2 + y_1y_2) \\ 2(x_2y_1 - x_1y_2) \\ x_1^2 + y_1^2 - x_2^2 - y_2^2 \end{pmatrix} \tag{4.16}$$

so that at the point $v = \begin{pmatrix} x_1 \\ x_2 \\ y_1 \\ y_2 \end{pmatrix} \in S^3$, the tangent map $\pi_* : T_vS^3 \rightarrow T_{\pi(v)}S^2$ is given by the matrix

$$\pi_* = 2 \begin{pmatrix} x_2 & x_1 & y_2 & y_1 \\ -y_2 & y_1 & x_2 & -x_1 \\ x_1 & -x_2 & y_1 & -y_2 \end{pmatrix} \tag{4.17}$$

4.2.3 The vertical subspace

Now, we know that in this coordinate representation of the Hopf bundle, the vertical space of the bundle at v, V_v, is the kernel of this matrix, $\ker(\pi_*)$. To obtain an explicit expression for V_v we first note that each $a \in T_v S^3$ may be written in terms of the basis $\{K_1 v, K_2 v, K_3 v\}$ for $T_v S^3$ described above:

$$a = c_1 K_1 v + c_2 K_2 v + c_3 K_3 v \qquad \text{for some constants } c_1, c_2, c_3 \in \mathbb{R} \tag{4.18}$$

Then by direct calculation we see that

$$\pi_*(K_1 v) \neq \begin{pmatrix} 0 \\ 0 \\ 0 \end{pmatrix}, \qquad \pi_*(K_2 v) \neq \begin{pmatrix} 0 \\ 0 \\ 0 \end{pmatrix}, \qquad \pi_*(K_3 v) = \begin{pmatrix} 0 \\ 0 \\ 0 \end{pmatrix} \tag{4.19}$$

so that in fact the vertical space at v is the space spanned by the vector obtained by applying quaternionic matrix K_3 to the position vector v:

$$\begin{aligned} V_v &= \ker(\pi_*)\big|_{T_v S^3} && (4.20)\\ &= \operatorname{span}\{K_3 v\} && (4.21)\\ &= \operatorname{span}\left\{ \begin{pmatrix} 0 & 0 & 1 & 0 \\ 0 & 0 & 0 & 1 \\ -1 & 0 & 0 & 0 \\ 0 & -1 & 0 & 0 \end{pmatrix} \begin{pmatrix} x_1 \\ x_2 \\ y_1 \\ y_2 \end{pmatrix} \right\} && (4.22)\\ &= \operatorname{span}\left\{ \begin{pmatrix} y_1 \\ y_2 \\ -x_1 \\ -x_2 \end{pmatrix} \right\} && (4.23) \end{aligned}$$

Remark 4.2.2. *As always, the term "span" refers to multiplication by real numbers only.*

For completeness, and to demonstrate the process explicitly, we briefly show how this translates to complex coordinates. Write V_v as

$$V_v = \operatorname{span}\{K_3 v\} = \left\{ \alpha \begin{pmatrix} y_1 \\ y_2 \\ -x_1 \\ -x_2 \end{pmatrix} : \alpha \in \mathbb{R} \right\} \tag{4.24}$$

and elements of this set are in correspondence with complex vectors as before:

$$\mathbb{R}^4 \ni \left[\alpha \begin{pmatrix} y_1 \\ y_2 \\ -x_1 \\ -x_2 \end{pmatrix} \right] \longleftrightarrow \left[\alpha \begin{pmatrix} y_1 \\ y_2 \end{pmatrix} + i\alpha \begin{pmatrix} -x_1 \\ -x_2 \end{pmatrix} \right] \in \mathbb{C}^2 \tag{4.25}$$

But

$$\alpha \begin{pmatrix} y_1 \\ y_2 \end{pmatrix} + i\alpha \begin{pmatrix} -x_1 \\ -x_2 \end{pmatrix} = -i\alpha \Big[\begin{pmatrix} x_1 \\ x_2 \end{pmatrix} + i \begin{pmatrix} y_1 \\ y_2 \end{pmatrix} \Big] \tag{4.26}$$

$$= -i\alpha \begin{pmatrix} z_1 \\ z_2 \end{pmatrix} \tag{4.27}$$

so that in complex coordinates, the vertical space at $z \in S^3 \subset \mathbb{C}^2$ is

$$V_z = \{-i\alpha z : \alpha \in \mathbb{R}\} = \text{span}\{iz\} \tag{4.28}$$

which is of course consistent with the fact that the vertical space is tangent to the group action at the identity: the group action is S^1, so applying the action to $z \in S^3$ in complex coordinates gives the point $e^{i\theta}z$, so a tangent vector to the curve of points generated by the action, at the identity of the action, is

$$\Big[\frac{d}{d\theta}(e^{i\theta}z)\Big]_{\theta=0} = ie^{i\theta}z\Big|_{\theta=0} = iz \tag{4.29}$$

and the vertical space is indeed the span of this vector.

4.2.4 The group action in real coordinates

The group action in complex coordinates is $\Phi : S^1 \times S^3 \to S^3, (e^{i\theta}, z) \mapsto e^{i\theta}z$. This translates to real coordinates as follows

$$e^{i\theta}z = \begin{pmatrix} e^{i\theta}z_1 \\ e^{i\theta}z_2 \end{pmatrix} \tag{4.30}$$

$$= \begin{pmatrix} (\cos\theta + i\sin\theta)(x_1 + iy_1) \\ (\cos\theta + i\sin\theta)(x_2 + iy_2) \end{pmatrix} \tag{4.31}$$

$$= \begin{pmatrix} x_1\cos\theta - y_1\sin\theta \\ x_2\cos\theta - y_2\sin\theta \end{pmatrix} + i \begin{pmatrix} x_1\sin\theta + y_1\cos\theta \\ x_2\sin\theta + y_2\cos\theta \end{pmatrix} \tag{4.32}$$

from which, using G_θ to denote the group action in real coordinates, we form the following 4-vector according to the above real-complex correspondence

$$G_\theta v = G_\theta \begin{pmatrix} x_1 \\ x_2 \\ y_1 \\ y_2 \end{pmatrix} = \begin{pmatrix} x_1\cos\theta - y_1\sin\theta \\ x_2\cos\theta - y_2\sin\theta \\ x_1\sin\theta + y_1\cos\theta \\ x_2\sin\theta + y_2\cos\theta \end{pmatrix} \tag{4.33}$$

$$= \begin{pmatrix} \cos\theta & 0 & -\sin\theta & 0 \\ 0 & \cos\theta & 0 & -\sin\theta \\ \sin\theta & 0 & \cos\theta & 0 \\ 0 & \sin\theta & 0 & \cos\theta \end{pmatrix} \begin{pmatrix} x_1 \\ x_2 \\ y_1 \\ y_2 \end{pmatrix} \tag{4.34}$$

$$= \begin{pmatrix} I_2\cos\theta & -I_2\sin\theta \\ I_2\sin\theta & I_2\cos\theta \end{pmatrix} v \tag{4.35}$$

so in real coordinates the group action has the form

$$G_\theta = \begin{pmatrix} I_2 \cos\theta & -I_2 \sin\theta \\ I_2 \sin\theta & I_2 \cos\theta \end{pmatrix} \tag{4.36}$$

Remark 4.2.3. *Demonstrating consistency again, we see that a tangent vector to the curve of points generated by the group action, in real coordinate form, at the identity, is*

$$\begin{aligned}
\Big[\frac{d}{d\theta}(G_\theta v)\Big]_{\theta=0} &= \Big[\frac{d}{d\theta}(G_\theta)\Big]_{\theta=0} v && (4.37)\\
&= \Big[\frac{d}{d\theta}\begin{pmatrix} I_2 \cos\theta & -I_2 \sin\theta \\ I_2 \sin\theta & I_2 \cos\theta \end{pmatrix}\Big]_{\theta=0} v && (4.38)\\
&= \begin{pmatrix} -I_2 \sin\theta & -I_2 \cos\theta \\ I_2 \cos\theta & -I_2 \sin\theta \end{pmatrix}_{\theta=0} v && (4.39)\\
&= \begin{pmatrix} 0 & -I_2 \\ I_2 & 0 \end{pmatrix} v && (4.40)\\
&= \begin{pmatrix} 0 & 0 & -1 & 0 \\ 0 & 0 & 0 & -1 \\ 1 & 0 & 0 & 0 \\ 0 & 1 & 0 & 0 \end{pmatrix} \begin{pmatrix} x_1 \\ x_2 \\ y_1 \\ y_2 \end{pmatrix} && (4.41)\\
&= \begin{pmatrix} -y_1 \\ -y_2 \\ x_1 \\ x_2 \end{pmatrix} && (4.42)
\end{aligned}$$

which shows that the vertical space is of course the same as before.

4.2.5 The group action in terms of the exponential map

The previous sections have shown that given a particular coordinate representation of the Hopf bundle, we can derive expressions for the vertical space and the action in both real and complex coordinates, and we demonstrated the process of passing from one to the other. However, we can also approach the problem from a more fundamental point of view, by using the relationship between a Lie group and its Lie algebra to describe the situation.

First, observe that

$$e^{-K_3\theta} = \begin{pmatrix} I_2 \cos\theta & -I_2 \sin\theta \\ I_2 \sin\theta & I_2 \cos\theta \end{pmatrix} = G_\theta \tag{4.43}$$

(The proof of this is a special case of (4.61).) This result is explained as follows:

Recall, if G is a Lie group, $\mathfrak{g}$ is its Lie algebra, $\xi \in \mathfrak{g}$ and $\exp : \mathfrak{g} \to G$ is the exponential map, then

$$t \mapsto \exp(t\xi), \qquad t \in \mathbb{R} \tag{4.44}$$

is the unique 1-parameter subgroup of G whose tangent vector at $t = 0$ is ξ, and we sometimes write

$$\exp(t\xi) = g_\xi(t) \in G \tag{4.45}$$

to emphasize the fact that $\exp(t\xi)$ is an element of the group. However, this result alone does not quite fit the scenario above, as can be seen by the fact that in our equation, $e^{-K_3\theta}$ is equal to a 4×4 matrix, G_θ, which is not obviously a member of the group S^1. The key to understanding the result then is to consider not just the Lie group, Lie algebra and 1-parameter subgroup, but instead *representations* of these.

Definition 4.2.1. *A map $\phi : G \to H$ is a Lie group homomorphism if it is a smooth homomorphism between Lie groups G and H. i.e. $\forall g_1, g_2 \in G, \phi(g_1 \circ g_2) = \phi(g_1) \circ \phi(g_2)$. If in addition the image group H is one of the general linear matrix Lie groups, $GL_n(\mathbb{R})$ or $GL_n(\mathbb{C})$ then ϕ is called a representation of G.*

Definition 4.2.2. *If $\mathfrak{g}$ and $\mathfrak{h}$ are Lie algebras, a map $\psi : \mathfrak{g} \to \mathfrak{h}$ is a Lie algebra homomorphism if it is linear and preserves brackets, i.e. $\psi[\xi, \eta] = [\psi(\xi), \psi(\eta)] \forall \xi, \eta \in \mathfrak{g}$. If in addition the image algebra $\mathfrak{h}$ is one of the the Lie algebras, $\mathfrak{gl}_n(\mathbb{R})$ or $\mathfrak{gl}_n(\mathbb{C})$, of the general linear matrix Lie groups, then ψ is called a representation of the Lie algebra $\mathfrak{g}$.*

So we can use matrices to represent Lie groups and Lie algebras. The specific fact we then need is that if we have an m-dimensional representation of $\mathfrak{g}$ (i.e. a set of $m \times m$ matrices satisfying $\mathfrak{g}$'s commutation relations), then its exponentiation gives an m-dimensional representation of G, which is again a set of $m \times m$ matrices. This is exactly what is going on here. Since the Lie algebra of a Lie group is isomorphic to the tangent space at the identity ($\mathfrak{g} \cong T_eG$), and $T_vS^3 = \text{span}\{K_1v, K_2v, K_3v\}$, $\{K_1, K_2, K_3\}$ is a basis for a *representation* of the Lie algebra of S^3 (or, strictly speaking, it is a basis for a representation of the Lie algebra of the Lie group $SU(2)$, $SU(2)$ being diffeomorphic to S^3, since the notion of group multiplication only makes sense in this context). So as parameter we use $\theta \in \mathbb{R}$, and if we have a vector in T_vS^3, say K_3v, then K_3 is a 4-dimensional representation of the corresponding Lie algebra element; and the map

$$\theta \to \exp(\theta K_3), \qquad \theta \in \mathbb{R} \tag{4.46}$$

yields a representation on $\mathbb{R}^4$ of the unique 1-parameter subgroup S^1 of S^3 (or, strictly, $U(1)$ of $SU(2)$) whose tangent vector at $\theta = 0$ is $K_3 v$. This explains the exponentiation calculation above, showing that if we select $K_3 v$ to be our vertical direction (and reverse the sign of θ for exact agreement), then the group action can be written as

$$G_\theta = e^{-K_3 \theta} \tag{4.47}$$

as before - which is of a course a 4-dimensional representation of the S^1 group action. This form of expression for the group action makes explicit the correspondence between the group action and vertical direction. We can in fact pick the vertical direction to be any direction within the tangent space $T_v S^3$ and calculate the real coordinate expression for the associated group action similarly, as follows. Take $a, b, c \in \mathbb{R}$, fixed, and let

$$\tilde{K} = aK_1 + bK_2 + cK_3 \tag{4.48}$$

Then

$$\begin{aligned}
\tilde{K}^2 &= (aK_1 + bK_2 + cK_3)(aK_1 + bK_2 + cK_3) && (4.49)\\
&= (-a^2 - b^2 - c^2)I_4 + (aK_1 bK_2 + \cdots + bK_2 aK_1 + \cdots) && (4.50)\\
&= (-a^2 - b^2 - c^2)I_4 + (ab(K_3) + \cdots + ab(-K_3) + \cdots) && (4.51)\\
&= (-a^2 - b^2 - c^2)I_4 && (4.52)
\end{aligned}$$

and writing $\alpha^2 = a^2 + b^2 + c^2$ we get $\tilde{K}^2 = -\alpha^2 I_4$, so that

$$
\begin{aligned}
e^{\tilde{K}\theta} &= \sum_{n=0}^{\infty} \frac{(\tilde{K}\theta)^n}{n!} && (4.53)\\
&= \sum_{n=0}^{\infty} \frac{(\tilde{K})^n\theta^n}{n!} && (4.54)\\
&= \sum_{n=0}^{\infty} \frac{(\tilde{K})^{2n}\theta^{2n}}{(2n)!} + \sum_{n=0}^{\infty} \frac{(\tilde{K})^{2n+1}\theta^{2n+1}}{(2n+1)!} && (4.55)\\
&= \sum_{n=0}^{\infty} \frac{((\tilde{K})^2)^n\theta^{2n}}{(2n)!} + \sum_{n=0}^{\infty} \frac{(\tilde{K})((\tilde{K})^2)^n\theta^{2n+1}}{(2n+1)!} && (4.56)\\
&= I_4 \sum_{n=0}^{\infty} \frac{(-\alpha^2)^n\theta^{2n}}{(2n)!} + \tilde{K} \sum_{n=0}^{\infty} \frac{(-\alpha^2)^n\theta^{2n+1}}{(2n+1)!} \qquad \text{since } \tilde{K}^2 = -\alpha^2 I_4 \\
&= I_4 \sum_{n=0}^{\infty} \frac{(-1)^n\alpha^{2n}\theta^{2n}}{(2n)!} + \tilde{K} \sum_{n=0}^{\infty} \frac{(-1)^n\alpha^{2n}\theta^{2n+1}}{(2n+1)!} && (4.57)\\
&= I_4 \sum_{n=0}^{\infty} \frac{(-1)^n(\alpha\theta)^{2n}}{(2n)!} + \frac{\tilde{K}}{\alpha} \sum_{n=0}^{\infty} \frac{(-1)^n(\alpha\theta)^{2n+1}}{(2n+1)!} && (4.58)\\
&= I_4\cos(\alpha\theta) - \frac{\tilde{K}}{\alpha}\sin(\alpha\theta) && (4.59)\\
&= I_4\cos(\alpha\theta) - \frac{\sin(\alpha\theta)}{\alpha}\Big[aK_1 + bK_2 + cK_3\Big] && (4.60)\\
&= \begin{pmatrix} \cos(\alpha\theta) & -b\frac{\sin(\alpha\theta)}{\alpha} & -c\frac{\sin(\alpha\theta)}{\alpha} & -a\frac{\sin(\alpha\theta)}{\alpha} \\ b\frac{\sin(\alpha\theta)}{\alpha} & \cos(\alpha\theta) & a\frac{\sin(\alpha\theta)}{\alpha} & -c\frac{\sin(\alpha\theta)}{\alpha} \\ c\frac{\sin(\alpha\theta)}{\alpha} & -a\frac{\sin(\alpha\theta)}{\alpha} & \cos(\alpha\theta) & b\frac{\sin(\alpha\theta)}{\alpha} \\ a\frac{\sin(\alpha\theta)}{\alpha} & c\frac{\sin(\alpha\theta)}{\alpha} & -b\frac{\sin(\alpha\theta)}{\alpha} & \cos(\alpha\theta) \end{pmatrix} && (4.61)
\end{aligned}
$$

So this is a real coordinate representation of the group action on $\mathbb{R}^4$ which results from choosing the vertical direction to be $\tilde{K}v \in T_vS^3$. Picking $a = b = 0$, $c = -1$ verifies the previous case, (4.43). This discussion shows that selecting any particular coordinate representation of the Hopf map, such as (4.16), is tantamount to selecting a group action, or indeed a vertical direction in the bundle.

Remark 4.2.4. *Notice that the period of this action is 2π iff $\alpha = \pm 1$, i.e. when $a^2 + b^2 + c^2 = 1$. Thus we have the interesting result that all 2π-periodic S^1 actions in the Hopf bundle are parametrized by S^2 in this way. This aspect of the bundle structure could well be a good subject for further investigation outside this thesis.*

One important point to make, the origin of which lies in the above calculation (step (4.60)), is that the group action for the $a = b = 0$, $c = -1$ case can be written

as

$$G_\theta = \begin{pmatrix} I_2 \cos\theta & -I_2 \sin\theta \\ I_2 \sin\theta & I_2 \cos\theta \end{pmatrix} = I_4 \cos\theta - K_3 \sin\theta \tag{4.62}$$

4.2.6 The horizontal subspace

Now, we know that $\{K_1 v, K_2 v, K_3 v\}$ is an orthogonal basis for $T_v S^3$, and that in the particular coordinate system for the Hopf map on which we are focusing, $K_3 v$ is the vertical direction. We also know that every horizontal space $H_v S^3$ must by definition satisfy two properties, firstly non-degeneracy, $T_v S^3 = V_v S^3 \bigoplus H_v S^3$, and secondly right-equivariance, $(\Phi_g)_*(H_v S^3) = H_{\Phi_g(v)} S^3$. Since $K_3 v$ is the vertical direction, the space spanned by vectors $\{K_1 v, K_2 v\}$ already satisfies the first of these conditions and has the added property of being orthogonal to the vertical direction. Moreover, this first condition remains satisfied even following the addition of some component of the vertical direction to each of the horizontal directions, say an amount δ_1 in the $K_1 v$ direction and an amount δ_2 in the $K_2 v$ direction, yielding the space spanned by vectors $\{K_1 v + \delta_1 K_3 v, K_2 v + \delta_2 K_3 v\}$. Write

$$\zeta_1(\delta_1) = K_1 + \delta_1 K_3$$
$$\zeta_2(\delta_2) = K_2 + \delta_2 K_3$$

so that

$$K_1 v + \delta_1 K_3 v = (K_1 + \delta_1 K_3) v = \zeta_1 v$$
$$K_2 v + \delta_2 K_3 v = (K_2 + \delta_2 K_3) v = \zeta_2 v$$

and the spaces we are looking at as potential horizontal subspaces are the spaces spanned by $\{\zeta_1 v, \zeta_2 v\}$ for various values of δ_1 and δ_2. The orthogonal case is just the $\delta_1 = \delta_2 = 0$ case, which is the natural - or canonical - connection. Now, for $span\{\zeta_1 v, \zeta_2 v\}$ to genuinely be a horizontal space of the bundle it must satisfy the equivariance property, and to check this, to see if this imposes any extra constraints on the system, in particular on the δ_is, we substitute real coordinate expressions for the various elements in to the equivariance condition equation, as follows.

4.2.7 Investigating equivariance of potential horizontal subspaces

In order for the space $span\{\zeta_1 v, \zeta_2 v\}$, at the point v, to satisfy right-equivariance, we require

$$(\Phi_g)_*(H_v S^3) = H_{\Phi_g(v)} S^3 \tag{4.63}$$

which in the current notation becomes

$$\mathrm{span}\Big\{(G_\theta)_*(\zeta_1 v), (G_\theta)_*(\zeta_2 v)\Big\} = \mathrm{span}\Big\{\zeta_1(G_\theta v), \zeta_2(G_\theta v)\Big\} \tag{4.64}$$

Keeping in mind that $G_\theta : S^3 \to S^3$, and $(G_\theta)_* : T_v S^3 \to T_{G_\theta(v)} S^3$, if $\mathcal{V} \in \mathbb{R}^4$ is a tangent vector to a path $v(t)$ on S^3 at $t = 0$, i.e. $\mathcal{V} = \frac{d}{dt} v(t)\big|_{t=0}$, we then have

$$\begin{aligned}
\Big[(G_\theta)_*\big|_v\Big]\mathcal{V} &= \Big[(G_\theta)_*\big|_v\Big]\frac{d}{dt}v(t)\big|_{t=0} && (4.65)\\
&= \frac{d}{dt}\Big[G_\theta(v(t))\Big]_{t=0} && (4.66)\\
&= G_\theta\Big[\frac{d}{dt}(v(t))\Big]_{t=0} \qquad \text{since } G_\theta \text{ is just a } \theta\text{-dependent matrix}\\
&= G_\theta \mathcal{V} && (4.67)
\end{aligned}$$

so $(G_\theta)_* = G_\theta$. This is of course exactly the same calculation and result as we saw before in (3.20), just using explicit coordinate representations for the group elements (both as points in the group and actions on the group). Thus the equivariance condition becomes

$$\mathrm{span}\Big\{G_\theta(\zeta_1 v), G_\theta(\zeta_2 v)\Big\} = \mathrm{span}\Big\{\zeta_1(G_\theta v), \zeta_2(G_\theta v)\Big\} \tag{4.68}$$

which in full K_i notation is

$$\begin{aligned}
&\mathrm{span}\Big\{G_\theta K_1 v + \delta_1 G_\theta K_3 v, G_\theta K_2 v + \delta_2 G_\theta K_3 v\Big\}\\
&= \mathrm{span}\Big\{K_1 G_\theta v + \delta_1 K_3 G_\theta v, K_2 G_\theta v + \delta_2 K_3 G_\theta v\Big\} \qquad (4.69)
\end{aligned}$$

But now, from (4.62) we have

$$G_\theta = I_4 \cos\theta - K_3 \sin\theta \tag{4.70}$$

which implies

$$\begin{aligned}
K_1 G_\theta &= K_1\cos\theta - K_1 K_3 \sin\theta &&= K_1\cos\theta + K_2\sin\theta && (4.71)\\
K_2 G_\theta &= K_2\cos\theta - K_2 K_3 \sin\theta &&= K_2\cos\theta - K_1\sin\theta && (4.72)\\
G_\theta K_1 &= K_1\cos\theta - K_3 K_1 \sin\theta &&= K_1\cos\theta - K_2\sin\theta && (4.73)\\
G_\theta K_2 &= K_2\cos\theta - K_3 K_2 \sin\theta &&= K_2\cos\theta + K_1\sin\theta && (4.74)
\end{aligned}$$

and

$$K_3 G_\theta = K_3\cos\theta - K_3 K_3 \sin\theta = K_3\cos\theta + I_4\sin\theta = G_\theta K_3 \tag{4.75}$$

Then using these expressions we find

$$
\begin{aligned}
& G_\theta K_1 \cos 2\theta + G_\theta K_2 \sin 2\theta \\
= \; & (K_1 \cos\theta - K_2 \sin\theta)\cos 2\theta + (K_2 \cos\theta + K_1 \sin\theta)\sin 2\theta \\
& \text{(using (4.73) and (4.74))} && (4.76) \\
= \; & (K_1 \cos\theta - K_2 \sin\theta)(\cos^2\theta - \sin^2\theta) + (K_2 \cos\theta + K_1 \sin\theta)(2\sin\theta\cos\theta) \\
= \; & K_1 \cos^3\theta - K_1 \sin^2\theta \cos\theta - K_2 \sin\theta \cos^2\theta + K_2 \sin^3\theta \\
& + 2K_2 \sin\theta \cos^2\theta + 2K_1 \sin^2\theta \cos\theta && (4.77) \\
= \; & K_1 \cos^3\theta + K_1 \sin^2\theta \cos\theta + K_2 \sin^3\theta + K_2 \sin\theta \cos^2\theta && (4.78) \\
= \; & K_1 \cos\theta(\cos^2\theta + \sin^2\theta) + K_2 \sin\theta(\sin^2\theta + \cos^2\theta) && (4.79) \\
= \; & K_1 \cos\theta + K_2 \sin\theta && (4.80) \\
= \; & K_1(I_4 \cos\theta - K_3 \sin\theta) && (4.81) \\
= \; & K_1 G_\theta && (4.82)
\end{aligned}
$$

and

$$
\begin{aligned}
& -G_\theta K_1 \sin 2\theta + G_\theta K_2 \cos 2\theta \\
= \; & -(K_1 \cos\theta - K_2 \sin\theta)\sin 2\theta + (K_2 \cos\theta + K_1 \sin\theta)\cos 2\theta \\
& \text{(using (4.73) and (4.74))} && (4.83) \\
= \; & -(K_1 \cos\theta - K_2 \sin\theta)(2\sin\theta\cos\theta) + (K_2 \cos\theta + K_1 \sin\theta)(\cos^2\theta - \sin^2\theta) \\
= \; & -2K_1 \sin\theta \cos^2\theta + 2K_2 \sin^2\theta \cos\theta + K_2 \cos^3\theta \\
& - K_2 \sin^2\theta \cos\theta + K_1 \sin\theta \cos^2\theta - K_1 \sin^3\theta && (4.84) \\
= \; & K_2 \cos^3\theta + K_2 \sin^2\theta \cos\theta - K_1 \sin^3\theta - K_1 \sin\theta \cos^2\theta && (4.85) \\
= \; & K_2 \cos\theta(\cos^2\theta + \sin^2\theta) - K_1 \sin\theta(\sin^2\theta + \cos^2\theta) && (4.86) \\
= \; & K_2 \cos\theta - K_1 \sin\theta && (4.87) \\
= \; & K_2(I_4 \cos\theta - K_3 \sin\theta) && (4.88) \\
= \; & K_2 G_\theta && (4.89)
\end{aligned}
$$

So to summarize:

$$
\begin{aligned}
K_1 G_\theta &= G_\theta K_1 \cos 2\theta + G_\theta K_2 \sin 2\theta \\
K_2 G_\theta &= -G_\theta K_1 \sin 2\theta + G_\theta K_2 \cos 2\theta \\
K_3 G_\theta &= G_\theta K_3 && (4.90)
\end{aligned}
$$

4.2.7.1 The canonical connection

For the canonical connection we have $\delta_1 = \delta_2 = 0$, and the equivariance condition is just

$$\text{span}\Big\{G_\theta K_1 v, G_\theta K_2 v\Big\} = \text{span}\Big\{K_1 G_\theta v, K_2 G_\theta v\Big\} \tag{4.91}$$

Then from linear algebra we know that for any vectors $v_1, v_2, w_1, w_2 \in \mathbb{R}^n$,

$$\begin{array}{rcl} \text{span}\{v_1, v_2\} = \text{span}\{w_1, w_2\} & \Leftrightarrow & \exists \text{ a nonsingular } 2 \times 2 \text{ matrix } M \text{ s.t.} \\ & & \begin{array}{ccc} [v_1|v_2] & = & [w_1|w_2] \quad M \\ (n \times 2) & & (n \times 2) \quad (2 \times 2) \end{array} \end{array} \tag{4.92}$$

where $[v_1|v_2]$ denotes the matrix whose columns are the vectors v_1, v_2. Thus we seek a nonsingular 2×2 matrix $M = \begin{pmatrix} m_{11} & m_{12} \\ m_{21} & m_{22} \end{pmatrix}$ s.t.

$$\Big[\ K_1 G_\theta v\ \Big|\ K_2 G_\theta v\ \Big] = \Big[\ G_\theta K_1 v\ \Big|\ G_\theta K_2 v\ \Big] \begin{pmatrix} m_{11} & m_{12} \\ m_{21} & m_{22} \end{pmatrix} \tag{4.93}$$

Write this as

$$K_1 G_\theta v = m_{11} G_\theta K_1 v + m_{21} G_\theta K_2 v \tag{4.94}$$

$$K_2 G_\theta v = m_{12} G_\theta K_1 v + m_{22} G_\theta K_2 v \tag{4.95}$$

and substitute the first two equations of (4.90) to give

$$G_\theta K_1 \cos 2\theta v + G_\theta K_2 \sin 2\theta v = m_{11} G_\theta K_1 v + m_{21} G_\theta K_2 v \tag{4.96}$$

$$-G_\theta K_1 \sin 2\theta v + G_\theta K_2 \cos 2\theta v = m_{12} G_\theta K_1 v + m_{22} G_\theta K_2 v \tag{4.97}$$

Then comparing coefficients we find

$$M = \begin{pmatrix} \cos 2\theta & -\sin 2\theta \\ \sin 2\theta & \cos 2\theta \end{pmatrix} \tag{4.98}$$

Therefore the equivariance condition is satisfied and $H_v = span\{K_1 v, K_2 v\}$ is a genuine horizontal subspace of the bundle. In addition, since M is a pure rotation, we see that

> *as a point v moves along a fibre in the bundle, the horizontal subspace formed by applying K_1 and K_2 to v spins around an axis in the vertical direction at a rate of double the rate of movement along the fibre.*

4.2.7.2 The general case connection

Similarly, when $\delta_1, \delta_2 \neq 0$, we seek nonsingular matrix $N = \begin{pmatrix} n_{11} & n_{12} \\ n_{21} & n_{22} \end{pmatrix}$ s.t.

$$\begin{aligned} &\left[\; K_1 G_\theta v + \delta_1 K_3 G_\theta v \;\middle|\; K_2 G_\theta v + \delta_2 K_3 G_\theta v \; \right] \\ &= \left[\; G_\theta K_1 v + \delta_1 G_\theta K_3 v \;\middle|\; G_\theta K_2 v + \delta_2 G_\theta K_3 v \; \right] \begin{pmatrix} n_{11} & n_{12} \\ n_{21} & n_{22} \end{pmatrix} \end{aligned} \tag{4.99}$$

Again, write this as

$$\begin{aligned} &K_1 G_\theta v + \delta_1 K_3 G_\theta v \\ &= n_{11} G_\theta K_1 v + n_{21} G_\theta K_2 v + (\delta_1 n_{11} + \delta_2 n_{21}) K_3 G_\theta v \qquad (4.100) \\ &K_2 G_\theta v + \delta_2 K_3 G_\theta v \\ &= n_{12} G_\theta K_1 v + n_{22} G_\theta K_2 v + (\delta_1 n_{12} + \delta_2 n_{22}) K_3 G_\theta v \qquad (4.101) \end{aligned}$$

$$\begin{aligned} \Leftrightarrow \qquad &\big[K_1 G_\theta + \delta_1 K_3 G_\theta \big] v \\ &= \big[n_{11} G_\theta K_1 + n_{21} G_\theta K_2 + (\delta_1 n_{11} + \delta_2 n_{21}) K_3 G_\theta \big] v \qquad (4.102) \\ &\big[K_2 G_\theta + \delta_2 K_3 G_\theta \big] v \\ &= \big[n_{12} G_\theta K_1 + n_{22} G_\theta K_2 + (\delta_1 n_{12} + \delta_2 n_{22}) K_3 G_\theta \big] v \qquad (4.103) \end{aligned}$$

then using equations (4.71)-(4.75) we get

$$\begin{aligned} &\big[(K_1 \cos\theta + K_2 \sin\theta) + \delta_1 (K_3 \cos\theta + I_4 \sin\theta) \big] v \\ &= \big[n_{11} (K_1 \cos\theta - K_2 \sin\theta) + n_{21} (K_2 \cos\theta + K_1 \sin\theta) \\ &+ (\delta_1 n_{11} + \delta_2 n_{21}) (K_3 \cos\theta + I_4 \sin\theta) \big] v \qquad (4.104) \\ &\big[(K_2 \cos\theta - K_1 \sin\theta) + \delta_2 (K_3 \cos\theta + I_4 \sin\theta) \big] v \\ &= \big[n_{12} (K_1 \cos\theta - K_2 \sin\theta) + n_{22} (K_2 \cos\theta + K_1 \sin\theta) \\ &+ (\delta_1 n_{12} + \delta_2 n_{22}) (K_3 \cos\theta + I_4 \sin\theta) \big] v \qquad (4.105) \end{aligned}$$

$$\begin{aligned} \Leftrightarrow \qquad &\big[\cos\theta K_1 + \sin\theta K_2 + \delta_1 \cos\theta K_3 + \delta_1 \sin\theta I_4 \big] v \\ &= \big[n_{11} (K_1 \cos\theta - K_2 \sin\theta) + n_{21} (K_2 \cos\theta + K_1 \sin\theta) \\ &+ (\delta_1 n_{11} + \delta_2 n_{21}) (K_3 \cos\theta + I_4 \sin\theta) \big] v \qquad (4.106) \\ &\big[- \sin\theta K_1 + \cos\theta K_2 + \delta_2 \cos\theta K_3 + \delta_2 \sin\theta I_4 \big] v \\ &= \big[n_{12} (K_1 \cos\theta - K_2 \sin\theta) + n_{22} (K_2 \cos\theta + K_1 \sin\theta) \\ &+ (\delta_1 n_{12} + \delta_2 n_{22}) (K_3 \cos\theta + I_4 \sin\theta) \big] v \qquad (4.107) \end{aligned}$$

$$
\begin{aligned}
\Leftrightarrow \quad & \big[\cos\theta K_1 + \sin\theta K_2 + \delta_1\cos\theta K_3 + \delta_1\sin\theta I_4\big]v \\
& = \big[(n_{11}\cos\theta + n_{21}\sin\theta)K_1 + (-n_{11}\sin\theta + n_{21}\cos\theta)K_2 \\
& +(\delta_1 n_{11} + \delta_2 n_{21})\cos\theta K_3 + (\delta_1 n_{11} + \delta_2 n_{21})\sin\theta I_4\big]v \qquad (4.108) \\
& \big[-\sin\theta K_1 + \cos\theta K_2 + \delta_2\cos\theta K_3 + \delta_2\sin\theta I_4\big]v \\
& = \big[(n_{12}\cos\theta + n_{22}\sin\theta)K_1 + (-n_{12}\sin\theta + n_{22}\cos\theta)K_2 \\
& +(\delta_1 n_{12} + \delta_2 n_{22})\cos\theta K_3 + (\delta_1 n_{12} + \delta_2 n_{22})\sin\theta I_4\big]v \qquad (4.109)
\end{aligned}
$$

Then since $v, K_1 v, K_2 v$ and $K_3 v$ are mutually orthogonal, we can equate coefficients to yield

$$
\begin{aligned}
\cos\theta &= n_{11}\cos\theta + n_{21}\sin\theta && (4.110)\\
\sin\theta &= -n_{11}\sin\theta + n_{21}\cos\theta && (4.111)\\
-\sin\theta &= n_{12}\cos\theta + n_{22}\sin\theta && (4.112)\\
\cos\theta &= -n_{12}\sin\theta + n_{22}\cos\theta && (4.113)\\
\delta_1 &= \delta_1 n_{11} + \delta_2 n_{21} && (4.114)\\
\delta_2 &= \delta_1 n_{12} + \delta_2 n_{22} && (4.115)
\end{aligned}
$$

The first four equations here are the same as in the case of the natural connection, and they imply

$$
N = \begin{pmatrix} \cos 2\theta & -\sin 2\theta \\ \sin 2\theta & \cos 2\theta \end{pmatrix} \qquad (4.116)
$$

However, given these n_{ij} values, there are no values of δ_1 and δ_2 other than zero which satisfy the final two equations. Hence we conclude that right-equivariance is not satisfied for spaces $span\{\zeta(\delta_1)v, \zeta(\delta_2)v\}$ unless $\delta_1 = \delta_2 = 0$, and so

> *the only equivariant horizontal subspace of this bundle is the subspace of the tangent space orthogonal to the vertical direction.*

4.2.8 The connection form interpretation

Sometimes it makes more sense to use the 1-form interpretation of the connection instead of writing out horizontal spaces explicitly. Again let $\mathcal{V} \in \mathbb{R}^4$ be a tangent vector to S^3 at v. Considering subspaces of $T_v S^3$ whose direct sum with the vertical direction gives the whole of $T_v S^3$, as we are, the 1-form associated with any particular such subspace is just the projection on to the vertical direction whose kernel is the

given subspace. Thus the 1-form associated with the orthogonal complement of the vertical space, $span\{K_1 v, K_2 v\}$, is given by

$$\omega_v(\mathcal{V}) = \langle K_3 v, \mathcal{V}\rangle, \qquad \forall v \in S^3, \mathcal{V} \in T_v S^3 \tag{4.117}$$

and the 1-form associated with the subspace $span\{\zeta_1(\delta_1)v, \zeta_2(\delta_2)v\}$ is

$$\omega_v^\delta(\mathcal{V}) = \langle K_3 v - \delta_1 K_1 v - \delta_2 K_2 v, \mathcal{V}\rangle, \qquad \forall v \in S^3, \mathcal{V} \in T_v S^3 \tag{4.118}$$

We now consider the equivariance condition for each of these cases again, but now in the 1-form interpretation. Recall, the equivariance condition is

$$\omega_{\Phi_g v}\big((\Phi_g)_* \mathcal{V}\big) = \Phi_g^{-1}\big(\omega_v(\mathcal{V})\big)\Phi_g \tag{4.119}$$

so in current notation, and using $(G_\theta)_* = G_\theta$, this becomes

$$\omega_{G_\theta v}\big(G_\theta \mathcal{V}\big) = G_\theta^T\big(\omega_v(\mathcal{V})\big)G_\theta \tag{4.120}$$

4.2.8.1 The canonical connection

Considering each side of (4.120) separately, with 1-form given by (4.117) we get

$$\begin{aligned}
\text{LHS} &= \omega_{G_\theta v}\big(G_\theta \mathcal{V}\big) && (4.121)\\
&= \langle K_3 G_\theta v, G_\theta \mathcal{V}\rangle && (4.122)\\
&= \langle G_\theta^T K_3 G_\theta v, \mathcal{V}\rangle && (4.123)\\
&= \langle K_3 v, \mathcal{V}\rangle \qquad \text{by (4.90)} && (4.124)
\end{aligned}$$

$$\begin{aligned}
\text{RHS} &= G_\theta^T\big(\omega_v(\mathcal{V})\big)G_\theta && (4.125)\\
&= \big(\omega_v(\mathcal{V})\big)G_\theta^T G_\theta && (4.126)\\
&= \omega_v(\mathcal{V}) && (4.127)\\
&= \langle K_3 v, \mathcal{V}\rangle && (4.128)
\end{aligned}$$

so the equivariance condition is satisfied.

4.2.8.2 The general case connection

Considering each side of (4.120) separately again, with 1-form given by (4.118) we get

$$\begin{aligned}
\text{LHS} &= \omega^{\delta}_{G_\theta v}\big(G_\theta \mathcal{V}\big) && (4.129)\\
&= \langle\ K_3 G_\theta v - \delta_1 K_1 G_\theta v - \delta_2 K_2 G_\theta v\ ,\ G_\theta \mathcal{V}\ \rangle && (4.130)\\
&= \langle\ G_\theta^T K_3 G_\theta v - \delta_1 G_\theta^T K_1 G_\theta v - \delta_2 G_\theta^T K_2 G_\theta v\ ,\ \mathcal{V}\ \rangle && (4.131)\\
&= \langle K_3 v - \delta_1(K_1 \cos 2\theta + K_2 \sin 2\theta)v \\
&\quad -\delta_2(-K_1 \sin 2\theta + K_2 \cos 2\theta)v\ ,\ \mathcal{V}\rangle \text{ by (4.90)} && (4.132)\\
&= \langle(-\delta_1 \cos 2\theta + \delta_2 \sin 2\theta)K_1 v \\
&\quad +(-\delta_1 \sin 2\theta - \delta_2 \cos 2\theta)K_2 v + K_3 v\ ,\ \mathcal{V}\ \rangle && (4.133)
\end{aligned}$$

$$\begin{aligned}
\text{RHS} &= G_\theta^T\big(\omega_v^\delta(\mathcal{V})\big)G_\theta && (4.134)\\
&= G_\theta^T\big(\ \langle K_3 v - \delta_1 K_1 v - \delta_2 K_2 v, \mathcal{V}\rangle\ \big)G_\theta && (4.135)\\
&= \langle K_3 v - \delta_1 K_1 v - \delta_2 K_2 v, \mathcal{V}\rangle G_\theta^T G_\theta && (4.136)\\
&= \langle K_3 v - \delta_1 K_1 v - \delta_2 K_2 v, \mathcal{V}\rangle && (4.137)
\end{aligned}$$

Then since $K_1 v, K_2 v$ and $K_3 v$ are orthogonal, equating coefficients gives

$$\begin{aligned}
-\delta_1 &= -\delta_1 \cos 2\theta + \delta_2 \sin 2\theta && (4.138)\\
-\delta_2 &= -\delta_1 \sin 2\theta - \delta_2 \cos 2\theta && (4.139)
\end{aligned}$$

for which the only solution is $\delta_1 = \delta_2 = 0$ and as before the equivariance condition fails for general δ_1, δ_2, confirming that the only horizontal subspace is the orthogonal complement of the vertical space.

4.3 Dynamics in the Hopf bundle using the quaternionic matrices

We now consider the $\mathbb{C}^2$ case of the system of linear ODEs around which much of this thesis is focused, and its description in terms of the quaternionic matrices. Let u be a point in the ambient space $\mathbb{C}^2$, and let the ODE system be

$$\dot{u} = Cu \qquad u(t) \in \mathbb{C}^2,\ C \in M_2(\mathbb{C}) \tag{4.140}$$

with appropriate initial conditions. We use t as the independent variable for the dynamics in this section to avoid confusion with the real part of $z_j = x_j + iy_j$. Write C as

$$C = A + iB \qquad A, B \in M_2(\mathbb{R}) \tag{4.141}$$

and let $z \in \mathbb{C}^2$ be the projection of u on to S^3, with r the norm of u, so we have:

$$u = rz, \qquad ||z|| = 1, \qquad r = ||u||, \qquad u \in \mathbb{C}^2, z \in S^3 \subset \mathbb{C}^2, r \in \mathbb{R} \tag{4.142}$$

The dynamics of r and z induced by $\dot{u} = Cu$ are then

$$\dot{r}r^{-1} = \mathrm{Re}(z^H C z) \tag{4.143}$$

$$\dot{z} = (I - zz^H)Cz + iz\mathrm{Im}(z^H C z) \tag{4.144}$$

and if we write the RHS side of (4.144) as $F(z)$:

$$F(z) := (I - zz^H)Cz + iz\mathrm{Im}(z^H C z) \tag{4.145}$$

then $F : S^3 \to T_z S^3$ (since $\dot{z} \in T_z S^3$), and equivariance is manifested in the equality

$$F(e^{i\theta} z) = e^{i\theta} F(z) \tag{4.146}$$

Now, using real coordinates as before,

$$z = \begin{pmatrix} z_1 \\ z_2 \end{pmatrix} = \begin{pmatrix} x_1 + iy_1 \\ x_2 + iy_2 \end{pmatrix} = \begin{pmatrix} x_1 \\ x_2 \end{pmatrix} + i \begin{pmatrix} y_1 \\ y_2 \end{pmatrix}, \qquad v = \begin{pmatrix} x_1 \\ x_2 \\ y_1 \\ y_2 \end{pmatrix} = \begin{pmatrix} x \\ y \end{pmatrix} \tag{4.147}$$

with $x = \begin{pmatrix} x_1 \\ x_2 \end{pmatrix}, y = \begin{pmatrix} y_1 \\ y_2 \end{pmatrix} \in \mathbb{R}^2$, $\dot{z} = F(z)$ transforms to

$$\dot{v} = (I_4 - vv^T)\Sigma v, \qquad v \in S^3 \tag{4.148}$$

where Σ is the 4×4 real matrix

$$\Sigma = \begin{pmatrix} A & -B \\ B & A \end{pmatrix} \tag{4.149}$$

We show this:

$$\begin{aligned}
\text{RHS (of (4.148))} &= (I_4 - vv^T)\Sigma v && (4.150)\\
&= \Sigma v - vv^T\Sigma v && (4.151)\\
&= \begin{pmatrix} A & -B \\ B & A \end{pmatrix}\begin{pmatrix} x \\ y \end{pmatrix} \\
&\quad -\begin{pmatrix} x \\ y \end{pmatrix}\begin{pmatrix} x^T & y^T \end{pmatrix}\begin{pmatrix} A & -B \\ B & A \end{pmatrix}\begin{pmatrix} x \\ y \end{pmatrix} && (4.152)\\
&= \begin{pmatrix} Ax - By \\ Bx + Ay \end{pmatrix} - \begin{pmatrix} x \\ y \end{pmatrix}\begin{pmatrix} x^T & y^T \end{pmatrix}\begin{pmatrix} Ax - By \\ Bx + Ay \end{pmatrix} && (4.153)\\
&= \begin{pmatrix} Ax - By \\ Bx + Ay \end{pmatrix} \\
&\quad -\begin{pmatrix} x \\ y \end{pmatrix}(x^TAx - x^TBy + y^TBx + y^TAy) && (4.154)\\
&= \begin{pmatrix} Ax - By - xx^TAx + xx^TBy - xy^TBx - xy^TAy \\ Bx + Ay - yx^TAx + yx^TBy - yy^TBx - yy^TAy) \end{pmatrix}
\end{aligned}$$

and

$$\begin{aligned}
\text{RHS (of (4.144))} &= (I - zz^H)Cz + iz\mathrm{Im}(z^HCz) && (4.155)\\
&= Cz - z\mathrm{Re}(z^HCz) && (4.156)\\
&= (A + iB)(x + iy) \\
&\quad -(x + iy)\mathrm{Re}\big[(x^T - iy^T)(A + iB)(x + iy)\big] && (4.157)\\
&= Ax - By + iBx + iAy \\
&\quad -(x + iy)\mathrm{Re}\big[(x^T - iy^T)(Ax - By + iBx + iAy)\big] && (4.158)\\
&= Ax - By + iBx + iAy \\
&\quad -(x + iy)\mathrm{Re}\big[x^TAx - x^TBy + ix^TBx + ix^TAy \\
&\quad -iy^TAx + iy^TBy + y^TBx + y^TAy\big] && (4.159)\\
&= Ax - By + iBx + iAy \\
&\quad -(x + iy)\big[x^TAx - x^TBy + y^TBx + y^TAy\big] && (4.160)\\
&= Ax - By - xx^TAx + xx^TBy - xy^TBx - xy^TAy \\
&\quad +i\big[Bx + Ay - yx^TAx + yx^TBy - yy^TBx - yy^TAy\big]
\end{aligned}$$

which verifies the transformation, proving equivalence between (4.144) and (4.148).

Now write the RHS of (4.148) as $\Omega(v)$:

$$\Omega(v) := (I_4 - vv^T)\Sigma v \qquad (4.161)$$

then $\Omega : S^3 \to T_v S^3$, and equivariance is manifested in the equality

$$\Omega(G_\theta v) = G_\theta \Omega(v) \tag{4.162}$$

Since $\dot{v} \in T_v S^3$ we can express it in terms of our orthonormal basis:

$$\dot{v} = \Omega(v) = \underbrace{\alpha_1(v)K_1 v + \alpha_2(v)K_2 v}_{\in H_v S^3} + \underbrace{\alpha_3(v)K_3 v}_{\in V_v S^3}, \qquad \alpha_i \in \mathbb{R} \tag{4.163}$$

with

$$\alpha_i(v) = \langle K_i v, \dot{v} \rangle = \langle K_i v, \Omega(v) \rangle \tag{4.164}$$

Note that we can also write α_i as

$$\begin{aligned}
\alpha_i(v) = \langle K_i v, \Omega(v) \rangle &= \langle K_i v, (I_4 - vv^T)\Sigma v \rangle && (4.165)\\
&= \langle K_i v, \Sigma v \rangle - \langle K_i v, vv^T \Sigma v \rangle && (4.166)\\
&= \langle K_i v, \Sigma v \rangle - (v^T \Sigma v)\langle K_i v, v \rangle && \\
&\quad \text{since } v^T \Sigma v \text{ is a scalar} && (4.167)\\
&= \langle K_i v, \Sigma v \rangle \qquad \text{by skew symmetry of } K_i && (4.168)
\end{aligned}$$

which helps in numerical calculations because of its reduced complexity.

4.3.1 Deriving the parallel transport equation

In this format, the phenomenon of parallel translation is particularly easy to understand - as v moves around S^3 in accordance with the equations of motion, there is another point on S^3, say w, which is related to v via some (t-dependent) group action, such that w has zero component in the vertical direction. We set $v(t) = G_{\theta(t)} w(t)$, and seek a formula for the phase $\theta(t) \in \mathbb{R}$ which keeps $w(t)$ horizontal.

$$\begin{aligned}
v(t) &= G_{\theta(t)} w(t) && (4.169)\\
\Rightarrow \dot{v}(t) &= \frac{dG_\theta}{d\theta}\dot{\theta} w(t) + G_{\theta(t)}\dot{w}(t) && (4.170)\\
&= -K_3 G_{\theta(t)}\dot{\theta} w(t) + G_{\theta(t)}\dot{w}(t) \qquad \text{since } \frac{dG_\theta}{d\theta} = -K_3 G_\theta && \\
&= -\dot{\theta} G_{\theta(t)} K_3 w(t) + G_{\theta(t)}\dot{w}(t) \qquad \text{since } K_3 G_\theta = G_\theta K_3 && \\
&= G_{\theta(t)}\big[-\dot{\theta} K_3 w(t) + \dot{w}(t) \big] && (4.171)\\
\Rightarrow G_{\theta(t)}^T \dot{v}(t) &= -\dot{\theta} K_3 w(t) + \dot{w}(t) && (4.172)
\end{aligned}$$

But

$$\begin{aligned}
\dot{v}(t) &= \alpha_1(v)K_1v + \alpha_2(v)K_2v + \alpha_3(v)K_3v && (4.173)\\
&= \alpha_1(G_\theta w)K_1G_\theta w \\
&\quad +\alpha_2(G_\theta w)K_2G_\theta w + \alpha_3(G_\theta w)K_3G_\theta w && (4.174)\\
\Rightarrow G^T_{\theta(t)}\dot{v}(t) &= \alpha_1(G_\theta w)G^T_\theta K_1G_\theta w \\
&\quad +\alpha_2(G_\theta w)G^T_\theta K_2G_\theta w + \alpha_3(G_\theta w)G^T_\theta K_3G_\theta w && (4.175)
\end{aligned}$$

So we have

$$\begin{aligned}
-\dot{\theta}K_3w(t) + \dot{w}(t) &= \alpha_1(G_\theta w)G^T_\theta K_1G_\theta w + \alpha_2(G_\theta w)G^T_\theta K_2G_\theta w \\
&\quad +\alpha_3(G_\theta w)G^T_\theta K_3G_\theta w && (4.176)
\end{aligned}$$

Now notice that

$$\begin{aligned}
\alpha_i(v) &= \langle K_iv, \Omega(v)\rangle && (4.177)\\
\Rightarrow \alpha_i(G_\theta w) &= \langle K_iG_\theta w, \Omega(G_\theta w)\rangle && (4.178)\\
&= \langle K_iG_\theta w, G_\theta\Omega(w)\rangle && (4.179)\\
&= \langle G^T_\theta K_iG_\theta w, \Omega(w)\rangle && (4.180)
\end{aligned}$$

then use (4.90) to get

$$\begin{aligned}
\alpha_1(G_\theta w) &= \langle G^T_\theta K_1G_\theta w, \Omega(w)\rangle && (4.181)\\
&= \langle (K_1\cos 2\theta + K_2\sin 2\theta)w, \Omega(w)\rangle && (4.182)\\
&= \cos 2\theta\langle K_1w, \Omega(w)\rangle + \sin 2\theta\langle K_2w, \Omega(w)\rangle && (4.183)\\
&= \cos 2\theta\alpha_1(w) + \sin 2\theta\alpha_2(w) && (4.184)
\end{aligned}$$

$$\begin{aligned}
\alpha_2(G_\theta w) &= \langle G^T_\theta K_2G_\theta w, \Omega(w)\rangle && (4.185)\\
&= \langle (-K_1\sin 2\theta + K_2\cos 2\theta)w, \Omega(w)\rangle && (4.186)\\
&= -\sin 2\theta\langle K_1w, \Omega(w)\rangle + \cos 2\theta\langle K_2w, \Omega(w)\rangle && (4.187)\\
&= -\sin 2\theta\alpha_1(w) + \cos 2\theta\alpha_2(w) && (4.188)
\end{aligned}$$

$$\begin{aligned}
\alpha_3(G_\theta w) &= \langle G^T_\theta K_3G_\theta w, \Omega(w)\rangle && (4.189)\\
&= \langle K_3w, \Omega(w)\rangle && (4.190)\\
&= \alpha_3(w) && (4.191)
\end{aligned}$$

then substituting these results, along with equations (4.90), in (4.176) gives the result

$$-\dot{\theta}K_3 w + \dot{w} = \alpha_1(w)K_1 w + \alpha_2(w)K_2 w + \alpha_3(w)K_3 w \tag{4.192}$$

which implies

$$\dot{w} \;=\; \underbrace{\alpha_1(w)K_1 w + \alpha_2(w)K_2 w}_{\text{horizontal}} \;+\; \underbrace{(\alpha_3(w) + \dot{\theta})K_3 w}_{\text{vertical}} \tag{4.193}$$

So for $w(t)$ to be a horizontal path, $\dot{w}(t)$ must have zero component in the vertical direction, which is the case iff $\alpha_3(w(t)) = -\dot{\theta}(t)$. But $\alpha_3(w) = \alpha_3(G_\theta w) = \alpha_3(v)$, so the condition on $\theta(t)$ for $w(t)$ to be horizontal, in terms of the original path $v(t)$, is in fact

$$\dot{\theta}(t) = -\alpha_3(v(t)) = -\langle K_3 v(t), \Sigma v(t)\rangle \tag{4.194}$$

Thus if we solve our system numerically for $v(t)$, then solving this equation for θ simultaneously will yield a curve $\theta(t)$ which gives a horizontal path $w(t) = G^T_{\theta(t)} v(t)$.

Remark 4.3.1. *This expression for $\dot{\theta}(t)$ may well look new, but it is of course just the same expression as was displayed in Chapter 3, i.e. equation (3.31), just written in terms of the real coordinate system of this case. To see this, write*

$$\begin{aligned}
\dot{\theta}(t) &= -\langle K_3 v(t), \dot{v}(t)\rangle && (4.195)\\
&= -\langle \begin{pmatrix} y_1(t) \\ y_2(t) \\ -x_1(t) \\ -x_2(t) \end{pmatrix}, \begin{pmatrix} \dot{x}_1(t) \\ \dot{x}_2(t) \\ \dot{y}_1(t) \\ \dot{y}_2(t) \end{pmatrix} \rangle && (4.196)\\
&= -y_1\dot{x}_1 - y_2\dot{x}_2 + x_1\dot{y}_1 + x_2\dot{y}_2 && (4.197)
\end{aligned}$$

Indeed, $\alpha_3(v)$ is just the natural connection form evaluated on $\Omega(v)$, see (4.117).

4.3.2 Numerical simulations

We present a few examples to illustrate how these concepts are implemented in numerics and how $\theta(t)$ behaves in some real situations.

A first example

Let

$$C = \begin{pmatrix} 3-i & 2+7i \\ 5+6i & 1+9i \end{pmatrix}, \qquad \text{so } A = \begin{pmatrix} 3 & 2 \\ 5 & 1 \end{pmatrix}, \quad B = \begin{pmatrix} -1 & 7 \\ 6 & 9 \end{pmatrix} \tag{4.198}$$

and integrate

$$\dot{v} = (I_4 - vv^T)\Sigma v \tag{4.199}$$

$$\dot{\theta}(t) = -\langle K_3 v(t), \Sigma v(t)\rangle \tag{4.200}$$

from $t = 0$ to t_{max}, using a variety of initial conditions. Note that C has eigenvector/value pairs

$$\lambda_1 = -0.3579 - 3.8460i \qquad \xi_1 = \begin{pmatrix} 0.8557 \\ -0.4301 + 0.2876i \end{pmatrix} \tag{4.201}$$

$$\lambda_2 = 4.3579 + 11.8460i \qquad \xi_2 = \begin{pmatrix} 0.4836 - 0.0845i \\ 0.8712 \end{pmatrix} \tag{4.202}$$

The Matlab code `integrate_real_coords1.m` performs this calculation, and produces output showing firstly the phase $\theta(t)$ required for $w(t)$ to remain horizontal as $v(t)$ moves around, and secondly the image on S^2 of the solution path $v(t)$ under the Hopf map. Figures 4.1-4.4 show the graphical output, with $t_{max} = 2$, $\theta(0) = 0$, for initial conditions $u(0) = \begin{pmatrix} 1+2i \\ 3+4i \end{pmatrix}, \begin{pmatrix} 1+2i \\ 30+4i \end{pmatrix}, \begin{pmatrix} -1-9i \\ -8+4i \end{pmatrix}, \begin{pmatrix} -i \\ i \end{pmatrix}$, respectively.

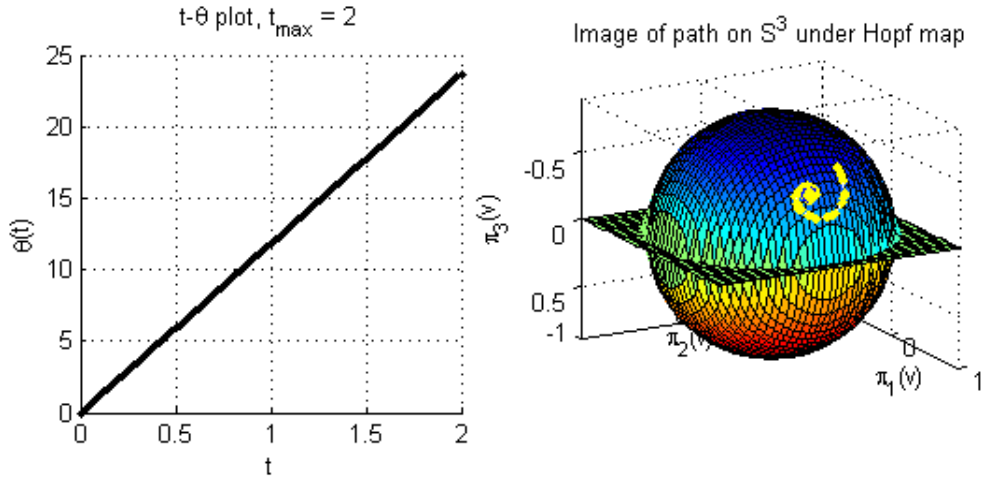

Figure 4.1: Phase required for parallel translation

Points to note about these numerical results:

- No significantly different behaviour, other than the cases shown, was observed in the system, even after testing a wide range of initial conditions.

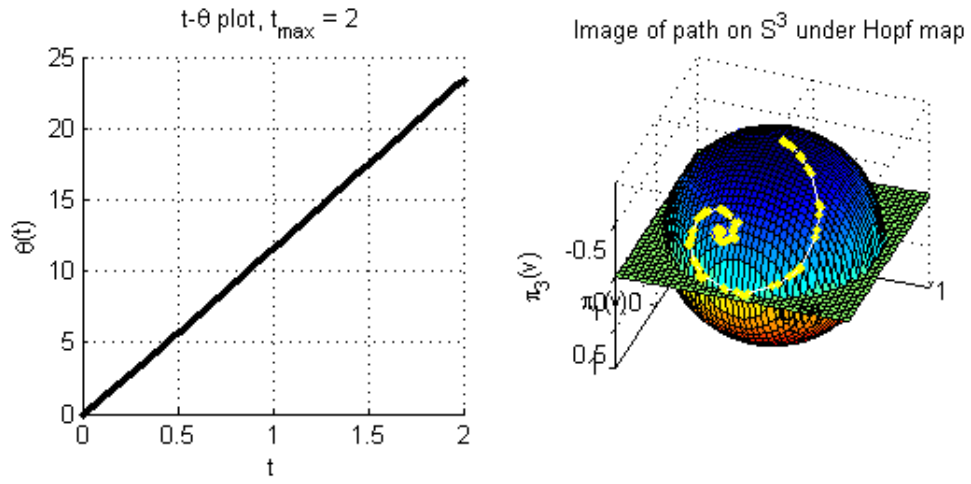

Figure 4.2: Phase required for parallel translation

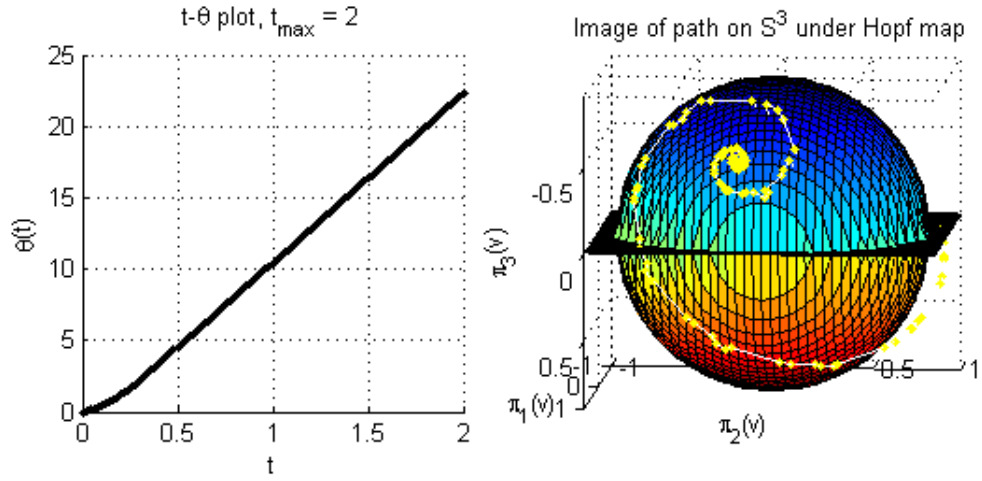

Figure 4.3: Phase required for parallel translation

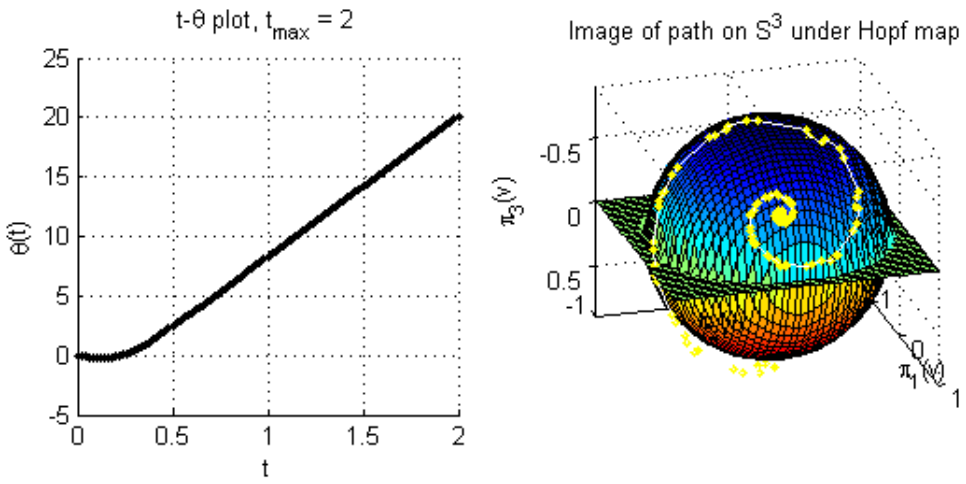

Figure 4.4: Phase required for parallel translation

- The phase $\theta(t)$ has very similar behaviour in all situations. Note however that for certain initial conditions there is a transitional region for small t, and θ may even go negative briefly, as in Figure 4.4.

- As t increases, the image path on S^2 always spirals in towards the same point, $\pi(v(t_{max})) \approx \begin{pmatrix} 0.8439 \\ -0.1473 \\ -0.5184 \end{pmatrix}$. This is of course just the image under the Hopf map of the dominant eigenvector of C. Sometimes the spiral crosses between upper and lower hemispheres, sometimes not, depending on the initial condition.

- The maximum time the simulation was allowed to run for was $t_{max} = 400$, and the behaviour did not change over that time.

- The fact that in each case the phase required to maintain horizontality in S^3 settles to a curve with constant gradient, while the image of the solution path on S^2 also settles to a fixed point implies that *the solution $v(t)$ on S^3 is attracted to and remains on a single periodic (i.e. S^1) orbit.* To see this, observe that since the point on the base manifold is stationary, any motion in the bundle must be only in the fibre over that point. But since the phase gives a measure of the motion *along fibres*, and the phase required to maintain horizontality is strictly increasing with t, there must be continuous motion in the bundle, which must necessarily be unidirectional inside a single S^1 fibre, and which therefore implies periodicity of the trajectory in the bundle space.

This is a very interesting piece of data to be able to extract from the system simply by looking at the problem from this new bundle perspective. To verify that $v(t)$ does in fact settle to a periodic orbit, the complex coordinates were plotted for a range of initial conditions; in each case the predicted behaviour was observed. Figure 4.5 shows plots of the two complex coordinates, the first shows the trajectory in $\mathbb{C}$ of the first complex coordinate, $v_1(t) + iv_3(t)$, and the second shows the trajectory in $\mathbb{C}$ of the second complex coordinate, $v_2(t) + iv_4(t)$. The plots confirm that the solution settles to a periodic orbit in S^3.

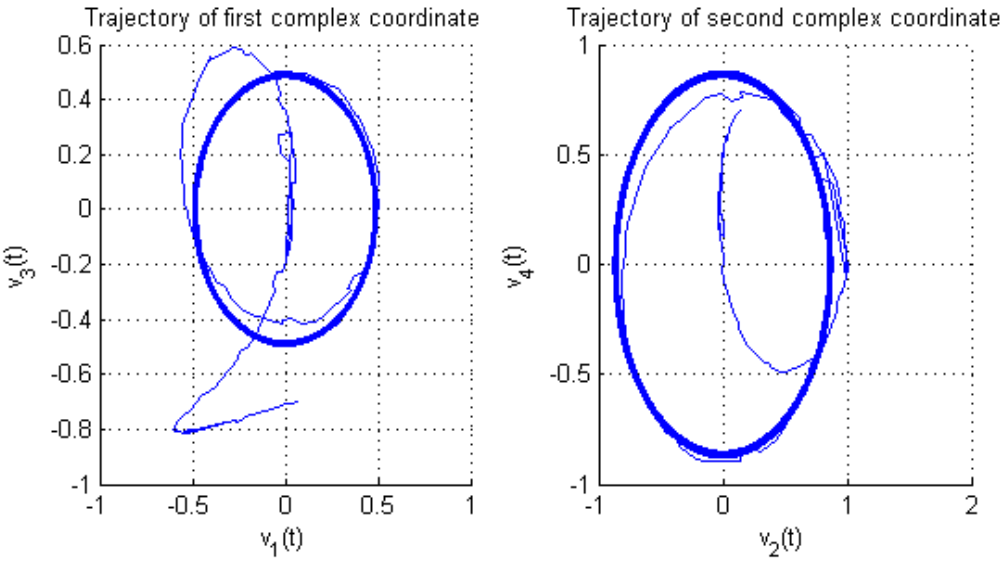

Figure 4.5: Plots of the two complex coordinates, illustrating periodicity

- Thus we are able to extract interesting geometrical information about the global dynamics of $\dot{u} = Cu$ just by looking at the system from this new perspective.

Another example

Trial and error was used to find the following system, which also exhibits interesting behaviour:

$$C = \begin{pmatrix} 9 + (5.9 + \epsilon)i & 2 + 8i \\ -9 + 4i & -1 + 9i \end{pmatrix}, \qquad \text{so } A = \begin{pmatrix} 9 & 2 \\ -9 & -1 \end{pmatrix}, \quad B = \begin{pmatrix} 5.9 + \epsilon & 8 \\ 4 & 9 \end{pmatrix} \tag{4.203}$$

As in the previous example, the code `integrate_real_coords1.m` solves the system numerically, but this time we use only one initial condition $u(0) = \begin{pmatrix} 1+2i \\ 3+4i \end{pmatrix}$, $\theta(0) = 0$, and observe the behaviour as ϵ varies. Figures 4.6-4.10 show the graphical output for the cases $\epsilon = 0, 0.01, 0.02248, 0.03, 0.05$, with t_{max} picked appropriately to show the relevant detail.

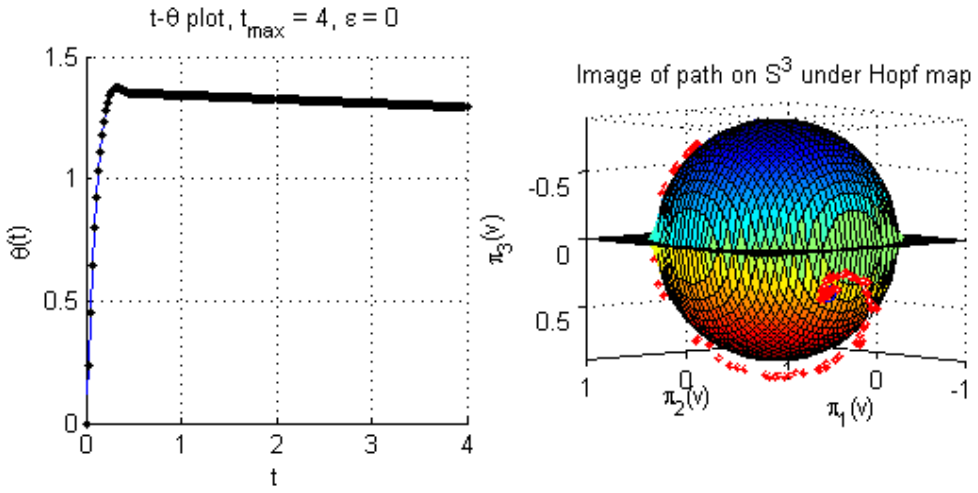

Figure 4.6: Phase required for parallel translation, $\epsilon = 0$

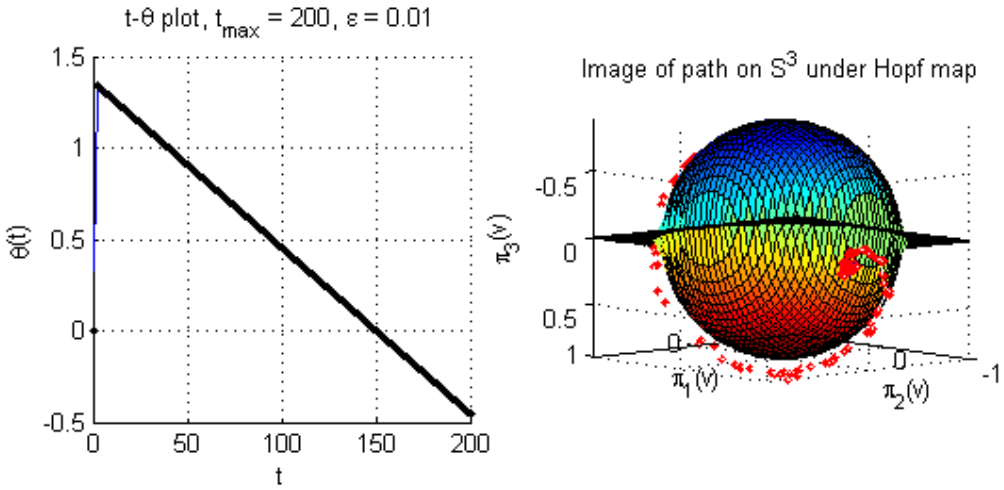

Figure 4.7: Phase required for parallel translation, $\epsilon = 0.01$

Remark 4.3.2. *Note how the trajectories on the S^2 pictures are raised off the surface of the sphere. This is just because the underlying sphere is plotted with diameter slightly less than 1, so that the points are easier to see.*

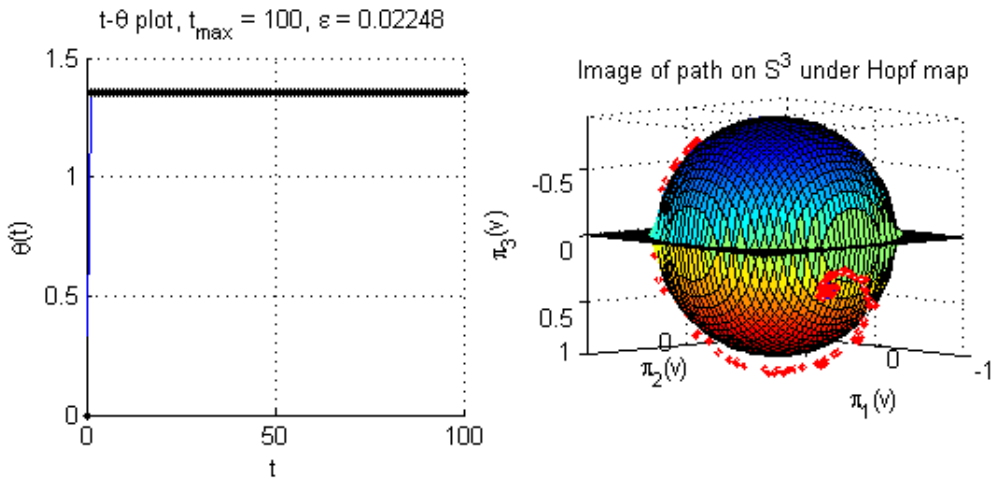

Figure 4.8: Phase required for parallel translation, $\epsilon = 0.02248$

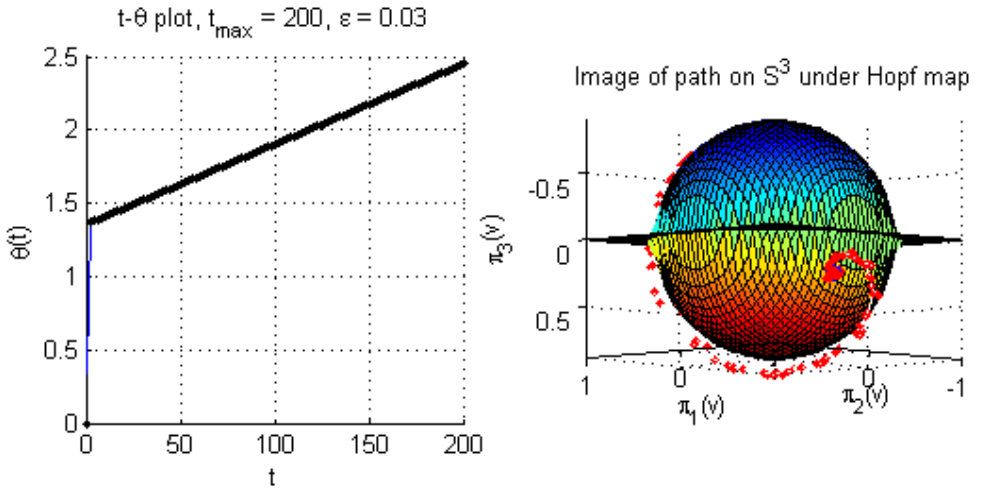

Figure 4.9: Phase required for parallel translation, $\epsilon = 0.03$

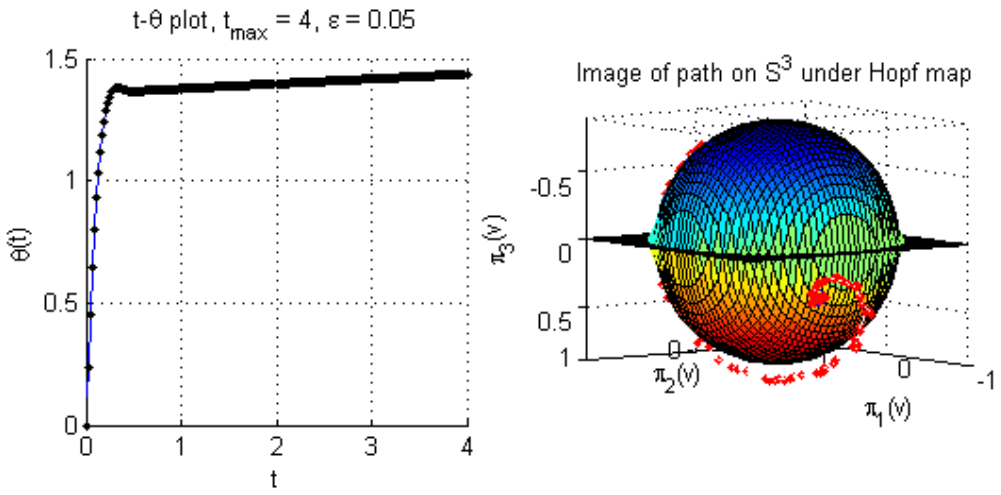

Figure 4.10: Phase required for parallel translation, $\epsilon = 0.05$

Notes on these numerical results:

- In all these simulations the trajectories on S^2 are virtually identical - from the point of view shown in these pictures, they begin at a point on the far side of the sphere, curl round under the sphere towards us, then spiral in to a point just below the equator.
- In Figures 4.6 and 4.10 we have $t_{max} = 4$ in order to highlight the extra detail in the $\theta(t)$ curve at small t, whereas in figures 4.7 and 4.9 we show longer time-scales in order to highlight how $\theta(t)$ has constant gradient over longer times.
- The behaviour observed in this example is very similar to the previous example: in general the phase has a brief transitional period for small t, then evens out to a constant gradient curve for the rest of the simulation, while the trajectory on the base manifold is attracted to a stationary point.
- However here we see how the phase required for parallel translation differs between different systems. ϵ parametrizes the systems, and as it varies between 0 and 0.05 we find that the gradient of the phase curve varies smoothly from negative to positive.
- The sequence of figures shows explicitly how the behaviour of the systems varies, depending on parameter ϵ. It shows that there is some critical value $\epsilon = \epsilon_0 \approx 0.2248$ with a phase curve of gradient zero, which separates systems

of positive and negative gradient phase curves. For the system with $\epsilon = \epsilon_0$, after the brief transitional period, there is no motion on the base manifold, and also no motion within the fibre above the stationary point on the base. This implies that the trajectory which starts at the given initial condition converges to a fixed point on S^3.

- For values of ϵ either side of ϵ_0, the trajectories converge to stationary points on the base manifold with constant periodic motion in the fibre above that point. The direction and speed of the S^1 motion are given by the gradient of the phase curve.

- Again we confirm that these inferences are correct by plotting the trajectories of the two complex coordinates for each of the ϵ values; these plots are shown in Figures 4.11-4.15.

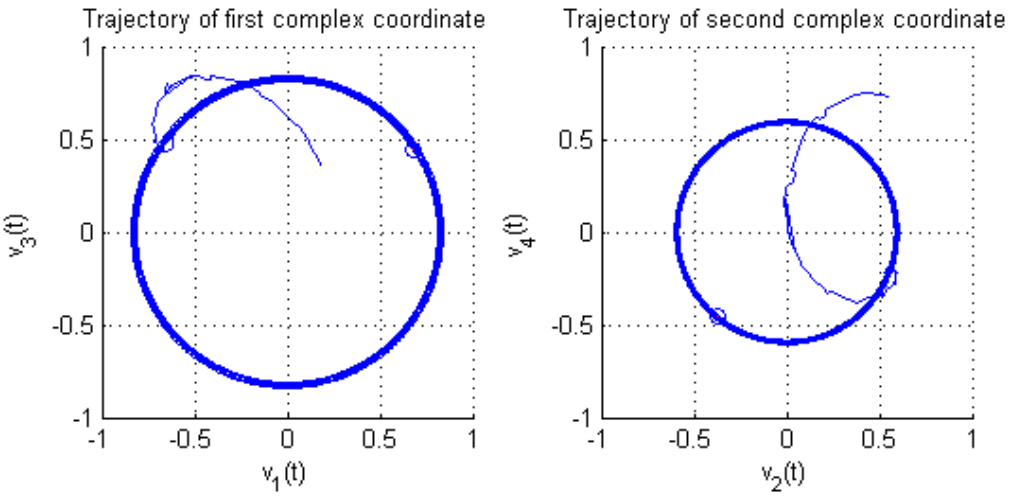

Figure 4.11: Plots of the two complex coordinates, $\epsilon = 0$

- Note that in Figures 4.11 and 4.12 the trajectories of both complex coordinates proceed in a *clockwise* direction, whereas in Figures 4.14 and 4.15 the trajectories proceed in a *counter-clockwise* direction. This conforms with the inference made from the gradient of the phase curve regarding the direction of motion in the fibre.

- What these figures do not convey is the speed of the dynamics: for the values of ϵ nearer to ϵ_0, the periodic trajectory is traversed *a lot* slower than for those values further from ϵ_0. Comparing 4.13 to the other figures, we see that in

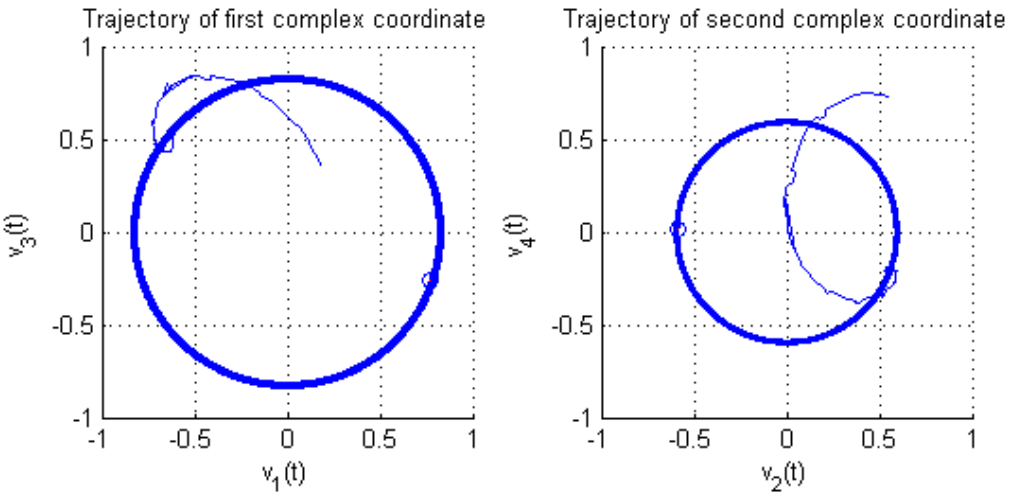

Figure 4.12: Plots of the two complex coordinates, $\epsilon = 0.01$

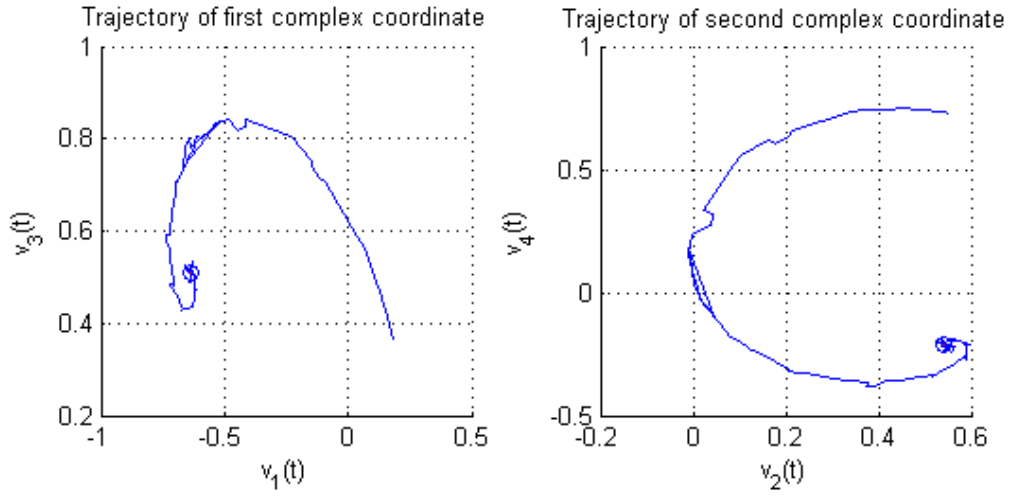

Figure 4.13: Plots of the two complex coordinates, $\epsilon = 0.02248$

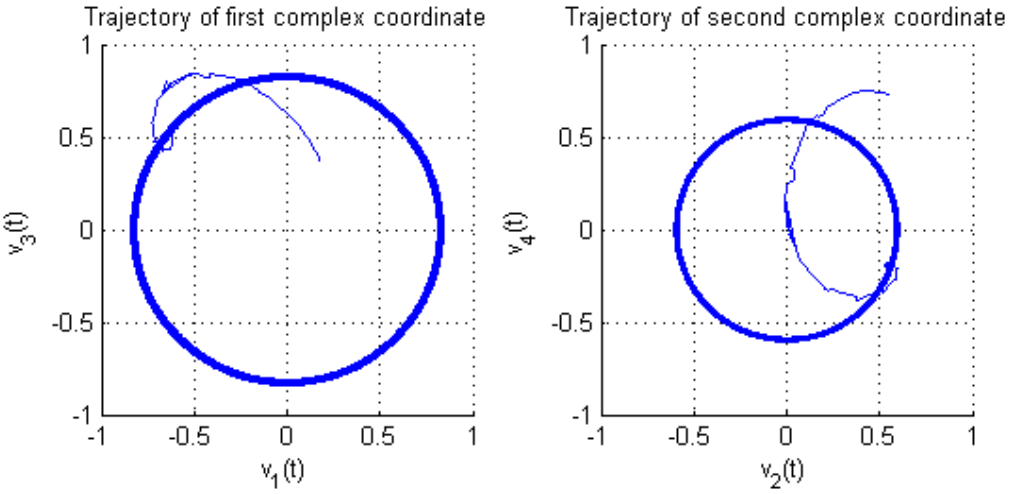

Figure 4.14: Plots of the two complex coordinates, $\epsilon = 0.03$

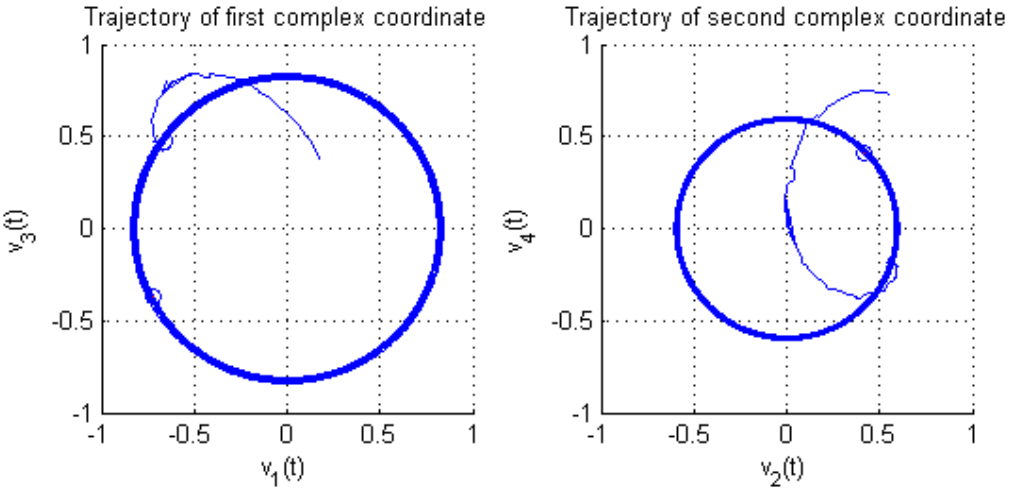

Figure 4.15: Plots of the two complex coordinates, $\epsilon = 0.05$

this case the trajectory consists of the first part only of the trajectories seen in the other cases - i.e. a short path going from the initial condition to the point of first contact with the periodic orbit. In the ϵ_0 case, the trajectory arrives at this point and stays there indefinitely, while for ϵ very close to ϵ_0, the trajectory arrives at this point then moves very slowly away from the point, around the periodic orbit, and remains on that path. Thus we have an unstable fixed point of the dynamics.

- Again, we have extracted a surprisingly large amount of important information about the dynamics of the systems just by using this new bundle/phase perspective. Techniques derived from these observations could potentially be used in practical situations where specific combinations of periodic orbits and stationary points are required to satisfy certain physical constraints.

Another example: the test-case

We now apply the concepts developed here to the test-case of Section 1.3. Recall, the system, written in its original notation is

$$u_x = A(x,\lambda)u, \qquad x \in \mathbb{R},\ \lambda \in \Lambda = \mathbb{C} \setminus \{(-\infty,-1]\},\ u = \begin{pmatrix} u_1 \\ u_2 \end{pmatrix} \in \mathbb{C}^2 \quad (4.204)$$

where

$$A(x,\lambda) = \begin{pmatrix} 0 & 1 \\ \lambda + 1 - 2f(x) & 0 \end{pmatrix} \quad (4.205)$$

$$f(x) = \frac{3}{2}\mathrm{sech}^2\frac{1}{2}x \quad (4.206)$$

and we want to integrate the system from $x = L$ to $-L$, using as initial condition

$$u_\infty(\lambda) = \xi_+(\lambda) = \begin{pmatrix} 1 \\ -\sqrt{\lambda+1} \end{pmatrix}, \quad (4.207)$$

which is the eigenvector corresponding to eigenvalue $\mu_+(\lambda) = -\sqrt{\lambda+1}$ of the system at infinity, $A_\infty(\lambda)$.

Now if we translate this to the notation of this section (taking care not to get the two matrices $A = A(x,\lambda)$ of (4.205) and $A = \mathrm{Re}(C)$ of (4.141) confused, and using independent variable t instead of x), we get

$$C = \begin{pmatrix} 0 & 1 \\ \lambda + 1 - 2f(t) & 0 \end{pmatrix} = A + iB \qquad \in M_2(\mathbb{C}) \quad (4.208)$$

$$A = \begin{pmatrix} 0 & 1 \\ \mathrm{Re}(\lambda) + 1 - 2f(t) & 0 \end{pmatrix}, \qquad B = \begin{pmatrix} 0 & 0 \\ \mathrm{Im}(\lambda) & 0 \end{pmatrix} \qquad \in M_2(\mathbb{R}) \tag{4.209}$$

so

$$\Sigma = \begin{pmatrix} A & -B \\ B & A \end{pmatrix} = \begin{pmatrix} 0 & 1 & 0 & 0 \\ \mathrm{Re}(\lambda) + 1 - 2f(t) & 0 & -\mathrm{Im}(\lambda) & 0 \\ 0 & 0 & 0 & 1 \\ \mathrm{Im}(\lambda) & 0 & \mathrm{Re}(\lambda) + 1 - 2f(t) & 0 \end{pmatrix} \tag{4.210}$$

then the equation of motion to solve is

$$\dot{v} = (I_4 - vv^T)\Sigma v, \qquad v = \begin{pmatrix} x_1 \\ x_2 \\ y_1 \\ y_2 \end{pmatrix} = \frac{1}{||u||} \begin{pmatrix} \mathrm{Re}(u_1) \\ \mathrm{Re}(u_2) \\ \mathrm{Im}(u_1) \\ \mathrm{Im}(u_2) \end{pmatrix} \in S^3 \subset \mathbb{R}^4 \tag{4.211}$$

and the parallel translation equation to be solved in conjunction with this is

$$\dot{\theta}(t) = -\langle K_3 v(t), \Sigma v(t) \rangle \tag{4.212}$$

The initial condition from the original system for the first of these two dynamics equations translates to

$$v(L) = \begin{pmatrix} x_1(L) \\ x_2(L) \\ y_1(L) \\ y_2(L) \end{pmatrix} = \frac{1}{\sqrt{u_\infty^H u_\infty}} \begin{pmatrix} 1 \\ \mathrm{Re}(-\sqrt{\lambda + 1}\ ) \\ 0 \\ \mathrm{Im}(-\sqrt{\lambda + 1}\ ) \end{pmatrix} \in S^3 \subset \mathbb{R}^4 \tag{4.213}$$

and for the second equation the initial value is arbitrary and does not affect the shape of the resulting $\theta(t)$ curve; we take $\theta(L) = 0$. We take $L = 10$ and solve the system for $t = L$ to $-L$ for a range of values of λ, in order to provide more concrete examples of how $\theta(t)$ behaves. The Matlab code `integrate_real_coords2.m` implements these simulations, and Figures 4.16-4.21 show the graphical output for the cases $\lambda = -1 + 0.5i, 0.1 + i, 0.8 + 0.1i, -0.75, -i, -1 - 0.1i$. The figures show three plots; the left plot shows the λ value under consideration, plotted alongside the three eigenvalues of the system (on the real axis); in the middle is the phase plot; and on the right is the image of the solution path under the Hopf map, as before.

Points to note about these numerical results:

- There are clearly some very interesting patterns here, and the phase $\theta(t)$ appears to vary with λ in a nontrivial way.

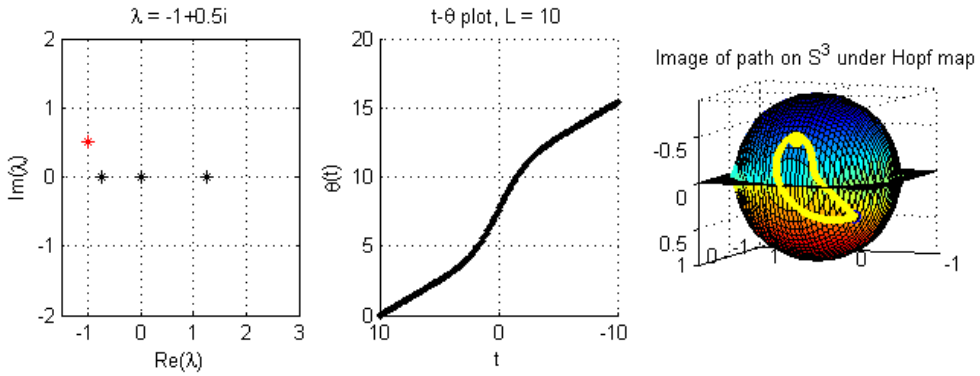

Figure 4.16: $\lambda = -1 + 0.5i$

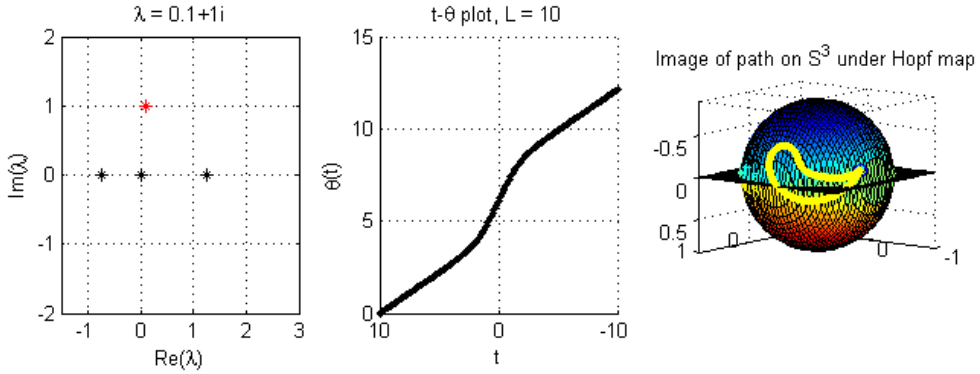

Figure 4.17: $\lambda = 0.1 + i$

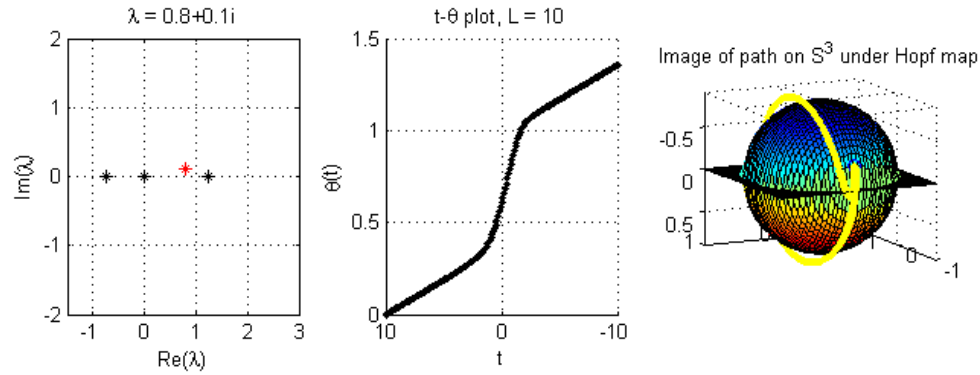

Figure 4.18: $\lambda = 0.8 + 0.1i$

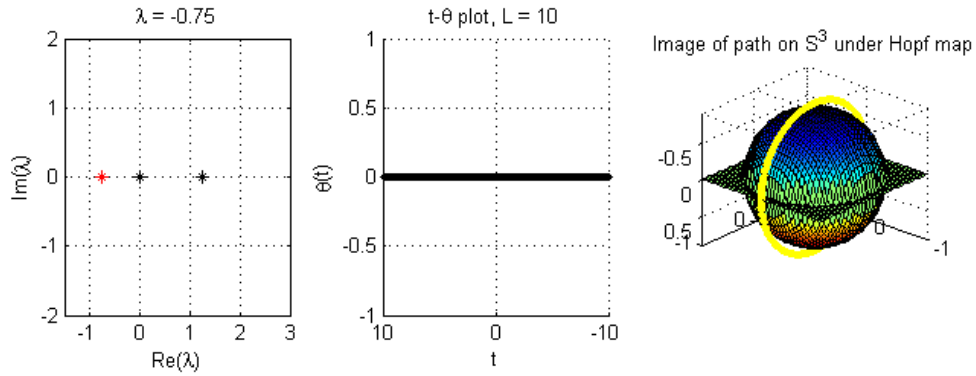

Figure 4.19: $\lambda = -0.75$

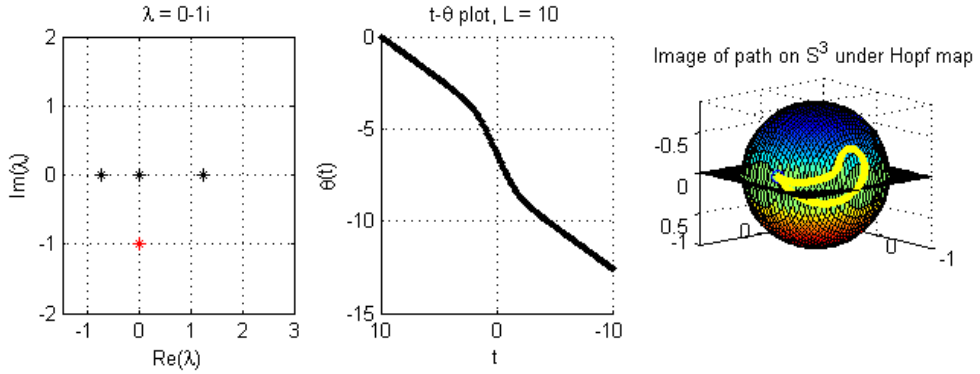

Figure 4.20: $\lambda = -i$

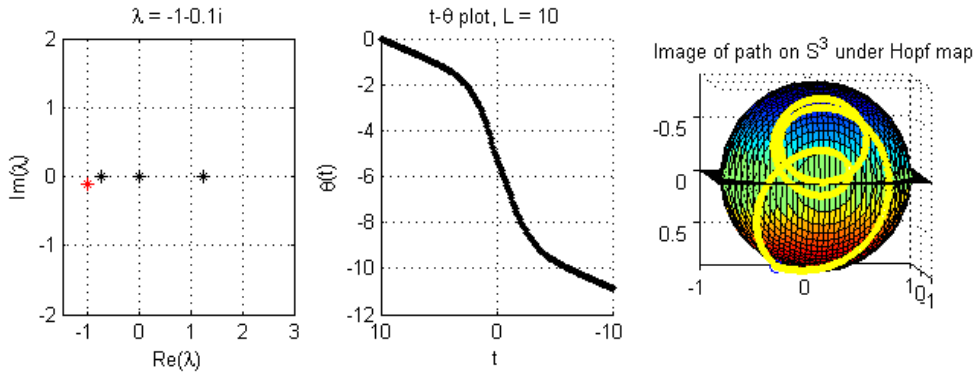

Figure 4.21: $\lambda = -1 - 0.1i$

- The image paths on S^2 also appear to be related to the values of λ used.
- The phase seems to be approximately a straight line with gradient proportional to $\mathrm{Im}(\lambda)$ with an S-shaped bend around the $t = 0$ region.
- As $\mathrm{Im}(\lambda)$ crosses the real axis the image path on S^2 seems to expand from a small closed loop to a larger closed loop, which then becomes a great circle on the sphere, and finally crosses over to the other side of the sphere and then contracts to a smaller closed loop approximately the mirror image of the original loop.
- The Matlab code `integrate_real_coords_phaselattice.m` was written to provide another perspective on the situation, by presenting all the phase data at $t = -L$ together in one picture. The program calculates the final phase $\theta(-L)$ for a lattice of λ values, and plots the resulting data as a surface over the $\lambda-$domain, $\mathbb{C}$. Figures 4.22 and 4.23 show the graphical output. Notes about these figures:
  - The horizontal plane axes are labelled by the indices of the surface array, not the actual real and imaginary λ components.
  - In Figure 4.22 the $\mathrm{Re}(\lambda)$ axis goes from -4 to $+8$, and the $\mathrm{Im}(\lambda)$ axis goes from $-2.1i$ to $+2i$. The surface mesh has intervals of 0.13 in both the real and imaginary directions.
  - Figure 4.23 is a close-up version of Figure 4.22, zoomed in on a small region containing the three discrete system eigenvalues, at $-\frac{3}{4}, 0, \frac{5}{4}$ on the real axis.
  - In Figure 4.23 the $\mathrm{Re}(\lambda)$ axis goes from -0.9 to $+1.6$, and the $\mathrm{Im}(\lambda)$ axis goes from $-0.1i$ to $+0.1i$. The surface mesh has intervals of 0.013 in both the real and imaginary directions.
  - These pictures are fascinating. The first figure shows the general pattern of the phase, and how the real component of λ seems to be driving the magnitude of the phase, while the imaginary part seems to determine its sign. The figure even shows the location of the branch cut in the λ-domain (where the continuous spectrum of the system is located), as we have a sign change in $\theta(-L)$ on either side of the cut.

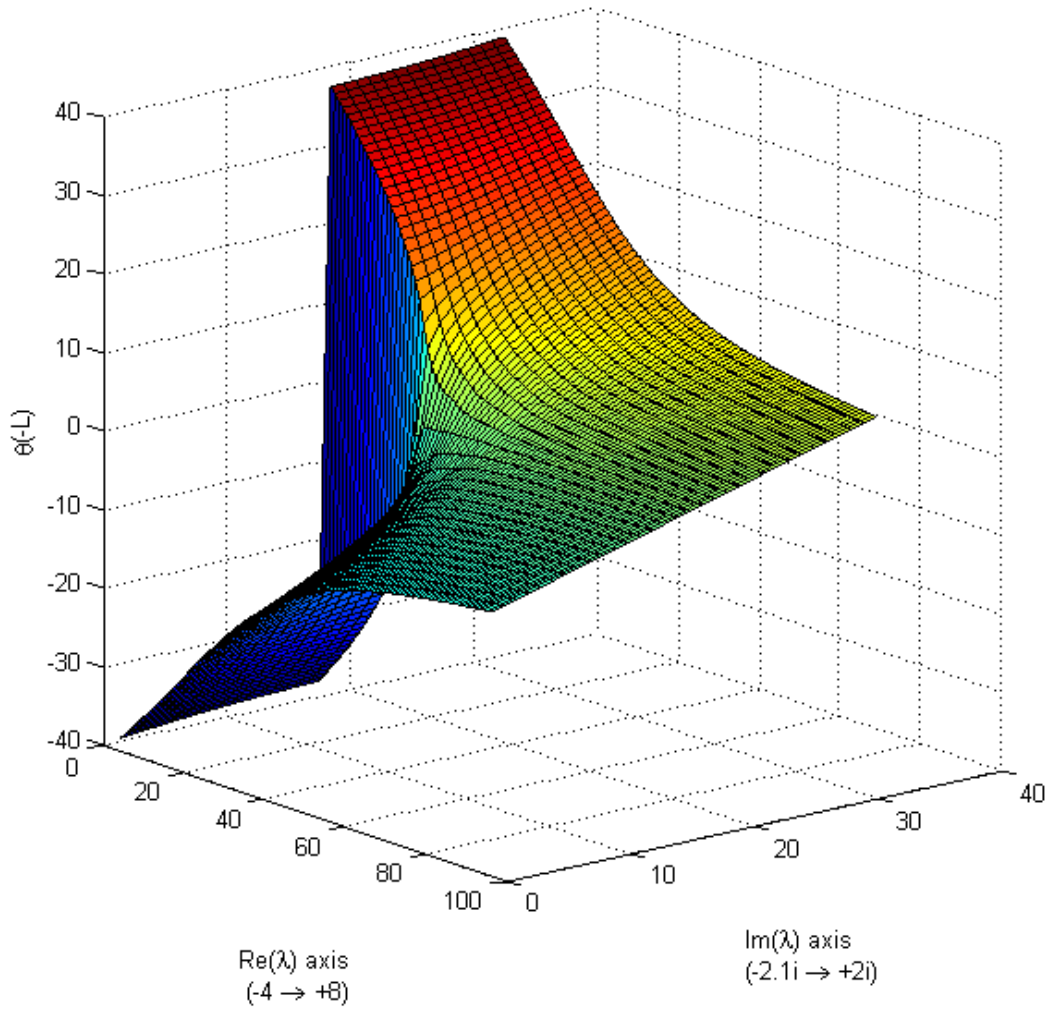

Figure 4.22: Test-case phase surface.

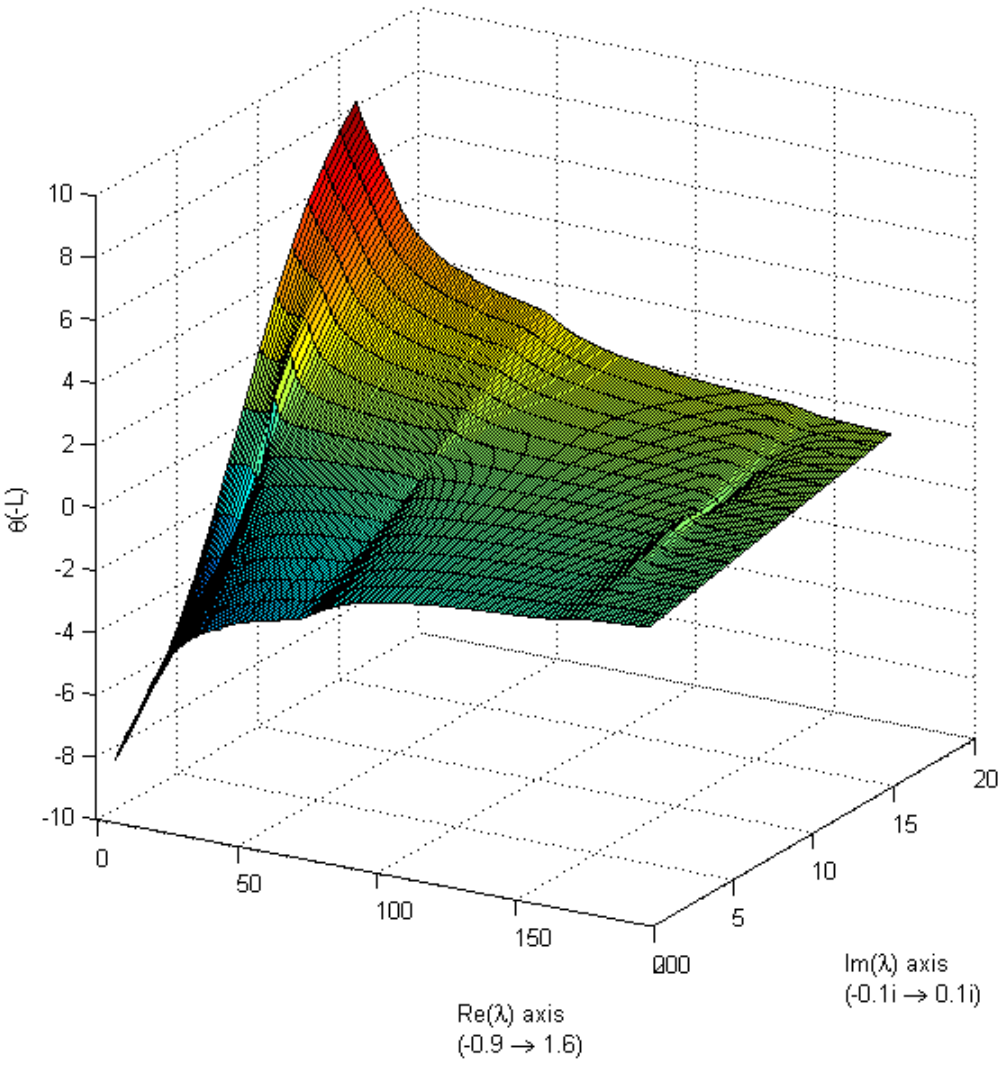

Figure 4.23: Close-up of test-case phase surface, showing ripples at eigenvalue locations ($\lambda = -\frac{3}{4}, 0, \frac{5}{4}$).

– The second figure shows that when we look in detail at a small region containing the system's discrete eigenvalues, we see that the phase at $-L$ is being affected in some way by the presence of the eigenvalues, manifested in slight ripples in the surface. This suggests that the information we are extracting by isolating the phase in this manner may be very deeply linked to fundamental system properties such as eigenvalue location, and that consequently there may be potential for developing methods which employ such a link to analyze systems in greater depth, or with greater ease, than is currently possible.

4.3.3 Summary of numerics

These numerical examples demonstrate the wealth of information which appears to be inextricably linked to the phase of a path on S^3, and the extent to which we may be able to extract crucial geometrical information about the dynamics of systems just by reframing problems in terms of fibre bundles and phases.

Chapter 5

Phase computations for the test-case and the central conjecture

In this chapter we consider the test-case in closer detail; we define three types of path in the system space, then calculate the phases associated with these paths. The numerical results here lead to the central conjecture of the thesis. Note that even though this system is on $\mathbb{C}^2$ and could therefore be treated using the simplified Hopf quaternion notation and equations of Chapter 4, we instead return to the general vector notation of Chapter 3, in order to place the phase calculation process in a general Hopf bundle setting, since subsequent numerical investigations will involve systems of higher dimensions.

5.1 Defining paths in the test-case system space

Recall, the test-case is the system

$$u_x = A(x,\lambda)u, \qquad x \in \mathbb{R},\ \lambda \in \Lambda = \mathbb{C} \setminus \{(-\infty,-1]\},\ u = u(x,\lambda) = \begin{pmatrix} u_1 \\ u_2 \end{pmatrix} \in \mathbb{C}^2 \tag{5.1}$$

with

$$A(x,\lambda) = \begin{pmatrix} 0 & 1 \\ \lambda + 1 - 2f(x) & 0 \end{pmatrix}, \qquad f(x) = \frac{3}{2}\mathrm{sech}^2\frac{1}{2}x \tag{5.2}$$

and we have

$$A_\infty(\lambda) = \lim_{x\to\pm\infty} A(x,\lambda) = \begin{pmatrix} 0 & 1 \\ \lambda + 1 & 0 \end{pmatrix} \tag{5.3}$$

with eigenvalue/vector pairs

$$\mu_{\pm}(\lambda) = \mp\sqrt{\lambda+1}, \qquad \xi_{\pm}(\lambda) = \begin{pmatrix} 1 \\ \mp\sqrt{\lambda+1} \end{pmatrix} \tag{5.4}$$

and the eigenvector corresponding to the eigenvalue of most negative real part, i.e. corresponding to the space of solutions to (5.1) bounded as $x \to +\infty$, is written

$$u_{\infty}(\lambda) = \xi_{+}(\lambda) = \begin{pmatrix} 1 \\ -\sqrt{\lambda+1} \end{pmatrix} \tag{5.5}$$

Being doubly asymptotically constant in x (and well-behaved $\forall x$), the system is amenable to analysis by the Evans function method. Consideration of this method reveals that due to the structure of the problem there are certain preferred paths within the system space, namely paths which involve eigenvectors of the system-at-infinity, A_{∞}. Then, since it is precisely this structure which permits the application of the Evans function method, and which hence leads to the determination of discrete eigenvalues λ of the underlying problem (see Section 1.2), we investigate paths based on this asymptotic structure, with a view to exploring whether there exist any further associations between the system and its eigenvalues. Define three types of path in the system space as follows:

- **Path γ_1 - paths of eigenvectors of $A_{\infty}(\lambda)$.** Since both the system-at-infinity and its eigenvector $u_{\infty}(\lambda)$ depend on λ, u_{∞} can be regarded as a map from the parameter space to the system space, $u_{\infty} : \Lambda \to \mathbb{C}^2$. Then let $\lambda : \mathbb{R} \to \Lambda$ be a *path* in the parameter space Λ, so that the composition $(u_{\infty} \circ \lambda)$ is a path of eigenvectors of $A_{\infty}(\lambda)$ in $\mathbb{C}^2$, along which the associated phase may be calculated. We call this type of path a γ_1 path. Furthermore, writing spherical projection as P, the map $(P \circ u_{\infty} \circ \lambda) : \mathbb{R} \to S^3$ is the path on S^3 along which the connection form is integrated to give the phase associated with a γ_1 path. We can then pick the λ-path to be an interesting path in Λ; in this work we focus on closed loops in λ-space, with special emphasis on consideration of whether the path encircles any of the discrete eigenvalues of the underlying system or not. In choosing a λ-path in Λ, attention should be paid to the location of known eigenvalues, continuous spectrum and any other system-specific properties.

- **Path γ_2 - paths of solutions to $u_x = Au$.** For any given $\lambda \in \Lambda$, solving (5.1) with initial condition $u_{\infty}(\lambda)$ yields a path of points in $\mathbb{C}^2$ along which the associated phase may be calculated. We call this type of path a γ_2 path.

Spherical projection of this solution path again gives the path on S^3 along which the connection form is integrated to give the phase associated with a γ_2 path. Note that since the initial condition $u_\infty(\lambda)$ is defined as the eigenvector to the system "at infinity", generating a γ_2 path by solving $u_x = Au$ numerically from this vector requires picking a real number $L > 0$ to represent the value of x in this limit. L should be large enough to give an acceptably small error. Thus $u(L, \lambda) = u_\infty(\lambda)$ is the initial condition from which numerical integration begins, and integration proceeds in the negative x direction, down to some other chosen value $x = L' < L$. In general for γ_2 paths, as with all numerical integration, attention should be paid to properties of the system which may affect the outcome of the computation, such as the presence of singularities of the system.

- **Path γ_3 - paths of flowed-forward paths of eigenvectors of $A_\infty(\lambda)$.** To generate a γ_3 path simply combine a γ_1 path with a host of γ_2 paths: take a γ_1 path on $\mathbb{C}^2$; then use each point of this path as the initial condition for solving $u_x = Au$, thereby generating a collection of γ_2 paths on $\mathbb{C}^2$. Define a γ_3 path to be the set of end points of the γ_2 paths, i.e. the collection of solution vectors $u(L', \lambda)$.

From Chapter 3 we have that for γ_1 and γ_3 paths the associated phase is given by expression (3.35):

$$\theta(s) = \int \Big(\frac{\mathrm{Im}(u(s)^H u_s(s))}{(u(s)^H u(s))} \Big) ds$$

while for γ_2 paths this reduces to (3.54):

$$\theta(s) = \int \Big(\frac{\mathrm{Im}(u(s)^H A u(s))}{(u(s)^H u(s))} \Big) ds$$

We illustrate these three paths in Figure 5.1, suppressing dimensions where appropriate.

Remark 5.1.1. *We could just as easily base the whole procedure around the eigenvectors of $A_{-\infty}(\lambda)$. (In this case a γ_1 path would be a path of eigenvectors of $A_{-\infty}(\lambda)$, a γ_2 path would be the solution path formed by integrating in the positive x direction, from $-L$ to $L' > -L$, and a γ_3 path would again be a path of γ_2-endpoints, $u(L', \lambda)$.) The effect of the asymptotic structure of the system on the results and concepts presented here could be a subject of further study beyond this thesis, in particular, looking at what happens if the systems $A_\infty(\lambda)$ and $A_{-\infty}(\lambda)$ are not the same; or if the system is only asymptotically constant in one of the limits, but not both (this case is briefly discussed in Section 6.3).*

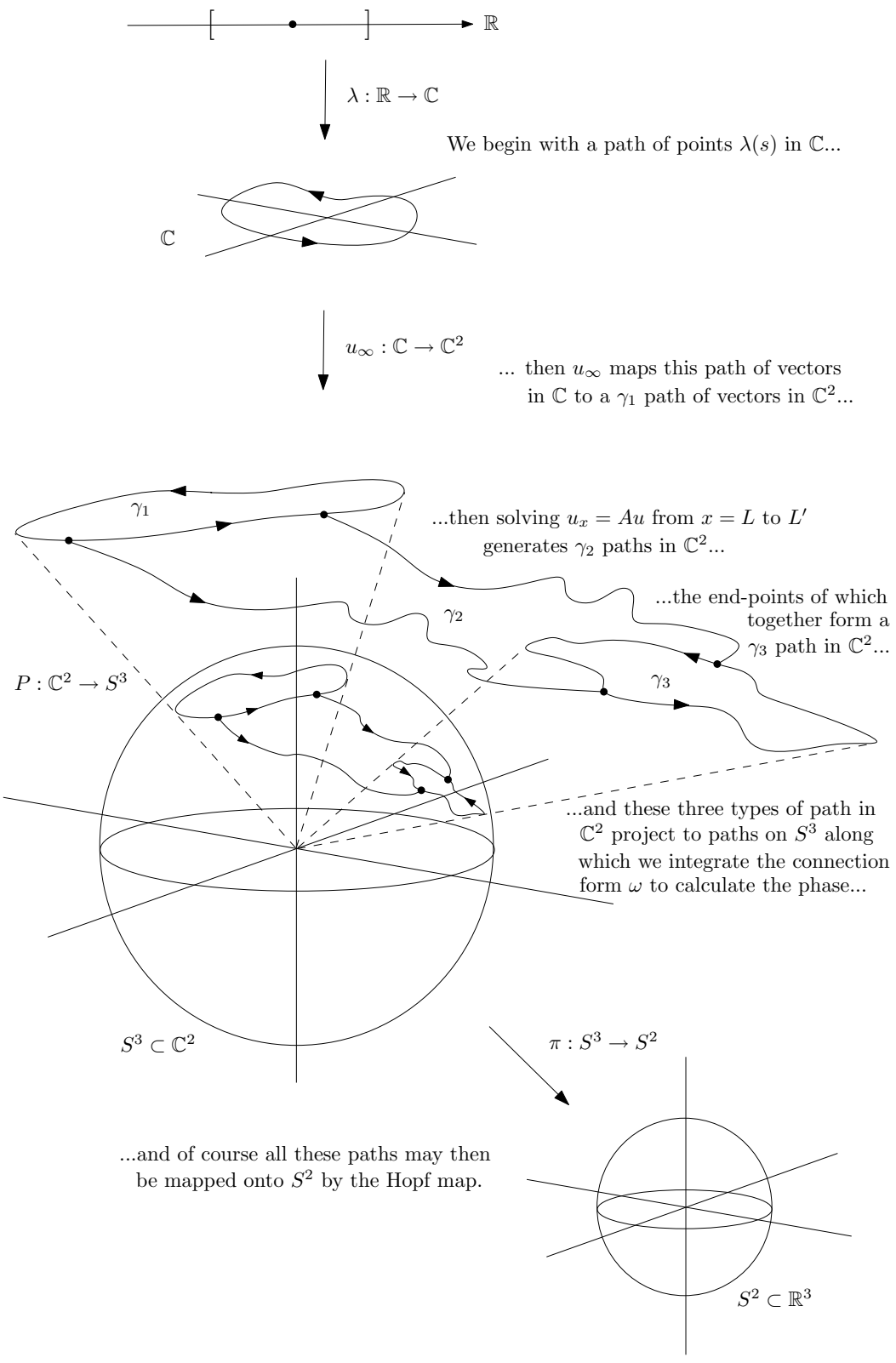

Figure 5.1: Illustrating the three types of path on S^3

5.2 Numerical results and details of path parametrization

5.2.1 Path γ_1

γ_1 parametrization

To generate γ_1 paths we use circular λ-paths in $\mathbb{C}$. Take centre λ_0 and radius r, and let s be the path parameter:

$$\lambda(s) = \lambda_0 + re^{is} \qquad \lambda_0 \in \mathbb{C}, r \in \mathbb{R}^+, s \in [0, 2\pi] \tag{5.6}$$

then use u_∞ to map this to a path $u(s)$ in $\mathbb{C}^2$:

$$u(s) = u_\infty(\lambda(s)) = \begin{pmatrix} 1 \\ -\sqrt{\lambda(s)+1} \end{pmatrix} \tag{5.7}$$

then since the phase curve associated with this path is given by

$$\theta(s) = \int \Big(\frac{\mathrm{Im}(u(s)^H u_s(s))}{(u(s)^H u(s))}\Big) ds \tag{5.8}$$

(as in (3.35)) and $u(s) = u(\lambda(s))$ here, we have $u_s = u_\lambda \lambda_s$, with

$$\lambda_s(s) = ire^{is} \tag{5.9}$$

$$u_\lambda = \begin{pmatrix} 0 \\ -\frac{1}{2\sqrt{\lambda(s)+1}} \end{pmatrix} \tag{5.10}$$

so the final expression for the associated phase curve for a γ_1 path is

$$\theta(s) = \int \frac{\mathrm{Im}[u^H u_\lambda \lambda_s]}{u^H u} ds \tag{5.11}$$

and the phase change around a γ_1 path is

$$\Delta\theta = \int_0^{2\pi} \frac{\mathrm{Im}[u(s)^H u_\lambda(s) \lambda_s(s)]}{u(s)^H u(s)} ds \tag{5.12}$$

Using the Runge-Kutta algorithm `ode45`, the Matlab code `integration_at_L.m` performs this numerical phase calculation. The solver `ode45` is used because it is the standard high-performance workhorse for most ODE problems dealt with in Matlab, and it is usually the most efficient [18]. Unless stated otherwise, the default absolute and relative tolerances of 10^{-6} and 10^{-3} respectively are used throughout all computations presented in this thesis. As always there is a balance between efficiency and accuracy, but in general it is found that the numerics produced using default tolerances provide sufficiently accurate results to represent well the large-scale patterns observed here.

Remark 5.2.1. *An alternative numerical scheme was also developed and implemented in order to verify the accuracy of the numerical results produced using the above code. This verification process consisted of deriving and solving the dynamics equations induced on the natural atlas of charts of* $\mathbb{C}P^{n-1}$ *(see e.g. [21], p.223). The results showed the two numerical methods to be consistent.*

For $\lambda_0 = 1 + 0.2i$, $r = 0.8$ and $\theta(0) = 0$, `integration_at_L.m` produces the graphical output shown in Figure 5.2. (The filename refers to the fact that L is the large number used to represent ∞.)

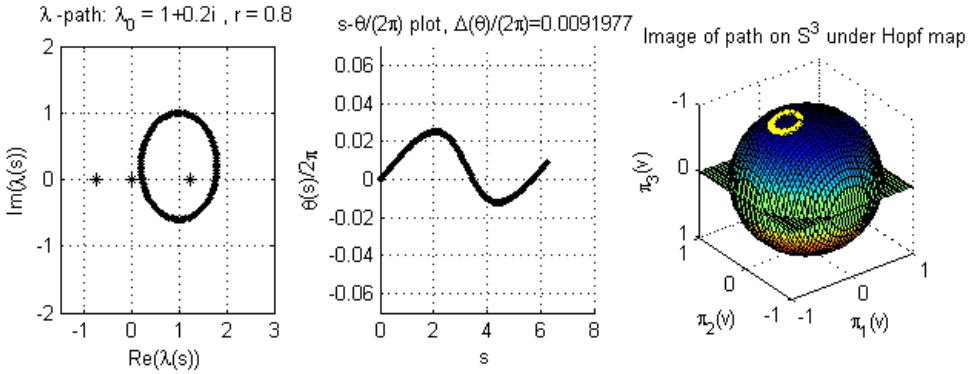

Figure 5.2: Graphical output for γ_1 path with $\lambda_0 = 1 + 0.2i, r = 0.8$

- **The plot on the left** shows the circular path traced out by $\lambda(s)$ as s goes from 0 to 2π, plus the three discrete eigenvalues of the system marked with asterisks. (Recall there is a continuous spectrum on the real axis from -1 to $-\infty$.)

- **The plot in the centre** shows how the phase $\theta(s)/2\pi$ varies as the λ-path is traversed. Note the scale factor 2π; although it has little effect on these results, this factor becomes important in future calculations, so we introduce it here for consistency.

- **The plot on the right** shows the image on S^2, under the Hopf map, of the path on S^3 obtained by spherical projection of the γ_1 path in $\mathbb{C}^2$. π_i represents the ith component of the Hopf map, while v represents points of the path on S^3 written as complex 2-vectors as usual.

As the program runs, it traces out the three curves, point by point, simultaneously.

γ_1 numerical results

Figures 5.3-5.9 show the same trio of output graphics for a variety of λ-paths, as defined by the λ_0 and r values, which are shown in the figures, again with $\theta(0) = 0$.

Table 5.1 summarizes the results for the γ_1 paths presented here.

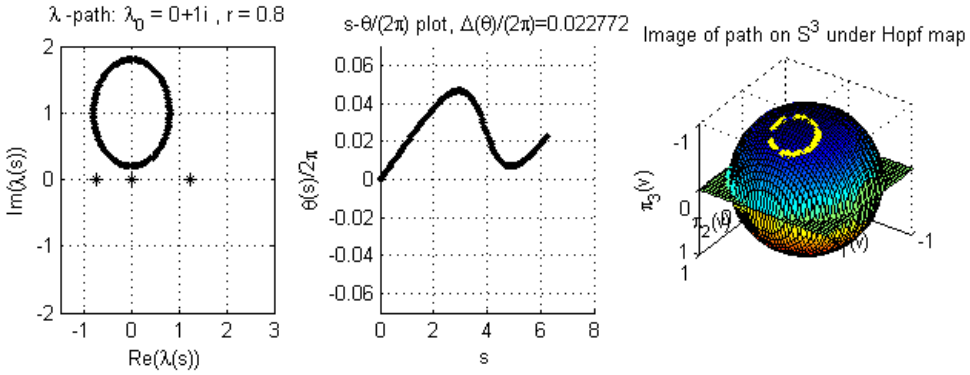

Figure 5.3: Graphical output for γ_1 path with $\lambda_0 = i, r = 0.8$

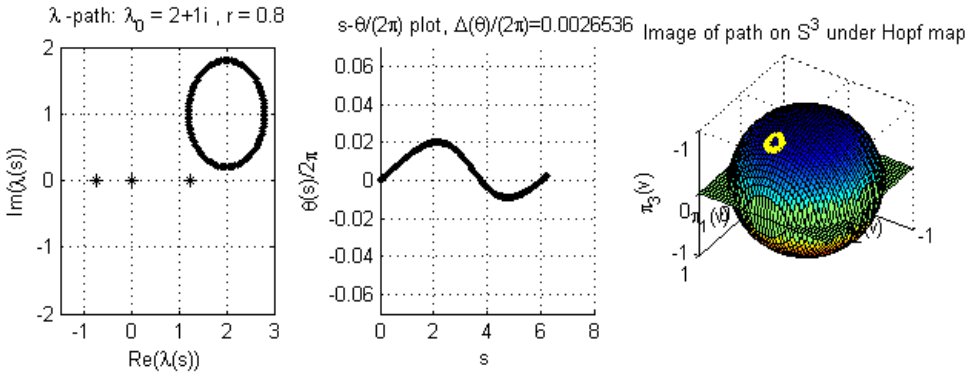

Figure 5.4: $\lambda_0 = 2 + i, r = 0.8$

γ_1 comments

The key points to note about the γ_1 path results (including both the results presented here and various other paths, of which these results are representative) are:

- The phase curve is periodic plus some slight shift away from the initial θ value (zero here).

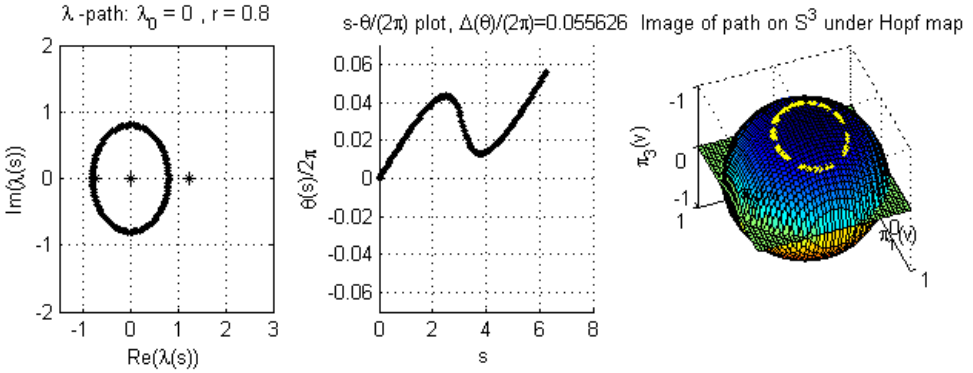

Figure 5.5: $\lambda_0 = 0, r = 0.8$

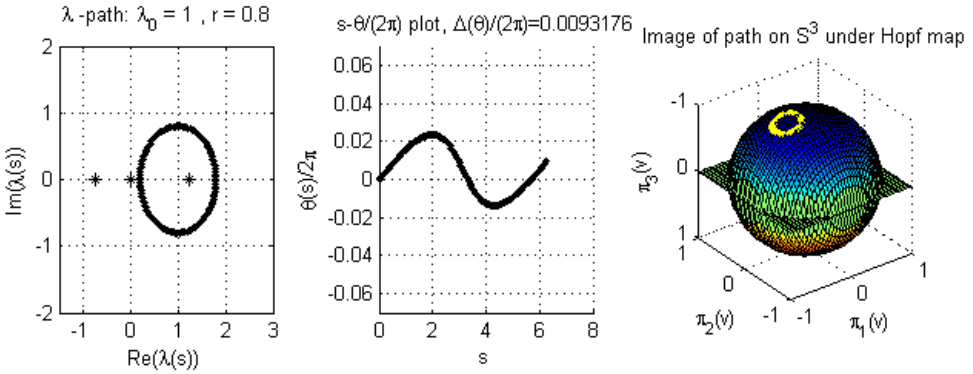

Figure 5.6: $\lambda_0 = 1, r = 0.8$

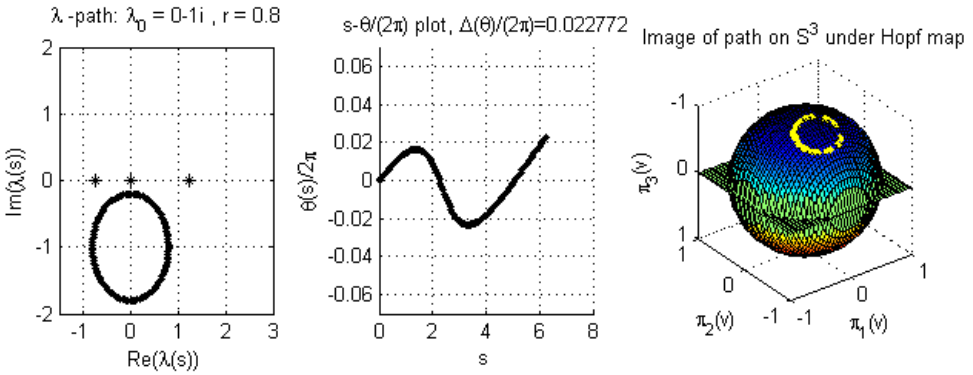

Figure 5.7: $\lambda_0 = -i, r = 0.8$

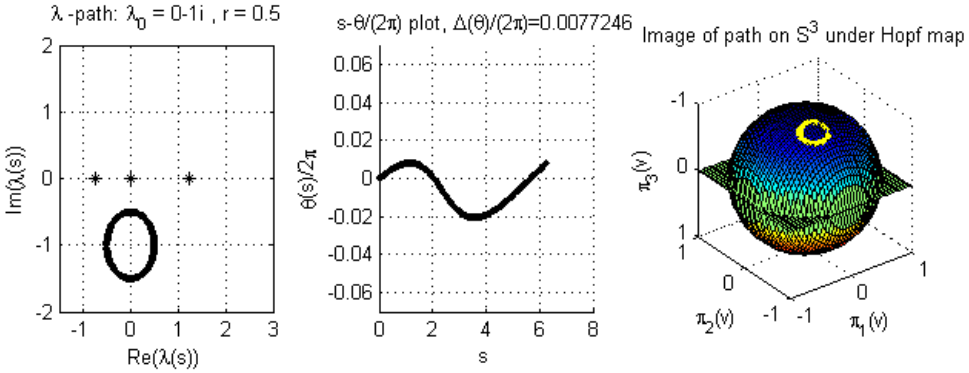

Figure 5.8: $\lambda_0 = -i, r = 0.5$

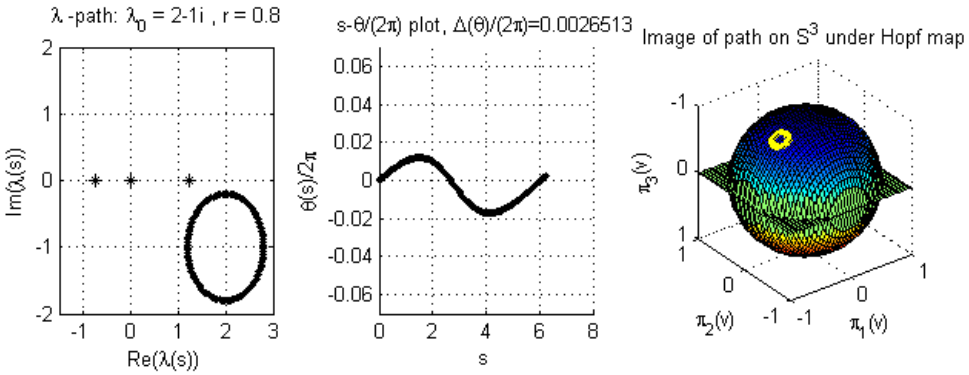

Figure 5.9: $\lambda_0 = 2 - i, r = 0.8$

Figure No.	centre of λ-path, λ_0	radius of λ-path, r	No. of system eigenvalues contained within λ-loop	$\Delta\theta/2\pi$
5.2	$1+0.2i$	0.8	1	0.00918
5.3	i	0.8	0	0.02277
5.4	$2+i$	0.8	0	0.00265
5.5	0	0.8	2	0.05563
5.6	1	0.8	1	0.00932
5.7	$-i$	0.8	0	0.02277
5.8	$-i$	0.5	0	0.00772
5.9	$2-i$	0.8	0	0.00265

Table 5.1: Summary of numerical results for γ_1 paths shown

- This shift factor appears to depend on the proximity of the λ-path to the continuous spectrum of the system: the closer it passes to this region, the less symmetric the phase curve is and the larger the shift. The system has a singularity at points on the continuous spectrum (the nearer the λ-path passes to this region, the closer the matrix $A(x,\lambda)$ comes to being degenerate for some x value). This singular behaviour may be leading to greater numerical inaccuracies being generated in this region. However, tuning of the stepsize variable and absolute and relative tolerances, and even the application of alternative ODE solvers, failed to eliminate these shift factors. Thus a complete explanation of this phenomenon would require a more rigorous study than we propose here, necessarily addressing the relative merits of various numerical methods under degenerate conditions; this could easily form the basis of a future study beyond this thesis.

- Thus the phase change $\Delta\theta$ around γ_1 paths appears to be zero plus some fluctuation, possibly due to numerical error.

- The path images on S^2 are closed, circular paths. Their being closed is a consequence of the λ-paths in $\mathbb{C}$ being closed, while their being circular is a consequence of both the λ-paths being circular and the precise forms of u_∞ and the Hopf map, since no numerics are used to generate these paths.

- The λ-path radius does not in itself appear to affect the phase curve.

- The system is symmetric about the real axis in the λ-plane.

5.2.2 Path γ_2

γ_2 parametrization

To generate γ_2 paths we fix λ then solve (5.1) numerically from $x = L$ down to $x = L' < L$ with initial condition

$$u(L, \lambda) = u_\infty(\lambda) = \begin{pmatrix} 1 \\ -\sqrt{\lambda + 1} \end{pmatrix}, \tag{5.13}$$

L is the large number used to approximate ∞ in computations. The path parameter is just the independent variable x in the ODE and the associated phase curve is given by

$$\theta(x) = \int \frac{\mathrm{Im}(u(x)^H A u(x))}{(u(x)^H u(x))} dx \tag{5.14}$$

as in (3.54), and the phase change is

$$\Delta\theta = \int_L^{L'} \frac{\mathrm{Im}[u^H A u]}{u^H u} dx \tag{5.15}$$

So to calculate the associated phase along γ_2 paths we append this equation for $\theta(x)$ to the ODE system (5.1) and integrate it in parallel. The Matlab code `integrate_x_direction.m` does this and, for $\lambda = 1+i$, $L = 10 = -L'$ and $\theta(L) = 0$, produces the graphical output shown in Figure 5.10. Note that throughout this sec-

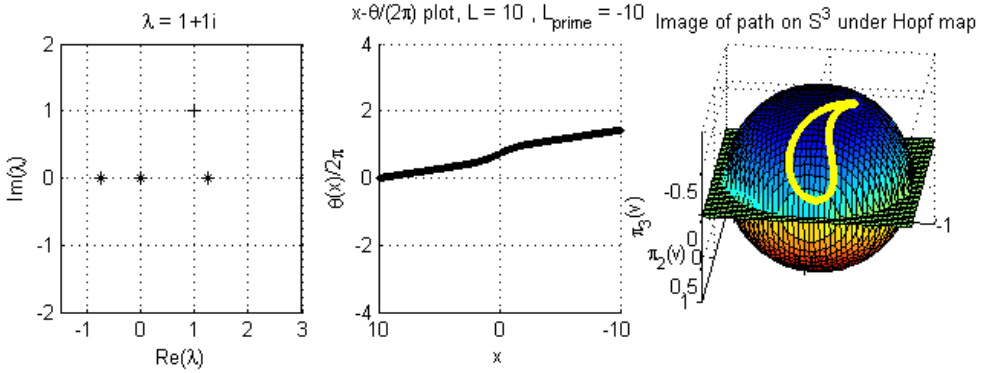

Figure 5.10: Graphical output for γ_2 path with $\lambda = 1 + i$, $L = 10 = -L'$

tion 5.2.2 only, the absolute and relative tolerance parameters used within `ode45` are set to 10^{-12} and 10^{-9} respectively (in order to give the clearest diagrams possible). The format of the diagrams is as before: the plot on the left shows the single value of λ being used (the plus sign), along with the three eigenvalues of the system (the asterisks); the plot in the middle shows how $\theta(x)$ changes as the path parameter

goes from L to L' in the calculation; and the plot on the right shows the image on S^2, under the Hopf map, of the projection of the γ_2 path on S^3. Again, as the program runs, the two curves on the right are traced out simultaneously point by point. Figure 5.11 shows a close-up of the plot on the right: the image trajectory on S^2 is roughly teardrop-shaped. However, what these still figures do not convey is

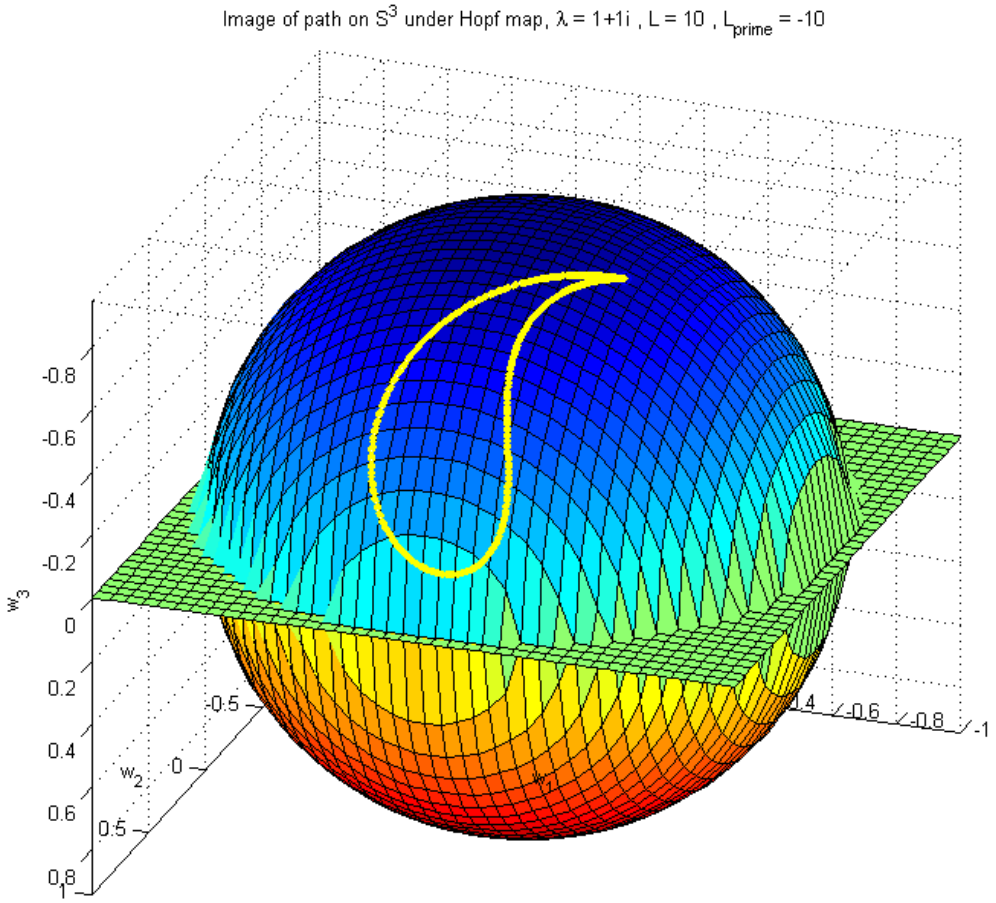

Figure 5.11: Close-up of right-most plot of Figure 5.10

the dynamics of the trajectory: the path begins at the apex of the teardrop, travels around the boundary of the shape then returns, along the other arm, to the apex.

γ_2 numerical results

Figures 5.12-5.22 show the same trio of graphics for a selection of λ values, with $L = 10 = -L'$ fixed. The spheres on the right have been rotated appropriately to give the best view of the trajectory.

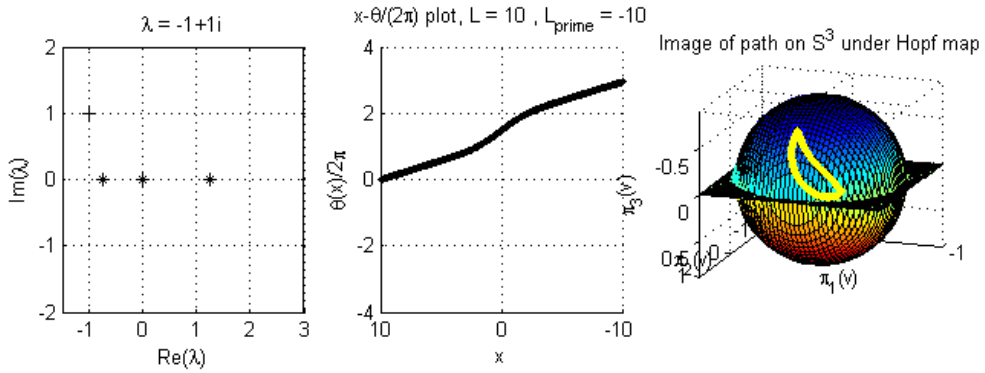

Figure 5.12: Graphical output for γ_2 path with $L = 10 = -L'$, $\lambda = -1 + i$

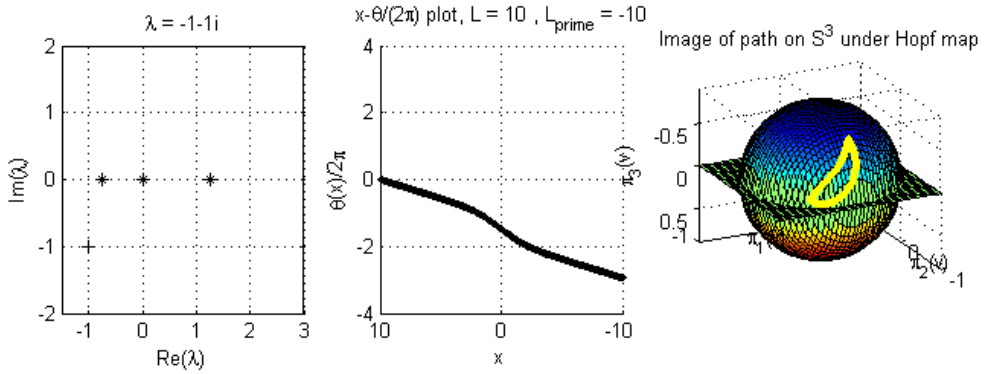

Figure 5.13: $\lambda = -1 - i$

Figures 5.23-5.25 show the trio of graphics for 3 different values of $L = -L'$, with $\lambda = 0.5 - 0.5i$ fixed.

Table 5.2 summarizes the results for the γ_2 paths presented here.

γ_2 comments

The key points to note about these numerical results are as follows:

- These results are the same as those presented in Section 4.3.2 of Chapter 4, since we now classify the path investigated there as a γ_2 path.

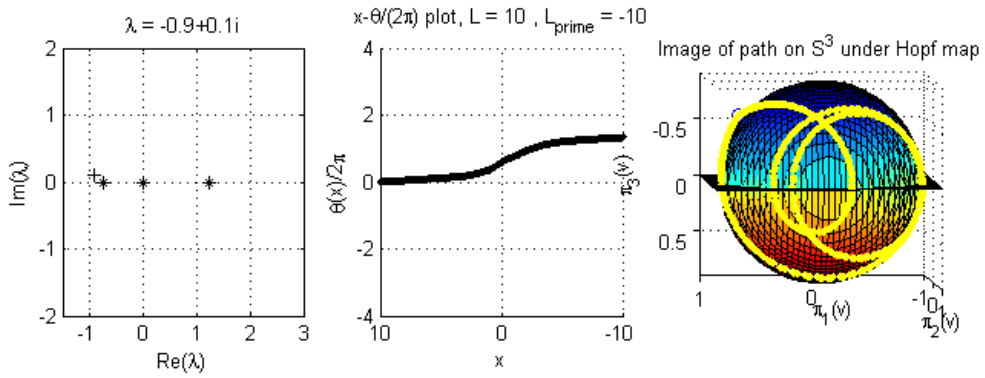

Figure 5.14: $\lambda = -0.9 + 0.1i$

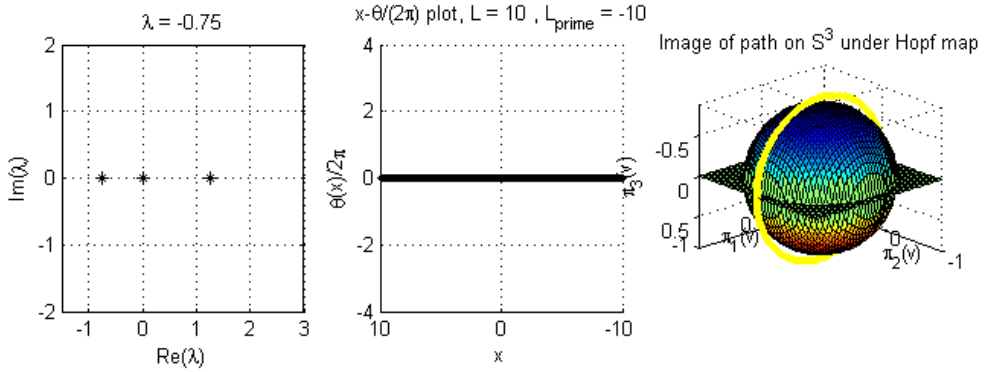

Figure 5.15: $\lambda = -0.75$

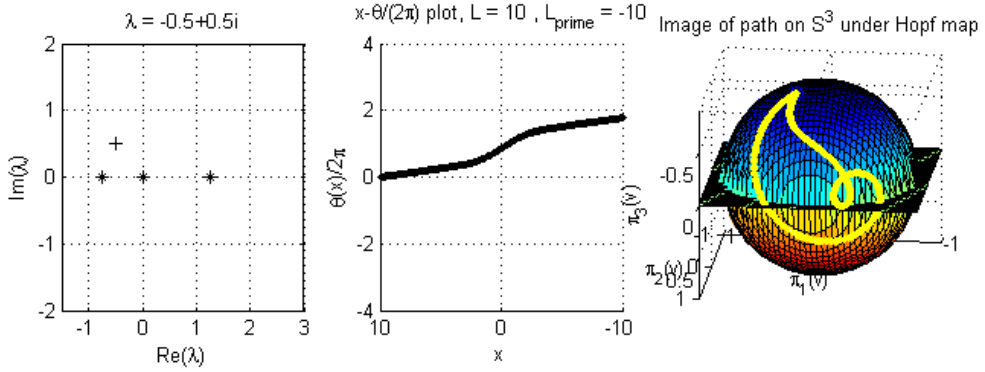

Figure 5.16: $\lambda = -0.5 + 0.5i$

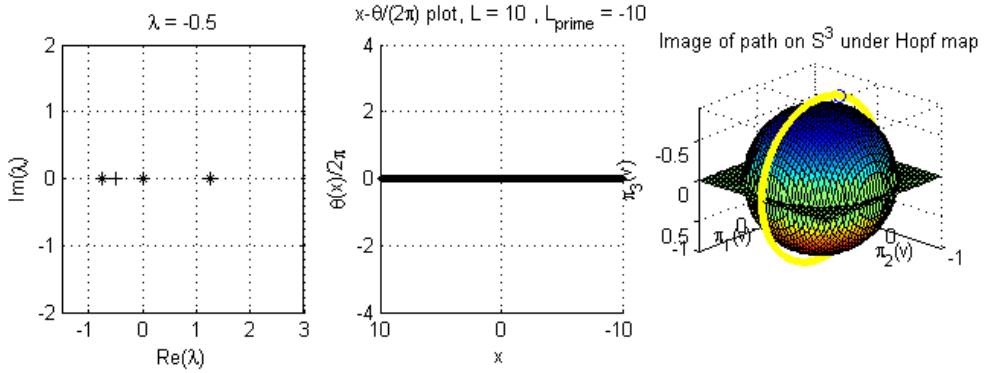

Figure 5.17: $\lambda = -0.5$

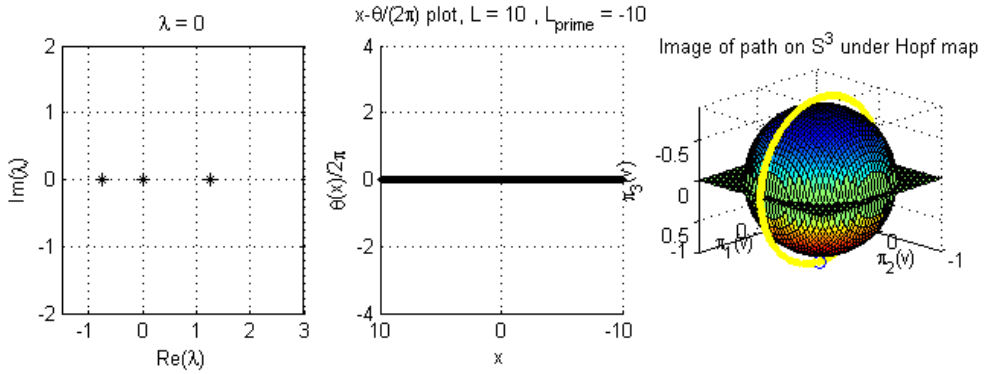

Figure 5.18: $\lambda = 0$

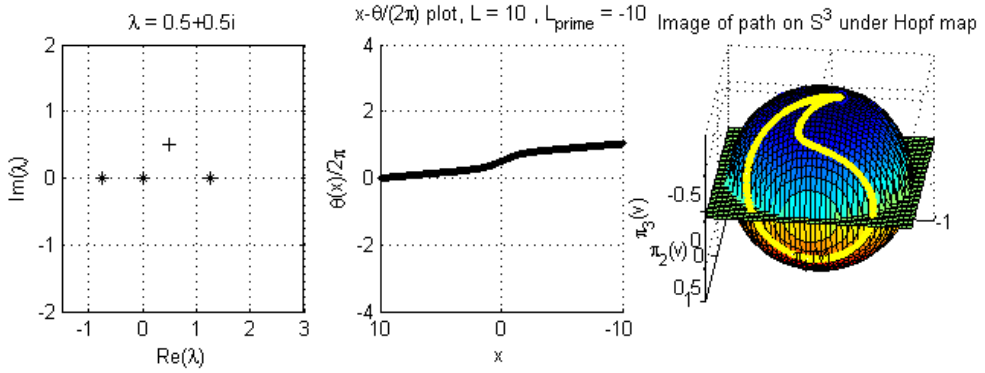

Figure 5.19: $\lambda = 0.5 + 0.5i$

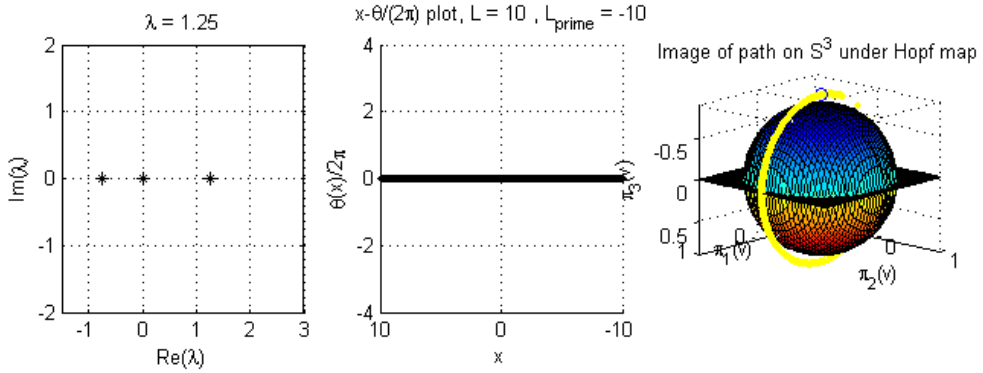

Figure 5.20: $\lambda = 1.25$

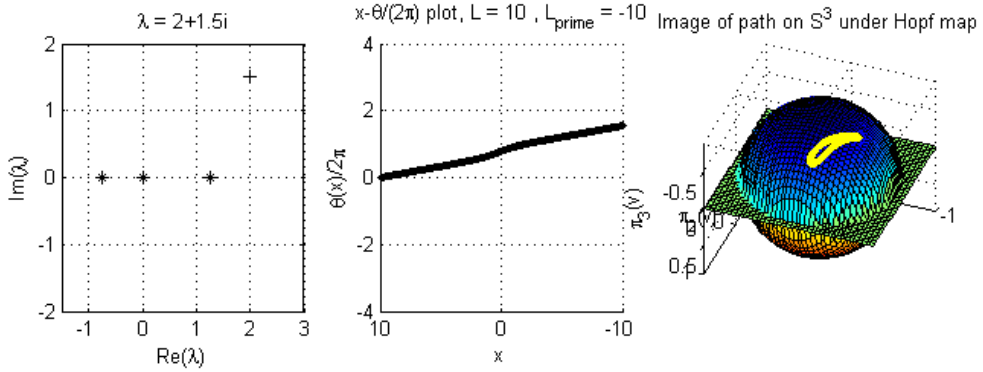

Figure 5.21: $\lambda = 2 + 1.5i$

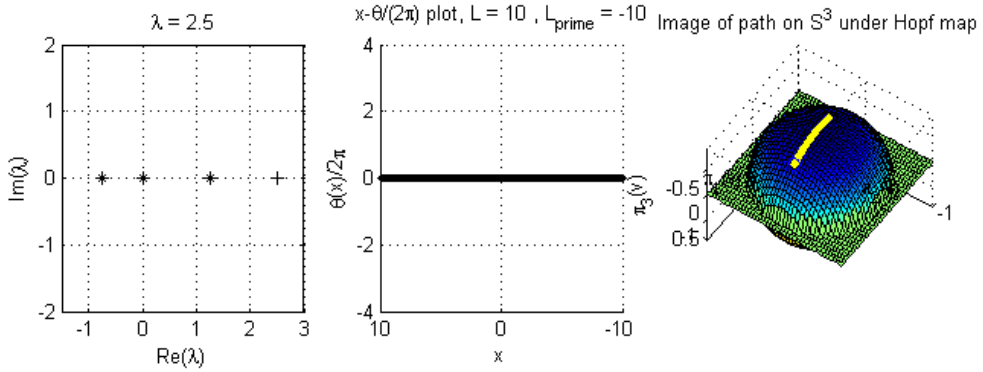

Figure 5.22: $\lambda = 2.5$

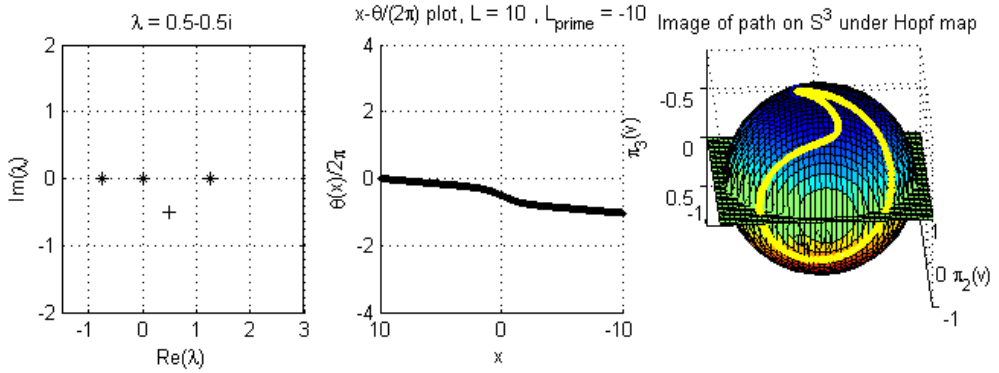

Figure 5.23: $\lambda = 0.5 - 0.5i$, $L = 10 = -L'$

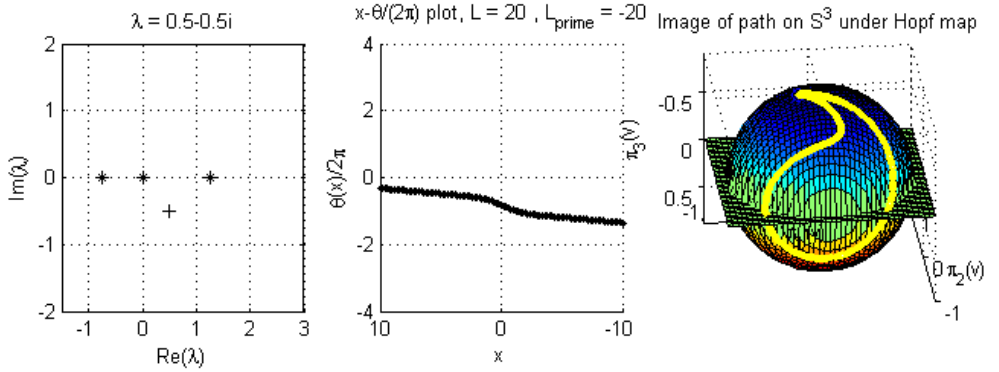

Figure 5.24: $\lambda = 0.5 - 0.5i$, $L = 20 = -L'$

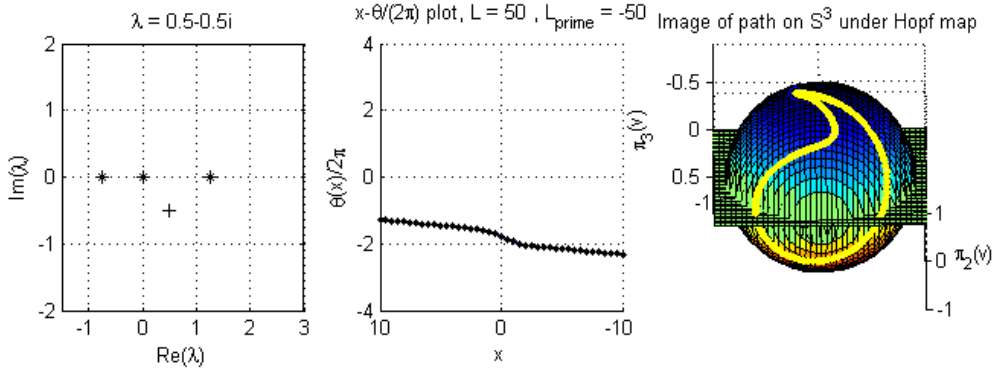

Figure 5.25: $\lambda = 0.5 - 0.5i$, $L = 50 = -L'$

Figure No.	λ	$L\ (= L')$	$\Delta\theta/2\pi$
5.10	$1+i$	10	1.4295
5.12	$-1+i$	10	2.9440
5.13	$-1-i$	10	-2.9440
5.14	$-0.9+0.1i$	10	1.3373
5.15	-0.75	10	0.0000
5.16	$-0.5+0.5i$	10	1.7737
5.17	-0.5	10	0.0000
5.18	0	10	0.0000
5.19	$0.5+0.5i$	10	1.0315
5.20	1.25	10	0.0000
5.21	$2+1.5i$	10	1.5476
5.22	2.5	10	0.0000
5.23	$0.5-0.5i$	10	-1.0315
5.24	$0.5-0.5i$	20	-1.6727
5.25	$0.5-0.5i$	50	-3.5961

Table 5.2: Summary of numerical results for γ_2 paths shown

- In contrast to γ_1 paths, γ_2 paths are not periodic but have fixed sign gradient or zero gradient - depending on $\mathrm{Im}(\lambda)$.
- These results essentially combine to form the same phase surface as shown in Figure 4.22.
- For $\mathrm{Im}(\lambda) \neq 0$ there is a symmetrical step in the phase curve in a region about $x = 0$. The size and location of this step is resistant to changes in L, as shown in Figures 5.23-5.25.
- For $\mathrm{Im}(\lambda) = 0$, $\theta(x)$ is constant and the image trajectory on S^2 is all or part of a great circle, as shown in Figures 5.15, 5.17, 5.18, 5.20 and 5.22. This includes the cases where λ is one of the system eigenvalues, but this has no apparent effect on the results.
- The image curves on S^2 are closed and depend closely on $\mathrm{Im}(\lambda)$. For large $|\mathrm{Im}(\lambda)|$ we get tiny loops, as in Figure 5.21. For smaller $|\mathrm{Im}(\lambda)|$ we get larger teardrop shapes, as in Figure 5.19. For $\mathrm{Im}(\lambda) = 0$ we get great circles or parts thereof, as in Figure 5.15. The sign of $\mathrm{Im}(\lambda)$ dictates which side of S^2 the trajectory appears on: as $\mathrm{Im}(\lambda)$ goes from large positive through zero to large

negative, small loops turn to larger teardrops on one side of S^2, which turn to a great circle then cross over to large teardrops then small loops on the other side of S^2.

- The image curves on S^2 show interesting behaviour when λ is near the continuous spectrum (and $\mathrm{Im}(\lambda) \neq 0$), as shown in Figures 5.14 and 5.16.
- The system is symmetric about the real axis in the λ-plane.

As interesting and deserving of further study these results may be, they form only part of a larger picture, which is described in the following γ_3 section.

5.2.3 Path γ_3

γ_3 parametrization

To generate γ_3 paths we begin with circular λ-paths in $\mathbb{C}$, as in the γ_1 case, parametrizing them just as before

$$\lambda(s) = \lambda_0 + re^{is} \qquad \lambda_0 \in \mathbb{C}, r \in \mathbb{R}^+, s \in [0, 2\pi] \tag{5.16}$$

Again use u_∞ to map this λ-path to a closed loop in $\mathbb{C}^2$. Then use points on this loop as initial conditions for generating γ_2 paths emanating from these points, the end points of which combine to form the points of the γ_3 path. Using this method the parameter for the λ-path, s, is also the parameter for the γ_3 path. We write the points of the γ_3 path as $u(L', \lambda(s))$; this is the vector in $\mathbb{C}^2$ which results from solving $u_x = Au$ from L to L' with initial condition $u_\infty(\lambda(s))$, and is consistent with previous notation.

So the expression for the phase curve associated with a γ_3 path is

$$\theta(s) = \int \frac{\mathrm{Im}[u(L', \lambda(s))^H u_s(L', \lambda(s))]}{u(L', \lambda(s))^H u(L', \lambda(s))} ds \tag{5.17}$$

and the phase change around the γ_3 path is

$$\Delta\theta = \int_0^{2\pi} \frac{\mathrm{Im}[u(L', \lambda(s))^H u_s(L', \lambda(s))]}{u(L', \lambda(s))^H u(L', \lambda(s))} ds \tag{5.18}$$

Now, in order to compute this phase, the value of the derivative of the path vector u w.r.t. path parameter s, $u_s(L', \lambda(s))$, must be known. But since there are no analytic expressions for any of these vectors, an approximation must be calculated explicitly at each integration step. The numerical procedure developed to evaluate

(5.18) here uses the Matlab procedure `ode45`, which is a fourth-order Runge-Kutta method with adaptive stepsize; it requires both of the values $u(L', \lambda(s)), u_s(L', \lambda(s))$ for *whichever* value of s it chooses at each step. $u(L', \lambda(s))$ is calculated as usual, and $u_s(L', \lambda(s))$ is constructed as follows. For a given parameter value $s_0 \in (0, 2\pi)$, we approximate the derivative $u_s(L', \lambda(s_0))$ by

$$u_s\big|_{s_0} = \frac{u(L', \lambda(s_0 + \delta)) - u(L', \lambda(s_0 - \delta))}{2\delta} \tag{5.19}$$

for small, real δ. The expressions $u(\cdot, \cdot)$ on the r.h.s. are of course the vectors obtained by integrating the system $u_x = Au$ from L to L' from initial conditions $u(L, \lambda(s_0 + \delta)) = u_\infty(\lambda(s_0 + \delta))$ and $u(L, \lambda(s_0 - \delta)) = u_\infty(\lambda(s_0 - \delta))$ respectively. Figure 5.26 illustrates the procedure clearly. It also shows that close attention must be paid to the accuracy of the approximation $u_s(L', \lambda(s_0))$, because having two parameter values close together does not guarantee that the corresponding points on the γ_3 path are close together, and it is these latter values which are used to calculate u_s.

The Matlab code `integration_at_L_prime.m` implements the procedure, calculating $\Delta\theta$ around paths of type γ_3, and for $\lambda_0 = 1 + 0.2i$, $r = 0.8$, $\theta(0) = 0$, $L = -L' = 10$ and $\delta = 2\pi/10000$, produces the graphical output shown in Figure 5.27.

γ_3 numerical results

Graphical output for the same selection of values of λ_0 and r as for the γ_1 paths in Section 5.2.1 is shown in Figures 5.28-5.34 (still with $\theta(0) = 0$, $L = -L' = 10$ and $\delta = 2\pi/10000$). The plots follow the same format as previously.

Following these, Figures 5.35-5.40 clearly show the effect of fixing the centre of the λ-path, $\lambda_0 = 2 - i$, while varying its radius, r.

Table 5.3 summarizes the results for the γ_3 paths presented here.

γ_3 comments

The key points to note about the numerical results for γ_3 paths are:

- The phase change $\Delta\theta$ is approximately equal to the number of discrete eigenvalues contained within the loop in λ-space.
- The path images on S^2 are the same as the path images on S^2 for the corresponding γ_1 paths. This is consistent with the fact that the images on S^2 of the γ_2 paths are closed.

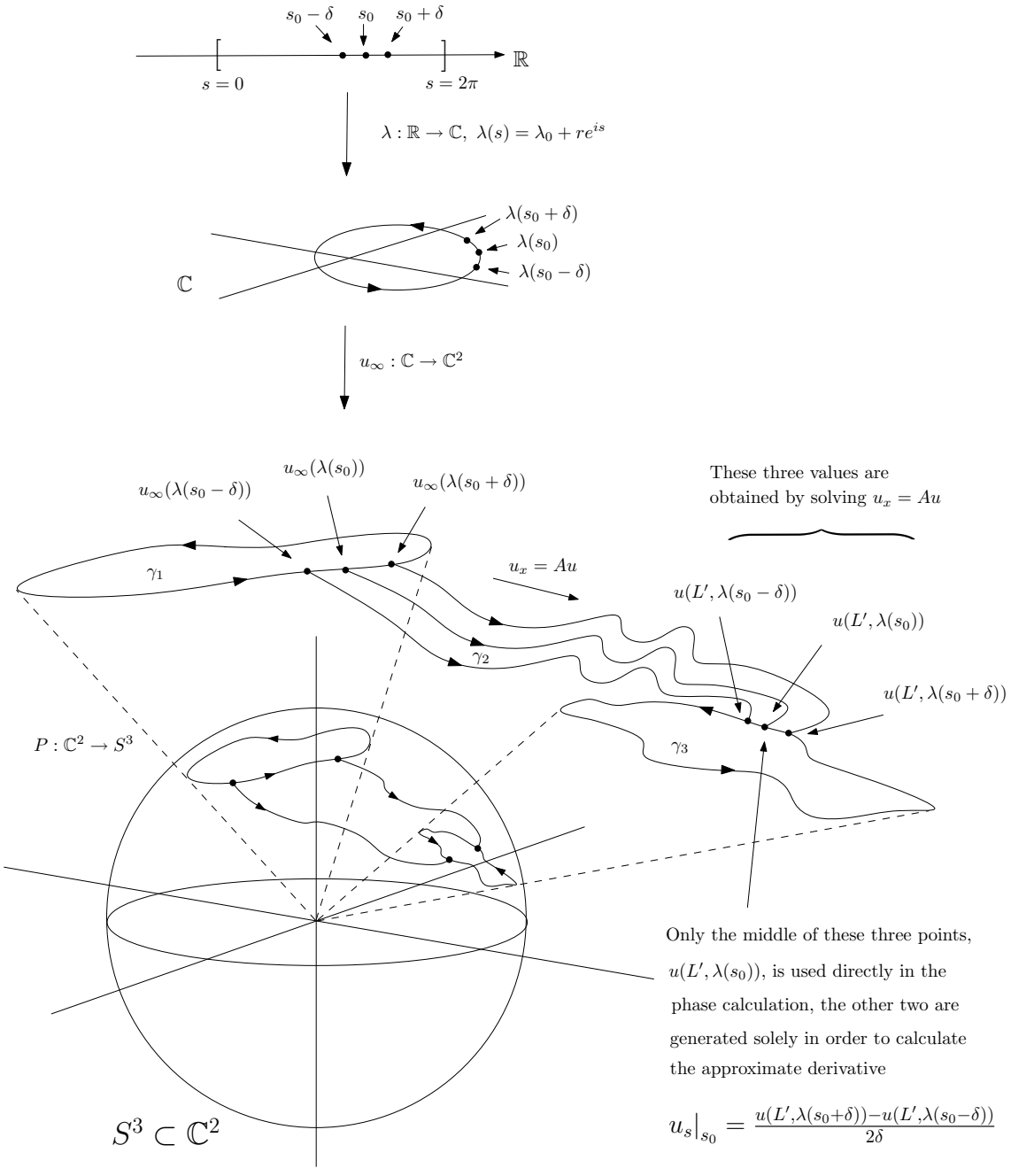

Figure 5.26: Calculating $u_s\big|_{s_0}$

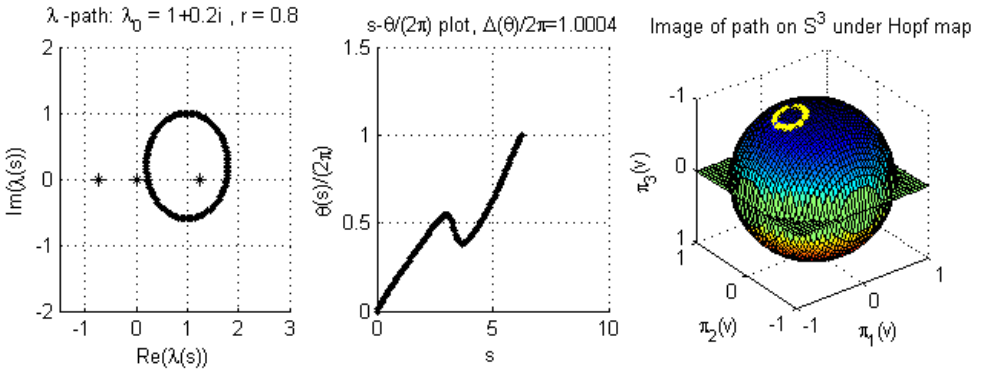

Figure 5.27: Graphical output for γ_3 path with $\lambda_0 = 1 + 0.2i, r = 0.8$

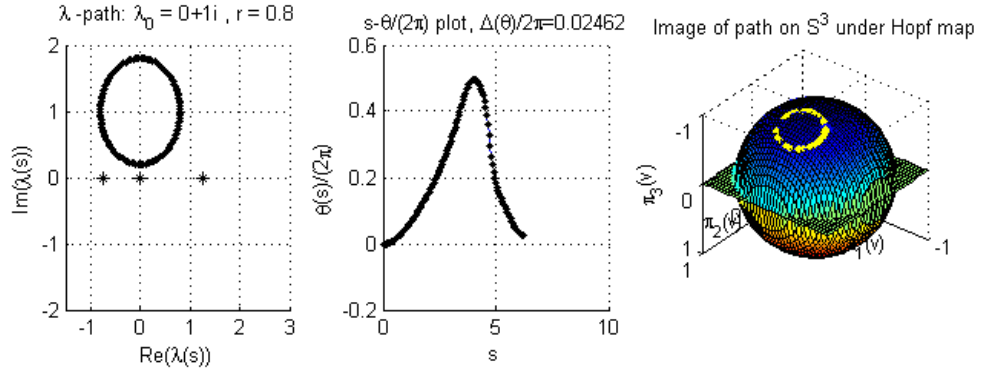

Figure 5.28: Graphical output for γ_3 path with $\lambda_0 = i, r = 0.8$

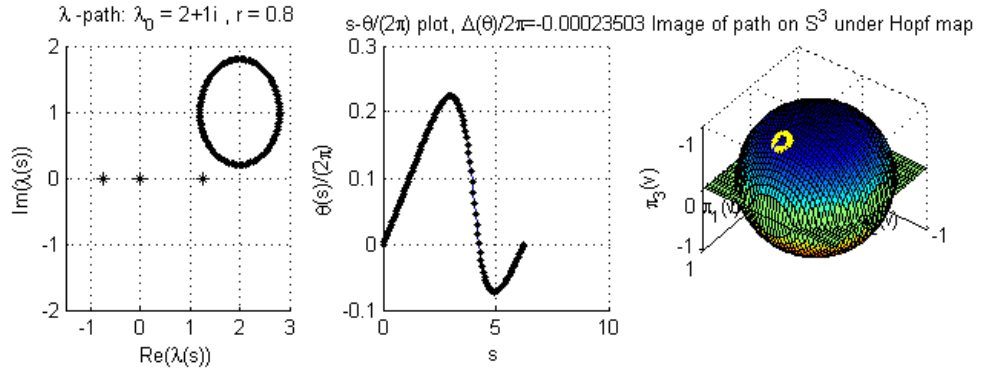

Figure 5.29: $\lambda_0 = 2 + i, r = 0.8$

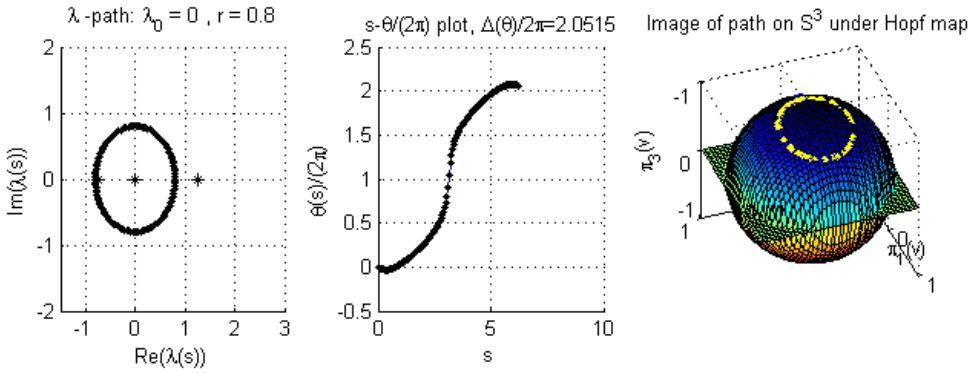

Figure 5.30: $\lambda_0 = 0, r = 0.8$

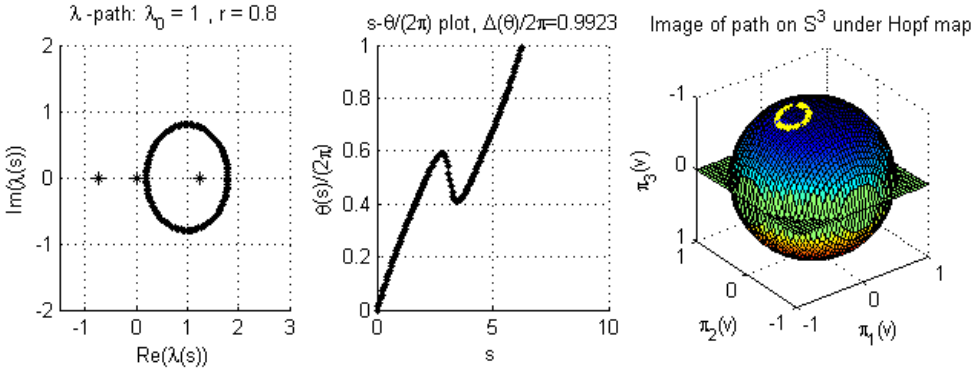

Figure 5.31: $\lambda_0 = 1, r = 0.8$

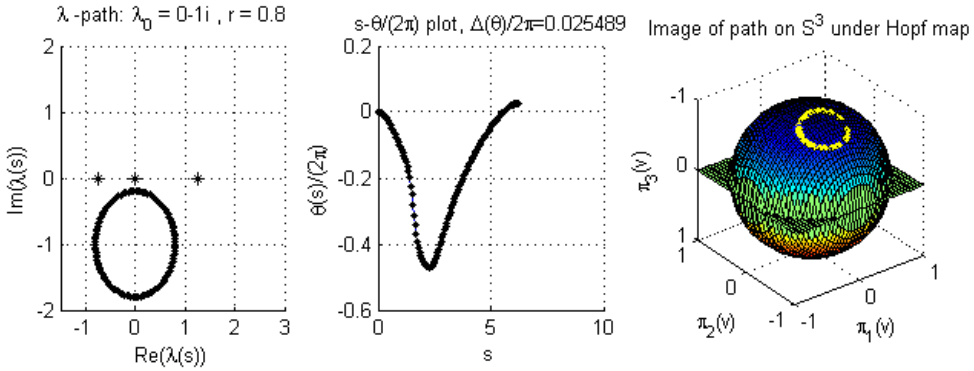

Figure 5.32: $\lambda_0 = -i, r = 0.8$

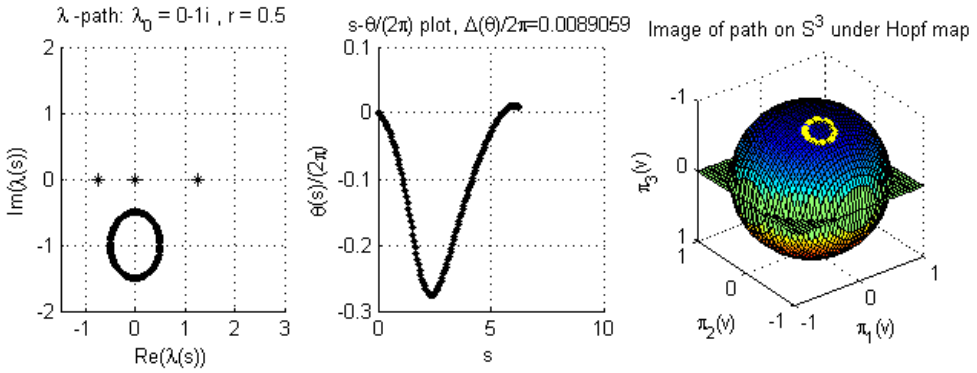

Figure 5.33: $\lambda_0 = -i, r = 0.5$

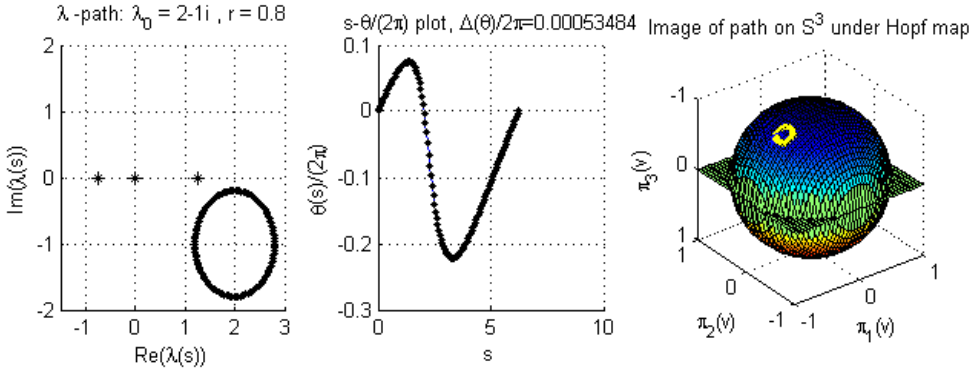

Figure 5.34: $\lambda_0 = 2 - i, r = 0.8$

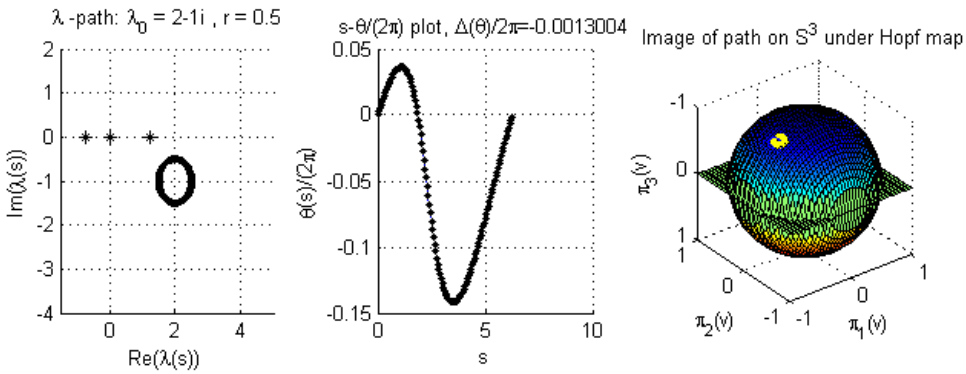

Figure 5.35: $\lambda_0 = 2 - i, r = 0.5$

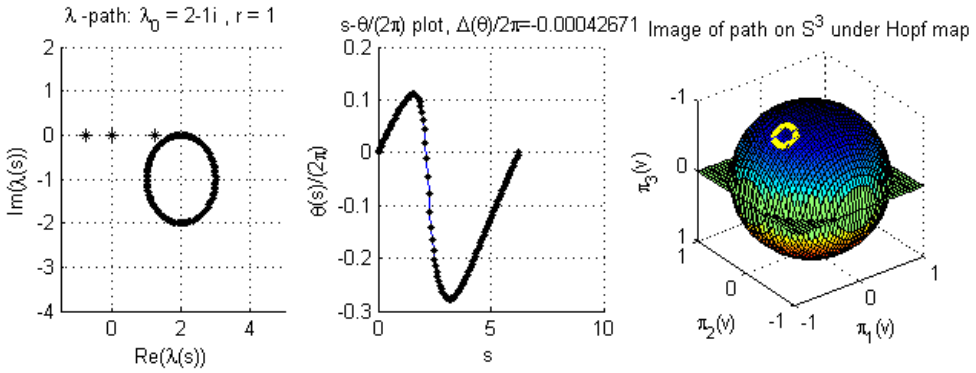

Figure 5.36: $\lambda_0 = 2 - i, r = 1.0$

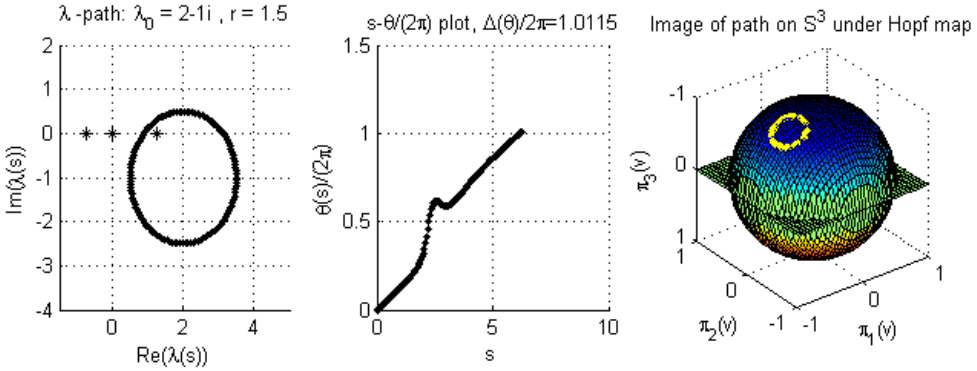

Figure 5.37: $\lambda_0 = 2 - i, r = 1.5$

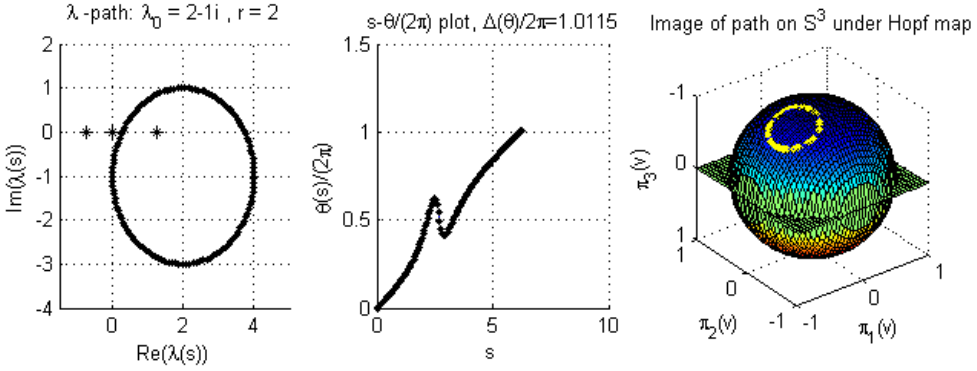

Figure 5.38: $\lambda_0 = 2 - i, r = 2.0$

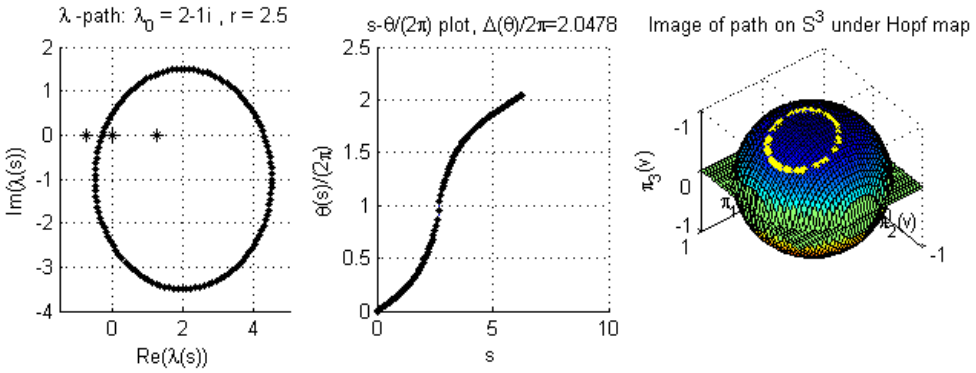

Figure 5.39: $\lambda_0 = 2 - i, r = 2.5$

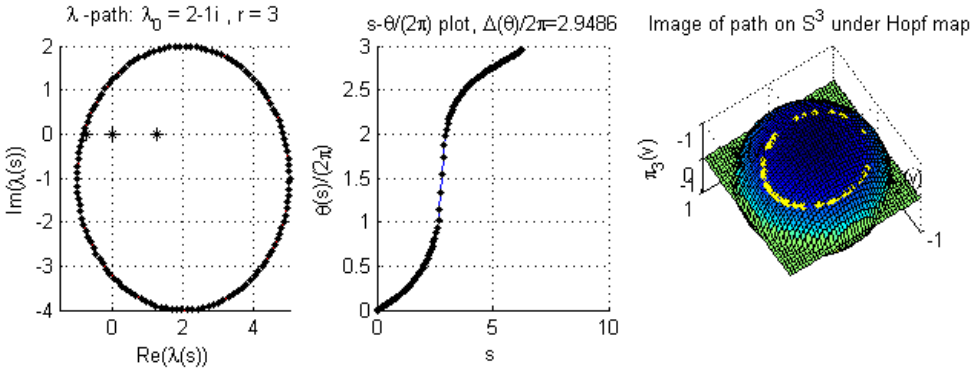

Figure 5.40: $\lambda_0 = 2 - i, r = 3.0$

Figure No.	centre of λ-path, λ_0	radius of λ-path, r	No. of system eigenvalues contained within λ-loop	$\Delta\theta/2\pi$
5.27	$1+0.2i$	0.8	1	1.0004
5.28	i	0.8	0	0.02462
5.29	$2+i$	0.8	0	-0.0002
5.30	0	0.8	2	2.0515
5.31	1	0.8	1	0.9923
5.32	$-i$	0.8	0	0.02549
5.33	$-i$	0.5	0	0.00891
5.34	$2-i$	0.8	0	0.000539
5.35	$2-i$	0.5	0	-0.00130
5.36	$2-i$	1.0	0	-0.00043
5.37	$2-i$	1.5	1	1.0115
5.38	$2-i$	2.0	1	1.0115
5.39	$2-i$	2.5	2	2.0478
5.40	$2-i$	3.0	3	2.9486

Table 5.3: Summary of numerical results for γ_3 paths shown

- Again, the proximity of the λ-path to the continuous spectrum affects the numerics: the further away the λ-path is from the continuous spectrum, the closer $\Delta\theta$ is to an exact integer. This will be for the same reason as in the γ_1 path case.

- The system is symmetric about the real axis in the λ-plane, as shown in Figures 5.28 and 5.32.

5.3 The central conjecture

Note that the computational procedure developed above applies equally well to systems of complex dimension greater than two, provided one important clarification is first made: the definition of γ_1 paths - which are of course essential for the generation of both γ_2 and γ_3 paths.

Definition 5.3.1. *For $n \geq 2$ let the vector $u_\infty(\lambda) \in \mathbb{C}^n$ be the eigenvector of $A_\infty(\lambda)$ corresponding to the eigenvalue of most negative real part. A γ_1 path is then a path composed entirely of these vectors, just as before.*

This definition is consistent with the test-case above, and has its origins in the Evans function method, where the subspace of solutions bounded as $x \to \infty$ is required for the numerical procedure. Now, the numerical results presented here for the test-case are very striking and lead us to propose the following conjecture:

> *For an eigenvalue problem $u_x = A(x, \lambda)u$ in $\mathbb{C}^n$ with the asymptotic structure described above (e.g. in (1.2)), the phase change $\Delta\theta/2\pi$ associated with a γ_3 path is equal to the number of discrete eigenvalues of the system contained within the loop in λ-space from which the γ_3 path is generated, provided the λ-path does not pass through any system eigenvalues or regions of continuous spectrum.*

Recall, the phase change $\Delta\theta$ is a measure of the motion (spinning) required in the fibres of the Hopf bundle to keep the path induced on S^{2n-1} by spherical projection of the γ_3 path horizontal w.r.t. the natural connection. That this seemingly obscure quantity $\Delta\theta/2\pi$ should be an integer, and moreover that this integer should be linked to a fundamental system property such as the presence or absence of a discrete eigenvalue is very interesting. It shows that the solution of $u_x = Au$ in this manner gives rise to a kind of λ-space-dependent differential evolution of the spinning in the fibres of the induced Hopf bundle, which is revealed in the integration of the natural connection form along paths derived from closed loops in λ-space.

Remark 5.3.1. *Furthermore, $\Delta\theta$ can be viewed as a holonomy of the Hopf bundle. To see this, reverse the perspective on the whole scenario: begin with the paths on the base manifold S^2 and observe that with each of these is associated a quantity $\Delta\theta$, which represents the shift in the fibre resulting from traversing the projection of the γ_3 path on S^3. But this quantity depends not only on the start and finish points of the paths, but on the specific paths taken on the base: two paths on S^2 which start and finish at exactly the same point will yield different values of $\Delta\theta$ if the numbers of discrete system eigenvalues encircled by the underlying loops in λ-space are different.*

Remark 5.3.2. *The concept of holonomy occurs frequently in physics, giving rise to various phase quantities similar to that considered here, induced by either given dynamics on a system space or the underlying geometry of the system space itself. In particular, we have the Berry phase of quantum physics [31], [32], [33], and the geometric phase of classical mechanics [32], [34], [35]. The latter is closely linked to the content of this thesis; in fact the phase calculated here is an example of a "reconstruction phase" (e.g. [14] p.168) of an equivariant dynamical system.*

Now, the phase change quantity here has been developed purely by considering solutions to ODEs in relation to an intrinsic Hopf bundle framework, and computing an associated bundle-theoretic quantity generated by these solutions. However, the similarity with certain previous results cannot be overlooked. In particular, the construction here is strikingly similar to the winding number of the Evans function around a closed contour, due to Alexander, Gardner and Jones [36]. Known as the stability index, this feature of the problem has been studied and applied extensively, and extended by Nii [37] and Austin and Bridges [38]. Although the theoretical foundation of the phase here appears to be very different to previous approaches, it cannot be ignored that we do indeed appear to have found a new algorithm for computing the Chern number of the augmented unstable bundle. If this is the case then the question arises as to what the relative merits of the two methods are. This will be a matter for further research, as will the development of the precise theoretical connection between these two apparently very different approaches to the same problem.

5.4 Further numerical experiments

Further numerical testing confirms that the $\Delta\theta$ result of the central conjecture persists under a variety of conditions, for example if we vary further the radius or centre of the circular path so as to contain different isolated eigenvalues, or different numbers of them, or if we vary L or L' in certain ways (see Section 5.4.2 below).

Note that if the λ-path used to generate a γ_3 path passes through a discrete eigenvalue, the $\Delta\theta$ result does not hold. Figures 5.41-5.43 show what happens in this case, for paths with centre $\lambda_0 = -i$ and radii $r = 0.99, 1.00, 1.01$.

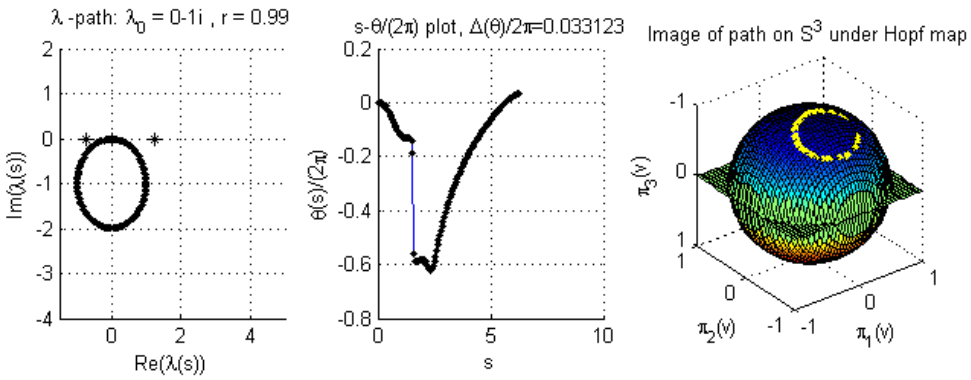

Figure 5.41: $\lambda_0 = -i, r = 0.99$

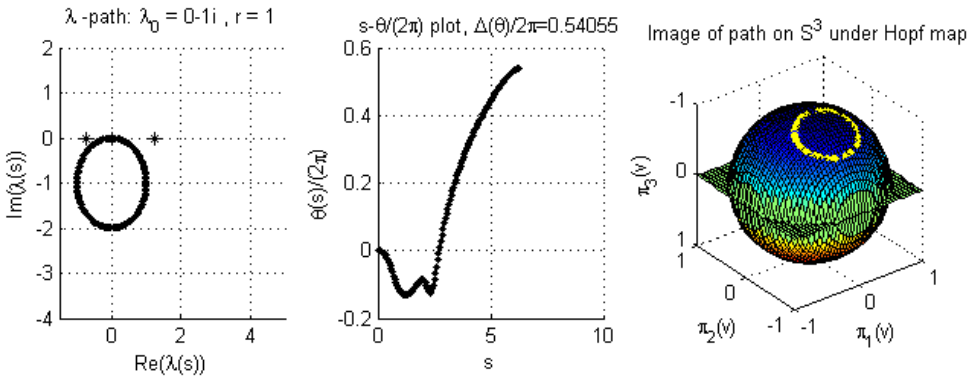

Figure 5.42: $\lambda_0 = -i, r = 1.00$

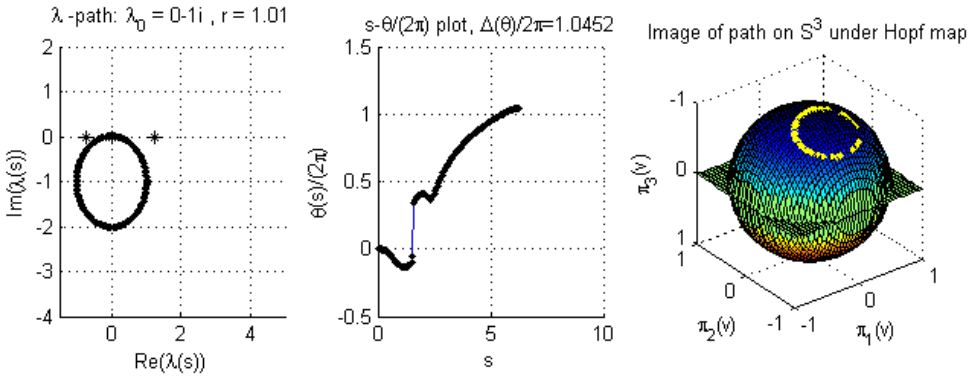

Figure 5.43: $\lambda_0 = -i, r = 1.01$

Figure 5.44 shows what happens when the λ-path passes through the continuous spectrum. In this case, when the branch cut in $\mathbb{C}$ is crossed, it basically reverses

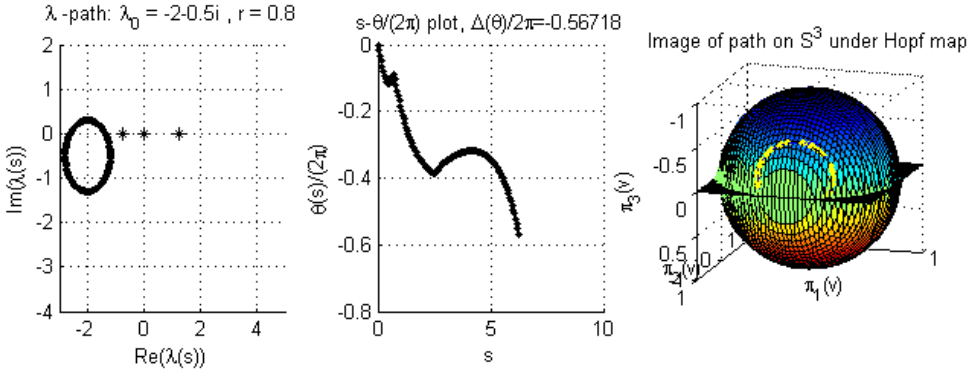

Figure 5.44: $\lambda_0 = -2 - 0.5i, r = 0.8$

the sign of everything: the phase curve gradient is reversed instantaneously (the three distinct segments would form a smooth curve if the latter two were flipped); and the path on S^2, which is traversing the arc shown on the upper hemisphere, instantaneously jumps to a similar arc on the upper hemisphere *on the other side* of the sphere (directly behind where the first arc is, though this can't be seen on the figure here). We now proceed with a few simple modifications of the existing computer code.

5.4.1 Searching for eigenvalues

The program `integration_at_L_prime.m` from Section 5.2.3 has been extended to create an algorithm which, assuming the validity of the central conjecture, searches $\mathbb{C}$ for discrete system eigenvalues by calculating the phase-changes associated with a large number of γ_3 paths parametrized by small circular paths centred at the nodes of a lattice of points in $\mathbb{C}$. The new program, called `lambda_plane_eval_search.m`, produces the graphics shown in Figures 5.45 and 5.46.

The first plot of Figure 5.45 shows the value of $\Delta\theta/2\pi$ (as an asterisk) at each of the lattice nodes, and the small circular paths traversed in parameter space; the second shows $\theta(s)/2\pi$ plotted against s along each of the paths, with all the different plots superimposed upon one another. These figures show clearly how the three eigenvalue-containing loops give $\Delta\theta/2\pi \approx 1$, while all other paths give $\Delta\theta/2\pi \approx 0$. Figure 5.46 shows a contour plot of the same phenomenon (which, although clearly not necessary in this simple case, serves as an introduction to the graphics format used in subsequent numerics where phase results are less apparent). Thus we have a numerical method of searching the complex plane for discrete eigenvalues. Despite its simplicity, this search method has the extremely desirable property of being global in nature, the consequences of which will be seen in the next chapter.

5.4.2 Varying the x-integration range lower limit L'

We briefly show how varying the lower limit, L', of the $u_x = Au$ integration embedded within the phase calculation for paths of type γ_3 affects the value of the resulting phase change $\Delta\theta$. The Matlab code `varying_L_prime.m` calculates the phase associated with paths of type γ_3 for a whole range of values of L', from L right down to $-L$, then plots these against the resulting $\Delta\theta/2\pi$ values, as shown in Figure 5.47. The numerical results show that when L' is near L (here $L = 10$) the phase result is roughly the same as the phase result for a γ_1 path, i.e. $\Delta\theta \approx 0$,

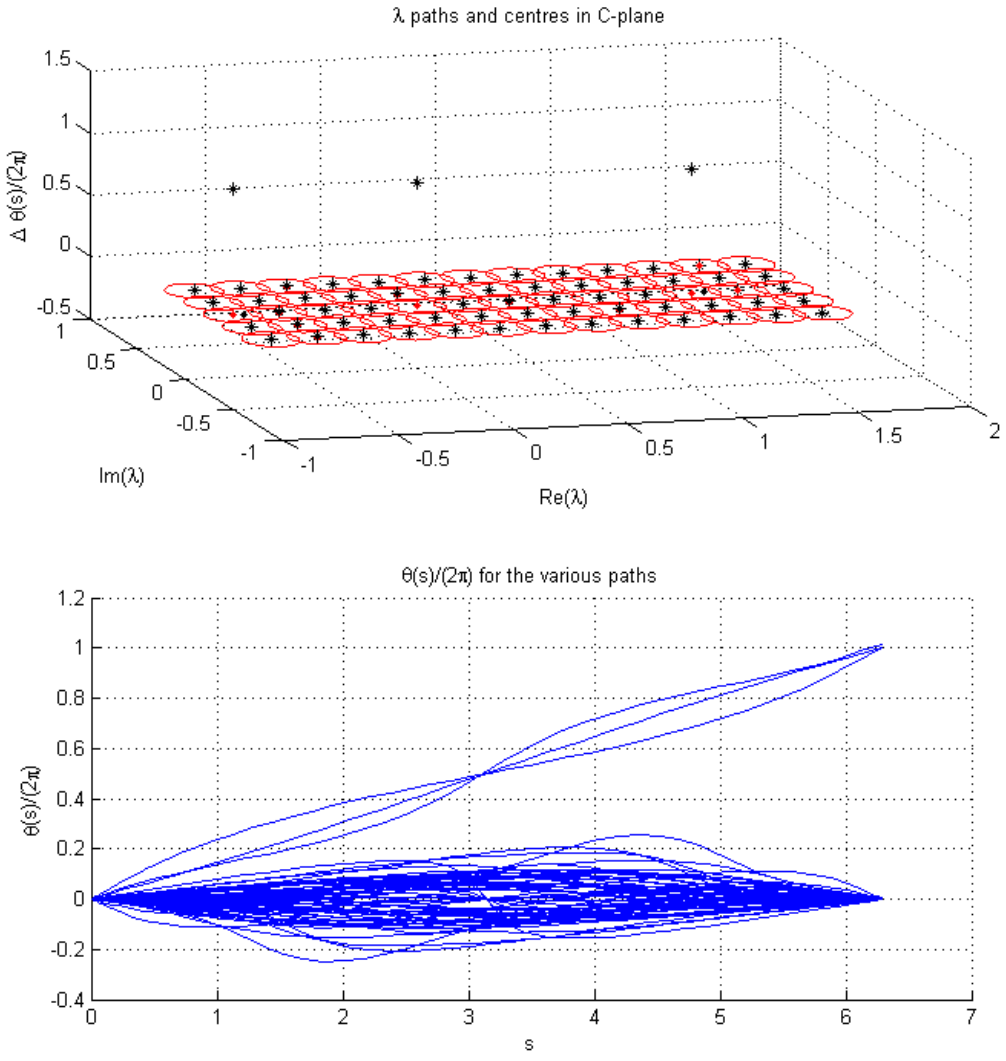

Figure 5.45: Searching $\mathbb{C}$ for discrete eigenvalues

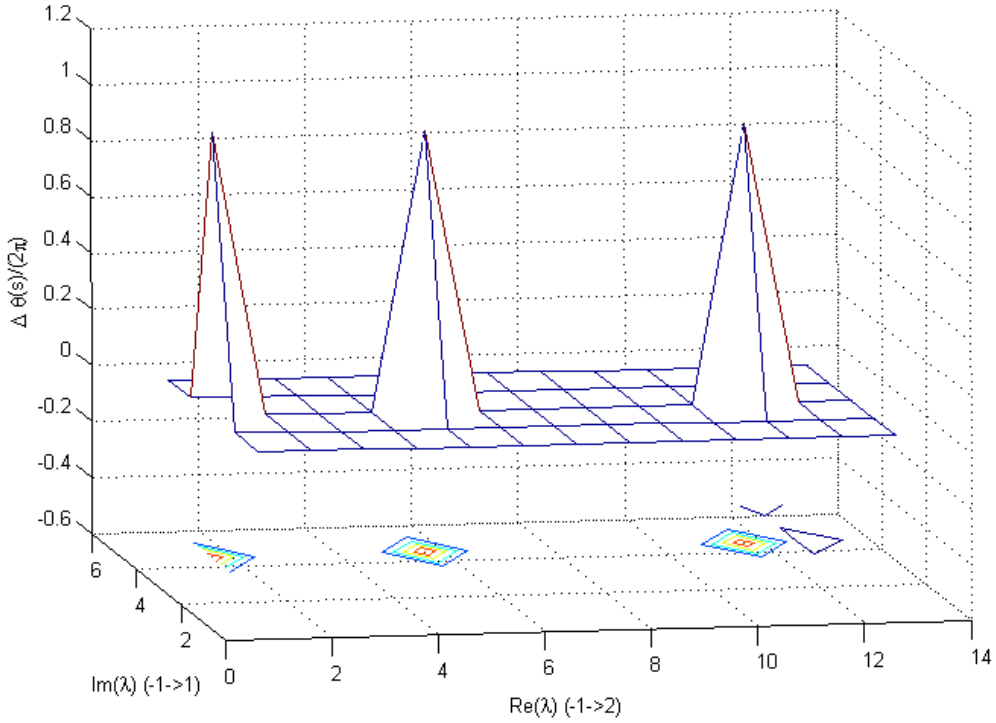

Figure 5.46: Searching $\mathbb{C}$ for discrete eigenvalues, contour plot.

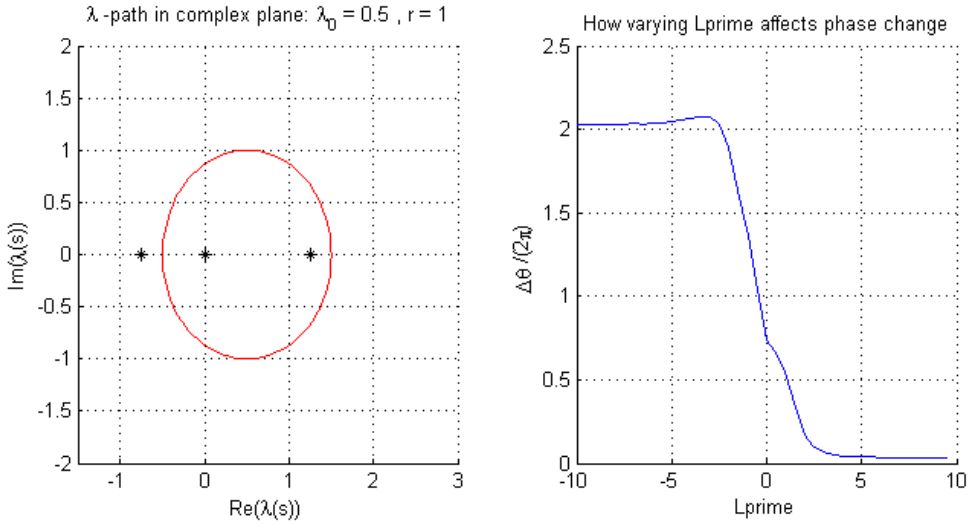

Figure 5.47: Results of varying L'. $\lambda_0 = 0.5, r = 1.0$.

while for values of L' near $-L$ the result is roughly the same as for the original γ_3 paths, with $L' = -L$. Situated about the value $L' = 0$ is a region of gradual transition from one regime to the other. Investigating the causes behind the shape of this curve could eventually be a subject for further study beyond this thesis, with obvious potential benefits for the computational speed of the Matlab codes used in this chapter or any programs derived therefrom.

This concludes our series of phase computations for the test-case, and paves the way for implementing phase computations in more complex, less-well understood systems and investigating further the validity of the central conjecture.

Chapter 6

Phase computations in a variety of systems

In this chapter we extend the concepts developed in the previous chapter by describing and presenting the results of a selection of numerical experiments involving phase curves for a range of eigenvalue systems of the same form as the test-case. The systems considered are:

- The Hocking-Stewartson pulse solution of the complex Ginzburg-Landau equation,
- The Rayleigh equation,
- The one-dimensional time-independent Schrödinger equation with a Morse potential.

6.1 The Hocking-Stewartson pulse

In [5], Afendikov and Bridges consider the complex Ginzburg-Landau equation in the scaled form

$$\rho e^{i\psi} A_t = A_{xx} - (1 + i\omega)^2 A + (1 + i\omega)(2 + i\omega)|A|^2 A \tag{6.1}$$

where $A(x, t)$ is complex-valued and $\rho > 0$, ω and ψ are given real parameters; and its Hocking-Stewartson pulse solution

$$A(x, t) = (\cosh x)^{-1-i\omega} \tag{6.2}$$

They formulate the linear stability problem for such a solution in terms of the Evans function. Their analysis results in an asymptotically constant 6-dimensional complex

linear system depending on the spectral parameter for the problem $\lambda \in \mathbb{C}$. Using the notation developed in this work, we write their system in our usual format as

$$u_x = A(x,\lambda)u, \qquad x \in \mathbb{R},\ \lambda \in \mathbb{C},\ u(x,\lambda) \in \mathbb{C}^6 \tag{6.3}$$

with

$$A(x,\lambda) = \begin{pmatrix} 0 & 0 & 1 & -1 & 0 & 0 \\ a_{32} & 0 & 0 & 0 & 0 & 0 \\ a_{42} & 0 & 0 & 0 & 0 & 1 \\ -a_{31} & 0 & 0 & 0 & 0 & -1 \\ -a_{41} & 0 & 0 & 0 & 0 & 0 \\ 0 & -a_{41} & -a_{31} & -a_{42} & a_{32} & 0 \end{pmatrix} \tag{6.4}$$

where the a_{ij} depend on x, λ, ρ, ω and ψ. Then

$$A_\infty(\lambda) = \lim_{x\to\pm\infty} A(x,\lambda) = \begin{pmatrix} 0 & 0 & 1 & -1 & 0 & 0 \\ -p(\lambda) & 0 & 0 & 0 & 0 & 0 \\ \tau(\lambda) & 0 & 0 & 0 & 0 & 1 \\ -\tau(\lambda) & 0 & 0 & 0 & 0 & -1 \\ p(\lambda) & 0 & 0 & 0 & 0 & 0 \\ 0 & -p(\lambda) & \tau(\lambda) & -\tau(\lambda) & -p(\lambda) & 0 \end{pmatrix} \tag{6.5}$$

where p and τ now depend on just λ, ρ, ω and ψ, and *not* x. The eigenvector of $A_\infty(\lambda)$ corresponding to the eigenvalue of most negative real part, $\sigma^+(\lambda)$, is (for $\sigma^+ \neq 0$)

$$\xi^+(\lambda) = \begin{pmatrix} 2\sigma^+ \\ -2p \\ (\sigma^+)^2 \\ -(\sigma^+)^2 \\ -2p \\ \sigma^+((\sigma^+)^2 - 2\tau) \end{pmatrix} \tag{6.6}$$

The Matlab code written for the test-case was modified to fit this situation, resulting in the programs

- `integration_at_L_prime_HSpulse.m`
- `lambda_plane_eval_search_HSpulse.m`.

As before, these calculate phases associated with γ_3 paths (which, to reiterate, are generated by integrating $u_x = Au$ from L to $-L$ starting from eigenvectors $\xi^+(\lambda)$).

6.1.1 Numerical results

We consider some of the cases discussed in [5], as defined by parameters ω, ρ, ψ:

Numerics for $\omega = 3$, $\rho = 1/\sqrt{5}$, $\psi = \tan^{-1}(2)$

From [5] it is known that for these parameter values the system has three discrete eigenvalues, all of which are real: a double root at $\lambda = 0$ and two simple roots at $\lambda \approx -7$ and $\lambda \approx +15$. Figure 6.1 shows the result of using

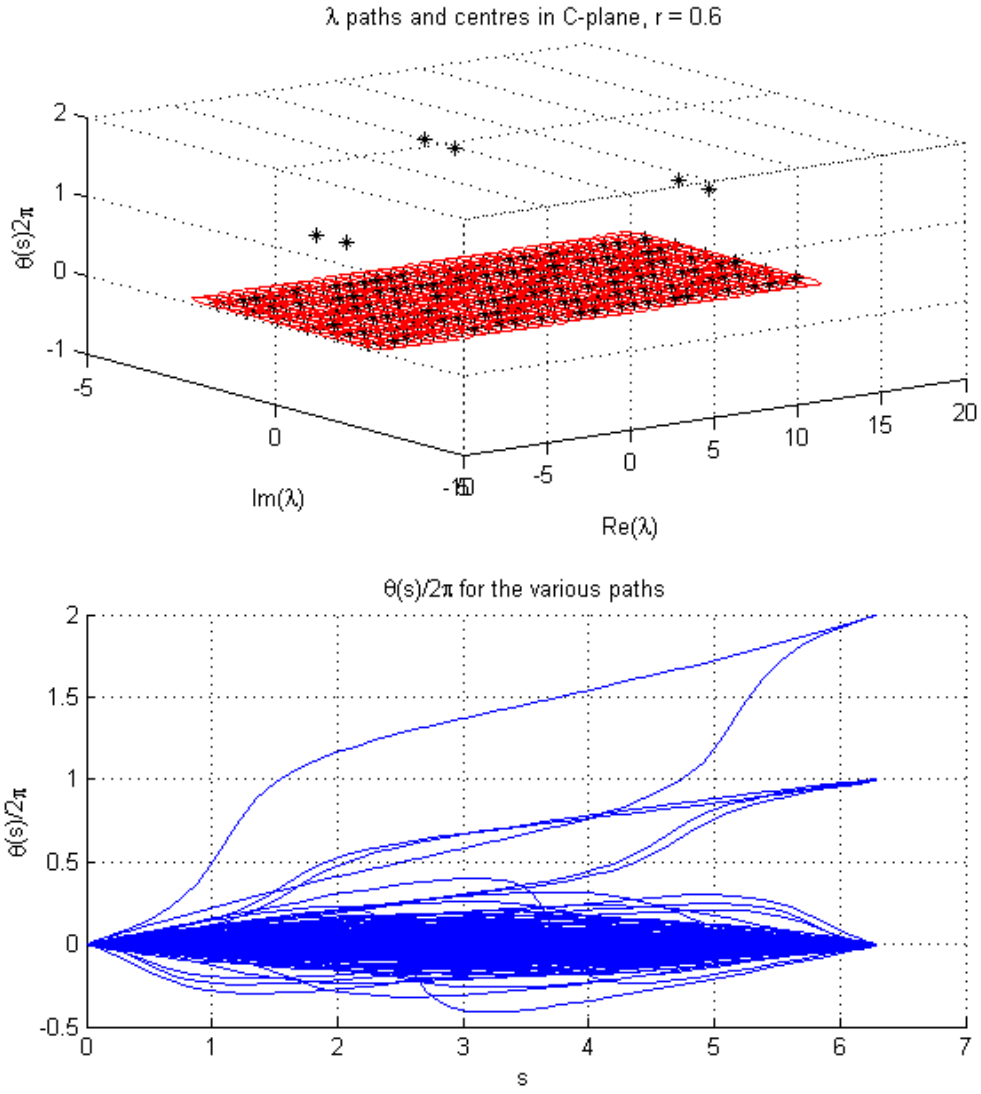

Figure 6.1: Phase change results for a lattice of λ-loops of radius $r = 0.6$, for $\omega = 3$, $\rho = 1/\sqrt{5}$, $\psi = \tan^{-1}(2)$

`lambda_plane_eval_search_HSpulse.m` to evaluate the phases associated with a large number of γ_3 paths generated by circles of radius $r = 0.6$ in λ-space, with

$L = 10 = -L'$ as before. Figure 6.2 shows the corresponding contour plot. These

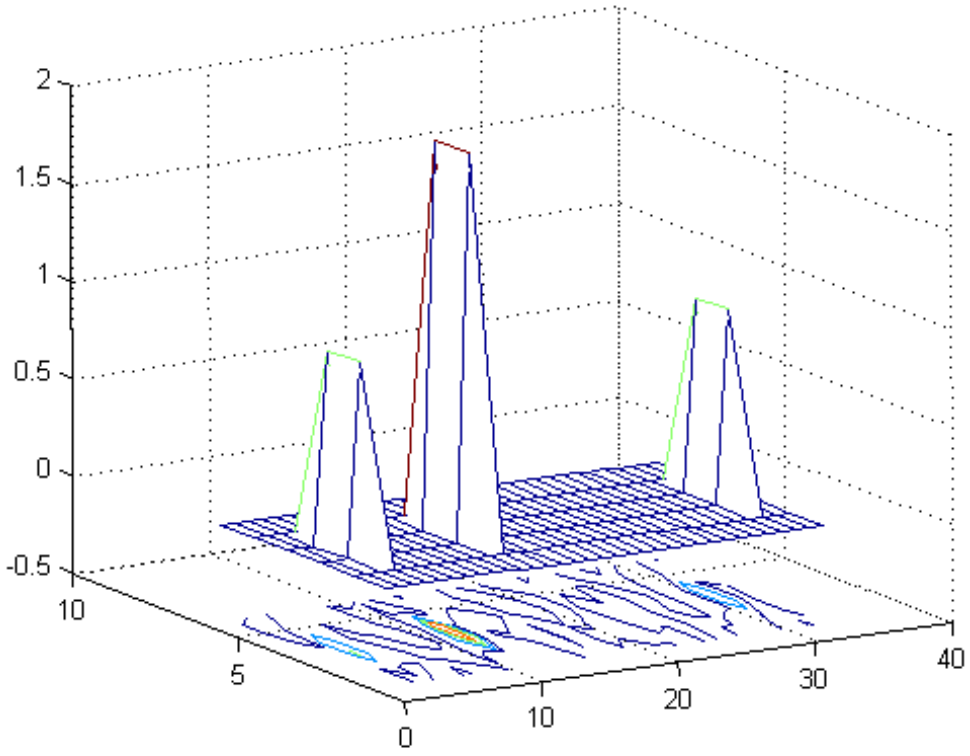

Figure 6.2: Contour plot corresponding to Figure 6.1

show clearly that the phase change associated with a γ_3 path generated by a given λ-loop corresponds precisely to the number of discrete eigenvalues within that loop. Note that here the double root gives a phase value of two, while the other two roots give a phase value of one and all other points give phase values of zero. The width of the peaks is due to the fact that the same discrete eigenvalue may be contained in more than one λ-loop (two in this case); the results produced thus depend not only on the radii of the λ-loops but also on the spacing of the lattice points which are the centres of the λ-loops. Despite these fine-tuning issues, the result here is clear.

We then focused on just the root at $\lambda \approx -7$ by decreasing the mesh size and the radii of the λ-loops and centering the mesh around the point $\lambda \approx -6.6357$, which is the eigenvalue location calculated using the Evans function in [5]. Figure 6.3 shows the results and Figure 6.4 shows the corresponding contour plot. The lattice spacing here is 0.01 and the radius used is $r = 0.006$. The striking new feature of these results is that the phase change values are no longer approximately integers

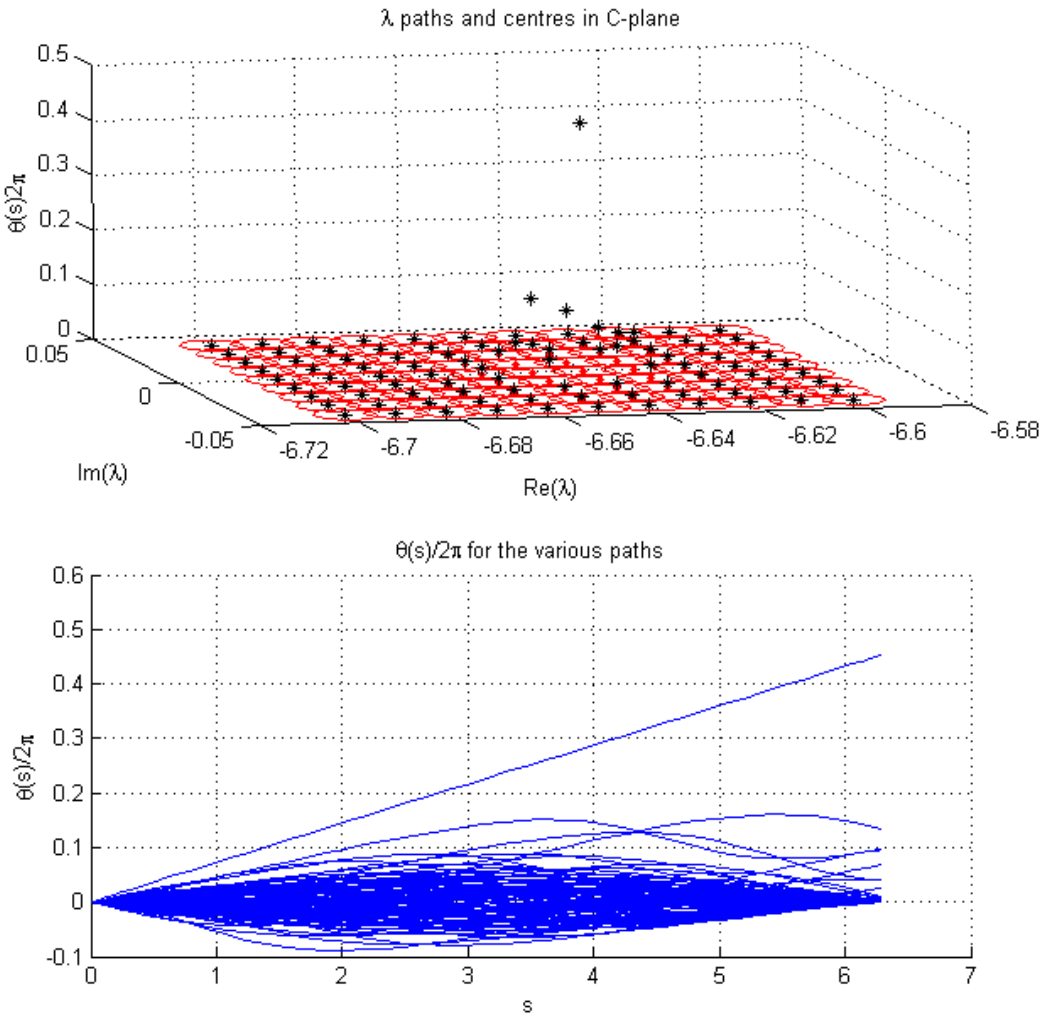

Figure 6.3: Phase change results for a lattice of λ-loops of radius $r = 0.006$, centred about $\lambda \approx -6.66$, for $\omega = 3$, $\rho = 1/\sqrt{5}$, $\psi = \tan^{-1}(2)$

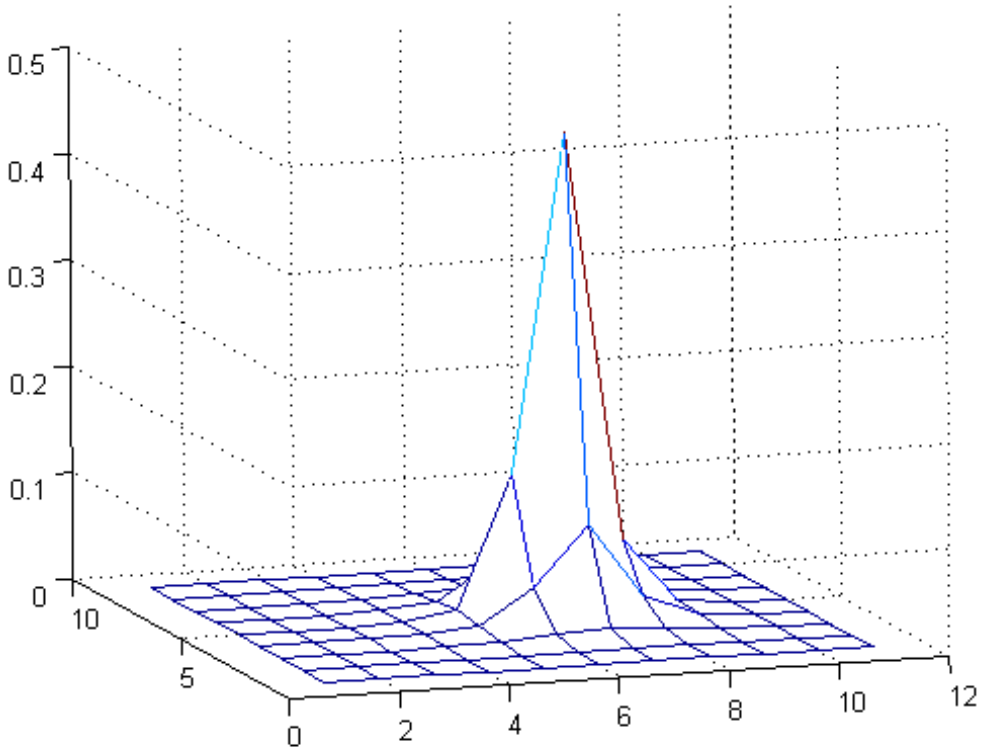

Figure 6.4: Contour plot corresponding to Figure 6.3

as in the previous cases, but occupy a range of values between approximately zero and 0.45. This suggests that the radius of the λ-loops may affect the phase change results after all, which was not seen previously because r was never chosen to be this small. Continuing in this vein, Figures 6.5 and 6.6 show the result of using an even finer mesh and decreasing the λ-loop radius still further, while keeping the lattice centred around the peak in phase values. The mesh spacing is now 0.0005 and the radius is $r = 0.0003$. Note that although the absolute phase values have decreased dramatically and are now of order 10^{-3}, their relative values are consistent with previous plots, and we retain the distinct peak at the same location, which moreover at this scale appears smooth. It should be noted that these numerical results clearly place the peak phase change at the value $\lambda \approx -6.641$ as opposed to the value $\lambda \approx -6.6357$ calculated in [5]; the discrepancy between these two values would be a matter for further research.

Since the dependence of the phase results on the λ-loop radius r, for small r, has been shown to be a matter of great importance in the numerics, we illustrate this relationship in Figure 6.7. The left plot shows several λ-paths encircling the double eigenvalue at $\lambda = 0$, with radii ranging from $r = 0.001$ up to $r = 1$, while the right plot shows the corresponding numerical phase results. These plots show that the phase changes range from approximately zero to approximately two, and that the integer phase result of the central conjecture holds only for $r > 0.01$ in this case. The cause of this deterioration in validity of the result is presently unclear. However, the preservation of the relative structure of the phase values for small r is an interesting result, as this may enable the location of the peak to be determined to as fine a scale as required.

Numerics for $\omega = 2 + \sqrt{5}$, $\rho = 1/\sqrt{5}$, $\psi = \tan^{-1}(2)$

From [5] it is known that for these parameter values the system has a discrete eigenvalue at $\lambda = 0$, which is a triple root of the Evans function. Thus we might expect to see a peak phase change of approximately 3 located at the origin in λ-space, and zero elsewhere. However, the numerical results do not follow this pattern, as shown in Figures 6.8 and 6.9, for which $r = 0.2$. Figures 6.10 and 6.11 have $r = 0.05$ and show a close-up of the region around the origin, where the triple root is believed to exist. Instead of the expected single peak of height 3, the numerics yield three separate peaks, each of phase change 1, one at the origin and one either side of this on the imaginary axis, at approximately $\pm 0.7i$.

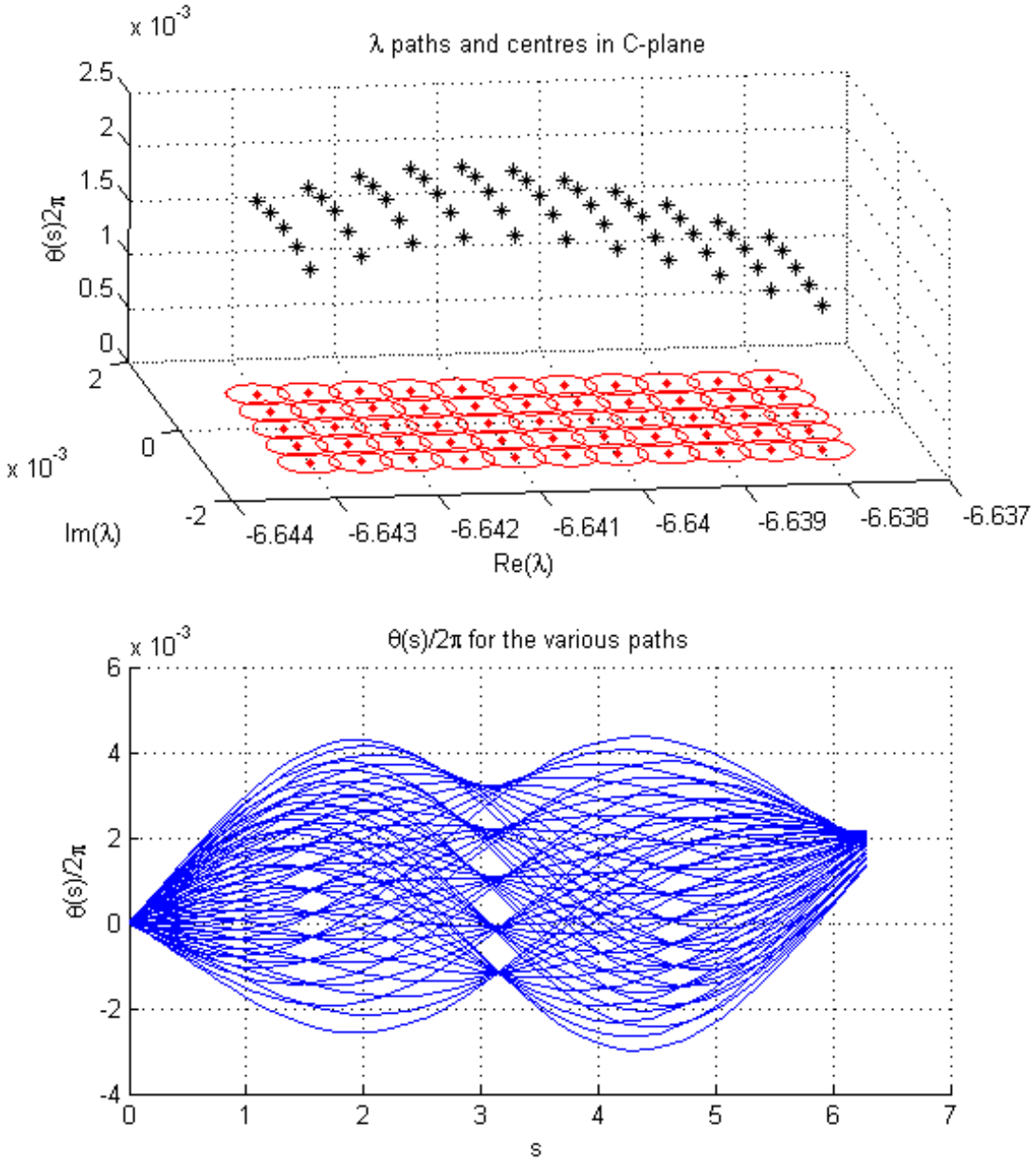

Figure 6.5: Phase change results for a lattice of λ-loops of radius $r = 0.0003$, centred about $\lambda \approx -6.641$, for $\omega = 3$, $\rho = 1/\sqrt{5}$, $\psi = \tan^{-1}(2)$

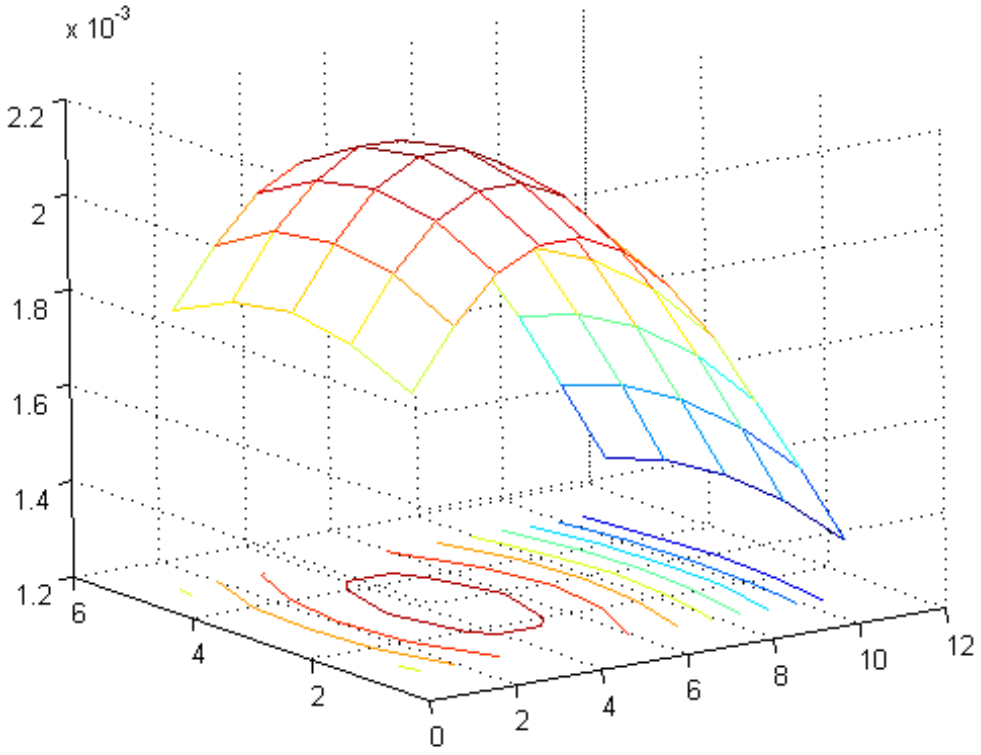

Figure 6.6: Contour plot corresponding to Figure 6.5

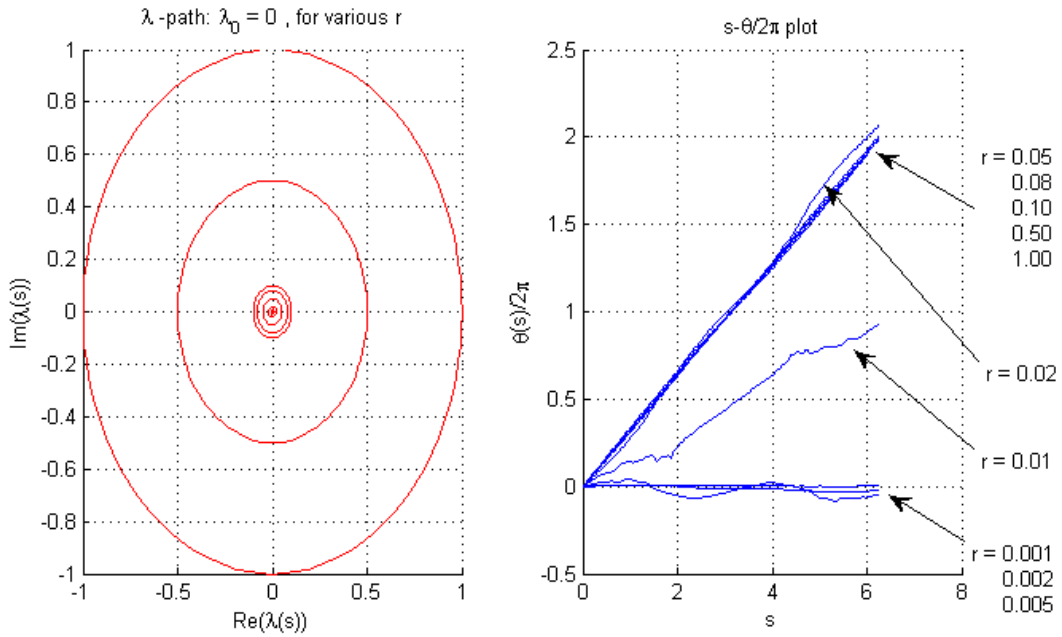

Figure 6.7: λ-paths of various radii encircling the double eigenvalue at the origin (left), and their corresponding phase results (right)

Numerics for $\omega = 0$, $\rho = 1$, $\psi = \pi/2$

For these parameter values equation (6.1) reduces to the nonlinear Schrödinger equation, as stated in [5]. The analytical results for the $\lambda = 0$ case indicate that there is a quadruple eigenvalue at the origin [39], which for small enough perturbations of ω and ψ splits in to a double eigenvalue at the origin plus two simple eigenvalues, $\lambda_1 < 0$ and $\lambda_2 > 0$ [40]. However, the phase numerics we present here are not consistent with this pattern of behaviour. For a large enough λ-loop radius, say $r = 0.3$, we do indeed see a phase change value of approximately 4 at the origin and zero elsewhere, as shown in Figures 6.12 and 6.13. However, this is simply an artifact of the mesh size, for when a finer mesh is used with a smaller loop radius, say $r = 0.02$, the numerics show *four* distinct peaks, each with a phase change of 1, located symmetrically about the origin at $\pm 0.1 \pm 0.1i$, and zero elsewhere. This is shown in Figures 6.14 and 6.15.

Numerics for $\omega = 0.03$, $\rho = 1$, $\psi = \pi/2$

Following on from the previous case, these parameter values represent a small perturbation of the constant ω, as described above. Again however, the phase results

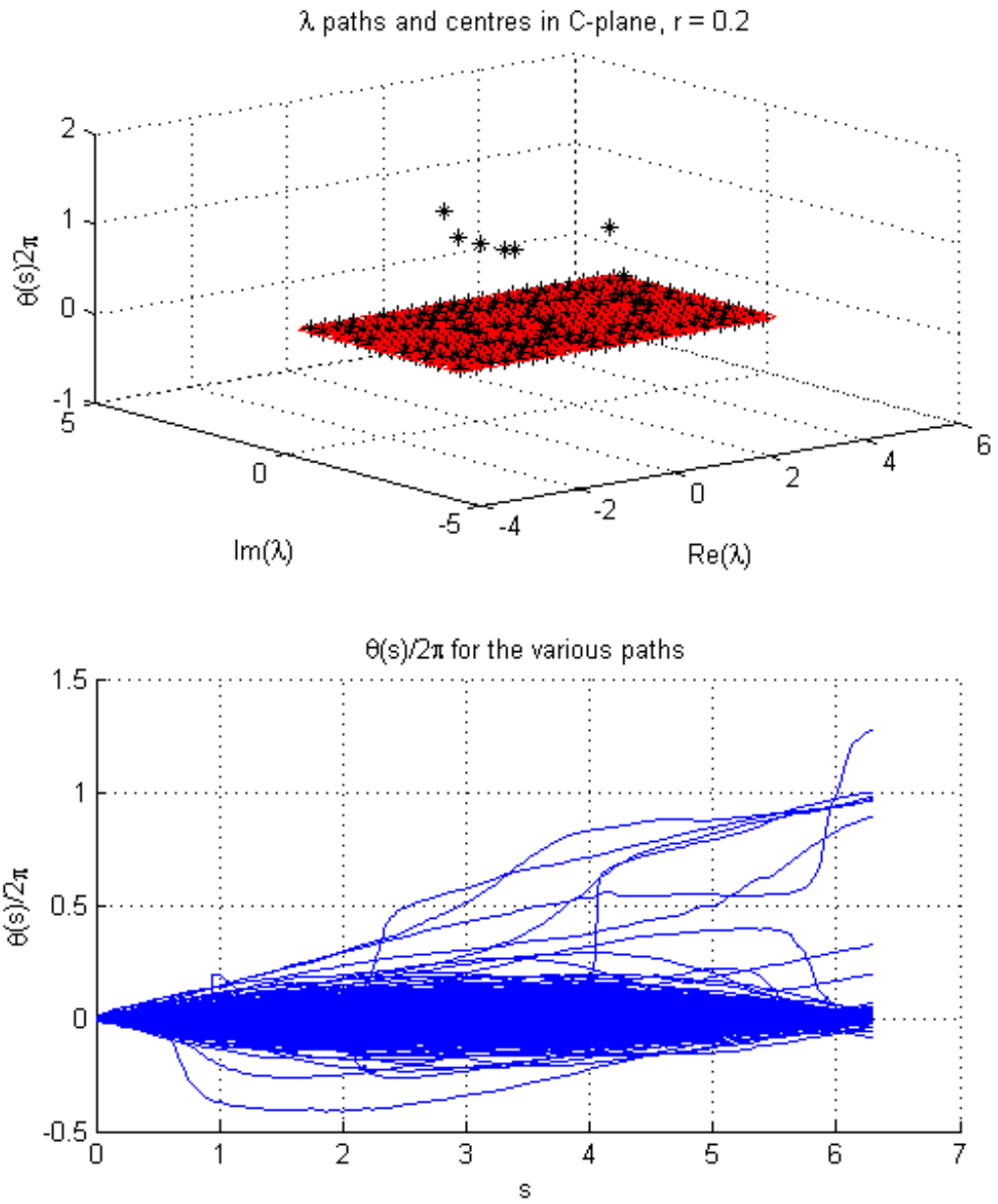

Figure 6.8: Phase change results for a lattice of λ-loops of radius $r = 0.2$, centred about $\lambda \approx 0$, for $\omega = 2 + \sqrt{5}$, $\rho = 1/\sqrt{5}$, $\psi = \tan^{-1}(2)$

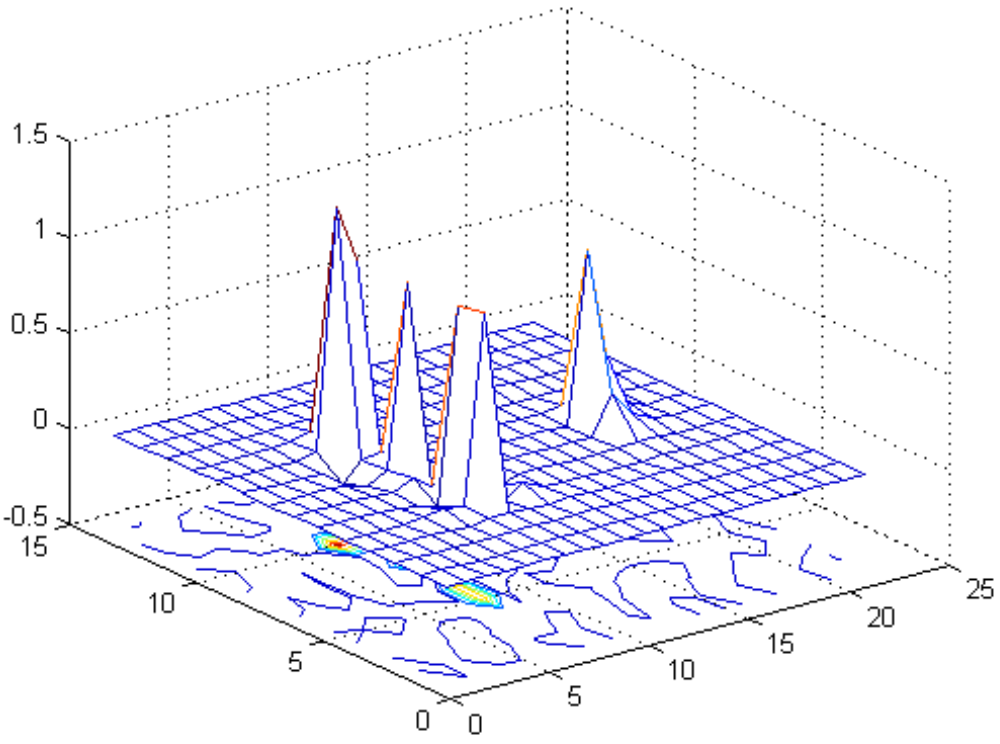

Figure 6.9: Contour plot corresponding to Figure 6.8

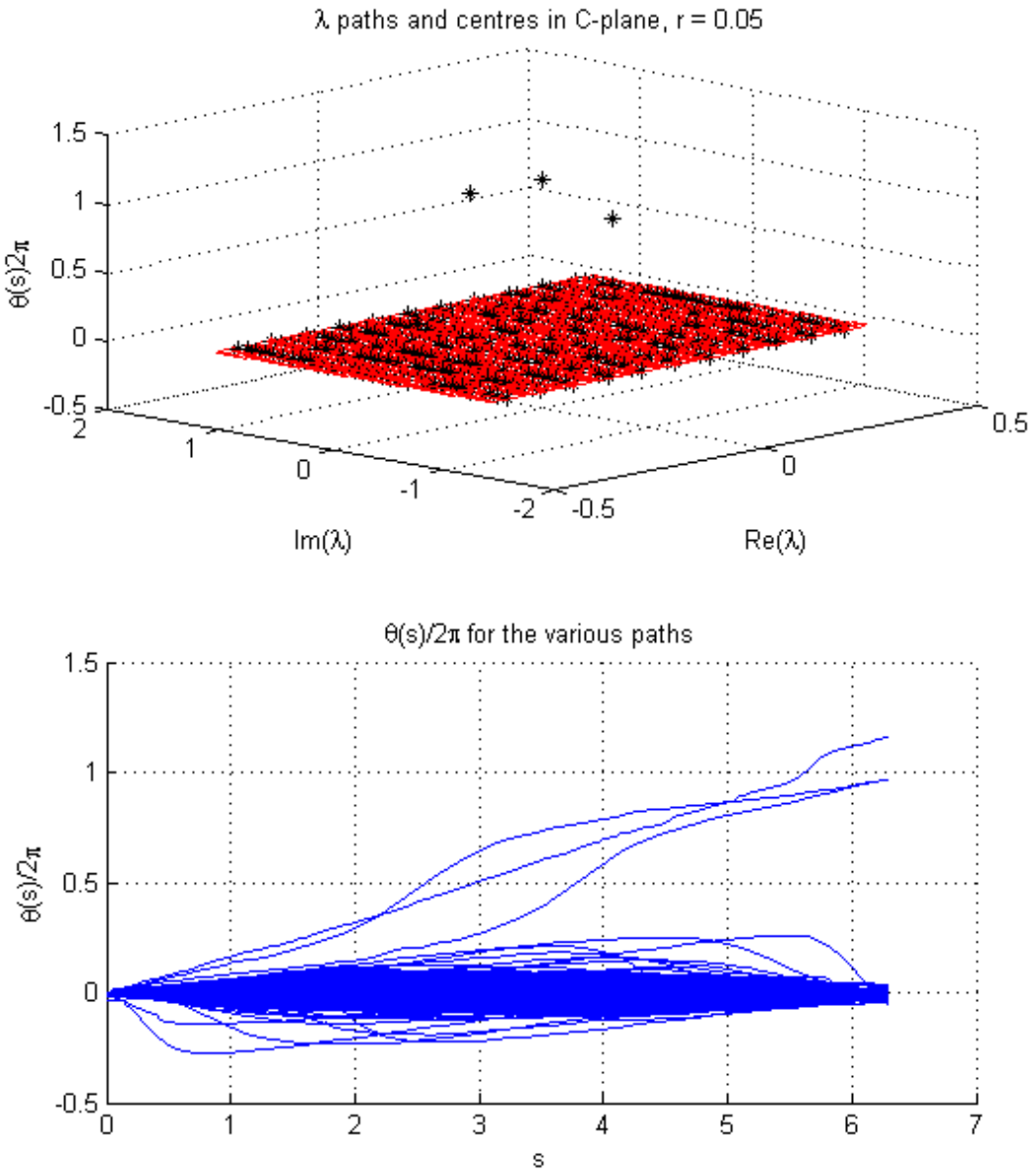

Figure 6.10: Phase change results for a lattice of λ-loops of radius $r = 0.05$, centred about $\lambda \approx 0$, for $\omega = 2 + \sqrt{5}$, $\rho = 1/\sqrt{5}$, $\psi = \tan^{-1}(2)$

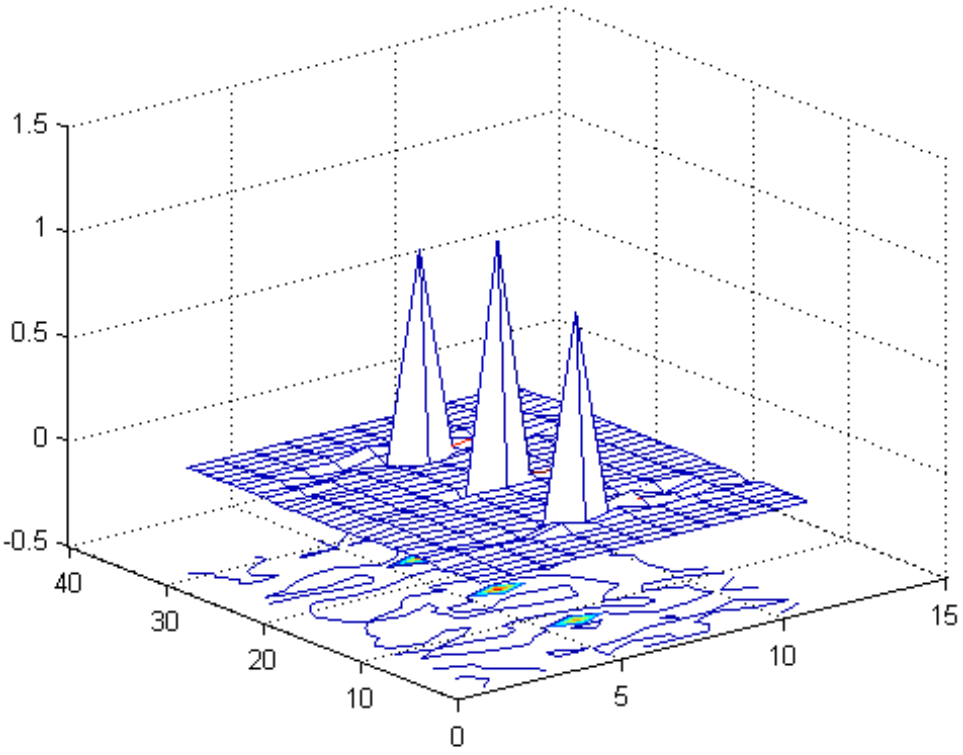

Figure 6.11: Contour plot corresponding to Figure 6.10

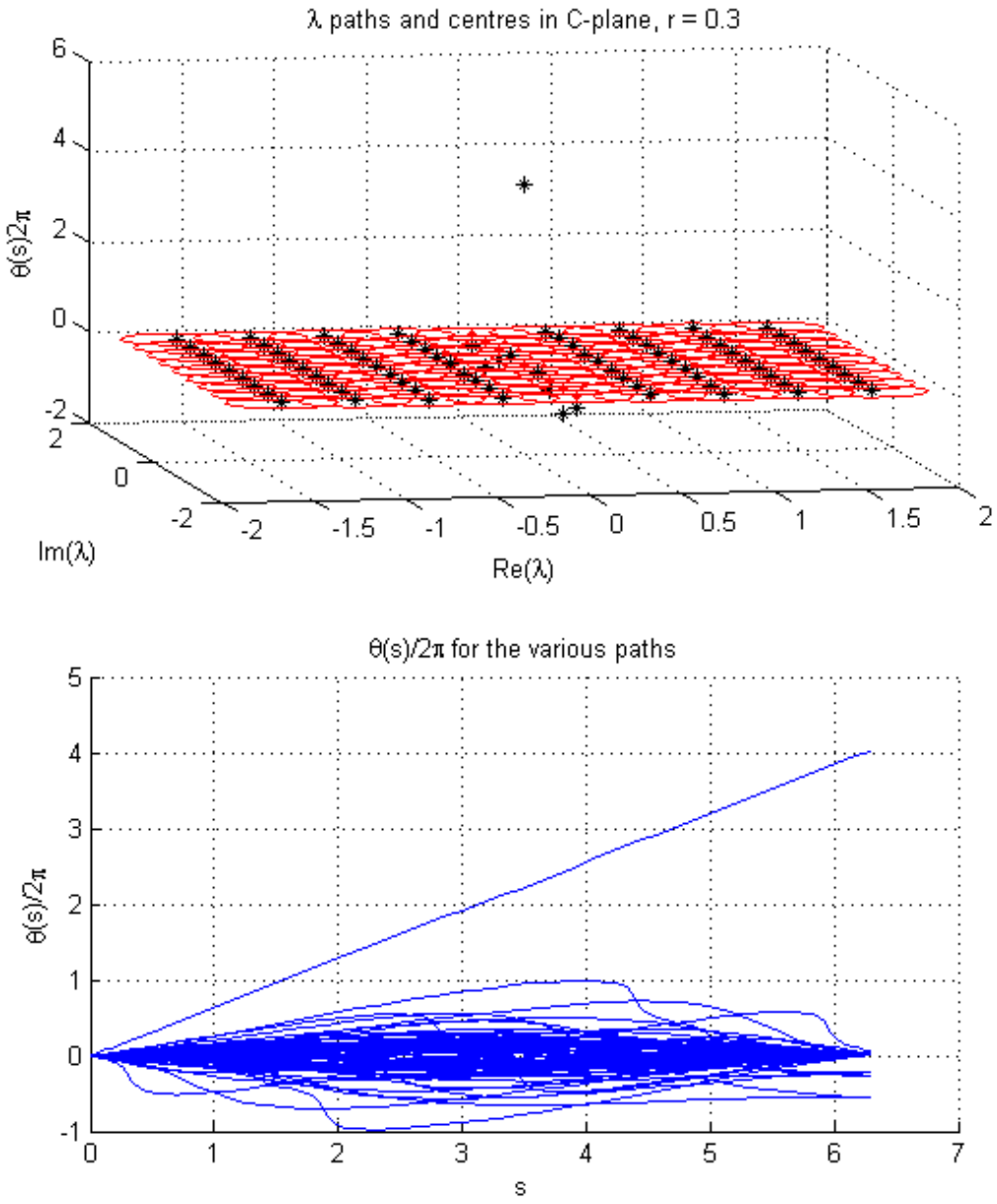

Figure 6.12: Phase change results for a lattice of λ-loops of radius $r = 0.3$, centred about $\lambda \approx 0$, for $\omega = 0$, $\rho = 1$, $\psi = \pi/2$

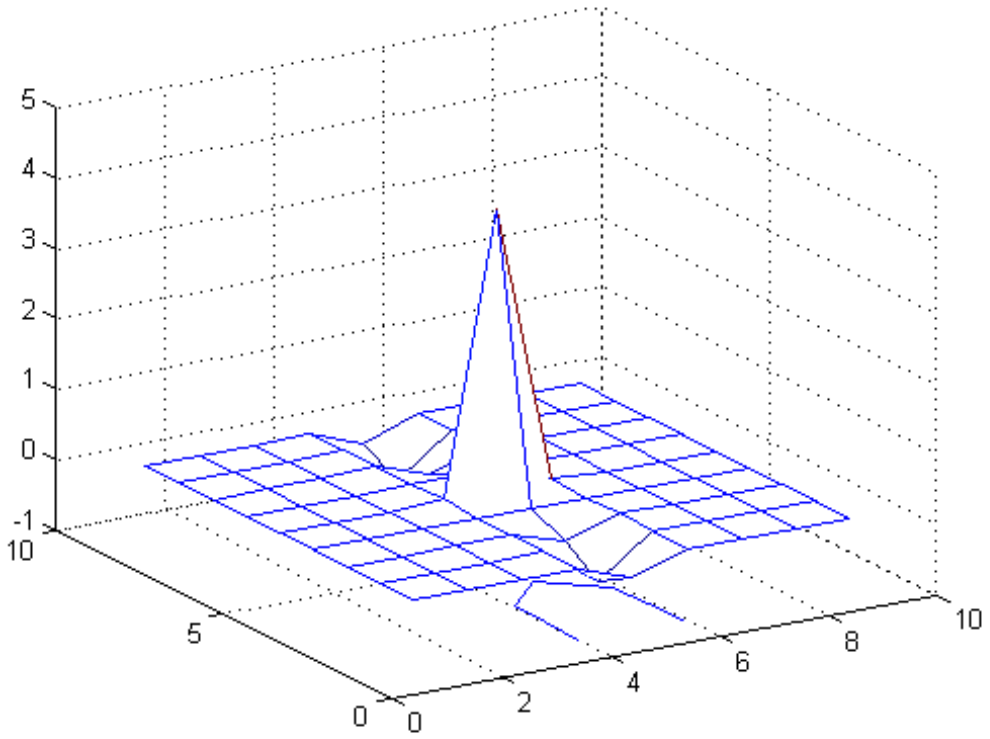

Figure 6.13: Contour plot corresponding to Figure 6.12

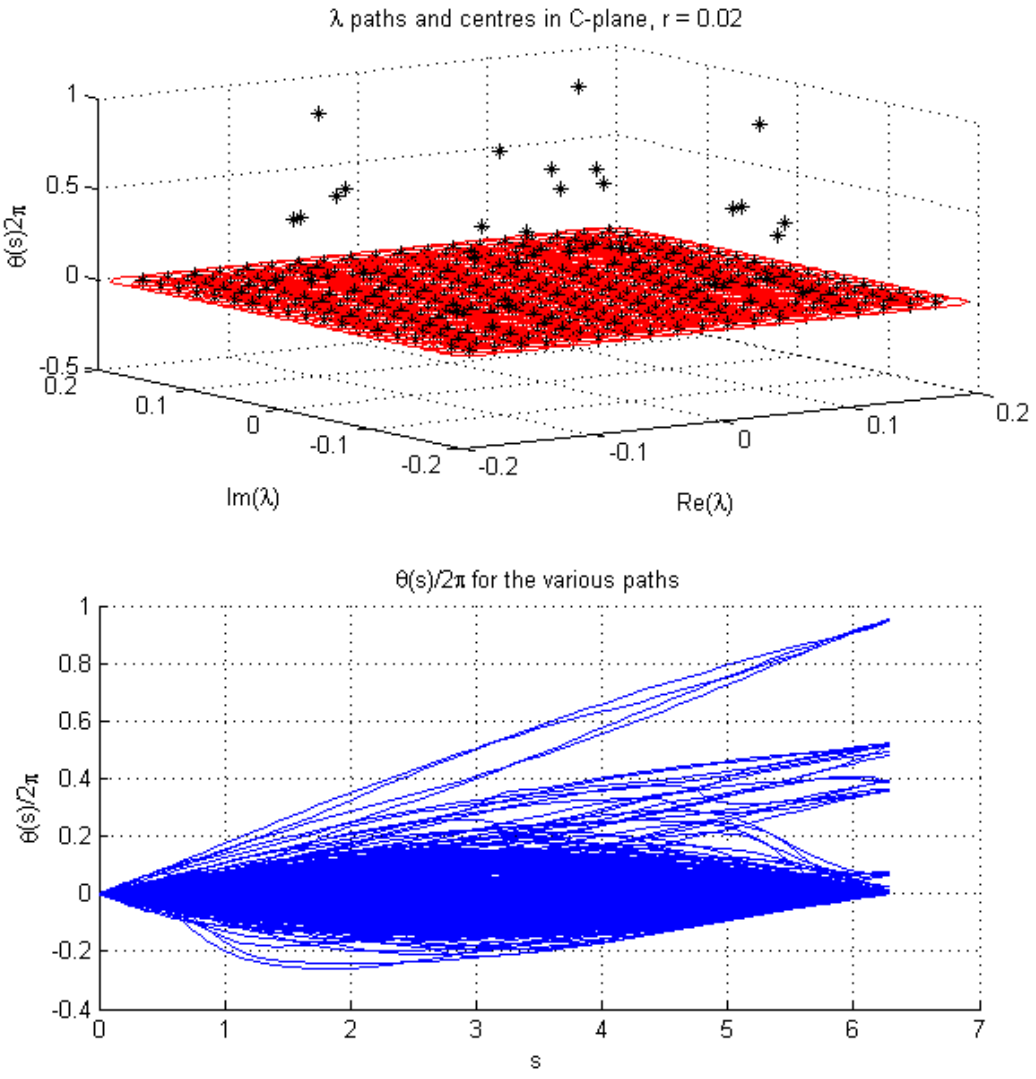

Figure 6.14: Phase change results for a lattice of λ-loops of radius $r = 0.02$, centred about $\lambda \approx 0$, for $\omega = 0$, $\rho = 1$, $\psi = \pi/2$

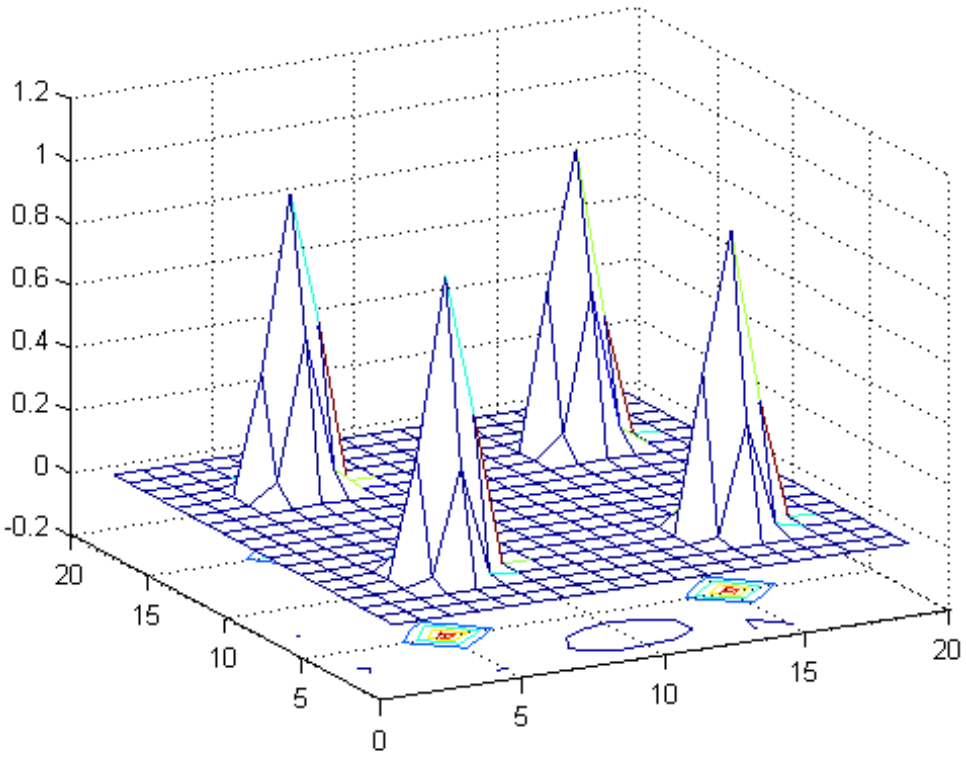

Figure 6.15: Contour plot corresponding to Figure 6.14

here do not display the same behaviour as described in [5]; instead of either the splitting described above or the triple root identified in [5] by the Evans function method, we see the two peaks in the left half-plane persist in a similar state to the $\omega = 0$ case, while in the right half-plane we now see a peak of height 2 on the real axis, as if the two separate right-half-plane peaks of the $\omega = 0$ case have coalesced. Figures 6.16 and 6.17 show these results, while Figure 6.18 shows a close-up contour plot of the two left-half-plane peaks. Figures 6.19, 6.20 and 6.21 show contour plots for $\omega = 0.028$, 0.029 and 0.0295, illustrating what happens in between the two $\omega = 0$ and $\omega = 0.03$ cases just presented. These results confirm that the two right-half-plane peaks do in fact coalesce to form a double-height peak as ω increases from zero. However, a more detailed investigation indicates that the value of ω at which the coalescence occurs is a little higher than 0.03, nearer to 0.0309, above which the two peaks split again, but now remain on the real axis. This is shown in Figures 6.22 and 6.23.

Numerics for $\omega = 0.5$, $\rho = 0.5$, $\psi = 2$

Since none of the published cases featured above, against which our numerics have been compared, involve known discrete eigenvalues with nonzero complex part, we present data for one final parameter set, in order to demonstrate some of the strange phase change patterns our programs may generate far away from the real axis for the HS pulse system. Figures 6.24-6.26 show the phase results for a narrow strip around the imaginary axis. Note that the $\mathrm{Re}(\lambda)$ axis for the lattice of points ranges from only -1.4 to +1.4, while the $\mathrm{Im}(\lambda)$ axis ranges from -15 to +15, which results in the stretched appearance observed on the diagrams. There is clearly some very strange behaviour exhibited in these results, unlike any seen previously. The two contour plots show a double-height peak at the origin and strange wave-like patterns symmetrical about the real axis, including two symmetrical single-height peaks. The only exception to this symmetry is the peak in the top left corner of the plot, at $\lambda \approx -1+13i$. Indeed, the lower plot of Figure 6.24 confirms that there is one λ-path which yields a phase change of approximately 2, two yielding approximately 1, and one further path yielding a value just above 1. However, for this latter result we see an erratic step change in the phase curve, indicating that the result is erroneous, possibly due to being so close to the lattice edge.

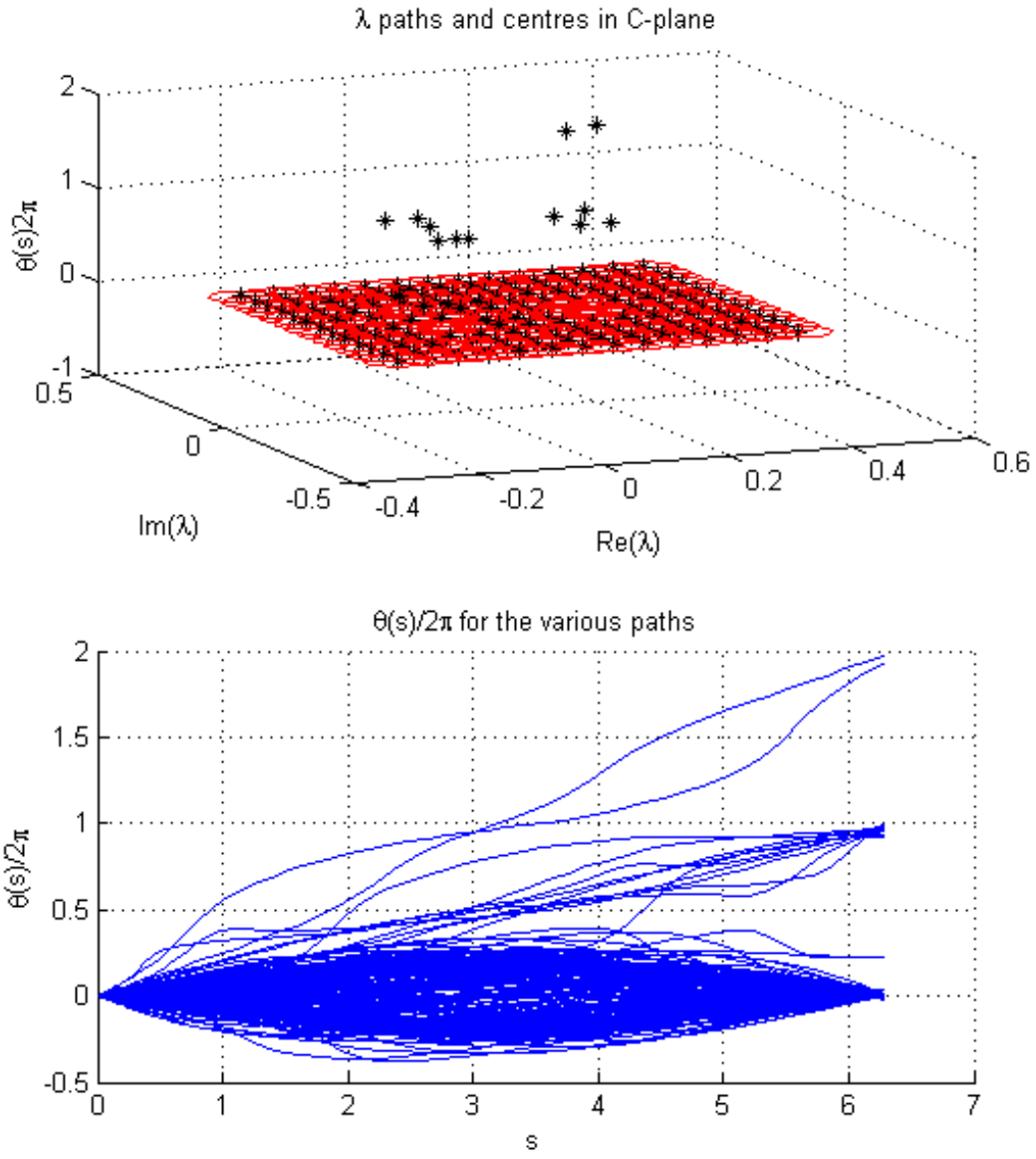

Figure 6.16: Phase change results for a lattice of λ-loops of radius $r = 0.03$, centred about $\lambda \approx 0$, for $\omega = 0.03$, $\rho = 1$, $\psi = \pi/2$

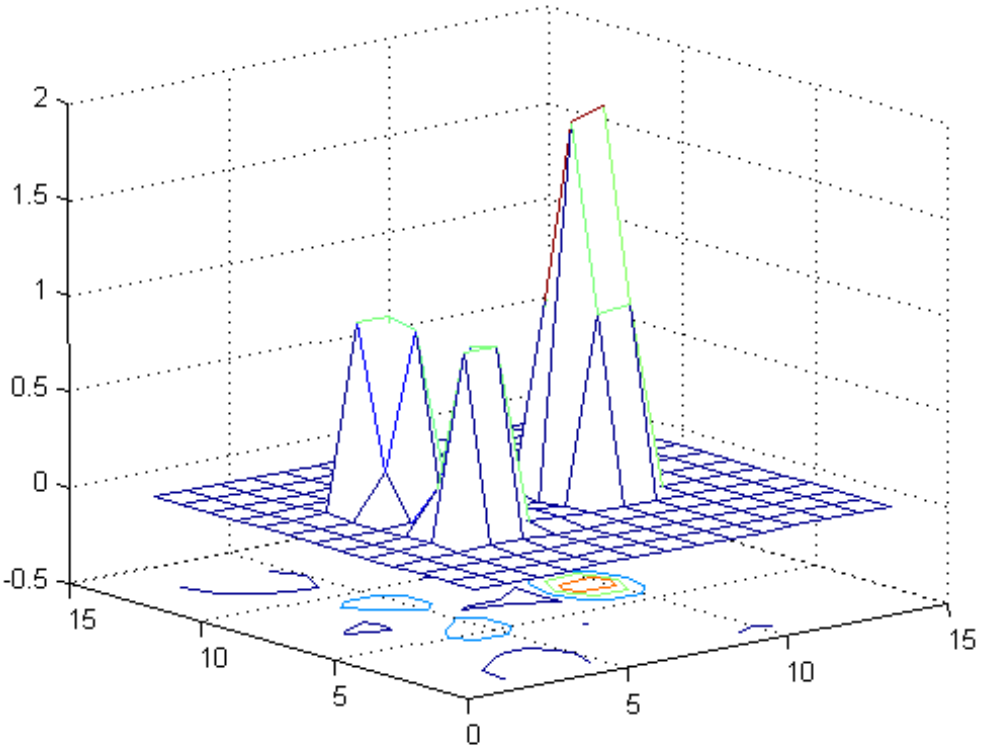

Figure 6.17: Contour plot corresponding to Figure 6.16

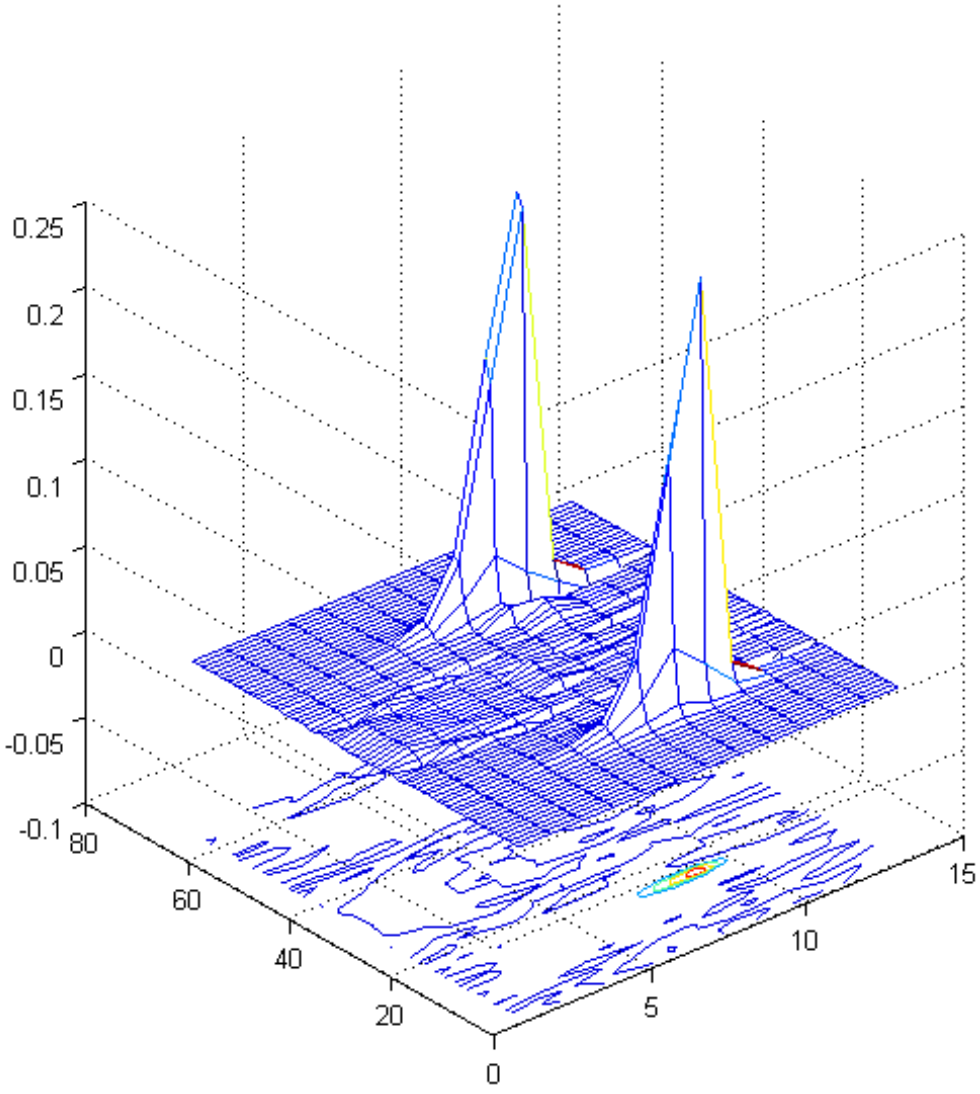

Figure 6.18: Contour plot close-up of the left half-plane of Figure 6.16, with $r = 0.003$

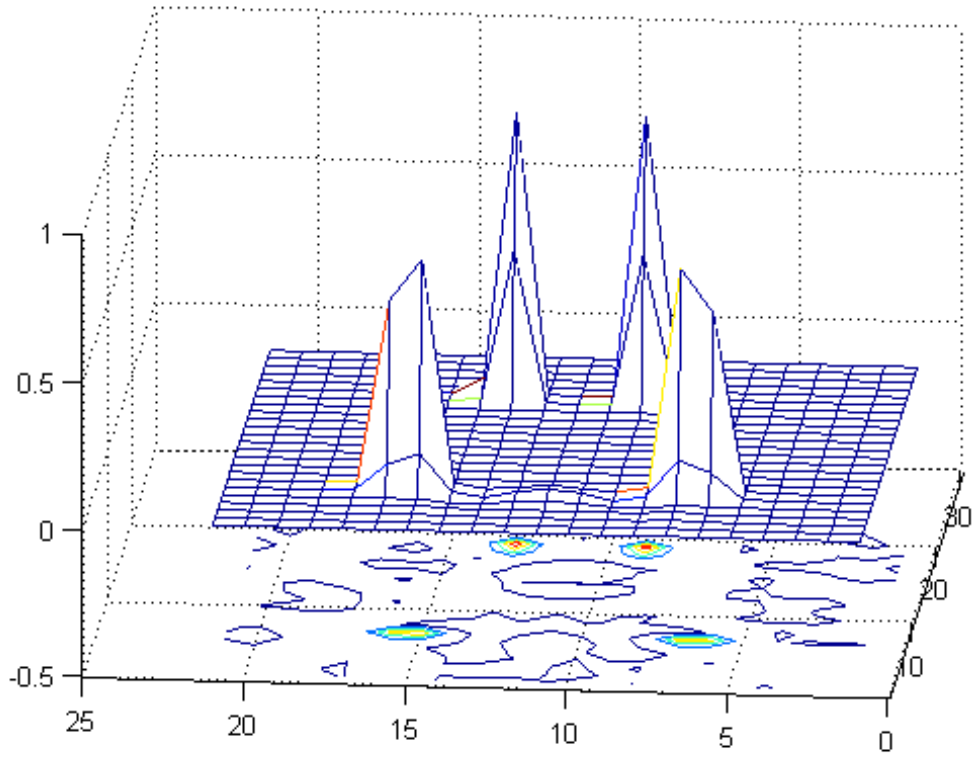

Figure 6.19: Contour plot of phase change results for a lattice of λ-loops of radius $r = 0.014$, centred about $\lambda \approx 0$, for $\omega = 0.028$, $\rho = 1$, $\psi = \pi/2$

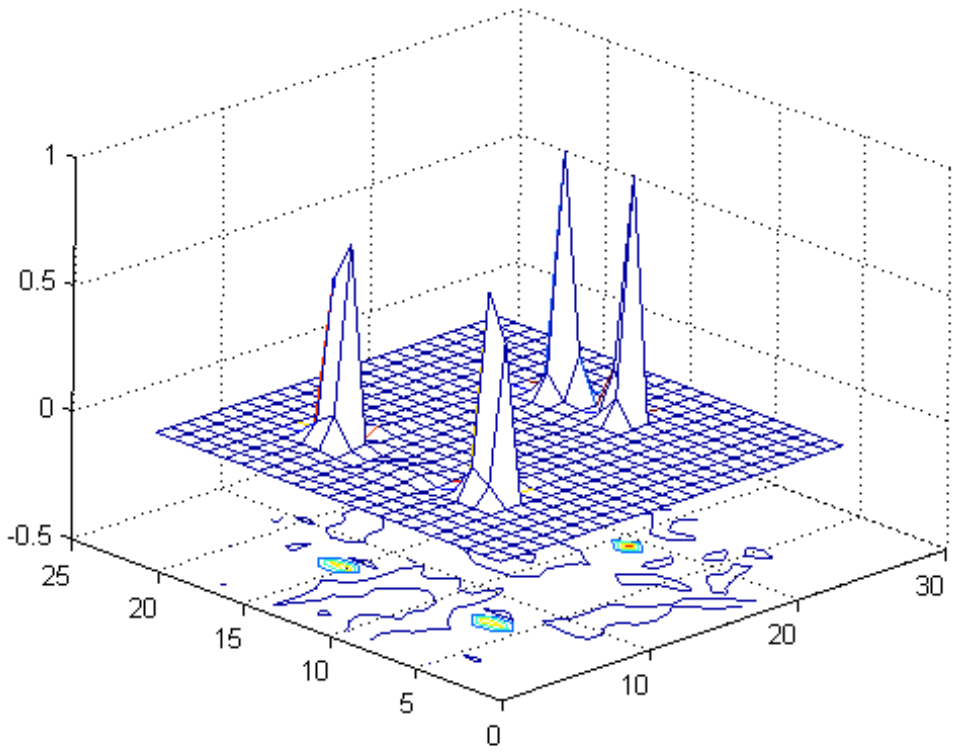

Figure 6.20: Contour plot of phase change results for a lattice of λ-loops of radius $r = 0.014$, centred about $\lambda \approx 0$, for $\omega = 0.029$, $\rho = 1$, $\psi = \pi/2$

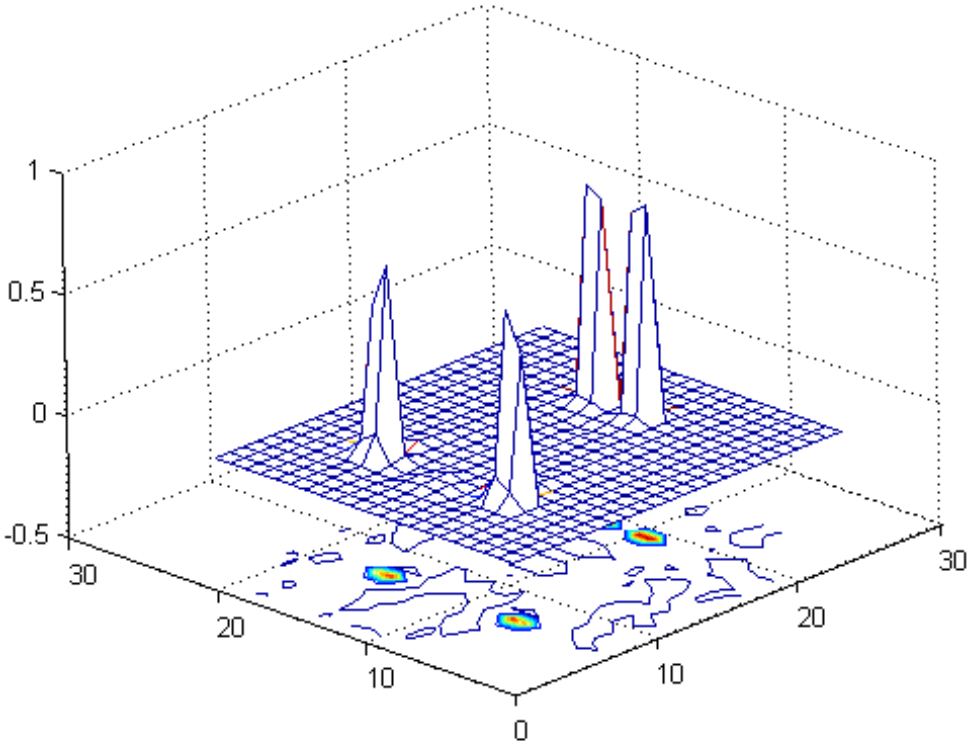

Figure 6.21: Contour plot of phase change results for a lattice of λ-loops of radius $r = 0.014$, centred about $\lambda \approx 0$, for $\omega = 0.0295$, $\rho = 1$, $\psi = \pi/2$

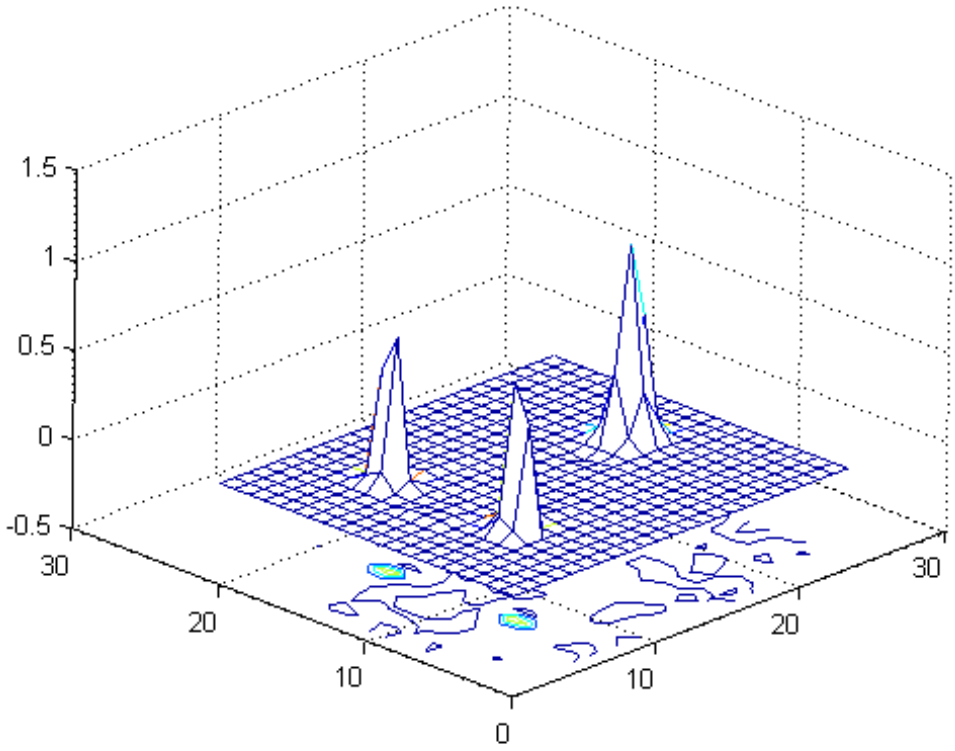

Figure 6.22: Contour plot of phase change results for a lattice of λ-loops of radius $r = 0.014$, centred about $\lambda \approx 0$, for $\omega = 0.0309$, $\rho = 1$, $\psi = \pi/2$

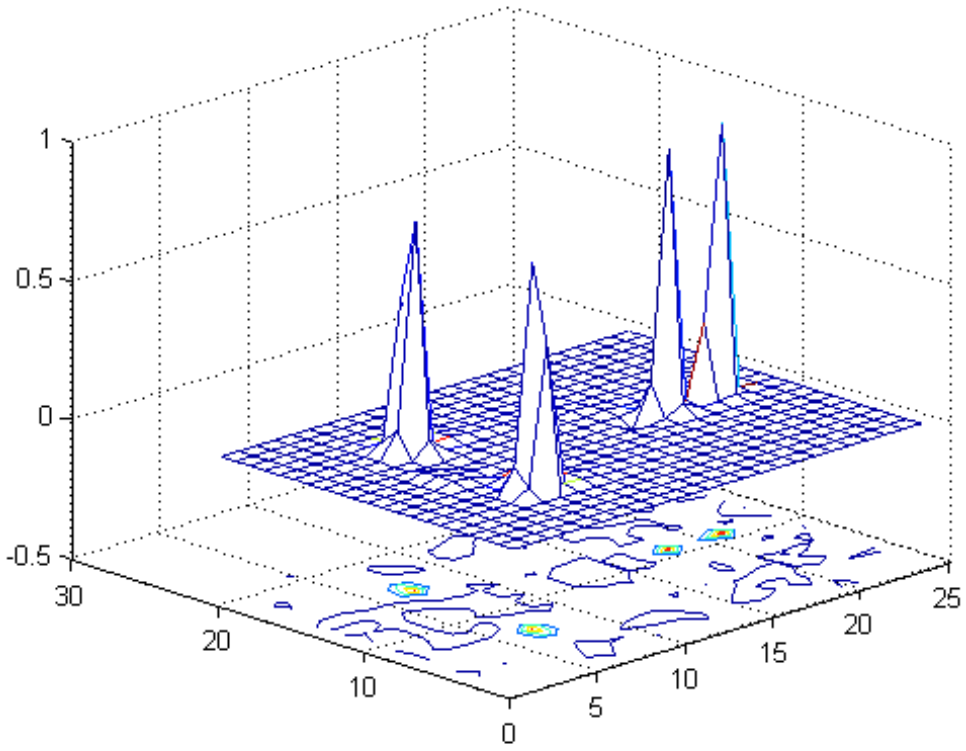

Figure 6.23: Contour plot of phase change results for a lattice of λ-loops of radius $r = 0.014$, centred about $\lambda \approx 0$, for $\omega = 0.032$, $\rho = 1$, $\psi = \pi/2$

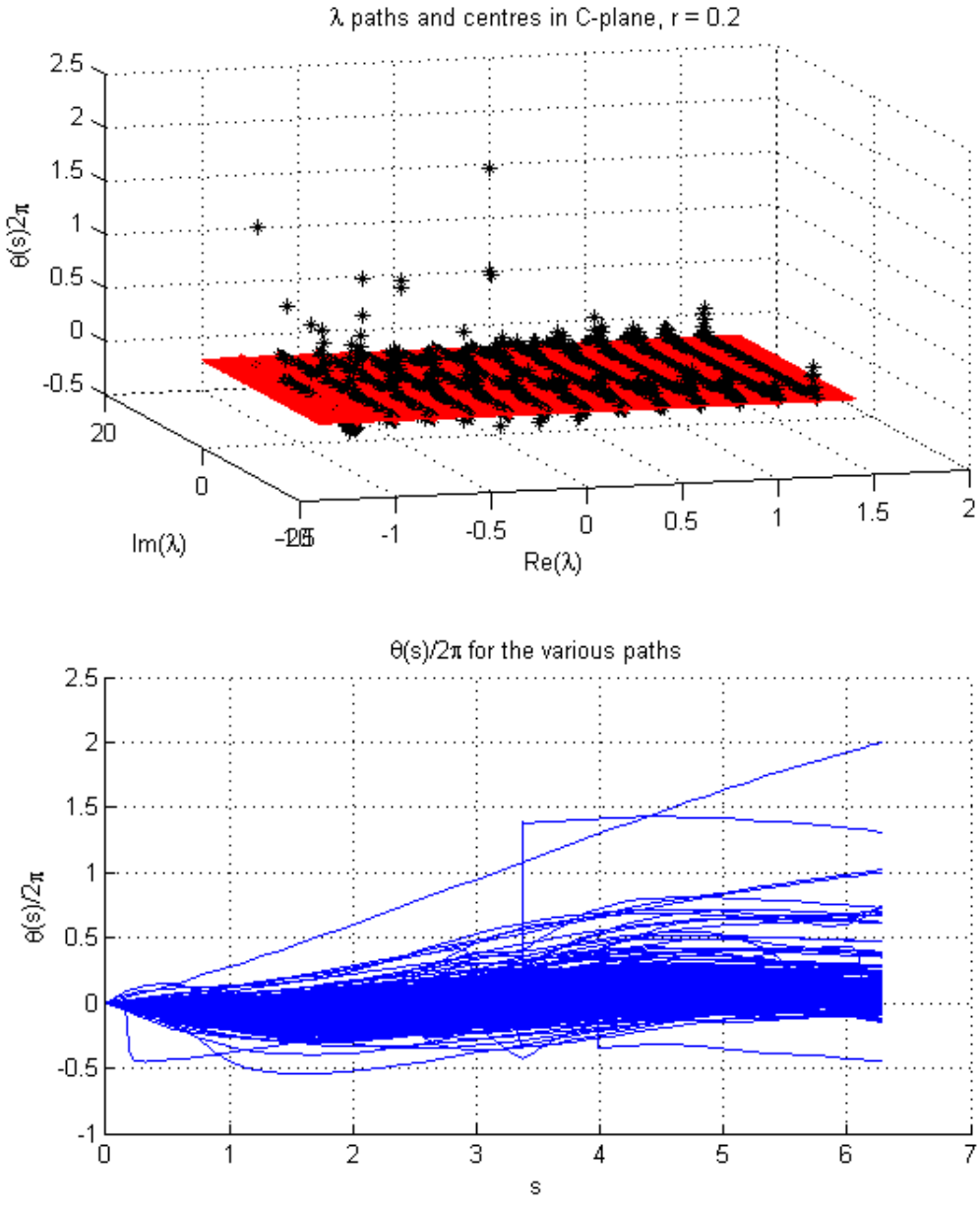

Figure 6.24: Phase change results for a lattice of λ-loops of radius $r = 0.2$, for $\omega = 0.5$, $\rho = 0.5$, $\psi = 2$

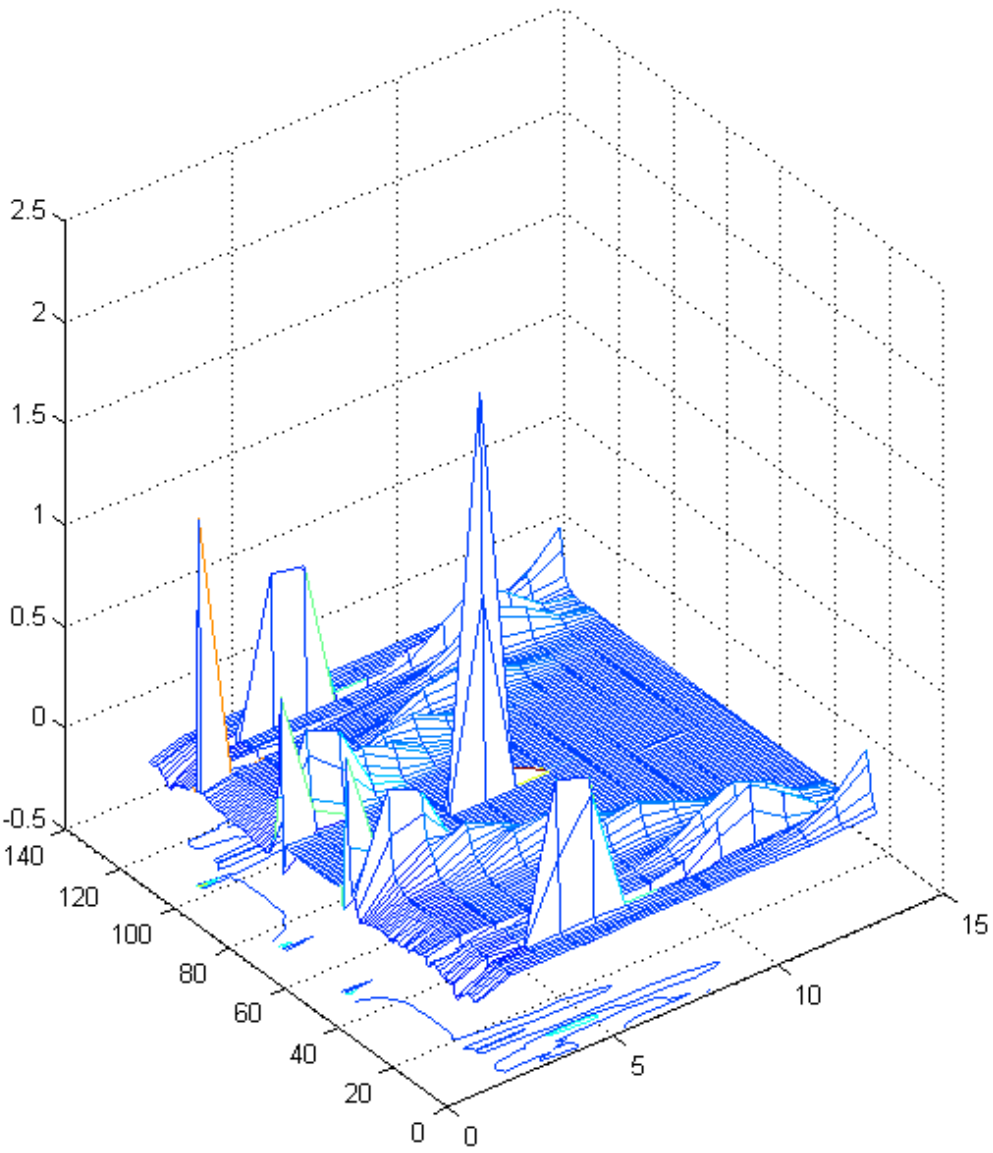

Figure 6.25: First contour plot corresponding to Figure 6.24

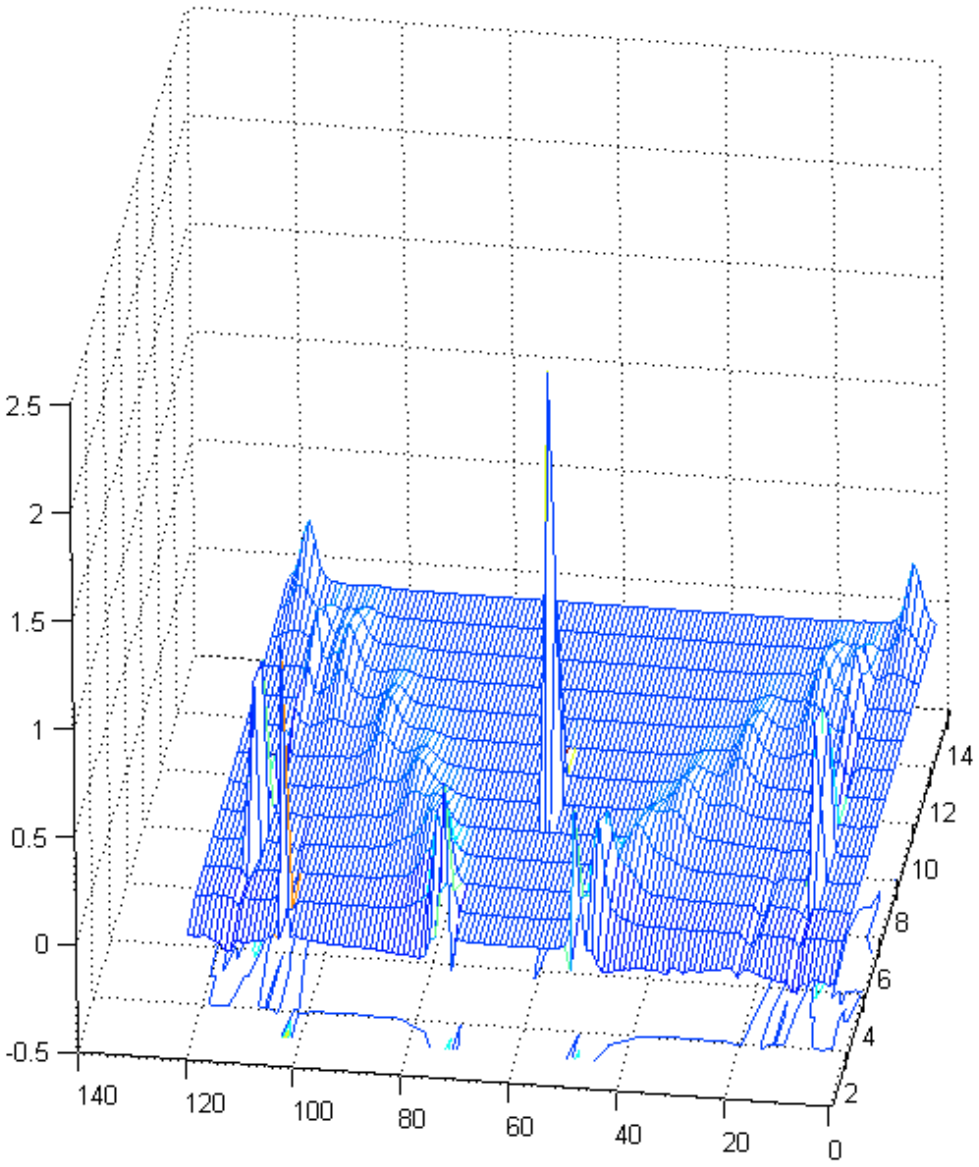

Figure 6.26: Second, slightly rotated, contour plot corresponding to Figure 6.24

6.1.2 Comments

Overall the numerical results are promising, however the lack of consistency with previous results is of concern. On the one hand, many of the phase results are very clear and show excellent correspondence with known eigenvalue location results, thus providing good evidence to support the central conjecture. On the other hand, other results are less clear, and despite showing very distinct patterns of phase peaks, for example in Figures 6.12-6.23, do not correspond to results of previous investigations. These discrepancies could either be due to the central conjecture being flawed (either globally, or just in this case for some reason), or due to previous results being flawed. Both of these options are plausible, the latter since for parameter values where there are serious discrepancies, the literature on the matter takes care to highlight the delicate nature of both the analytical and numerical results - indeed there is a lack of solid numerical evidence for the results claimed. Having said that, it is important to remember that the central conjecture here has no theoretical grounding as yet, and that there is still at least one unresolved accuracy issue in the algorithm used (the loop radius) and there may well be others. Even if there is some flaw in either the numerics here or their interpretation, it is still hard to imagine that such distinctive results do not have some precise mathematical meaning; resolving these issues will require further work.

6.2 The Rayleigh Equation

The second example considered is the Rayleigh equation, which is a reduced version of the Taylor-Goldstein equation, an ODE eigenvalue problem on $\mathbb{C}^2$ of great interest in fluid mechanics and oceanography. The Rayleigh equation is

$$(U(z)-c)\left(\frac{d^2\phi}{dz^2}-k^2\phi\right)-U''(z)\phi=0 \qquad \phi(z)\in\mathbb{C},\ z\in\mathbb{R} \tag{6.7}$$

where $c\in\mathbb{C}$ is an eigenvalue parameter, k is a real parameter, typically in the range $[-2,2]$, and $U(z)\in\mathbb{R}$ is the mean velocity profile, given by

$$U(z)=\frac{1}{2}(1+\tanh z) \tag{6.8}$$

Writing this in matrix format yields the equation

$$\begin{pmatrix}\phi\\ \phi_z\end{pmatrix}_z=\begin{pmatrix}0 & 1\\ \frac{U''}{U-c}+k^2 & 0\end{pmatrix}\begin{pmatrix}\phi\\ \phi_z\end{pmatrix} \tag{6.9}$$

then setting $u = \begin{pmatrix} u_1(z) \\ u_2(z) \end{pmatrix} = \begin{pmatrix} \phi \\ \phi_z \end{pmatrix}$ casts the problem in our standard format

$$u_z = A(z,c)u \qquad u(z) \in \mathbb{C}^2,\ z \in \mathbb{R},\ c \in \mathbb{C} \tag{6.10}$$

with

$$A(z,c) = \begin{pmatrix} 0 & 1 \\ \frac{U''}{U-c} + k^2 & 0 \end{pmatrix} \tag{6.11}$$

Regarding the asymptotic behaviour of the system we have

$$\tanh z \ \rightarrow\ \pm 1 \text{ as } z \rightarrow \pm\infty \tag{6.12}$$

$$\Rightarrow\ U(z) = \frac{1}{2}(1+\tanh z) \ \rightarrow\ \begin{cases} +1 \text{ as } z \rightarrow +\infty \\ 0 \text{ as } z \rightarrow -\infty \end{cases} \tag{6.13}$$

$$\text{and} \qquad U''(z) = -\tanh z \operatorname{sech}^2 z \ \rightarrow\ 0 \text{ as } z \rightarrow \pm\infty \tag{6.14}$$

so that

$$\frac{U''}{U-c} \rightarrow 0 \text{ as } z \rightarrow +\infty \text{ except perhaps when } c = 1 \tag{6.15}$$

$$\text{and } \frac{U''}{U-c} \rightarrow 0 \text{ as } z \rightarrow -\infty \text{ except perhaps when } c = 0 \tag{6.16}$$

and therefore $\forall c \neq 0, 1$,

$$A_\infty(c) = \lim_{z \rightarrow \pm\infty} A(z,c) = \begin{pmatrix} 0 & 1 \\ k^2 & 0 \end{pmatrix}, \tag{6.17}$$

which has eigenvalue/vector pairs $\left\{k, \begin{pmatrix} 1 \\ k \end{pmatrix}\right\}$ and $\left\{-k, \begin{pmatrix} 1 \\ -k \end{pmatrix}\right\}$. Thus for $k > 0$, the eigenvalue of $A_\infty(c)$ of most negative real part is $-k$, with corresponding eigenvector $\begin{pmatrix} 1 \\ -k \end{pmatrix}$. Note that even though the system-at-infinity is actually independent of the system eigenvalue parameter c here, we still write $\lim_{z\rightarrow\pm\infty} A(z,c)$ as $A_\infty(c)$ to maintain consistency with the framework set up previously. In fact there are several aspects of this problem which differ radically from previous examples. Of particular importance is the fact that as z varies, $U(z)$ takes all values between 0 and 1, so that whenever $c \in [0,1]$ there will be *some* value of z at which the denominator $U(z) - c$ goes to zero, which may cause problems with any numerical integration scheme implemented there.

We avoid some of the potential difficulties here by focusing on one special case: it may be shown, by constructing an exact solution explicitly, that $c = \frac{1}{2}$ is an eigenvalue of the system when $k = -1, 0, 1$. The numerical results presented here centre around the $k = 1$ case; we ensure that c stays away from 0 and 1, and keep in

mind that whenever a path in c-space ($cf.$ λ-space in previous cases) crosses the real axis between 0 and 1 the numerics *may* behave erratically due to the denominator $U - c$ going to zero. The Matlab code was modified appropriately, resulting in the programs

- `integration_at_L_prime_taylor_goldstein.m`
- `lambda_plane_eval_search_taylor_goldstein.m`.

As usual these calculate phases associated with γ_3 paths, which in this case are generated by integrating $u_x = Au$ from L to $-L$ starting from the eigenvector $\begin{pmatrix} 1 \\ -k \end{pmatrix}$.

6.2.1 Numerical results

Numerics for $k = 1$

All of the results presented for this system concern a lattice of points located between the values 0 and 1 in c-space, approximately centred on $c = \frac{1}{2}$. The lattice spacing is 0.03 and the radius of the c-loops centred at the lattice nodes is $r = 0.02$ ($cf.$ λ-loops in previous cases). The standard values $\theta(0) = 0$, $L = 10 = -L'$ and $\delta = 2\pi/10000$ remain in use. The graphical output is of the same format as previously; Figures 6.27 and 6.28 show the plots for the case $k = 1$. The phase change is approximately 0 everywhere except at the location of the known eigenvalue $c = \frac{1}{2}$, at which its value is approximately 1. The phase results along the real axis between 0 and 1 are slightly less uniform than elsewhere in the lattice, as discussed, though this does not detract from the overall picture.

Numerics for $k = 0.8, 1.1$

Figures 6.29, 6.30 and 6.31, 6.32 show the phase results for $k = 0.8$ and $k = 1.1$ respectively. Note that the height scale is much larger in the latter two plots, so the peak values are in fact much lower than the former plots. For $k = 0.8$ we see two clear, smooth phase results yielding two distinct peaks of height ≈ 1 either side of the real axis at 0.5. The other phase results are all ≈ 0, although on the lower plot of the first figure there are now many erratic step changes in the phase. By observing the plotting process continuously it was confirmed that these and only these data are generated by numerics in the vicinity of the real axis in c-space. This is a pattern observed throughout all of the results here.

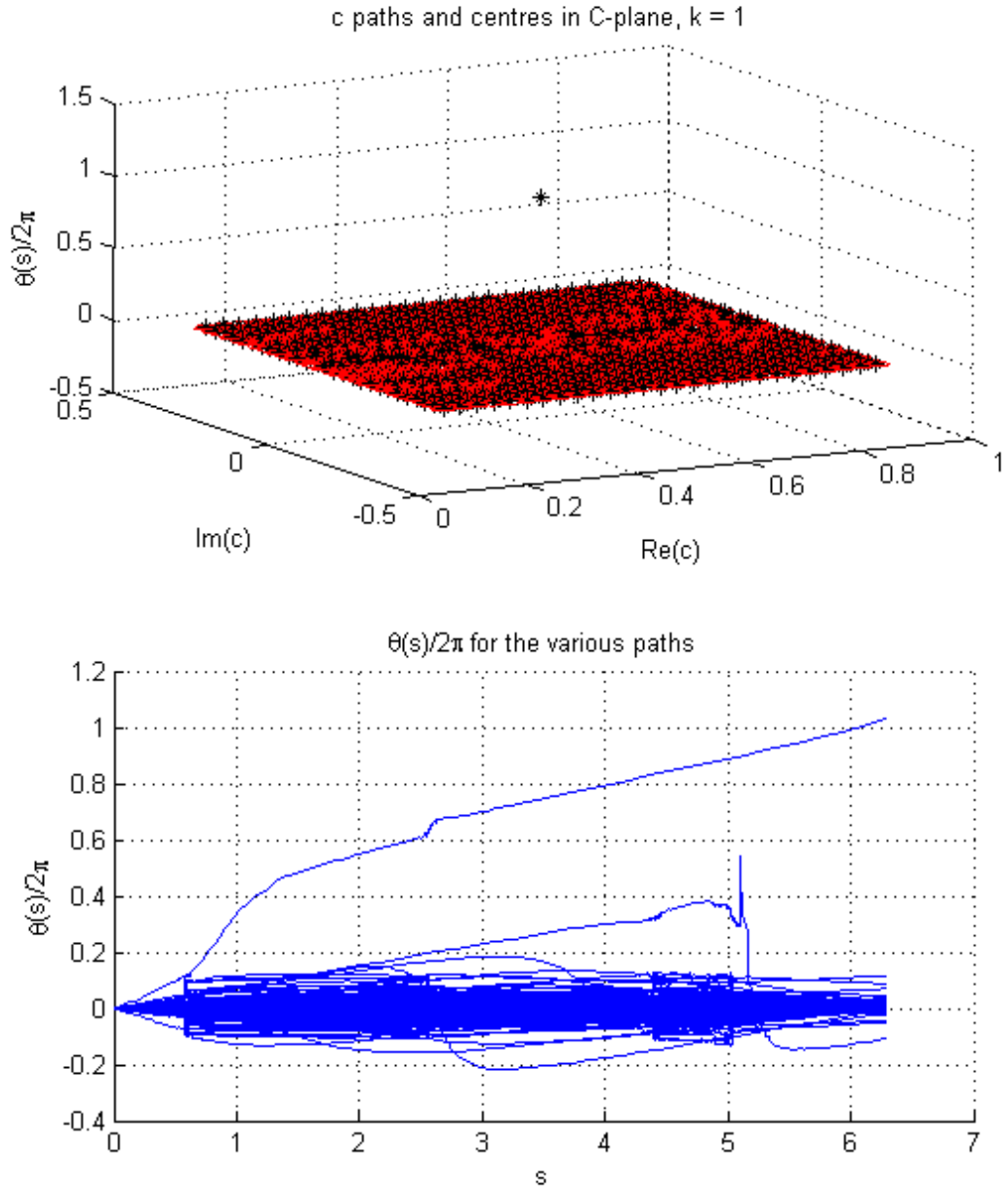

Figure 6.27: Phase change results for a lattice of c-loops of radius $r = 0.02$, centred about $c \approx 0.5$, for $k = 1.0$

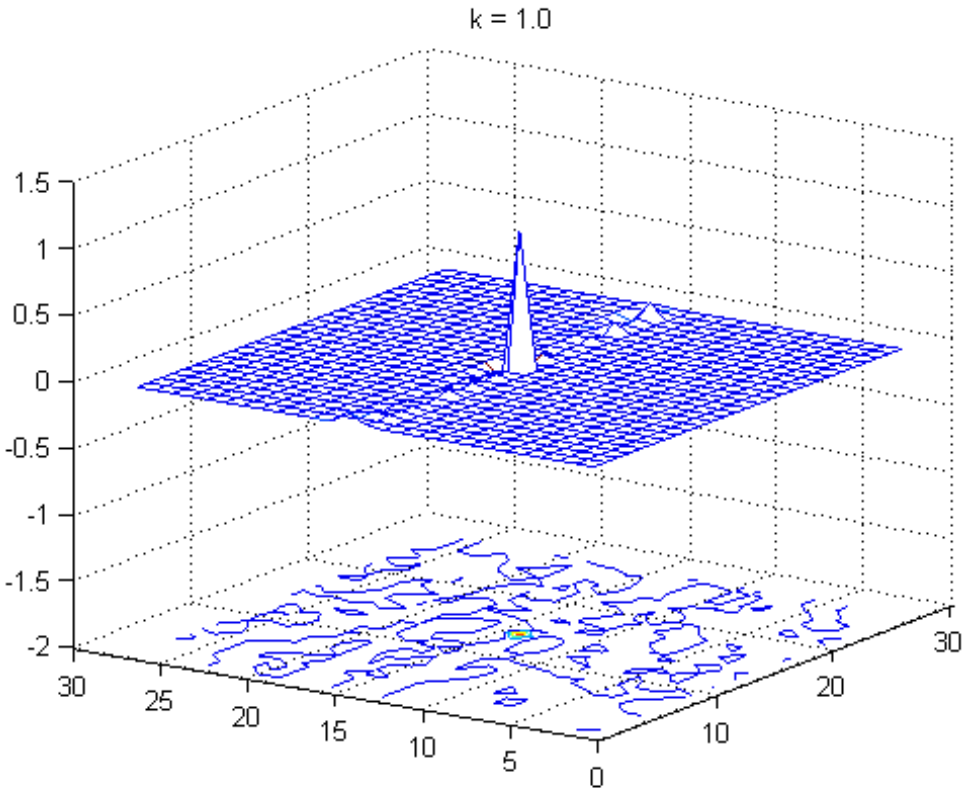

Figure 6.28: Contour plot corresponding to Figure 6.27

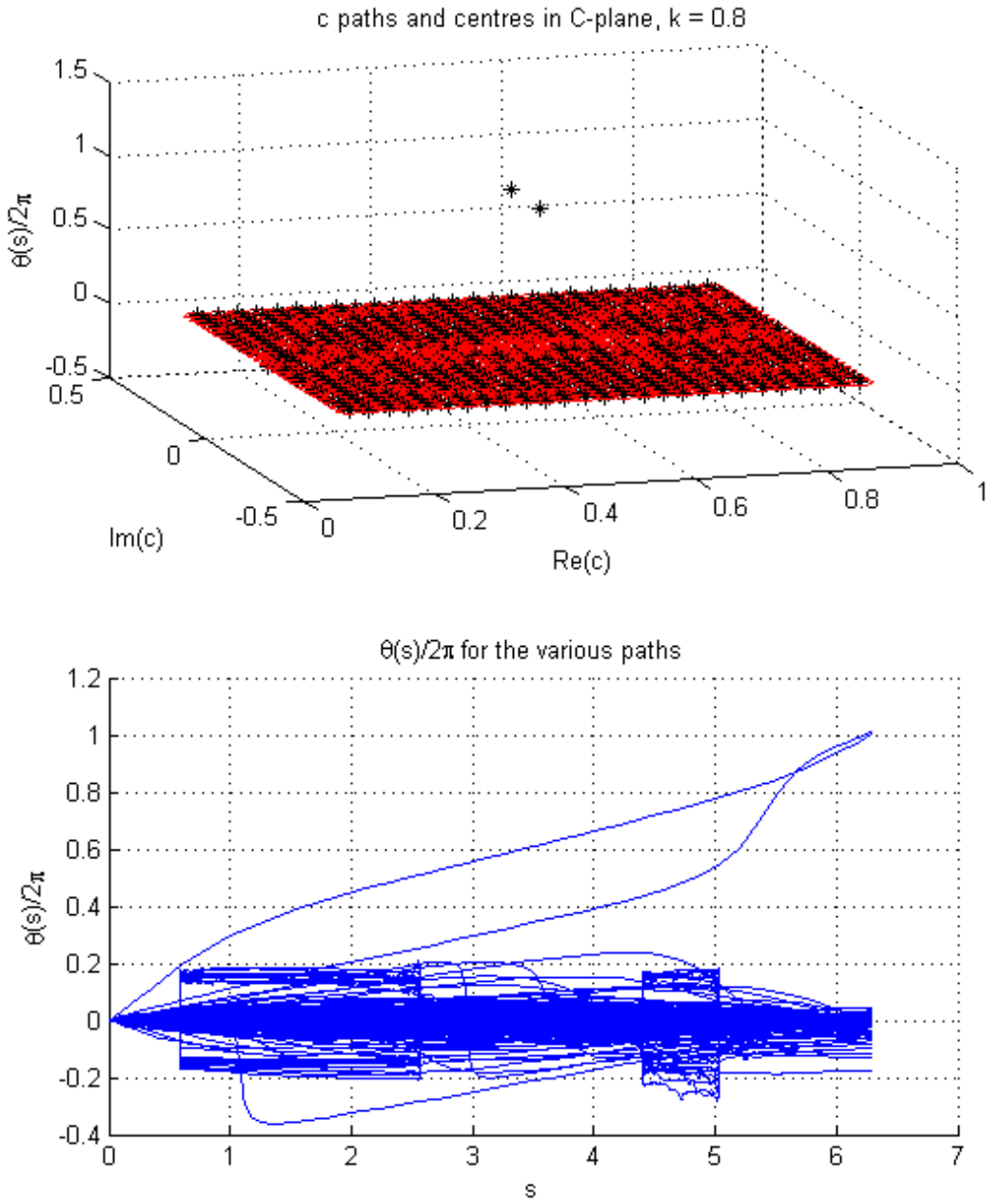

Figure 6.29: Phase change results for a lattice of c-loops of radius $r = 0.02$, centred about $c \approx 0.5$, for $k = 0.8$

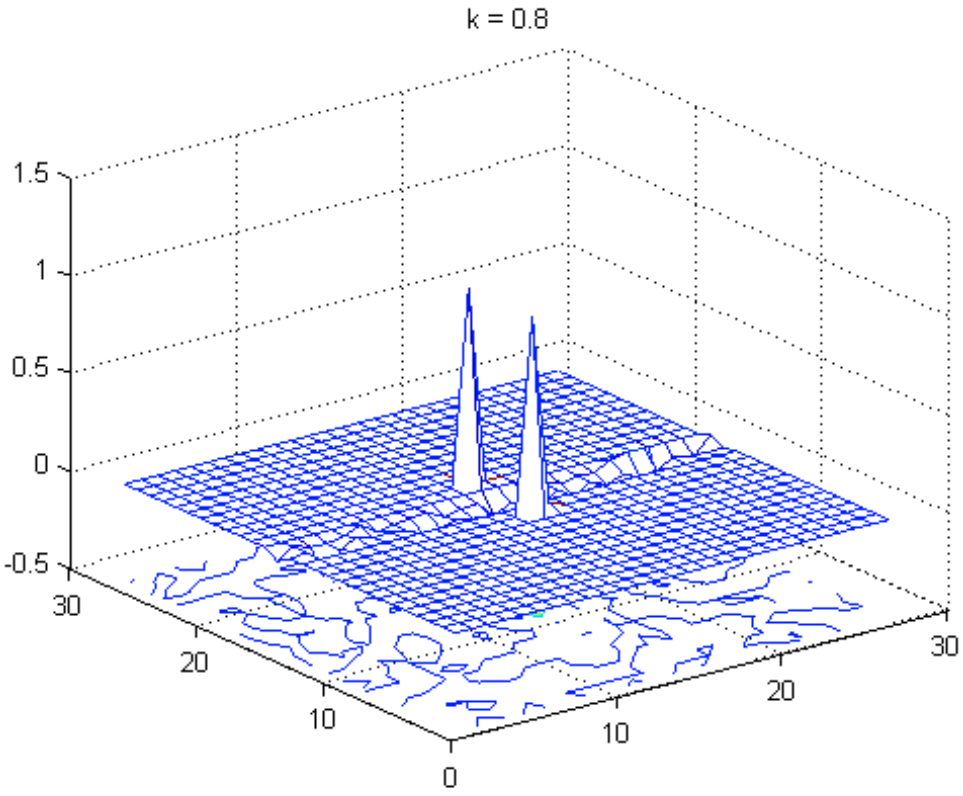

Figure 6.30: Contour plot corresponding to Figure 6.29

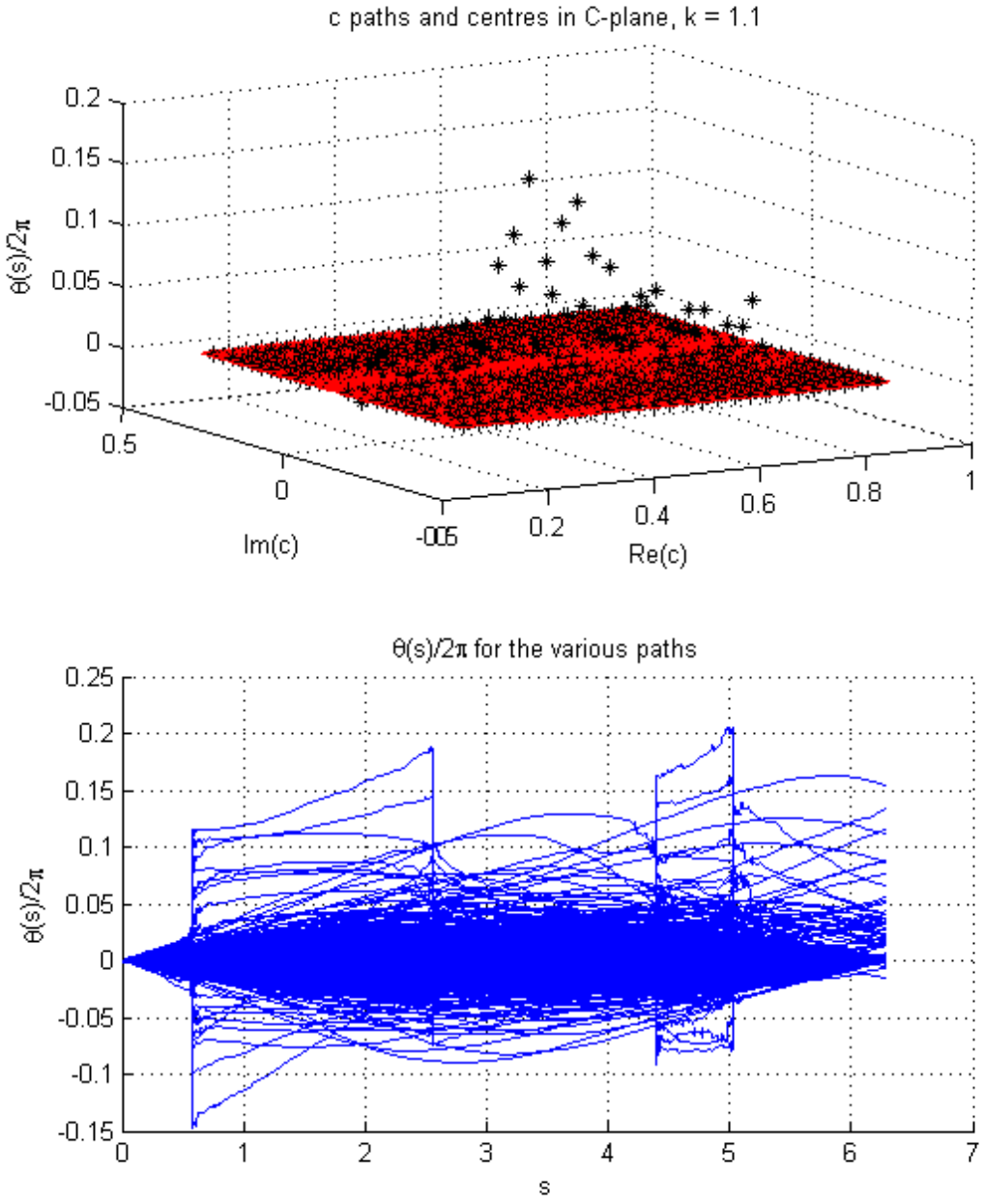

Figure 6.31: Phase change results for a lattice of c-loops of radius $r = 0.02$, centred about $c \approx 0.5$, for $k = 1.1$

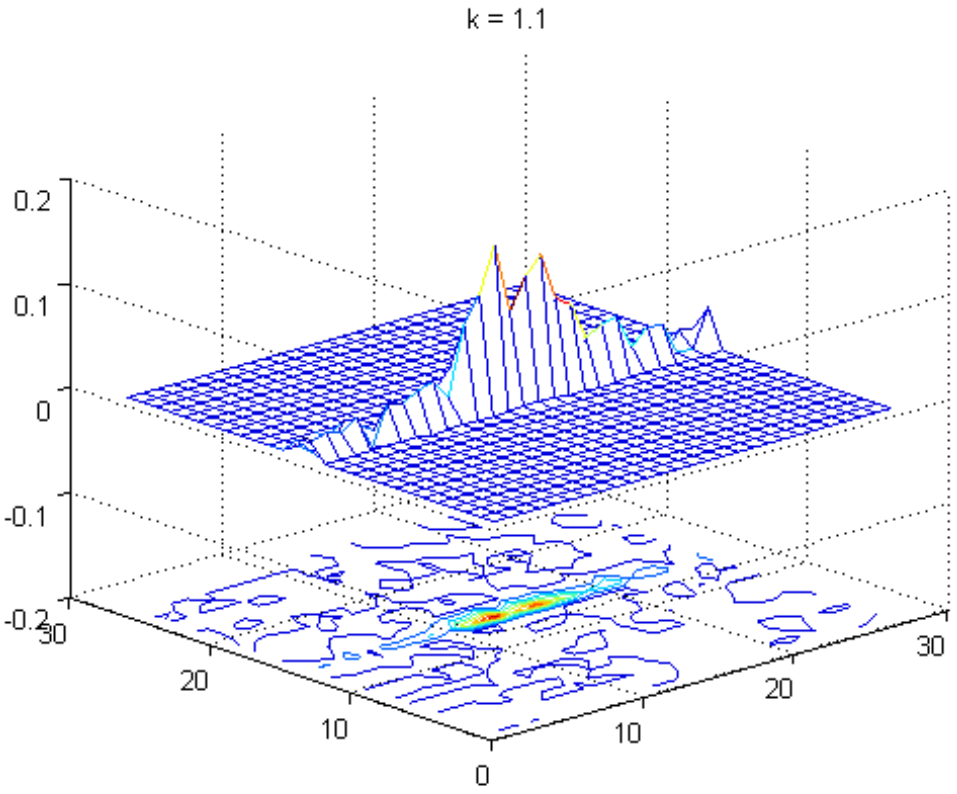

Figure 6.32: Contour plot corresponding to Figure 6.31

Numerics for $k \in [0.5, 1.5]$

Using precisely the same lattice dimensions as above, Figures 6.33-6.43 show contour plots for $k = 0.5, 0.6, 0.7, 0.8, 0.9, 0.98, 1.0, 1.1, 1.2, 1.3, 1.4$.

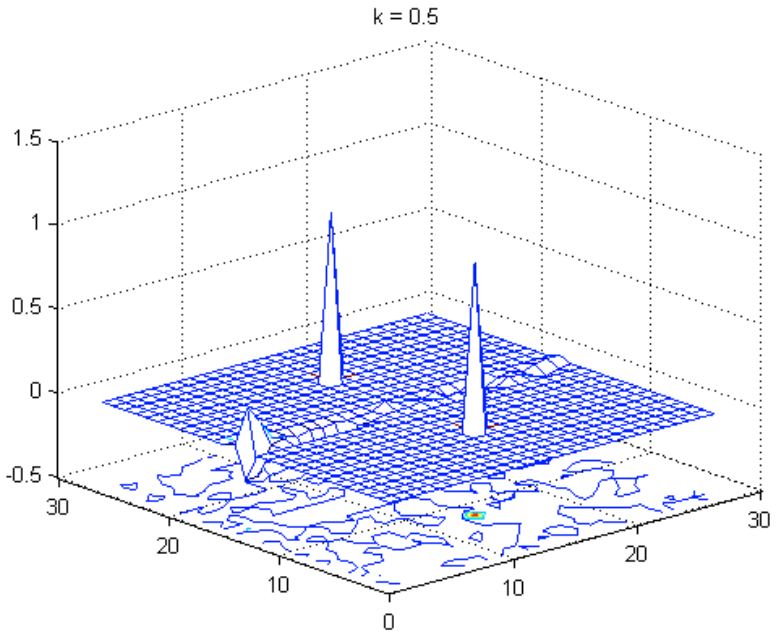

Figure 6.33: Contour plot for $k = 0.5$

6.2.2 Comments

The pattern is clear: as k increases from 0.5 to 1.0, the two peaks of height ≈ 1 coalesce, forming the single peak at $c = 0.5$ for $k = 1$. Then as k increases further there are no such emphatic results, just a line of fluctuating data along the real axis with a slight residual hump at $c = 0.5$, which is most likely just due to fluctuations in error in the numerical procedure. Thus if the central conjecture is to be believed and the distinct peaks in phase change do indeed correlate to the presence of a discrete system eigenvalue, then these results indicate the existence of an imaginary pair of system eigenvalues, of real part 0.5, for $k \in [0.5, 1.0)$, which coalesce to the known value for $k = 1$ then disappear for $k \in (1, 1.4]$.

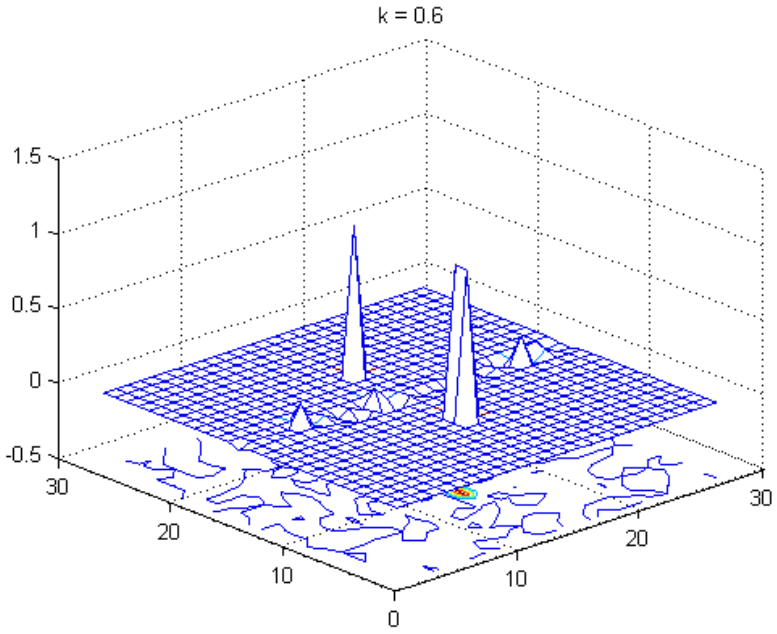

Figure 6.34: Contour plot for $k = 0.6$

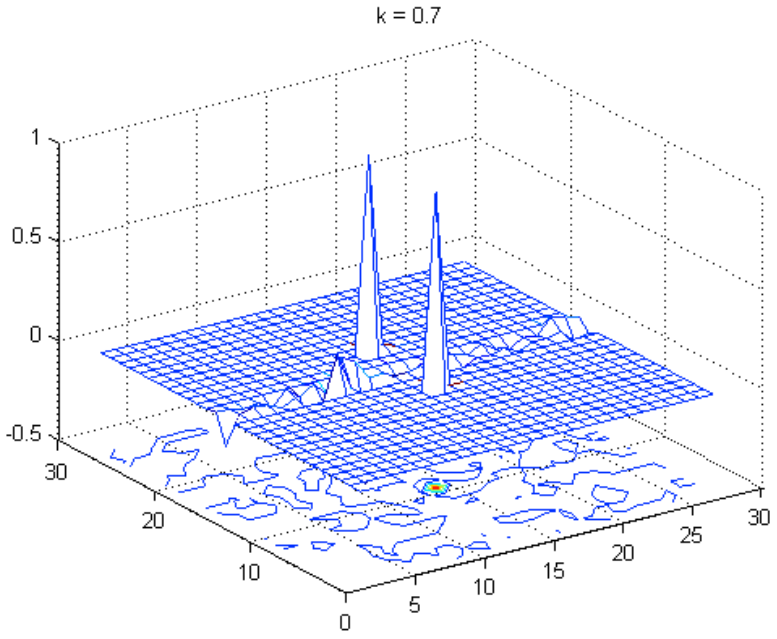

Figure 6.35: Contour plot for $k = 0.7$

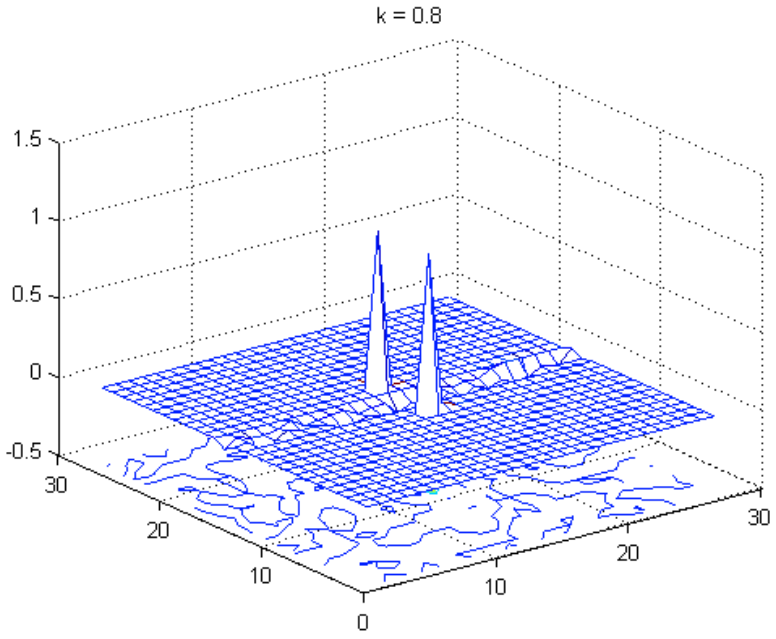

Figure 6.36: Contour plot for $k = 0.8$

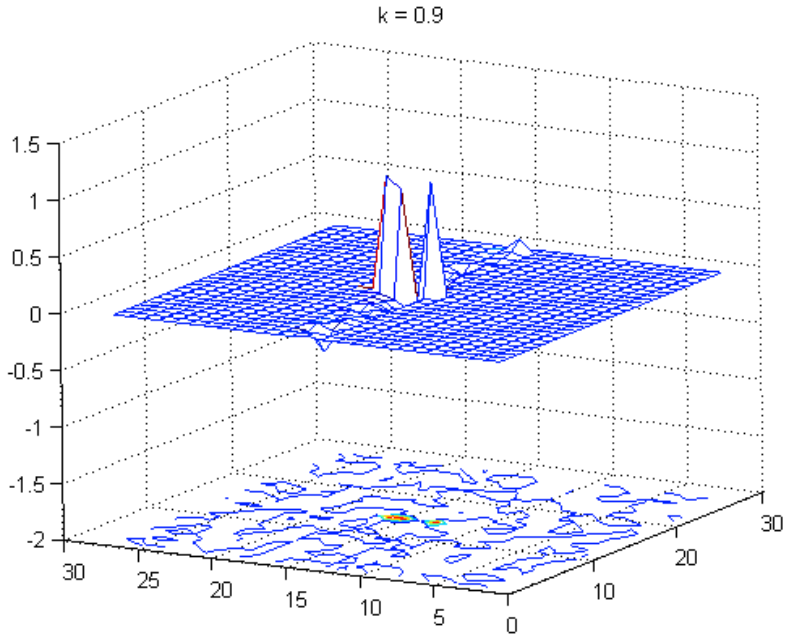

Figure 6.37: Contour plot for $k = 0.9$

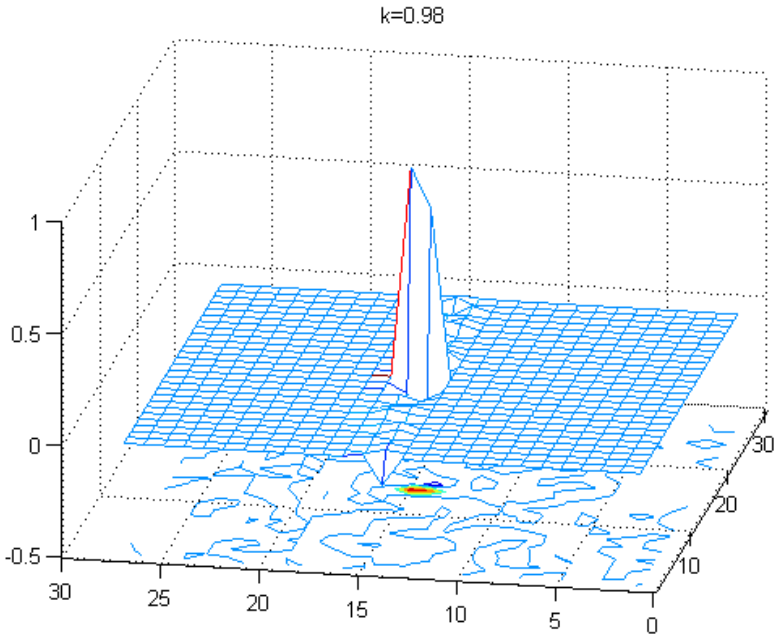

Figure 6.38: Contour plot for $k = 0.98$

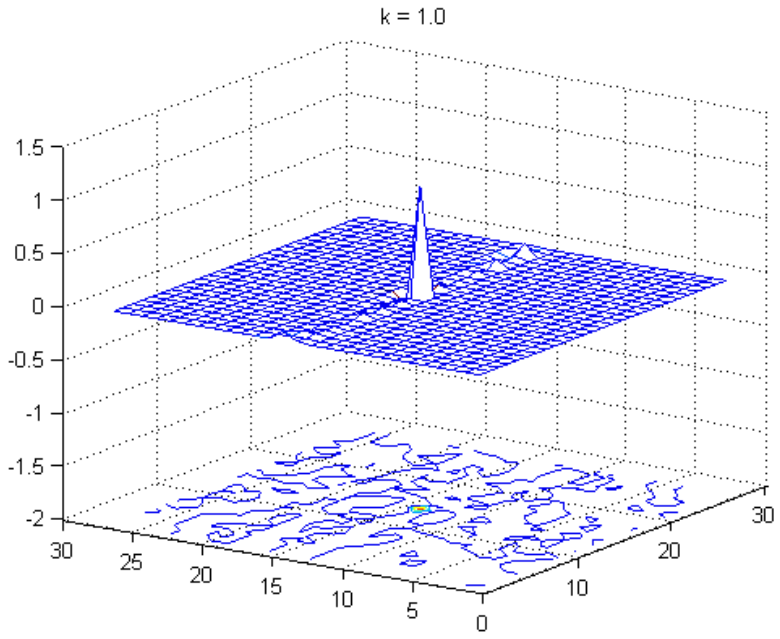

Figure 6.39: Contour plot for $k = 1.0$

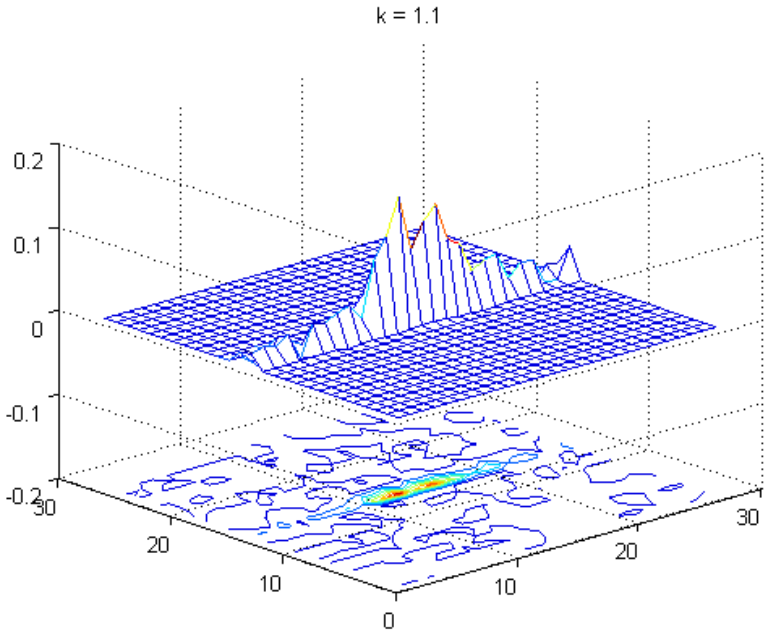

Figure 6.40: Contour plot for $k = 1.1$

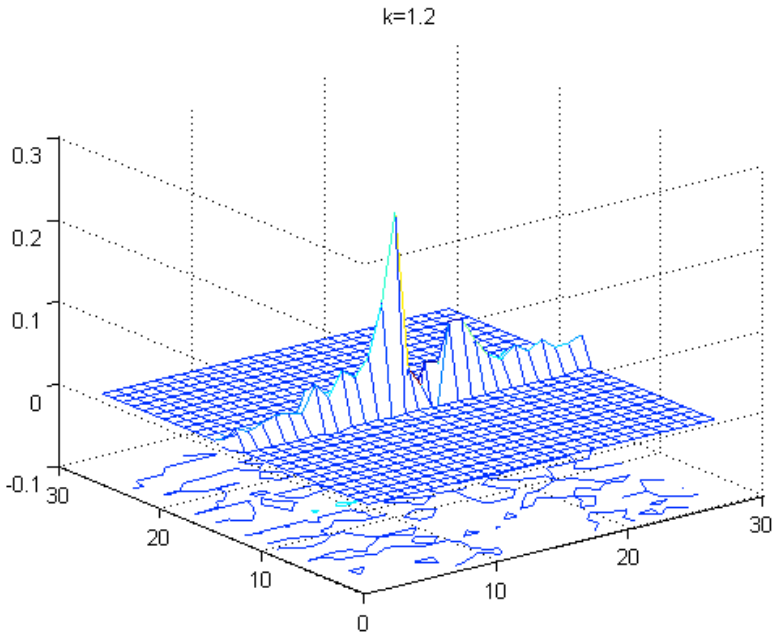

Figure 6.41: Contour plot for $k = 1.2$

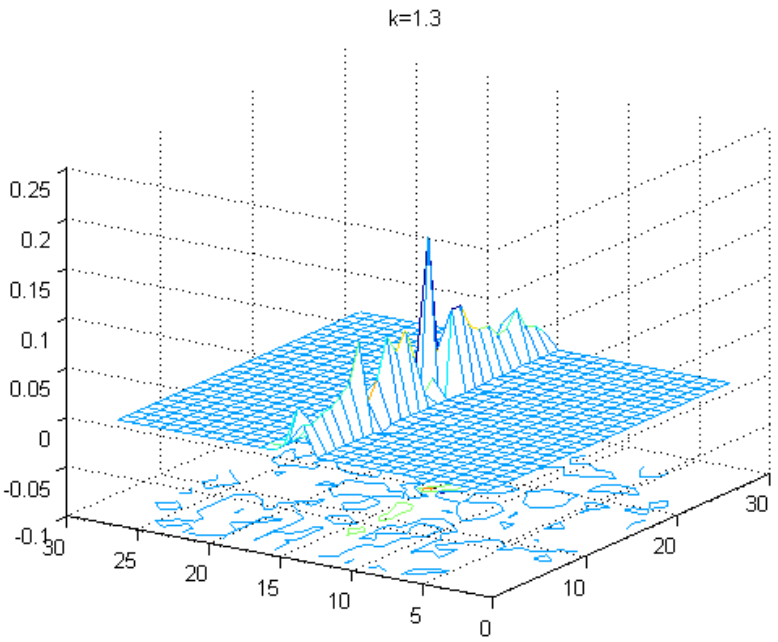

Figure 6.42: Contour plot for $k = 1.3$

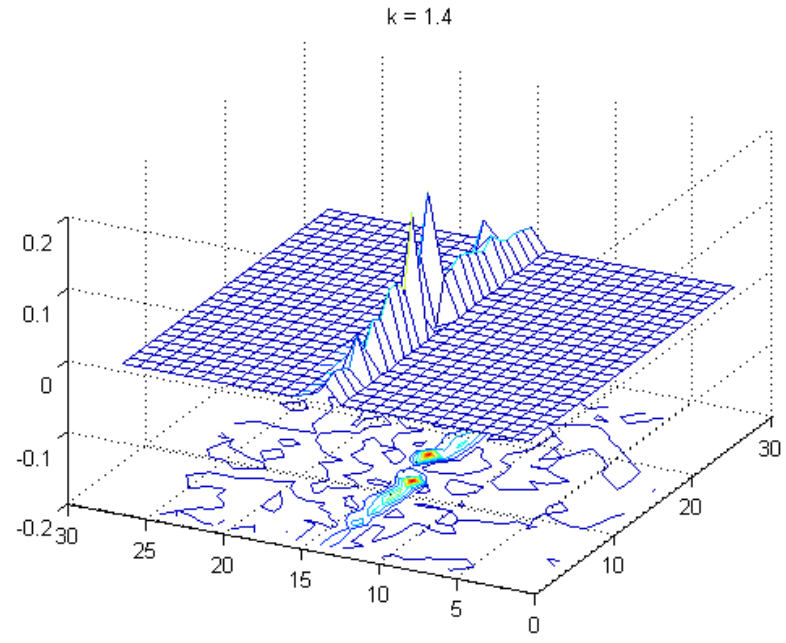

Figure 6.43: Contour plot for $k = 1.4$

6.3 The Schrödinger equation

The final example considered is the one-dimensional time-independent Schrödinger equation with a Morse potential. In [41], Liu *et al.* investigate a shooting method for solving the 1-D Schrödinger equation

$$-\frac{1}{2}\frac{d^2\psi}{dx^2} + V(x)\psi = E\psi \qquad x \in \mathbb{R},\ \psi(x) \in \mathbb{C},\ V(x) \in \mathbb{R},\ E \in \mathbb{R} \tag{6.18}$$

where $E < 0$ is an energy eigenvalue of the system, $V(x)$ is a given potential and $\psi(x)$ is the wave function. They convert the problem to the dynamical system

$$\begin{pmatrix} \dot{\phi} \\ \dot{\psi} \end{pmatrix} = \begin{pmatrix} 0 & -B(x,E) \\ 1 & 0 \end{pmatrix} \begin{pmatrix} \phi \\ \psi \end{pmatrix} \tag{6.19}$$

$$B(x) = 2(E - V(x)) \tag{6.20}$$

and take $V(x)$ to be the Morse potential

$$V(x) = D[e^{-2\omega x} - 2e^{-\omega x}] \tag{6.21}$$

$$\text{with} \quad D = 12 \tag{6.22}$$

$$\omega = 0.204124 \tag{6.23}$$

They consider boundary conditions

$$\begin{pmatrix} \phi(a) \\ \psi(a) \end{pmatrix} = \begin{pmatrix} 1 \\ 0 \end{pmatrix}, \qquad \begin{pmatrix} \phi(b) \\ \psi(b) \end{pmatrix} = \begin{pmatrix} 1 \\ 0 \end{pmatrix}, \qquad a < b \in \mathbb{R} \tag{6.24}$$

and set $a = -b = -13.5$. The system has 24 discrete eigenvalues, all of which lie in the interval $(-12, 0)$, and are given by

$$E_n = -12 + (n + 1/2) - \frac{1}{48}(n + 1/2)^2, \qquad n = 0, \ldots, 23. \tag{6.25}$$

Writing the system in our standard format gives

$$u_x = A(x,E)u \qquad u(x) \in \mathbb{C}^2,\ x \in \mathbb{R},\ E \in \mathbb{C} \tag{6.26}$$

with

$$A(x,E) = \begin{pmatrix} 0 & -B(x,E) \\ 1 & 0 \end{pmatrix} \tag{6.27}$$

However, this system strays even further away from the format of the original problem, because now it is only asymptotically constant on one side:

$$B(x,E) \to 2E \text{ as } x \to +\infty \tag{6.28}$$

$$\text{but} \qquad B(x,E) \text{ does not converge as } x \to -\infty \tag{6.29}$$

and

$$A_{+\infty}(E) = \lim_{x \to +\infty} A(x, E) = \begin{pmatrix} 0 & -2E \\ 1 & 0 \end{pmatrix}, \tag{6.30}$$

which has eigenvalue/vector pairs $\left\{ \pm\sqrt{-2E}, \begin{pmatrix} \pm\sqrt{-2E} \\ 1 \end{pmatrix} \right\}$. Now, since $A(x, E)$ does not converge as $x \to -\infty$, it is not possible to find the eigenvectors corresponding to both the stable and unstable manifolds of the system-at-infinity, as required for the standard Evans function analysis. However, the technique developed here only uses eigenvectors of the system at one of the boundaries, so the eigenvectors at large $x = b$ may be used as initial data for integrating the system down to $x = a$, thus generating γ_3 paths as usual. Note that selecting the integration range $[a, b]$ is a slightly more delicate matter than previously because when $V(x)$ is small at one end of the range, it is large at the other. We take $a = -b = -13.5$. Again, the Matlab code was modified to fit the example at hand, yielding programs

- `integration_at_L_prime_schrodinger.m`
- `lambda_plane_eval_search_schrodinger.m`.

6.3.1 Numerical results

Figures 6.44 and 6.45 show the results of the numerical phase computations in the usual format, using a lattice of points with spacing 0.2 and E-loops of radius $r = 0.14$. The 24 eigenvalues given in (6.25) are also shown beneath the lattice for easy comparison of their location with the phase results. Figure 6.46 shows a close-up of the lattice near to the origin where the eigenvalues are closer together.

6.3.2 Comments

Accounting for the obvious issues regarding lattice spacing and overlapping E-loops, which are particularly evident due to the eigenvalue spacing here, the phase change peaks show excellent agreement with the known eigenvalue locations.

Remark 6.3.1. *Motivated by the choice of boundary conditions (6.24) used in [41], the numerical algorithm was modified slightly to use as starting vectors for the γ_2 paths not the eigenvectors of the system-at-infinity, (6.30), but instead just the constant vector* $\begin{pmatrix} 1 \\ 0 \end{pmatrix}$. *Exactly the same distinctive results were observed, with the phase change reflecting precisely the number of eigenvalues contained within the corresponding E-loop. This introduces the possibility that the use of the eigenvectors*

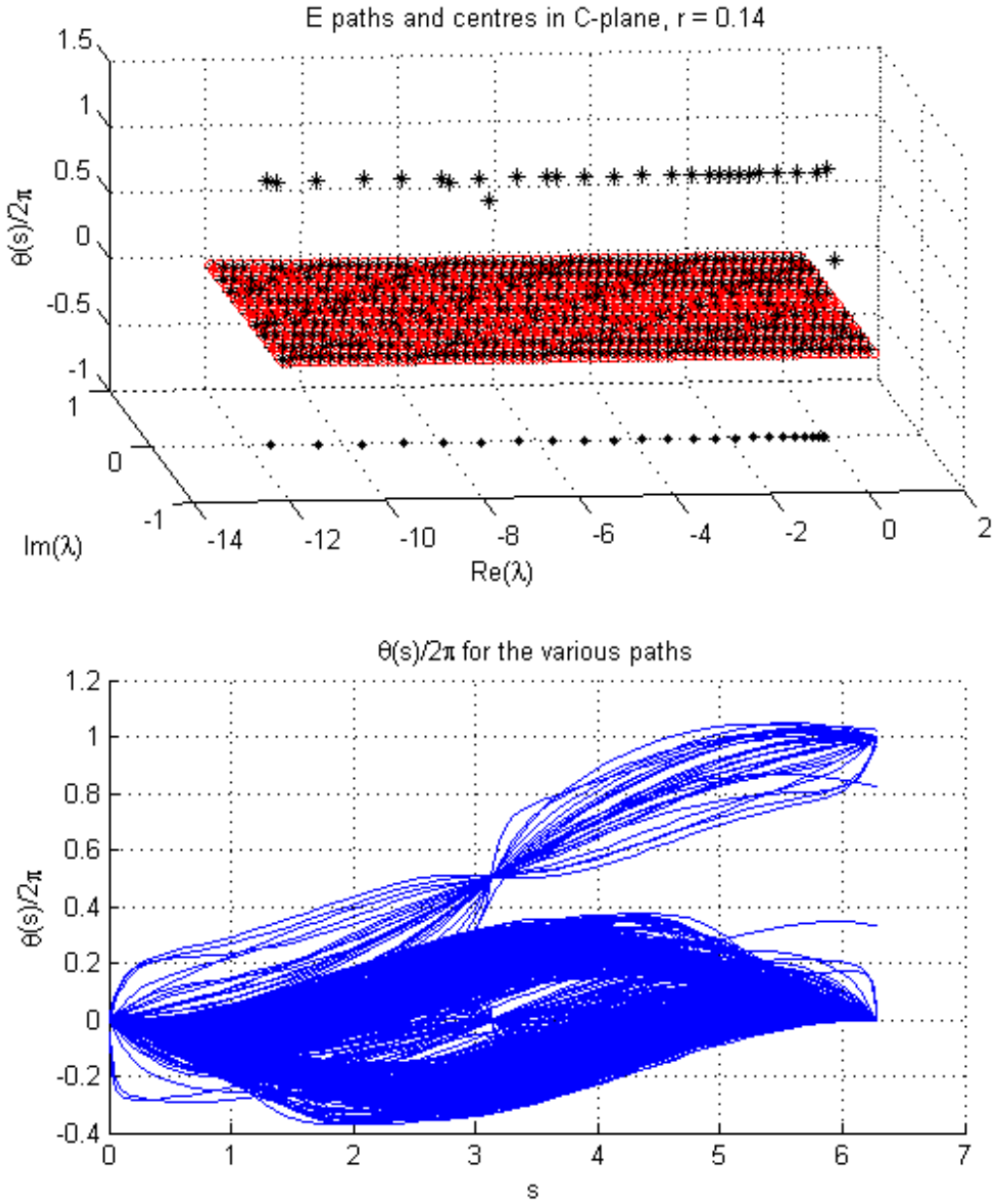

Figure 6.44: Phase change results for a lattice of E-loops of radius $r = 0.14$. Note that in addition to the usual elements on the top plot, the 24 exact eigenvalue locations are shown as points beneath the lattice.

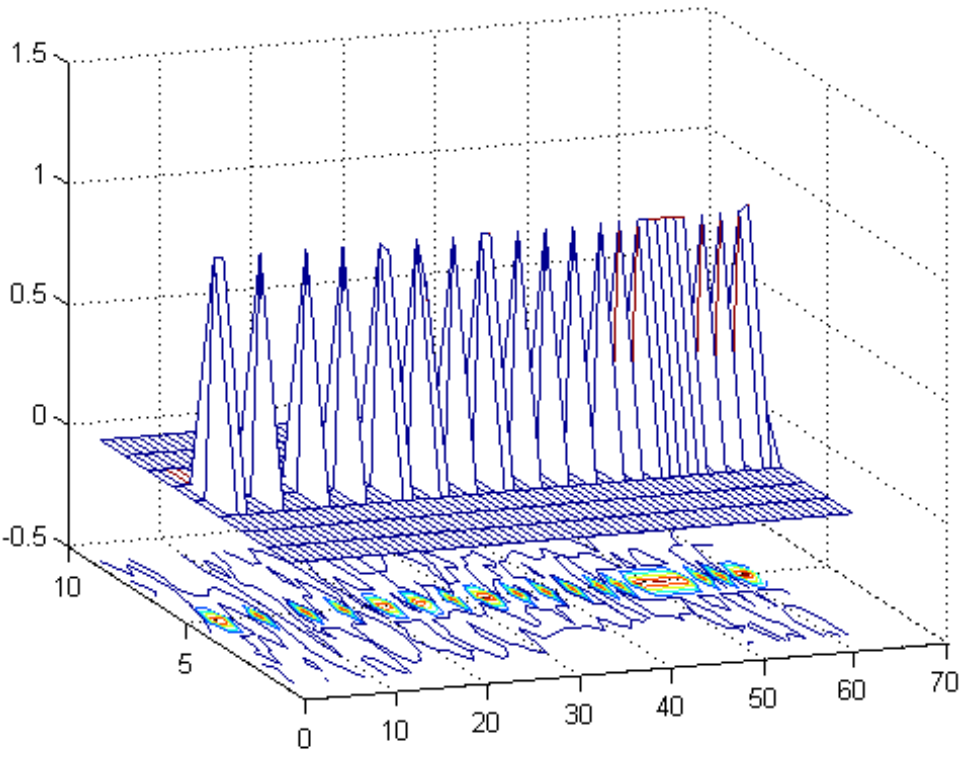

Figure 6.45: Contour plot corresponding to Figure 6.44

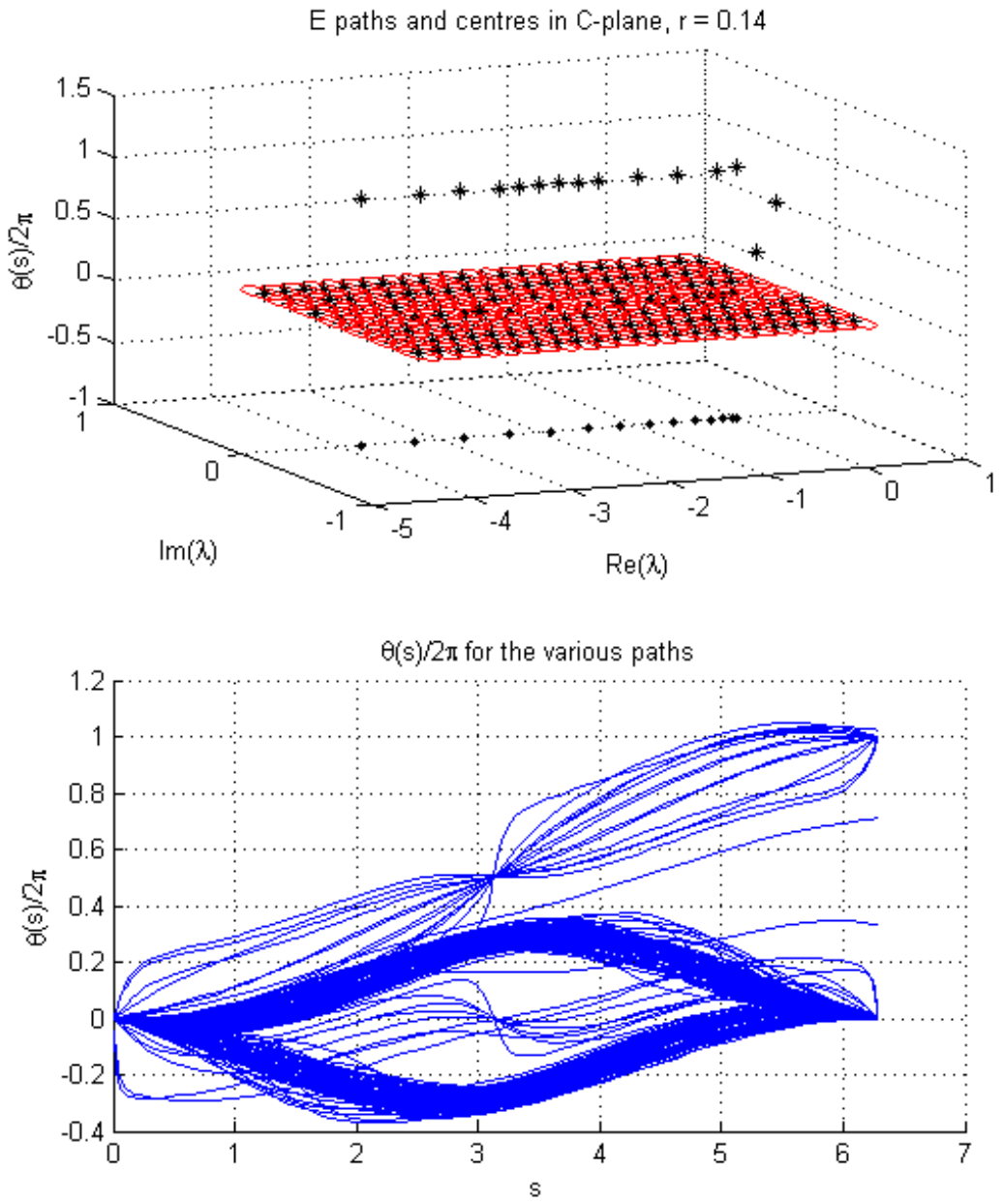

Figure 6.46: Phase change results for a lattice of E-loops of radius $r = 0.14$. Note that in addition to the usual elements on the top plot, the 14 exact eigenvalue locations within this region are shown as points beneath the lattice.

of the system-at-infinity as initial data when integrating the system may in fact be an entirely redundant element of the proposed numerical scheme after all. Clarification of this aspect of the problem would require extensive further testing.

The numerical results presented in this chapter show the application of the phase theory to computations in several current research scenarios, demonstrating clearly that the phase is an important concept in dynamical systems, even if it is not yet understood well enough. The big question which has been raised here is: if there is such good correlation between phase changes and discrete eigenvalue locations for *so* many of the cases, where does the flaw lie in the cases where agreement is less good?

Chapter 7

Concluding remarks and discussion

7.1 General discussion

This thesis identifies and makes precise the process of choosing to view paths on $\mathbb{C}^n$ in terms of a much-overlooked geometrical framework. This perspective has not been investigated in this context or depth before. The work shows it to be a framework within which many kinds of dynamical problems on $\mathbb{C}^n$ may be addressed, in particular differential eigenvalue problems on unbounded intervals, and goes some way to understanding the role of the complex geometric structures now seen to be present in even the simplest of ODE systems.

The work documents the logical flow of concepts identified which leads to the important realization that when viewed in terms of the hierarchy of spaces here, every path on $\mathbb{C}^n \setminus \{0\}$ has connected with it an underlying "ticking-clock"-like phase quantity, geometrical in origin, the full consequences of which are not yet fully understood, though clearly important and potentially immensely useful. Our description of this phase quantity is mathematically precise, though its interpretation is still incomplete. Progress here would require further understanding of the mathematical role of the phase - the *effects* of which we have been able to observe in several numerical experiments, but the full implications of which are still unresolved.

The work provides a balanced report of the developments made, combining as it does a mixture of theoretical review and progress with computational experiments and results based thereon. It is hoped that this approach creates a rounded picture of the research, in order to act simultaneously as effective motivation and foundation for further research on the topic.

7.2 Summary of achievements

The original contributions to the mathematical literature detailed in this work are quite varied and are summarized here according to three categories:

- *Interpretation of known theory.* We have produced a concise review of the concepts concerning fibre bundles required in order to follow the subsequent material in the thesis. The original diagrams on which this review is based render the thesis as a whole much more accessible, which is a key consideration for a work such as this which crosses traditional subject boundaries in mathematics. A numerical perspective on bundle elements is emphasized.

- *Theoretical developments.* We have explored in detail the much-overlooked Hopf bundle structure $U(1) \to S^{2n-1} \to \mathbb{C}P^{n-1}$ intrinsic to every copy of $\mathbb{C}^n$, and identified the significance of local coordinates, connection forms, parallel transport and the resulting phase quantity in this context. In doing so we have elucidated the mathematical foundation underlying the apparently simple process of integrating a connection 1-form along a path in the Hopf bundle. We have produced a conjecture concerning the meaning of the phase; i.e. that in linear systems of the specific form considered, the Hopf bundle phase associated with a closed path generated in the proposed manner by a closed path in parameter space reflects precisely the number of discrete eigenvalues of the linear system contained within that path. We have explored and refined the quaternionic matrix description of the $S^1 \to S^3 \to S^2$ Hopf bundle, providing explicit new descriptions of the horizontal and vertical subspaces and their relationships to the group action; we have proved that the natural connection is the only connection for this bundle. We have derived the parallel transport/phase equation for this reduced quaternionic matrix case, and in doing so have provided yet another new, intuitive perspective on the geometry of the Hopf bundle, demonstrating explicitly how the horizontal/vertical splitting relates to linear ODE dynamics within the bundle.

- *Computational applications.* We have developed a number of algorithms for calculating the Hopf bundle phase associated with specific types of paths in $\mathbb{C}^n$, both using the quaternionic matrix framework for the $\mathbb{C}^2$ case, and the general framework for the $\mathbb{C}^n$ case. We have conducted and reported on a wide range of numerical experiments involving calculating phases associated with the various paths, for a range of systems. We have thus identified many of the

factors affecting the outcomes of the computations, including: the type of the path in $\mathbb{C}^n$ (i.e. $\gamma_1, \gamma_2, \gamma_3$), and for γ_3 paths, the properties of the generating path in λ-space, such as loop radius, number of discrete eigenvalues contained therein, crossings of continuous spectrum and asymptotic limit approximation values L, L'. The results have provided a great deal of supporting evidence for the central conjecture, although there is also a high level of complexity in the results which still requires deciphering. Again this would require further understanding of the mathematical role of the phase. We have applied the numerical schemes to several live research topics, and produced data indicative of important new results concerning discrete eigenvalue locations.

7.3 Future work directions

Due to the fundamental nature of both the geometrical framework investigated and the numerical results discovered, there are many possible directions for continuing this research. One of the main issues that needs addressing is the lack of knowledge of the mathematical properties of the phase. We have identified this quantity and its origins precisely, and have been able to observe some of its behaviour numerically, however we have only been able to conjecture the most interesting mathematical property suggested by the numerics, concerning the spectral properties of 1-parameter-dependent linear systems. Mathematical clarification of the situation is an open problem; it also appears to be quite a difficult problem. The connections between the work here and previous bundle-related results of Alexander, Gardner and Jones [36] need to be identified.

In addition we can continue to investigate phase changes in differential eigenvalue problems experimentally. The following specific issues are open to investigation:

- What is the role of the λ-loop radius r used in generating γ_3 paths? Is the pattern shown in Figure 6.7 found to apply in different systems, and if so does it have the same characteristics, i.e. is $r \approx 0.02$ always the smallest radius yielding the approximately-integer phase change result? Can we characterize the pattern more precisely through further numerical tests, and what ultimately is the cause of this behaviour?

- What happens if the closed loops in λ-space used to generate γ_3 paths are not circular? How does this relate to the previous point, i.e. could we instead

characterize phase change results in terms of the *area* contained within λ-loops? How does a given phase change result depend upon the proximity of the underlying λ-loop to a discrete eigenvalue or continuous spectrum?

- What happens if, as considered in Remark 6.3.1, we do not restrict ourselves to using eigenvectors of the asymptotic system as initial conditions for integrating the linear system and thus generating γ_2 paths - and hence γ_3 paths? This could be a very important issue because it may affect some of the assumptions made in this work, and may require the central conjecture to be modified slightly. More importantly however, it may also vastly increase the range of systems to which our results apply, by no longer requiring the system to satisfy the specific asymptotic conditions considered here. We have seen indications that this will be the case - that the asymptotic-eigenvalue initial condition is in fact redundant, because the phase change results are the same even in its absence - but this area does require further investigation.

- What is the effect on numerics of using alternative connections?

- Running the programs on faster computer systems would be of great benefit, since the larger simulations reported here have typically taken up to ten hours to complete on a standard 2.40Ghz machine. This would allow far more detailed testing of systems.

- Given a system of the standard format considered in this report ($u_x = A(x, \lambda)u$ with appropriate asymptotic conditions), is it of relevance whether it is a system induced on an exterior algebra space by some other more basic system, or not? We have not mentioned this issue at all so far, but it may be worth considering because much of the literature on the Evans function (to which this work is closely related) concerns the process of inducing systems on exterior algebra spaces in order to construct a suitable geometric framework in which the Evans function method will operate successfully. For example the HS-pulse system of Section 6.1 is in fact an induced system on $\bigwedge^2(\mathbb{C}^4)$ (derived in [5]), whereas the Taylor-Goldstein system of Section 6.2 is not. Yet they are both amenable to our analysis because they are of our standard format, and they both yield numerical results following patterns in support of the central conjecture.

- As a final thought, it may be worth considering how to deconstruct $\mathbb{C}^n$ in an analogous manner using bundle structures others than the $U(1)$-Hopf bundle chosen here. For example what about the quaternion-based $SU(2)$-Hopf bundle $S^3 \to S^7 \to S^4$, or indeed other generalized Hopf fibrations? Could this lead to a more complicated multi-dimensional phase quantity? Or perhaps we can extend the analysis to include the general case principal $U(k)$-bundle of the Stiefel manifold over the Grassmannian, $U(k) \to \mathrm{St}_{\mathbb{C}}(k,n) \to \mathrm{Gr}_{\mathbb{C}}(k,n)$, of which our work is just the simplest, $n = 1$ case.

It may well transpire that the most realistic method for continuing to investigate the topics reported in this thesis will be to carry out a whole host of detailed numerical experiments such as those listed above, in order to gradually build up a reliable picture of the numerical properties of the Hopf phase quantity. It is envisaged that this approach could eventually lead to a level of insight sufficient to begin forming the concrete mathematical characterization of the phase quantity required for any scientifically rigorous statements to be made and - hopefully - applied to real physical systems in future.

References

[1] Allen, L. and Bridges, T.J. Numerical exterior algebra and the compound matrix method. *Numer. Math.*, **92**:197–232, 2002.

[2] Allen, L. and Bridges, T.J. Flow past a swept wing with a compliant surface: stabilizing the attachment-line boundary layer. *Stud. Appl. Math.*, **110**:333-349, 2003.

[3] Allen, L. and Bridges, T.J. Hydrodynamic stability of the Ekman boundary layer including interaction with a compliant surface: a numerical framework. *Euro. J. Mech. B/Fluids*, **22**:239–258, 2003.

[4] Pego, R.L., Smereka, P. and Weinstein, M.I. Oscillatory instability of traveling waves for a KdV-Burgers equation. *Physica D*, **67**:45–65, 1993.

[5] Afendikov, A.L. and Bridges, T.J. Instability of the Hocking-Stewartson pulse and its implications for three-dimensional Poiseuille flow. *Proc. R. Soc. Lond. A*, **457**:257–272, 2001.

[6] Bridges, T.J., Derks, G. and Gottwald, G. Stability and instability of solitary waves of the fifth-order KdV equation: a numerical framework. *Physica D*, **172**:190–216, 2002.

[7] Page, D.N. Geometrical description of Berry's phase. *Physical Review A*, **36**:3479–3481, 1987.

[8] Bohm, A., Boya, L.J. and Kendrick, B. Derivation of the geometrical phase. *Physical Review A*, **43**:1206–1210, 1991.

[9] Bohm, A., Mostafazadeh, A., Koizumi, H., Niu, Q. and Zwanziger, J. *The Geometric Phase In Quantum Systems*. Springer, 2003.

[10] Lee, J.M. *Introduction to Smooth Manifolds*. Springer-Verlag, 2003.

[11] Morita, S. *Geometry of Differential Forms.* American Mathematical Society, 2001.

[12] Kobayashi, S. and Nomizu, K. *Foundations of Differential Geometry Volume 1.* Wiley, 1996.

[13] Isham, C.J. *Modern Diffrential Geometry For Physicists, 2nd Ed.* World Scientific, 2003.

[14] Chruściński, D. and Jamiołkowski, A. *Geometric Phases in Classical and Quantum Mechanics.* Birkhauser, 2004.

[15] Sternberg, S. *Lectures on Diffrential Geometry.* AMS Chelsea, 1983.

[16] Walschap, G. *Metric Structures in Diffrential Geometry.* Springer, 2004.

[17] Spivak, M. *Differential Geometry Volume II.* Publish or Perish Inc., 1979.

[18] Higham, D.J. and Higham, N.J. *Matlab Guide Second Edition.* Society For Industrial And Applied Mathematics, 2005.

[19] Abraham, R., Marsden, J.E. and Ratiu, T. *Manifolds, Tensor Analysis, and Applications.* Springer-Verlag, 1998.

[20] Barden, D. and Thomas, C. *An Introduction To Differential Manifolds.* Imperial College Press, 2003.

[21] Chern, S.S., Chen, W.H. and Lam, K.S. *Lectures On Differential Geometry.* World Scientific, 2000.

[22] Cushman, R.H. and Bates, L.M. *Global Aspects of Classical Integrable Systems.* Birkhauser, 1997.

[23] Bridges, T.J. The Orr-Sommerfeld equation on a manifold. *Proc. Roy. Soc. Lond. A*, **455**:3019–3040, 1999.

[24] Humpherys, J. and Zumbrun, K. An efficient shooting algorithm for Evans function calculations in large systems. *Physica D*, **220**:116–126, 2006.

[25] Hanson, A.J. *Visualizing Quaternions.* Elsevier, 2006.

[26] Drury, L.O. Numerical solution of Orr-Sommerfeld-type equations. *J. Comput. Phys.*, **37(1)**:133–139, 1980.

[27] Hairer, E., Lubich, C. and Wanner, G. *Geometric Numerical Integration.* Springer, 2002.

[28] Edelman, A., Arias, T.A. and Smith, S.T. The geometry of algorithms with orthogonality constraints. *SIAM J. Matrix Anal. Appl.*, **20**:303–353, 1998.

[29] Bridges, T.J. and Reich, S. Computing Lyapunov exponents on a Stiefel manifold. *Physica D*, **156**:219–238, 2001.

[30] Hou, B. and Hou, B. *Differential Geometry For Physicists.* World Scientific, 1997.

[31] Berry, M.V. Quantal phase factors accompanying adiabatic changes. *Proc. R. Soc. A*, **392**:45–57, 1984.

[32] Berry, M.V. Classical adiabatic angles and quantal adiabatic phase. *J. Phys. A*, **18**:15–27, 1985.

[33] Berry, M.V. The quantum phase, five years after, in *Geometric Phases in Physics,* eds. A. Shapere, F. Wilczek. World Scientific, 1989.

[34] Hannay, J.H. Angle variable holonomy in adiabatic excursion of an integrable Hamiltonian. *J. Phys. A: Math. Gen.*, **18**:221–230, 1985.

[35] Berry, M.V. and Hannay, J.H. Classical non-adiabatic angles. *J. Phys. A*, **21**:L325–331, 1988.

[36] Alexander, J., Gardner, R. and Jones, C. A topological invariant arising in the stability analysis of travelling waves. *J. Reine. Angew. Math.*, **410**:167–212, 1990.

[37] Nii, S. An extension of the stability index for traveling wave solutions and its application for bifurcations. *SIAM J. Math. Anal.*, **28**:402–433, 1997.

[38] Austin, F.R. and Bridges, T.J. A bundle view of boundary value problems: generalizing the Gardner-Jones bundle. *J. Differential Equations*, **189**:412–439, 2003.

[39] Weinstein, M. Modulational stability of ground states of nonlinear schrödinger equations. *SIAM J. Math. Anal.*, **16**:472–491, 1985.

[40] Kapitula, T. Stability criterion for bright solitary waves of the perturbed cubic-quintic Schrödinger equation. *Physica D*, **116**:95–120, 1998.

[41] Liu, X.S., Qi, Y.Y., He, J.F. and Ding, P.Z. Recent progress in symplectic algorithms for use in quantum systems. *Commun. Comput. Phys.*, **2**:1–53, 2007.